
# The physics of Ion Coulomb Crystals: Thermodynamics, Quantum control, and Quantum Simulators

**GA No. 249958**

## Deliverable No. D4.1

## Characterization of decoherence and noise rate limit in the ion-trap setups

Partner responsible for the deliverable:
MPQ/ALU, USIEG, UCM

| Dissemination level | | |
|---|---|---|
| PU | Public | X |
| PP | Restricted to other programme participants (including the Commission Services) | |
| RE | Restricted to a group specified by the consortium (including the Commission Services) | |
| CO | Confidential, only for members of the consortium (including the Commission Services) | |


The research leading to these results has received funding from the European Union's Seventh Framework Programme (FP7/2007-2013) under grant agreement n° 249958.



| Deliverable: D4.1 | Status: | | |
|---|---|---|---|
| Due date: May 31, 2012 | Achieved | Partially achieved | Not achieved |
| Delivery date: May 2012 | X | | |

**Title: Characterization of decoherence and noise rate limit in the ion trap setups**

**Short Description:** Reports on the characterization of the sources and the properties of noise and decoherence of the ion trap environment, the limitations these impose on the quantum mechanical coherence and possible ways to mitigate those.

**Work achieving the deliverable:** The work contributing to this deliverable is threefold. First, the rates of noise and decoherence in a surface ion trap have been investigated theoretically and experimentally, with the results reported in [1]. Second, two and more qubit entanglement operations exploiting magnetic field gradients have been implemented, revealing the reduced decoherence caused by highly excited motional states on operations crucial for experimental quantum simulations addressing quantum spin Hamiltonians, the results published in [2]. Third, further investigations have been pursued and related proposals have been published [3,4,5] how to further mitigate the impact of decoherence. Two manuscripts propose to increase the exploitable interaction rates for experimental quantum simulations within a new toolbox by exploiting phonons directly (non-perturbative approach) to simulate particles [3,4]. The third proposes robust trapped-ion quantum logic gates by continuous dynamical decoupling – mitigating the influence of noise sources, such as magnetic field fluctuations on operations crucial for experimental quantum simulations on quantum spin Hamiltonians [5].

**References:**

[1] "Experimental quantum simulations of many-body physics with trapped ions", Ch. Schneider, D. Porras, and T. Schaetz, Rep. Prog. Phys. **75**, 024401 (2012)

[2] "Designer spin-pseudo-molecule implemented with trapped ions in a magnetic gradient", A. Khromova, Ch. Piltz, B. Scharfenberger, T. F. Gloger, M. Johanning, A. F. Varón, and Ch. Wunderlich, Phys. Rev. Lett. 108, 220502 (2012)

[3] "Synthetic Gauge Fields for Vibrational Excitations of Trapped Ions", A. Bermudez, T. Schaetz, D. Porras, Phys. Rev. Lett. 107, 150501 (2011)

[4] "Photon-Assisted-Tunneling Toolbox for Quantum Simulations in Ion Traps", A. Bermudez, T. Schaetz, D. Porras, New J. Phys. 14, 053049 (2012)

[5] "Robust trapped-ion quantum logic gates by continuous dynamical decoupling", A. Bermudez, P. O. Schmidt, M. B. Plenio, and A. Retzker, Phys. Rev. A 85, 040302(R)(2012)

Partners owning: UCM, USIEG, MPQ/ALU

Partners contributed: UCM, USIEG, MPQ/ ALU, UULM.ITP

Made available to: everybody (published articles): see above

Rep. Prog. Phys. **75** (2012) 024401 (33pp) doi:10.1088/0034-4885/75/2/024401

# Experimental quantum simulations of many-body physics with trapped ions

**Ch Schneider**[1,2], **Diego Porras**[3] **and Tobias Schaetz**[1,2]

[1] Max-Planck-Institut für Quantenoptik, Hans-Kopfermann-Straße 1, 85748 Garching, Germany
[2] Albert-Ludwigs-Universität Freiburg, Physikalisches Institut, Hermann-Herder-Str. 3, 79104 Freiburg, Germany
[3] Departamento de Física Teórica I, Universidad Complutense, 28040 Madrid, Spain

E-mail: tobias.schaetz@mpq.mpg.de

Received 24 August 2009, in final form 10 August 2011
Published 17 January 2012
Online at stacks.iop.org/RoPP/75/024401

**Abstract**
Direct experimental access to some of the most intriguing quantum phenomena is not granted due to the lack of precise control of the relevant parameters in their naturally intricate environment. Their simulation on conventional computers is impossible, since quantum behaviour arising with superposition states or entanglement is not efficiently translatable into the classical language. However, one could gain deeper insight into complex quantum dynamics by experimentally simulating the quantum behaviour of interest in another quantum system, where the relevant parameters and interactions can be controlled and robust effects detected sufficiently well. Systems of trapped ions provide unique control of both the internal (electronic) and external (motional) degrees of freedom. The mutual Coulomb interaction between the ions allows for large interaction strengths at comparatively large mutual ion distances enabling individual control and readout. Systems of trapped ions therefore exhibit a prominent system in several physical disciplines, for example, quantum information processing or metrology. Here, we will give an overview of different trapping techniques of ions as well as implementations for coherent manipulation of their quantum states and discuss the related theoretical basics. We then report on the experimental and theoretical progress in simulating quantum many-body physics with trapped ions and present current approaches for scaling up to more ions and more-dimensional systems.

(Some figures may appear in colour only in the online journal)

## Contents



 

## 1. Introduction

Simulations and deeper understanding of the dynamics of some tens of interacting spins are already intractable with the most powerful classical computers. For instance, the generic state of 50 spin-1/2 particles is defined by $2^{50}$ numbers and to describe its evolution a $2^{50} \times 2^{50}$ matrix has to be exponentiated [1]. Recently, one of the ten most powerful supercomputers, JUGENE in Jülich, was exploring this regime. The current record was set by simulating a system of 42 quantum bits (qubits), equivalent to 42 spin-1/2 particles [2, 3].

In any case, it will not help to increase the impressive classical calculation capabilities to simulate only slightly larger quantum systems. Each doubling of the computational power will just allow the addition of one spin/qubit to the system (approximately after two years, according to Moore's law [4]). Furthermore, simply pursuing this path of exponential growth in the computer's classical capabilities would require an exponential shrinking of its electronic components[4]. The structure size currently amounts to approximately 30 nm, a distance spanned by roughly 100 atoms. If gifted engineers further miniaturize the sizes of their structures, 'currents' of a few electrons will 'flow' on 'wires' spanned by a few atoms only. As a consequence, quantum effects will have to be considered for future classical computers, leading to serious consequences. Electrons charging a capacitor, for example, currently realize a storage of logical information: a charged capacitor represents a 'one', a discharged capacitor a 'zero'. What, if the few electrons, classically well caught within the potential of the capacitor, follow their natural quantum mechanical paths and simply escape through the walls by tunnelling?

However, allowing for quantum effects in a controlled way might also be exploited as a feature. Richard Feynman originally proposed [5] using a well controlled quantum system to efficiently track problems that are very hard to address on classical computers and named the device a 'quantum computer' (QC). Nowadays his proposal can be seen closer to the description of a quantum simulator (QS)[5]. In any case, his idea has been theoretically investigated and further developed to the concept of a universal QC. Fulfilling a well-defined set of prerequisites, known as diVincenzo's criteria [6, 7], should make possible running any classical and quantum algorithm by a stroboscopic sequence of operations. These have to act on single qubits, for example, changing their state, and on pairs of qubits performing changes on one qubit, conditional on the state of its mate.

Hundreds of groups worldwide work on many approaches in different fields of atomic, molecular and solid-state systems to realize their version of the envisioned QC. For a concise review see, for example, [8].

However, even assuming an ideal system and perfect operations will require the control of the order of $10^3$ logical qubits as a basis for translating any algorithm or the quantum dynamics of a complex system into a sequence of stroboscopic gate operations on a potential universal QC [9]. Residual decoherence will cause computational errors and must be minimized to allow for high operational fidelities (∼99.99%–99.9%) [10]. At present, only then the errors could be overcome by quantum error correction, at the price of a reasonable but still tremendous overhead of ancilla qubits, approximately another 100 per logical qubit. In total, of the order of $10^5$ qubits are required. Even though there appear to be no fundamental obstacles for enhancing the fidelities of the operations and for scaling the size of the systems [11], there is still challenging technological development ahead. The realization of a universal QC is not expected within the next decades.

A shortcut via analogue QS has been taken into consideration [5] to allow deeper insight into the dynamics of quantum systems. 'Analogue' emphasizes that the dynamics of the system are not translated into an algorithm of gate operations on subsets of qubits. In contrast, a system of quantum particles is required, where (1) the initial state and its dynamics can be precisely controlled, (2) as many relevant parameters as possible manipulated and (3) the readout of the important characteristics of the final state performed in an efficient way. If the system's evolution was governed by a Hamiltonian suspected to account for the quantum effects of interest, we would be able to experimentally investigate the physics of interest isolated from disturbances, close to Feynman's original proposal. The requirements on the number of quantum particles and fidelities of operations for analogue QS are predicted to be substantially relaxed compared with QC [12]. However, it remains to be investigated which

[4] The electronic components are arranged in two dimensions and, only recently, the third dimension is exploited. However, sufficient cooling has to be provided.

[5] Depending on the context, the abbreviations 'QC' and 'QS' may also stand for quantum computation and quantum simulation, respectively.

realistic assumption on different sources of decoherence in the particular system will lead to a sufficiently small impact on the dedicated QS [13]. It is predicted that QS are less prone to decoherence, for example, in simulating robust effects such as quantum phase transitions (QPT). Therefore, they do not require any precautions in contrast to QC, which suffer from the costly overhead due to quantum error correction. It was even proposed to establish decoherence as an asset [1]. In this context, decoherence is not to be seen as a source of errors, as in the field of universal QC, but as a resource to simulate its natural counterpart. For example, decoherence is suspected to be responsible and required for enhanced efficiencies of (quantum) processes in biological systems at $T \sim 300\,\mathrm{K}$ [14, 15].

To discuss the different requirements for different analogue QS, we can distinguish between two categories of simulations. One category deals with problems where QS provide a simulated counterpart that allows intriguing questions that are not directly tractable in the laboratory to be experimentally addressed. Examples are highly relativistic effects such as Hawking and Unruh radiation or the zitterbewegung of a freely moving particle predicted by Dirac's equation (see also [12]). The second category of simulations deals with objectives that are (probably fundamentally) not accessible with classical computation, for example, the complex quantum dynamics of spins in solid-state systems, as mentioned above. A promising strategy is to initialize an analogue QS in a state that can be prepared easily in the system of choice according to step (1) introduced above. Evolving the system adiabatically by changing its parameters according to (2) allows a new state to be reached that is hard or impossible to reach otherwise, for example, via a QPT. The aim here is not to simulate the effects including all disturbances and peculiarities, because the analogue QS would then become as complex as the system to be simulated. The aim can be to investigate whether the simplified model still yields the effects observable in nature and, thereby, to gain a concise deeper understanding of their relevant ingredients. However, there remains room for the important discussion as to whether the specific dynamics emulate nature or simulate the implemented model (Hamiltonian) and whether the results allow the drawing of further conclusions.

In any case, it has to be emphasized that analogue QS are intrinsically not universal. That is, different realizations of a QS will allow the simulation of different systems. Even more important, different approaches for the identical models (Hamiltonians) might allow cross-checking of the validity of the QSs [16].

There are several systems proposed to implement analogue QS, offering different advantages [12] to address the physics in many-body systems. One of them consists of neutral atoms within optical lattices [17–20]. Another promising candidate is based on trapped ions [21–23], originally suggested by Cirac and Zoller in 1995 [24] in the context of QC. Trapped ions already compete at the forefront of many fields, were ultimate accuracy and precision is required, such as metrology (see, for example, [25]). Trapped ions offer unique operational fidelities, individual addressability and short- as well as long-range interactions due to Coulomb forces.

Many models of both categories of QS are promising candidates or already addressed by trapped ions. Examples for the first category are emanating from the fields of cosmology [26–28], relativistic dynamics [29–34], quantum field theory [35], quantum optics [36] including quantum walks as a potential tool for QSs [15, 37–40], chemistry [41], and biology [42, 43]. For the second category, quantum spin Hamiltonians [21], Bose–Hubbard [22] and spin–boson [44] models were proposed to describe solid-state systems and their simulation would allow the observation and investigation of a rich variety of QPTs [45]. A summary and concise description of theoretical proposals on QS of both categories based on trapped ions and first experimental results up to the year 2008 can be found in [46].

This report aims to describe the current status of the field of experimental, analogue QS addressing many-body physics, its challenges and possible ways to address them. The first proof-of-principle experiment was achieved [47] and extended recently [48, 49] on a few trapped ions in linear radio-frequency (RF) traps. The main challenge for QS remains to scale up towards 50–100 ions or even beyond. A simulated system of this size would reach far beyond the regime accessible via classical computation and, even more importantly, allow open scientific questions to be addressed.

The report is organized as follows. In section 2 we introduce the tools available for QS by briefly summarizing the types of traps, different ions species and different technical implementations of the control of the electronic and motional degrees of freedom. In section 3 we derive the mathematical description based on [21, 50, 51]. We aim at extending the existing formalism to be directly applicable to more dimensions and individual trapping conditions envisioned in arrays of ions. We apply this formalism to a basic building block of QC, a two qubit phase gate on the radial modes measured in our group, and emphasize similarities and differences between the application of similar operations for analogue QS. This section is supplemented by a detailed appendix. In section 4, we interpret the interactions in the context of analogue QS, which should be sufficient for understanding the subsequent discussion of the experimental implementations without going through the details of section 3. In section 5, we first depict the proof-of-principle experiments on a few trapped ions in linear RF traps. Based on the state-of-the-art capabilities we present in the second part of this section a summary of proposals to study many-body physics in a variety of solid-state systems. The two following sections are dedicated to two proposals aiming for scaling up the systems. In section 6, we discuss potential realizations of a two-dimensional array of RF surface-electrode traps. They are conceptually similar to promising approaches in Penning traps [50, 52, 53]. We will also introduce an alternative approach based on ions in optical traps in section 7, thus, trying to combine the advantages of trapped ions and optical lattices. Finally, we conclude in section 8.

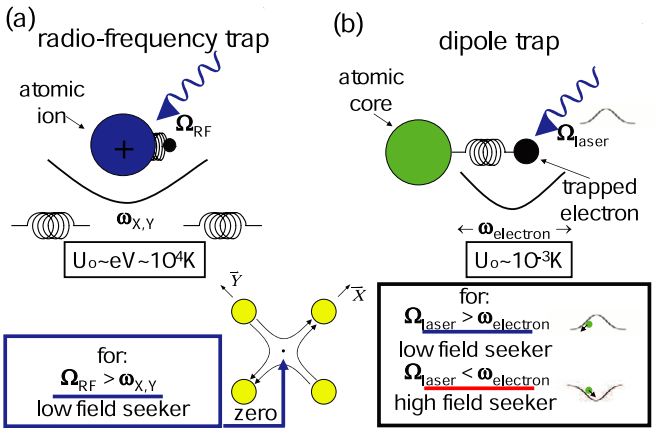


**Figure 1.** Two concepts for trapping charged particles. Both concepts require electromagnetic fields (blue sinusoidal arrow). (*a*) In RF traps, an RF field at frequency $\Omega_{RF}/(2\pi)$ applied to quadrupole electrodes (yellow circles) interacts with a charged atom directly. The time averaged confining pseudopotential allows the ion to oscillate at frequencies $\omega_{X/Y}/(2\pi)$ approximately an order of magnitude smaller than $\Omega_{RF}/(2\pi)$. Since $\Omega_{RF} > \omega_{X/Y}$, the trapping field can be understood as blue-detuned with respect to the 'resonance' frequency $\omega_{X/Y}$, consequently the ion will seek the field minimum in the centre of the quadrupole (field lines indicated by black arrows). Typical depths of the pseudopotential are of the order of $k_B \times 10^4$ K. (*b*) In optical traps, the optical field is typically applied via laser beams that provide an intensity dependent ac Stark shift of the electronic levels of the atom or ion. The frequency $\Omega_{laser}$ of the laser can be detuned blue (red) with respect to the relevant electronic resonance frequency $\omega_{electron}$ and therefore forces the atom/ion to seek low (high) fields. Typical depths of the pseudopotential are of the order of $k_B \times 10^{-3}$ K.

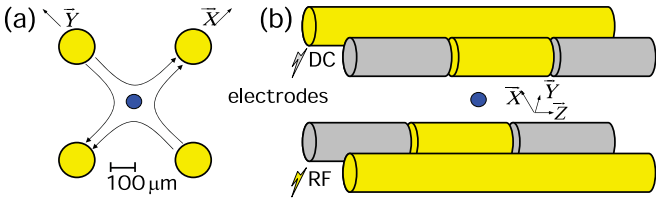


**Figure 2.** Schematic of the three-dimensional electrode geometry of a linear RF trap. (*a*) Cross section through the central quadrupole electrodes (yellow) providing the radial confinement for the ion (blue disk). (*b*) Side view, where segments (grey) are used to apply dc voltages providing a static potential well along the $Z$-axis. Combined with the radial ($X$, $Y$) pseudopotential due to the RF field, a three-dimensional confinement is achieved. The ion is stored in ultra-high vacuum and is well protected against disturbances from the environment. However, the fairly open geometry allows access to the external (motional) and internal (electronic) degrees of freedom, for example, with focused laser beams.

## 2. Tools required for experimental quantum simulations

In this section, we describe the requirements to implement analogue QS based on trapped ions. Most of these tools have been developed over the last decades, many for the purpose of quantum information processing (QIP) with the main focus on QC.

### *2.1. Ion traps and Coulomb crystals*

Isolating and trapping of individual particles as well as the precise control of their motional (external) degrees of freedom is key for many high precision measurements. Several trapping concepts have been developed for and implemented with ions, such as RF traps [54], Penning traps [55] and optical traps [56]. The physics of these devices, for example, of RF traps and optical dipole traps, is closely related. Electromagnetic multipole fields act on the charge or induce electric dipole moments. The resulting forces on the particles lead in time average to a confining pseudopotential. The two concepts are compared in figure 1.

However, there was a delay of more than a decade between trapping charged atoms in RF fields [57, 58] and trapping neutral particles with optical fields [59]. One explanation is that RF traps provide potential depths of the order of several eV $\approx k_B \times 10^4$ K, while optical traps typically store particles up to $k_B \times 10^{-3}$ K only. This discrepancy is mainly due to the comparatively large Coulomb force that RF fields can exert on charges. The RF field at typical frequencies $\Omega_{RF}/(2\pi) =$ 10 MHz–100 MHz directly acts on the massive ion. The related motional frequencies within the deep pseudopotential amount to a few MHz. Optical fields, in contrast, oscillate more than six orders of magnitude faster: too fast for the massive atomic core to follow. In a simplified picture, the optical field has to induce a dipole moment of the electron and the atomic core first to allow for a subsequent interaction of the dipole with the optical field. Similar to RF traps, the optical field results in a pseudopotential, which is close to identical for neutral atoms and charged ions [60].

Here we focus first on ions in linear RF traps. The concept for the radial confinement is depicted in figures 1(*a*) and 2. The RF field applied to two opposing electrodes of the quadrupole can provide a radially confining pseudopotential. Similar to a quadrupole mass filter, one can find voltages for given parameters (electrode geometry and mass/charge ratio of the ion species) that allow for stable confinement in two dimensions. Additional dc voltages add a static harmonic potential to complete the three-dimensional confinement that can be assumed to be harmonic. Dependent on the application, these dc voltages can be applied to electrodes realized as rings or needles along the axis or by a segmentation of the quadrupole electrodes (see figure 2(*b*)). A confined ion will oscillate with frequency $\omega_Z/(2\pi)$ along the trap axis and with frequencies $\omega_{X/Y}/(2\pi)$ in the radial directions. The radial oscillation is superimposed by a fast oscillation at frequency $\Omega_{RF}/(2\pi)$ (so-called micromotion), which increases with increasing distance of the ion from the trap centre, such that the RF field does not vanish anymore.

Typical parameters for conventional setups are a minimal ion–electrode distance $h \sim 100\,\mu$m –1000 $\mu$m allowing for RF voltages of the order of 1000 V.

Different laser cooling schemes can be applied to reduce the total energy of motion of the ion [51]. Doppler cooling [61–64] of several ions already allows a regime to be entered, where the kinetic energy ($k_B T \sim$ mK) of the ions becomes significantly smaller than the energy related to the mutual Coulomb repulsion. Hence, the ions cannot exchange their position anymore. A phase transition from the gaseous (liquid)

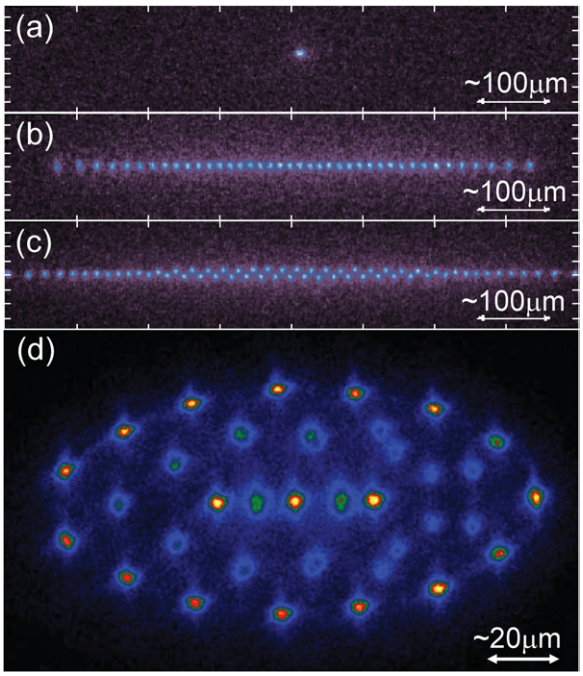


**Figure 3.** Fluorescence images of laser-cooled ions in a common confining potential of a linear RF trap (see figure 2), forming differently structured Coulomb crystals. (*a*) A single ion ($Mg^+$). (*b*) A linear chain of 40 ions at $\omega_{X/Y} \gg \omega_Z$. The axis of the chain coincides with the trap $Z$-axis, which is identically orientated in the rest of the images. (*c*) A linear chain embedding a two-dimensional zigzag structure of 60 ions for $\omega_{X/Y} > \omega_Z$. (*d*) A three-dimensional structure of more than 40 ions at $\omega_{X/Y} \gtrsim \omega_Z$. The enhanced signal-to-noise ratio in (*d*) is achieved by extended exposure. Structural phase transitions can be induced between one-, two- and three-dimensional crystals, for example by reducing the ratio of radial to axial trapping frequencies.

plasma to a crystalline structure occurs [65, 66]. On the one hand, the resulting Coulomb crystals (see figure 3) provide many similarities with solid state crystals already partially explaining why Coulomb crystals appear naturally suited to simulate many-body physics. (1) The ions reside on individual lattice sites. (2) The motion of the ions (external degree of freedom) can be described easiest in terms of common motional modes with the related quanta being phonons. The phonons in Coulomb crystals allow long-range interactions to be mediated between the spins associated with the ions. In a different context, the phonons can also be interpreted as bosonic particles, for example, capable of tunnelling between lattice sites simulated by the ions (see also section 5.2). On the other hand, there are advantageous differences compared with solid-state crystals. (3) Coulomb crystals typically build up in ultra-high vacuum ($(10^{-9}$–$10^{-11})$ mbar) and are very well shielded against disturbances from the environment, thus providing long coherence times. (4) Coulomb crystals feature lattice constants of a few micrometres (see figure 3), dependent on the trapping potential counteracting the mutual Coulomb repulsion. Compared with a solid, where distances are of the order of Ångstroms ($10^{-10}$ m) the density of the structure in one dimension is reduced by five, in three dimensions by fifteen orders of magnitude. This allows for individual addressing of the ions and for individual preparation, control and readout of their electronic and motional states. (5) The Coulomb interaction between the charged ions is not shielded within the crystal, as in Coulomb crystals the charge of all ions has the same sign in contrast to ionic crystals in solid-state systems. However, it should be mentioned that, as opposed to quantum solids, the quantum statistics of the ions is not relevant due to the suppression of the mutual exchange processes.

It has to be pointed out that it is possible to deterministically achieve phase transitions between different structures of Coulomb crystals for large numbers of ions [65, 66]. When the ratio of radial to axial confinement is reduced or the number of confined ions is increased, we observe the transition from a linear chain of ions via a two-dimensional zigzag structure to a three-dimensional structure (see figures 3(*b*)–(*d*)).

Despite the unique conditions in Coulomb crystals in linear RF traps and the high fidelities of operations, current experimental approaches to QS (and QC) are still limited to a small number of ions. The approaches include of the order of ten ions arranged in a linear chain [49, 67]. This is accomplished by choosing the radial confinement much stronger than the axial one. The linear chain orientates along the weakest ($Z$) direction, where tiny oscillations of the cooled ions around the minimum of the pseudopotential ($X$ and $Y$) and thus micromotion still remains negligible.

For the purposes of a QC and QS, scaling to a larger number of spins and more dimensions while keeping sufficient control over all required degrees of freedom remains the challenge of the research field. Using longer linear chains confined in anharmonic axial potentials [68] might provide a way to reach a number of ions in the system that in principle already exceeds capabilities of a classical supercomputer. Another way might be the use of RF ring traps offering periodic boundary conditions for static Coulomb crystals [65, 66] and even (more-dimensional) crystalline beams of ions [69–71]. A microfabricated ring trap is currently being developed and fabricated at Sandia National Laboratories [72].

The two main limitations for further scaling of the number of ions in a common potential, from a practical point of view, are (1) the emergence of $3N$ normal modes for $N$ ions plus their sum and difference frequencies that lead to an increasingly crowded phonon spectrum (already for each spatial dimension separately). Individual spectral components become difficult to identify and off-resonant couplings to 'spectator' transitions [50] are hard to avoid. However, under certain conditions, QSs are predicted to allow for coupling to all modes simultaneously, see for example [21]. (2) QSs based on ions in large, more-dimensional Coulomb crystals suffer from additional challenges, for example, intrinsic micromotion (due to the displacement from the minimum of the pseudopotential), an inhomogeneous ion spacing (due to space charge effects) and the coupling between modes of all three spatial dimensions.

One approach for scalability might be to generate a spin-off from the QIP community based on their new concept of a surface-electrode geometry for RF traps [73, 74] (see figure 14). Currently, this design is tested with the aim to allow for networks of interconnected linear traps. This constitutes a promising possibility to realize the multiplex architecture of

memory and processor traps for universal QC [75]. However, for QS we need a miniaturized array of traps allowing for more-dimensional interactions, as discussed in section 6.

It has to be emphasized that there are other concepts for trapping ions, a prominent one being Penning traps. Penning traps provide trapping potentials of similar parameters as RF traps. A strong, static magnetic field and a dc electric field yield a stable confinement of large, rotating Coulomb crystals. Storing many cool ions in a Penning trap, naturally provides, for example, a large triangular lattice of ions [76–78] that is also predicted to be well suited for QS [79]. Promising results are on their way [52, 53]. Another challenging proposal for QS involves trapping ions optionally simultaneously with atoms in optical lattices [80] (see section 7).

### 2.2. Ions

A large variety of different atomic ions have already been used for the purpose of QIP. Every ion or, more specifically, every isotope has different properties, for example, regarding the level scheme or the charge–mass ratio, and thus can meet different requirements of a QS. However, they all have a single valence electron leading to an alkali-like level scheme. Most prominent are the earth alkali ions $Be^+$, $Mg^+$, $Ca^+$, $Sr^+$ and $Ba^+$. A similar electronic structure has $Zn^+$, $Cd^+$ and $Hg^+$, followed by $Yb^+$ [81].

Typically, two electronic levels with sufficiently long coherence times are chosen as qubit or spin states $|\downarrow\rangle$ and $|\uparrow\rangle$, respectively. (In principle, however, the restriction to two states is not required and the use of up to 60 states has been proposed for (neutral) holmium [82].) The types of qubits can be divided into two classes: in optical qubits, the states are encoded in two states with a dipole-forbidden transition at an optical frequency. An example is $^{40}Ca^+$ with $|\downarrow\rangle := |S_{1/2}\rangle$ and $|\uparrow\rangle := |D_{5/2}\rangle$. The lifetime of $|\uparrow\rangle$ is on the order of 1 s, which defines the upper bound for its coherence time. In hyperfine/Zeeman qubits, two sublevels from the ground state manifold are chosen as $|\downarrow\rangle$ and $|\uparrow\rangle$. An applied magnetic field lifts the degeneracy within the manifolds of electronic levels to allow for spectrally resolving the dedicated states. The states of hyperfine/Zeeman qubits have extremely long lifetimes and coherence times on the order of minutes have been observed [83, 84]. As an example for a hyperfine/Zeeman qubit, an excerpt of the level scheme of $^{25}Mg^+$ is shown in figure 4. The transition frequencies in hyperfine/Zeeman qubits are in the microwave regime.

### 2.3. Basic operations

The quantized oscillation of the ions in the harmonically approximated potential of the trap gives rise to motional states, which are typically expressed in terms of Fock states $|n\rangle$. Independent of the choice of qubit we will require three different types of couplings to electronic states and/or motional states to assemble the toolbox for QC and QS based on trapped ions (for details see section 3).

(a) *Coupling of the electronic states only* ($|\downarrow\rangle|n\rangle \rightleftarrows |\uparrow\rangle|n\rangle$). This operation can be used to implement Rabi flops between the electronic states and serves as a one-qubit gate of a potential QC. In the context of QS it can be interpreted as simulated magnetic field (see also section 3.2).

(b) *Coupling of the electronic and motional states* ($|\downarrow\rangle|n\rangle \rightleftarrows |\uparrow\rangle|n'\rangle$). This operation can drive Rabi flops between electronic states and different motional states, for example on the first red ($n' = n - 1$) or blue sideband ($n' = n + 1$) (see also section 3.2). It can be used to create entanglement between the electronic and motional states and is an important ingredient for both sideband cooling and the readout of the motional state (see below).

(c) *State-dependent forces (for example,* $|\downarrow\rangle|n\rangle \rightarrow |\downarrow\rangle|n+1\rangle$). These forces lead to state-dependent displacements. They can be used for conditional interactions between multiple ions, which are exploited for quantum gates (see sections 3.3 and 3.4) or effective spin–spin interactions in the simulation of quantum spin Hamiltonians (see section 3.5).

Operations (a)–(c) can be realized for both classes of qubits in the optical regime and for hyperfine/Zeeman qubits additionally via microwave fields [50, 51].

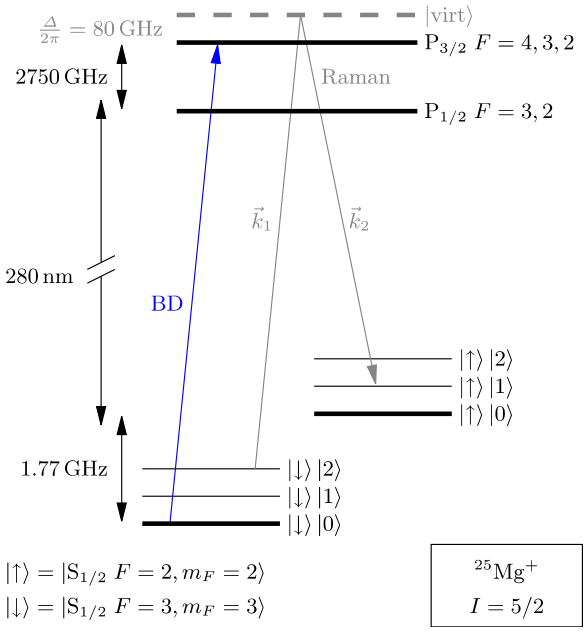


**Figure 4.** Excerpt of the level scheme of $^{25}Mg^+$ as an example of a hyperfine qubit (not to scale). $^{25}Mg^+$ has a nuclear spin of $I = 5/2$ and thus a hyperfine-split ground state ($S_{1/2}$, $F = 3$ and $S_{1/2}$, $F = 2$). By applying a static magnetic field of a few Gauss, the degeneracy of the Zeeman sublevels is lifted. The Doppler cooling laser (labelled 'BD') is $\sigma^+$ polarized and detuned red by $\Gamma/2 \approx 2\pi \times 20$ MHz from the cycling transition $S_{1/2}$, $F = 3$, $M_F = 3 \leftrightarrow P_{3/2}$, $F = 4$, $M_F = 4$. Here, $\Gamma$ denotes the linewidth of the P levels. The level $|\downarrow\rangle := |S_{1/2}, F = 3, M_F = 3\rangle$ and the level $|\uparrow\rangle := |S_{1/2}, F = 2, M_F = 2\rangle$ are chosen as qubit states or (simulated) spin states, respectively. The ion is optically pumped into $|\downarrow\rangle$ during cooling. The electronic state is read out by a variant of 'BD', which is resonant on the cycling transition. Hence, an ion in the state $|\downarrow\rangle$ will fluoresce, while an ion in state $|\uparrow\rangle$ is off-resonant by almost $50\Gamma$ and will remain dark. The motional states of one of the motional modes are indicated as 'ladders' on top of the electronic states. Two laser beams (labelled 'Raman') detuned by $\Delta$ from the $P_{3/2}$ level can be used to drive two-photon stimulated-Raman transitions between $|\downarrow\rangle$ and $|\uparrow\rangle$. A flop on the first red sideband is indicated by the arrows from $|\downarrow\rangle|2\rangle \rightarrow |\uparrow\rangle|1\rangle$.

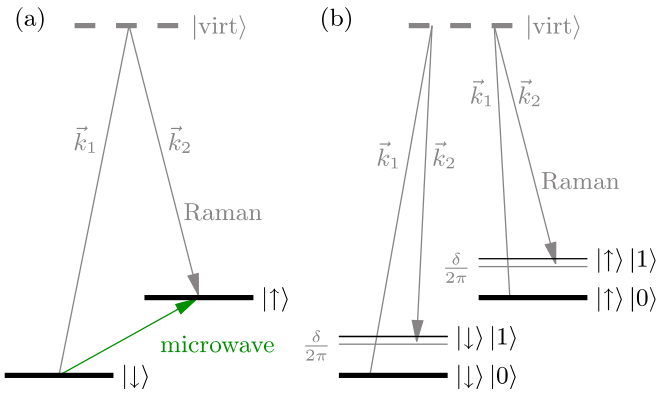


**Figure 5.** Implementations of different interaction types for hyperfine/Zeeman qubits. (*a*) An operation of type (a) can be implemented, for example, by two-photon stimulated-Raman transitions driven by a pair of laser beams (shown without motional dependence) or directly by a microwave field. These types of interactions can be used for single-qubit gates in QC and to simulate the effective magnetic field in the simulation of quantum spin Hamiltonians. (*b*) State-dependent forces (see type (c) in the text) can be created by two beams detuned by approximately the frequency of a motional mode. This interaction is used in the geometric phase gate for the displacement pulse [110, 123] or in the simulation of the quantum Ising Hamiltonian to create the effective spin–spin interaction [21, 47].

*Coupling via optical fields.* Optical qubit states can be linked by a single, nearly resonant laser beam with frequency $\omega_\mathrm{I}$ and wave vector $\vec{k}_\mathrm{I}$. Due to the lifetime of the $|\uparrow\rangle$ state of $1/\Gamma \sim 1$ s, the linewidth of the laser has to be very narrow ($\sim$1 Hz). Operations (a) and (b) can be implemented directly (see section 3.2). State-dependent forces (c) can be provided by a bichromatic light field (see, for example, [85–87] and also section 3.3).

In hyperfine/Zeeman qubits, the single laser beam can be substituted by two beams with frequencies $\omega_1$, $\omega_2$ and wavevectors $\vec{k}_1$, $\vec{k}_2$ driving two-photon stimulated-Raman transitions. The beams are detuned by $\Delta \gg \Gamma$ from a third level, for example, a P level (compare figure 4) with a typical lifetime $1/\Gamma$ of the order of few nanoseconds. In the mathematical treatment, this third level can be adiabatically eliminated for large detunings and the interaction gains the form of an interaction with a single beam of frequency $\omega_\mathrm{I} = |\omega_1 - \omega_2|$ and wavevector $\vec{k}_\mathrm{I} = \vec{k}_1 - \vec{k}_2$. The requirement of a narrow linewidth holds only for the difference frequency $\omega_\mathrm{I}$, which can be fulfilled comparatively easily: the two beams can be generated from the same laser using acousto-optical modulators driven by a stable microwave source, while the requirements on the frequency stability of the laser are relaxed. For operation (a), the frequency $\omega_\mathrm{I}$ has to (approximately) meet the transition frequency of the qubit states (see figure 5(*a*)). For operation (b), $\vec{k}_\mathrm{I}$ in addition must not vanish to achieve a sufficient momentum transfer to the ions, see figure 4 and section 3.2. Therefore, the two beams are typically orthogonal ($|\vec{k}_\mathrm{I}| \approx \sqrt{2}|\vec{k}_1|$) or counter-propagating ($|\vec{k}_\mathrm{I}| \approx 2|\vec{k}_1|$). The state-dependent forces (c) can be implemented by nearly resonant beams ($\omega_\mathrm{I} \approx 0$) and beam geometries as for operation (b) (see figure 5(*b*), sections 3.3–3.5 and section 4).

The main technical drawback of using two-photon stimulated-Raman transitions is decoherence due to spontaneous emission after off-resonantly populating the third level. This limitation can be mitigated by increasing the detuning $\Delta$ and the intensities $I_{1/2}$ of the beams, since the interaction strength scales with $I_{1/2}/\Delta$, while the spontaneous emission rate scales with $I_{1/2}/\Delta^2$.

*Coupling via microwave fields.* Alternatively, transitions between the electronic states in hyperfine/Zeeman qubits can be driven laser-less by microwave fields. This allows the direct realization of operation (a). However, due to the comparatively long wavelength and the related small momentum transfer ($|\vec{\hbar k}_\mathrm{I}| \to 0$), only negligible coupling to the motional modes can be achieved directly and additional efforts are required to provide operations (b) and (c) [88, 89]: by applying a static magnetic field gradient along the axis of an ion chain, the transition frequency between $|\downarrow\rangle$ and $|\uparrow\rangle$ becomes site-dependent due to position-dependent Zeeman shifts. The ions can be individually addressed by applying microwave fields with these site-dependent frequencies $\omega_\mathrm{I}$. In addition, this causes state-dependent forces as in the Stern–Gerlach experiment and allows for coupling to the motional modes. The main challenge here is to provide sufficiently large magnetic field gradients and to cope with state-dependent transition frequencies, if high operational fidelities are required (see, for example, [90]).

As an alternative to the static magnetic field gradients, alternating magnetic fields due to microwave currents in electrodes of surface-electrode traps (see section 6) have been proposed [91] and first promising results have been achieved [92, 93]. Due to the small height of the ion above the electrode in this type of trap, a sufficiently large ac Zeeman shift can be generated, which can be treated analogously to the ac Stark shift created by laser beams in two-photon stimulated-Raman transitions discussed above. However, the small height above the electrodes leads to further challenges (compare section 6) and high microwave powers are required.

### 2.4. Initialization and readout

*Initialization of motional and electronic states.* The initialization into one of the qubit states, for example $|\downarrow\rangle$, can be achieved with near-unity efficiency by optical pumping [94]. Regarding the motional modes, the initialization includes Doppler cooling in all three dimensions leading to a thermal state with an average phonon number $\bar{n}$ of typically a few to ten quanta. This pre-cooling is required to reach the Lamb–Dicke regime (see section 3.2), where subsequent resolved sideband cooling [95–97] or cooling utilizing electromagnetically induced transparency can be applied [98, 99]. These cooling schemes lead close to the motional ground state $|0\rangle$ ($n = 0$ with probability of 98% in [97]) of the dedicated modes.

*Readout of electronic and motional states.* We distinguish the two electronic states by observing state-dependent laser fluorescence. The dipole allowed transition to an excited state starting in the state $|\downarrow\rangle$ is driven resonantly (see the transition labelled 'BD' in figure 4) in a closed cycle completed by spontaneous emission back to the state $|\downarrow\rangle$ due to selection rules. For state $|\uparrow\rangle$ the detection laser is off-resonant. The ion

therefore appears 'bright' for $|\downarrow\rangle$, while it remains 'dark' for $|\uparrow\rangle$ [100–103]. Typically, a few per mill of the scattered photons are detected by a photomultiplier tube or a CCD camera. The fidelity of this detection scheme has been shown experimentally to exceed 99.99% for averaged and even individual measurements [104, 105]. However, additional possibilities to enhance the detection efficiency, for example by methods developed for QC using ancilla qubits [106–108], cannot be applied to analogue QS, since all ions participate during the simulation. For the detection of the motional state, it can be mapped to the electronic state via an operation of type (b) and derived from the result of the spin state detection described above [109].

## 3. Theoretical excursion

The following calculations (section 3.1 and 3.2) are the mathematical description of the toolbox that is available for both QCs and QSs. Detailed discussions can be found, for example, in [50] or [51]. We summarize important equations in the following and extend the mathematical description to be applicable to scaled approaches of QSs, for example, two-dimensional arrays of ions in individual traps. We will continue with the description of an implementation of the effective spin–spin interaction for ions appearing in quantum spin Hamiltonians. In order to investigate it isolated from other interactions, we will first discuss it from the point of view of quantum gates [110] in sections 3.3 and 3.4. Finally, in section 3.5, we use all tools to derive and discuss the quantum Ising Hamiltonian based on [21] as an example. The mathematical descriptions will be required to pursue proposals described in section 5.2.

This section aims at deriving the mathematical treatment of the simulation of a quantum Ising Hamiltonian. It underlines the approximations and transformations applied in these calculations and discusses the related corrections compared with the ideal quantum Ising model, which grow in importance in regard to scaled systems described in section 6. Readers who are more interested in a pictorial description of the simulation of a quantum Ising Hamiltonian may skip this section and continue to section 4.

### 3.1. Theoretical basics

In the following we consider two-level systems only. The Hamiltonian describing the energy of the electronic states of $N$ such systems is given by

$$\hat{\mathcal{H}}_\mathrm{e} = \sum_{i=1}^{N} \frac{\hbar\omega_{\uparrow\downarrow}}{2}\hat{\sigma}_z^{(i)} + \underbrace{N\hbar\frac{\omega_\uparrow+\omega_\downarrow}{2}}_{=\text{const (omitted)}}, \tag{3.1}$$

where $\hbar\omega_{\uparrow/\downarrow}$ denote the energies of the states $|\downarrow\rangle$ and $|\uparrow\rangle$, respectively, $\omega_{\uparrow\downarrow} := \omega_\uparrow - \omega_\downarrow$, and the operator $\hat{\sigma}_z^{(i)}$ the Pauli operator (compare appendix B, equation (B.1)) acting on the $i$th ion.

The ions are considered to be trapped in a common harmonic potential or several individual potentials, which can be approximated to harmonic order. The corresponding Hamiltonian in terms of the normal modes of the oscillation reads

$$\hat{\mathcal{H}}_\mathrm{m} = \sum_{m=1}^{3N}\hbar\omega_m\left(\hat{a}_m^\dagger\hat{a}_m + \frac{1}{2}\right). \tag{3.2}$$

Here, $\hat{a}_m$ and $\hat{a}_m^\dagger$ are the annihilation and creation operators of the $m$th mode, respectively, and $\omega_m$ the corresponding frequency. In the following, the constant terms $\hbar\omega_m/2$ will also be omitted and the abbreviation $\hat{\mathcal{H}}_0 := \hat{\mathcal{H}}_\mathrm{e} + \hat{\mathcal{H}}_\mathrm{m}$ will be used.

An interaction of an ion with the electric field $\vec{E}$ of a laser beam is described by $-\hat{\vec{\mu}}\cdot\vec{E}(\vec{r},t)$, where $\hat{\vec{\mu}}$ denotes the electric dipole operator for the transition $|\downarrow\rangle \leftrightarrow |\uparrow\rangle$ and $\vec{E}(\vec{r},t)$ the field at the site of the ion. The Hamiltonian describing the interaction of the field with $N$ ions becomes

$$\hat{\mathcal{H}}_\mathrm{I} = \sum_{i=1}^{N}\hbar\Omega_\mathrm{I}^{(i)}\left(\mathrm{e}^{\mathrm{i}(\vec{k}_\mathrm{I}^{(i)}\cdot\hat{\vec{r}}^{(i)}-\omega_\mathrm{I}t+\varphi_\mathrm{I}^{(i)})} + \mathrm{h.c.}\right)\hat{\kappa}^{(i)}. \tag{3.3}$$

Here, $\Omega_\mathrm{I}^{(i)} = -\mu E^{(i)}/2 \in \mathbb{R}$ is the interaction strength at site $i$, $\vec{k}_\mathrm{I}^{(i)}$ the wavevector at site $i$, $\hat{\vec{r}}^{(i)}$ the position of the $i$th ion, $\omega_\mathrm{I}$ the frequency of the field and $\varphi_\mathrm{I}^{(i)}$ an additional phase. In the most general form, the operator $\hat{\kappa}^{(i)}$ can be expressed as a linear combination of Pauli operators $\hat{\sigma}_{x/y/z}^{(i)}$ and the identity operator $\hat{\mathbb{1}}^{(i)}$ (see appendix B):

$$\hat{\kappa}^{(i)} := \alpha_0\hat{\mathbb{1}}^{(i)} + \alpha_1\hat{\sigma}_x^{(i)} + \alpha_2\hat{\sigma}_y^{(i)} + \alpha_3\hat{\sigma}_z^{(i)}, \tag{3.4}$$

with the prefactors $\alpha_j \in \mathbb{R}$, which are determined by the polarization of the electric field and angular momenta of the states encoding $|\downarrow\rangle$ and $|\uparrow\rangle$ (see also section 3.4 for some examples).

The position operator $\hat{\vec{r}}^{(i)}$ in equation (3.3) is decomposed into the equilibrium position $\vec{x}_0^{(i)}$ and the displacement $\hat{\vec{x}}^{(i)} = \hat{\vec{r}}^{(i)} - \vec{x}_0^{(i)}$. The terms $\vec{k}_\mathrm{I}^{(i)}\cdot\vec{x}_0^{(i)}$ give rise to a constant phase, which we absorb into $\varphi_\mathrm{I}^{(i)} + \vec{k}_\mathrm{I}^{(i)}\cdot\vec{x}_0^{(i)} \to \varphi_\mathrm{I}^{(i)}$.

The displacement of the ion from its equilibrium position $\hat{\vec{x}}^{(i)}$ is expressed in terms of the normal modes of motion

$$\hat{\vec{x}}^{(i)} = \sum_{m=1}^{3N}\left(b_{m,i}\hat{q}_m\vec{e}_X + b_{m,i+N}\hat{q}_m\vec{e}_Y + b_{m,i+2N}\hat{q}_m\vec{e}_Z\right), \tag{3.5}$$

where $b_{m,i}$ are the elements of an (orthogonal) transformation matrix (compare appendix A, equation (A.8)). Expressing the operators $\hat{q}_m$ of the normal modes in terms of the creation and annihilation operators yields

$$\hat{q}_m = q_{m0}\left(\hat{a}_m + \hat{a}_m^\dagger\right) \qquad \text{with} \quad q_{m0} := \sqrt{\frac{\hbar}{2M\omega_m}}, \tag{3.6}$$

where $M$ denotes the mass of one ion. Hence, the scalar product appearing in the Hamiltonian yields

$$\vec{k}_\mathrm{I}^{(i)}\cdot\hat{\vec{x}}^{(i)} = \sum_{m=1}^{3N}\eta_m^{(i)}\left(\hat{a}_m + \hat{a}_m^\dagger\right), \tag{3.7}$$

where the Lamb–Dicke parameter of the $m$th mode and $i$th site has been introduced:

$$\eta_m^{(i)} := q_{m0}\left(b_{m,i}\vec{k}_\mathrm{I}^{(i)}\cdot\vec{e}_X + b_{m,i+N}\vec{k}_\mathrm{I}^{(i)}\cdot\vec{e}_Y + b_{m,i+2N}\vec{k}_\mathrm{I}^{(i)}\cdot\vec{e}_Z\right). \tag{3.8}$$

To summarize, the interaction term of the Hamiltonian gains the form

$$\hat{\mathcal{H}}_\mathrm{I} = \sum_{i=1}^{N} \hbar\Omega_\mathrm{I}^{(i)} \left( \mathrm{e}^{\mathrm{i}\left[\sum_{m=1}^{3N} \eta_m^{(i)} \left(\hat{a}_m + \hat{a}_m^\dagger\right) - \omega_\mathrm{I} t + \varphi_\mathrm{I}^{(i)}\right]} + \mathrm{h.c.} \right) \hat{\kappa}^{(i)}. \tag{3.9}$$

The transformation into the interaction picture

$$\hat{\mathcal{H}}_\mathrm{I}' = \hat{U}_0^\dagger \hat{\mathcal{H}}_\mathrm{I} \hat{U}_0 \qquad \text{with} \quad \hat{U}_0 := \mathrm{e}^{-\mathrm{i}\hat{\mathcal{H}}_0 t/\hbar} \tag{3.10}$$

can be carried out for each site separately, hence

$$\hat{\mathcal{H}}_\mathrm{I}'^{(i)} = \hat{U}_0^{(i)^\dagger} \hat{\mathcal{H}}_\mathrm{I}^{(i)} \hat{U}_0^{(i)} \qquad \text{with} \quad \hat{U}_0^{(i)} := \mathrm{e}^{-\mathrm{i}\hat{\mathcal{H}}_0^{(i)} t/\hbar}, \tag{3.11}$$

where $\hat{\mathcal{H}}_\mathrm{I}^{(i)}$ is the Hamiltonian corresponding to the $i$th ion and $\hat{\mathcal{H}}_\mathrm{I} = \sum_{i=1}^{N} \hat{\mathcal{H}}_\mathrm{I}^{(i)}$.

The operator $\hat{\kappa}^{(i)}$ (equation (3.4)) related to the electronic states reads as follows in the interaction picture (compare equation (B.15)):

$$\hat{\kappa}'^{(i)} = \mathrm{e}^{\mathrm{i}\omega_{\uparrow\downarrow} t \hat{\sigma}_z^{(i)}/2} \hat{\kappa}^{(i)} \mathrm{e}^{-\mathrm{i}\omega_{\uparrow\downarrow} t \hat{\sigma}_z^{(i)}/2} \tag{3.12}$$

$$= \frac{1}{2}\left[\alpha_0 \hat{\mathbb{1}}^{(i)} + \left(\alpha_1 + \frac{\alpha_2}{\mathrm{i}}\right) \mathrm{e}^{\mathrm{i}\omega_{\uparrow\downarrow} t} \hat{\sigma}_+^{(i)} + \alpha_3 \hat{\sigma}_z^{(i)}\right] + \mathrm{h.c.} \tag{3.13}$$

Here, we introduced $\hat{\sigma}_+^{(i)} := \hat{\sigma}_x^{(i)} + \mathrm{i}\hat{\sigma}_y^{(i)}$ and $\hat{\sigma}_-^{(i)} := \hat{\sigma}_x^{(i)} - \mathrm{i}\hat{\sigma}_y^{(i)}$.

The terms in equation (3.9) containing the motional operators transform as follows (compare equation (C.10)):

$$\mathrm{e}^{\mathrm{i}\omega_m t \hat{a}_m^\dagger \hat{a}_m} \mathrm{e}^{\mathrm{i}\eta_m^{(i)}\left(\hat{a}_m + \hat{a}_m^\dagger\right)} \mathrm{e}^{-\mathrm{i}\omega_m t \hat{a}_m^\dagger \hat{a}_m}$$

$$= \exp\left(\mathrm{i}\eta_m^{(i)}\left[\hat{a}_m \mathrm{e}^{-\mathrm{i}\omega_m t} + \hat{a}_m^\dagger \mathrm{e}^{\mathrm{i}\omega_m t}\right]\right). \tag{3.14}$$

Hence, it yields the following expression for the complete Hamiltonian in the interaction picture:

$$\hat{\mathcal{H}}_\mathrm{I}'^{(i)} = \hbar\Omega_\mathrm{I}^{(i)} \left\{ \exp\left(\mathrm{i}\left[\sum_{m=1}^{3N} \eta_m^{(i)} \left(\hat{a}_m \mathrm{e}^{-\mathrm{i}\omega_m t} + \hat{a}_m^\dagger \mathrm{e}^{\mathrm{i}\omega_m t}\right) - \omega_\mathrm{I} t + \varphi_\mathrm{I}^{(i)}\right]\right) + \mathrm{h.c.} \right\} \hat{\kappa}'^{(i)}. \tag{3.15}$$

At this point fast rotating terms which average out on short timescales are neglected (rotating wave approximation, RWA). For $\Omega_\mathrm{I}^{(i)} \ll \omega_{\uparrow\downarrow}$ we distinguish between two cases: In the first case, $\omega_\mathrm{I} \ll \omega_{\uparrow\downarrow}$, terms containing $\mathrm{e}^{\pm\mathrm{i}\omega_{\uparrow\downarrow} t}$ are neglected (see figure 5(*b*) for an example of an implementation). (If $\alpha_1 = \alpha_2 = 0$, nothing will change and the Hamiltonian will still be exact.) In the second case, $|\omega_\mathrm{I} - \omega_{\uparrow\downarrow}| \ll \omega_{\uparrow\downarrow}$, all terms but $\mathrm{e}^{\pm\mathrm{i}(\omega_{\uparrow\downarrow} - \omega_\mathrm{I})t}$ are neglected (see figure 5(*a*)):

$$\hat{\mathcal{H}}_\mathrm{I}'^{(i)(\mathrm{RWA})} = \hbar\Omega_\mathrm{I}^{(i)} \exp\left(\mathrm{i}\left[\sum_{m=1}^{3N} \eta_m^{(i)} \left(\hat{a}_m \mathrm{e}^{-\mathrm{i}\omega_m t} + \hat{a}_m^\dagger \mathrm{e}^{\mathrm{i}\omega_m t}\right) - \omega_\mathrm{I} t + \varphi_\mathrm{I}^{(i)}\right]\right) \left(\alpha_0 \hat{\mathbb{1}}^{(i)} + \alpha_3 \hat{\sigma}_z^{(i)}\right) + \mathrm{h.c.}$$

$$\text{for } \omega_\mathrm{I} \ll \omega_{\uparrow\downarrow}, \tag{3.16}$$

$$\hat{\mathcal{H}}_\mathrm{I}'^{(i)(\mathrm{RWA})} = \frac{\hbar}{2}\Omega_\mathrm{I}^{(i)} \exp\left(\mathrm{i}\left[\sum_{m=1}^{3N} \eta_m^{(i)} \left(\hat{a}_m \mathrm{e}^{-\mathrm{i}\omega_m t} + \hat{a}_m^\dagger \mathrm{e}^{\mathrm{i}\omega_m t}\right) - \left(\omega_\mathrm{I} - \omega_{\uparrow\downarrow}\right) t + \varphi_\mathrm{I}^{(i)}\right]\right) \left(\alpha_1 + \frac{\alpha_2}{\mathrm{i}}\right) \hat{\sigma}_+^{(i)} + \mathrm{h.c.}$$

$$\text{for } |\omega_\mathrm{I} - \omega_{\uparrow\downarrow}| \ll \omega_{\uparrow\downarrow}. \tag{3.17}$$

### 3.2. $\hat{\sigma}_x/\hat{\sigma}_y$ interaction

The time evolution corresponding to $\hat{\mathcal{H}}_\mathrm{I}'^{(i)(\mathrm{RWA})}$ in equation (3.17) is involved. The time evolution is calculated for a single ion $i$ and a single motional mode $m$, for example, in [50, 51]. As some simplifications (Lamb–Dicke regime, see below) are not always justified for experiments, we will summarize this calculation here. (The index $m$ is skipped in this section.)

In this case the Hamiltonian simplifies to

$$\hat{\mathcal{H}}_\mathrm{I}'^{(\mathrm{RWA})} = \frac{\hbar}{2}\Omega_\mathrm{I} \exp(\mathrm{i}[\eta(\hat{a}\mathrm{e}^{-\mathrm{i}\omega t} + \hat{a}^\dagger \mathrm{e}^{\mathrm{i}\omega t}) - (\omega_\mathrm{I} - \omega_{\uparrow\downarrow})t + \varphi_\mathrm{I}]) \times \left(\alpha_1 + \frac{\alpha_2}{\mathrm{i}}\right) \hat{\sigma}_+ + \mathrm{h.c.} \tag{3.18}$$

Writing the state vector in the basis of electronic states $|s\rangle$ and motional Fock states $|n\rangle$,

$$|\psi(t)\rangle = \sum_{s\in\{\downarrow,\uparrow\}} \sum_n c_{s,n}(t)|s,n\rangle, \tag{3.19}$$

the Schrödinger equation yields

$$\mathrm{i}\hbar\dot{c}_{s',n'}(t) = \sum_{s\in\{\downarrow,\uparrow\}} \sum_n \langle s',n'|\hat{\mathcal{H}}_\mathrm{I}'^{(\mathrm{RWA})}|s,n\rangle c_{s,n}(t). \tag{3.20}$$

Matrix elements of the Hamiltonian vanish for $s' = s$. We obtain for the non-vanishing matrix elements [95, 111] (compare appendix D)

$$\langle\uparrow,n'|\hat{\mathcal{H}}_\mathrm{I}'^{(\mathrm{RWA})}|\downarrow,n\rangle = \frac{\hbar}{2}\Omega_\mathrm{I}\mathrm{e}^{\mathrm{i}\left(-(\omega_\mathrm{I}-\omega_{\uparrow\downarrow})t+\varphi_\mathrm{I}\right)} \left(\alpha_1 + \frac{\alpha_2}{\mathrm{i}}\right) \times \langle n'|\hat{D}\left(\mathrm{i}\eta\mathrm{e}^{\mathrm{i}\omega t}\right)|n\rangle \langle\uparrow|\hat{\sigma}_+|\downarrow\rangle$$

$$= \hbar\Omega_{n',n}\left(\alpha_1 + \frac{\alpha_2}{\mathrm{i}}\right) \mathrm{i}^{|n'-n|} \mathrm{e}^{\mathrm{i}\left([(n'-n)\omega - (\omega_\mathrm{I}-\omega_{\uparrow\downarrow})]t+\varphi_\mathrm{I}\right)}, \tag{3.21}$$

where $\hat{D}(\lambda) := \mathrm{e}^{\lambda\hat{a}^\dagger - \lambda^*\hat{a}}$ denotes the displacement operator and

$$\Omega_{n',n} := \Omega_\mathrm{I}\mathrm{e}^{-\eta^2/2}\eta^{|n'-n|}\sqrt{\frac{n_<!}{n_>!}} L_{n_<}^{(|n'-n|)}(\eta^2). \tag{3.22}$$

Here, $L_n^{(\alpha)}(x)$ are the associated Laguerre polynomials, $n_< := \min(n',n)$, and $n_> := \max(n',n)$. Analogously, we obtain $\langle\downarrow,n|\hat{\mathcal{H}}_\mathrm{I}'^{(\mathrm{RWA})}|\uparrow,n'\rangle = \langle\uparrow,n'|\hat{\mathcal{H}}_\mathrm{I}'^{(\mathrm{RWA})}|\downarrow,n\rangle^*$.

We define $\delta := (\omega_\mathrm{I} - \omega_{\uparrow\downarrow}) - (n'-n)\omega$. For small detunings $|\delta| \ll \omega$ and interaction strengths $|\Omega_{n',n}| \ll \omega$ (resolved sideband regime), we apply an RWA neglecting terms rotating faster than $\mathrm{e}^{\pm\mathrm{i}\delta t}$. Equation (3.20) can then be solved for each subset $|n',\uparrow\rangle$ and $|n,\downarrow\rangle$ separately:

$$\dot{c}_{\uparrow,n'}(t) = -\mathrm{i}\Omega_{n',n}\left(\alpha_1 + \frac{\alpha_2}{\mathrm{i}}\right) \mathrm{i}^{|n'-n|} \mathrm{e}^{-\mathrm{i}(\delta t - \varphi_\mathrm{I})} c_{\downarrow,n}(t), \tag{3.23}$$

$$\dot{c}_{\downarrow,n}(t) = -\mathrm{i}\Omega_{n',n}\left(\alpha_1 + \frac{\alpha_2}{\mathrm{i}}\right)^* (-\mathrm{i})^{|n'-n|} \mathrm{e}^{\mathrm{i}(\delta t + \varphi_\mathrm{I})} c_{\uparrow,n'}(t). \tag{3.24}$$

The solution of the system of differential equations yields Rabi oscillations between the states $|\downarrow,n\rangle \leftrightarrow |\uparrow,n'\rangle$ (compare appendix E):

$$\begin{pmatrix} c_{\uparrow,n'}(t) \\ c_{\downarrow,n}(t) \end{pmatrix} = \begin{bmatrix} \left(\cos(X_{n',n}t) + \frac{\delta}{2}\frac{\mathrm{i}}{X_{n',n}}\sin(X_{n',n}t)\right)\mathrm{e}^{-\mathrm{i}\delta t/2} & \frac{Y_{n',n}}{X_{n',n}}\sin(X_{n',n}t)\mathrm{e}^{-\mathrm{i}\delta t/2} \\ -\frac{Y^*_{n',n}}{X_{n',n}}\sin(X_{n',n}t)\mathrm{e}^{\mathrm{i}\delta t/2} & \left(\cos(X_{n',n}t) - \frac{\delta}{2}\frac{\mathrm{i}}{X_{n',n}}\sin(X_{n',n}t)\right)\mathrm{e}^{\mathrm{i}\delta t/2} \end{bmatrix} \begin{pmatrix} c_{\uparrow,n'}(0) \\ c_{\downarrow,n}(0) \end{pmatrix} \tag{3.25}$$

with $Y_{n',n} := -\mathrm{i}\Omega_{n',n}(\alpha_1 + \alpha_2/\mathrm{i})\mathrm{i}^{|n'-n|}\mathrm{e}^{\mathrm{i}\varphi_1}$ and $X_{n',n} := \sqrt{(\delta^2/4) + |Y_{n',n}|^2}$.

In the Lamb–Dicke regime, $\eta\langle(\hat{a} + \hat{a}^\dagger)^2\rangle^{1/2} \ll 1$, equation (3.22) can be expanded to first order in $\eta$:

$$\Omega^{(\mathrm{LDR})}_{n-1,n} = \Omega_\mathrm{I}\eta\sqrt{n} \qquad \text{(first red sideband)}, \tag{3.26}$$

$$\Omega^{(\mathrm{LDR})}_{n,n} = \Omega_\mathrm{I} \qquad \text{(carrier)}, \tag{3.27}$$

$$\Omega^{(\mathrm{LDR})}_{n+1,n} = \Omega_\mathrm{I}\eta\sqrt{n+1} \qquad \text{(first blue sideband)}. \tag{3.28}$$

Successive red sideband transitions $|\downarrow\rangle|n\rangle \rightarrow |\uparrow\rangle|n-1\rangle$ followed by dissipative repumping to $|\downarrow\rangle|n-1\rangle$ with high probability are routinely used for sideband cooling close to the motional ground state $|n=0\rangle$ [95–97].

If the Lamb–Dicke parameter becomes effectively zero, the motional dependence will vanish (see equations (3.26) and (3.28)). The only remaining transition is the carrier transition equation (3.27) affecting the electronic states only. This is the case, for example, for two-photon stimulated-Raman transitions with co-propagating beams or for microwave driven transitions in hyperfine qubits, where $\vec{k}_\mathrm{I} \approx 0$. In systems with more than one ion, the ions will not be motionally coupled. That is why equation (3.25) also holds for each site separately in such systems.

order in the Lamb-Dicke parameters $\eta^{(i)}_m$. A subsequent RWA neglecting terms rotating faster than $\mathrm{e}^{\pm\mathrm{i}\delta_m t}$ with $\delta_m := \omega_\mathrm{I} - \omega_m$ yields

$$\begin{aligned}\hat{\mathcal{H}}'^{(i)(\mathrm{LDR})}_\mathrm{I} &= \hbar\Omega^{(i)}_\mathrm{I}\mathrm{e}^{\mathrm{i}\left(-\omega_\mathrm{I}t+\varphi^{(i)}_1\right)} \\ &\times\left[1 + \mathrm{i}\sum_{m=1}^{3N}\eta^{(i)}_m\left(\hat{a}_m\mathrm{e}^{-\mathrm{i}\omega_m t} + \hat{a}^\dagger_m\mathrm{e}^{\mathrm{i}\omega_m t}\right)\right] \\ &\times\left(\alpha_0\hat{\mathbb{1}}^{(i)} + \alpha_3\hat{\sigma}^{(i)}_z\right) + \mathrm{h.c.}\end{aligned} \tag{3.31}$$

$$\begin{aligned}\Rightarrow \hat{\mathcal{H}}'^{(i)(\mathrm{LDR})(\mathrm{RWA})}_\mathrm{I} &= \mathrm{i}\hbar\Omega^{(i)}_\mathrm{I}\sum_{m=1}^{3N}\eta^{(i)}_m\mathrm{e}^{\mathrm{i}(-\delta_m t+\varphi^{(i)}_1)}\hat{a}^\dagger_m \\ &\times\left(\alpha_0\hat{\mathbb{1}}^{(i)} + \alpha_3\hat{\sigma}^{(i)}_z\right) + \mathrm{h.c.}\end{aligned} \tag{3.32}$$

Note that equation (3.32) breaks up into a sum over terms that depend on only one mode $m$ and one site $i$ each.

With the excursion in appendix F the total time evolution operator in the interaction picture reads

$$\begin{aligned}\hat{U}'^{(\mathrm{LDR})(\mathrm{RWA})}_\mathrm{I}(t,t_0) &= \exp\left(\mathrm{i}\left[\sum_{i=1}^{N}\sum_{m=1}^{3N}\frac{\Omega^{(i)}_\mathrm{I}\eta^{(i)}_m}{\delta_m}(\mathrm{e}^{-\mathrm{i}\delta_m(t-t_0)} - 1)\mathrm{e}^{-\mathrm{i}\delta_m t_0}\mathrm{e}^{\mathrm{i}\varphi^{(i)}_1}\hat{a}^\dagger_m\left(\alpha_0\hat{\mathbb{1}}^{(i)} + \alpha_3\hat{\sigma}^{(i)}_z\right) + \mathrm{h.c.}\right]\right) \\ &\times\exp\left(-\mathrm{i}\sum_{i=1}^{N}\sum_{j=1}^{N}\sum_{m=1}^{3N}\frac{\Omega^{(i)}_\mathrm{I}\Omega^{(j)}_\mathrm{I}\eta^{(i)}_m\eta^{(j)}_m}{\delta^2_m}\left(\alpha_0\hat{\mathbb{1}}^{(i)} + \alpha_3\hat{\sigma}^{(i)}_z\right)\otimes\left(\alpha_0\hat{\mathbb{1}}^{(j)} + \alpha_3\hat{\sigma}^{(j)}_z\right)\right. \\ &\times\left.\left[\delta_m(t-t_0)\cos\left(\varphi^{(i)}_\mathrm{I} - \varphi^{(j)}_\mathrm{I}\right) - \sin\left(\delta_m(t-t_0) - \left(\varphi^{(i)}_\mathrm{I} - \varphi^{(j)}_\mathrm{I}\right)\right)\right]\right).\end{aligned} \tag{3.33}$$

Equation (3.25) simplifies for resonant carrier transitions ($\delta = 0$) and a pure $\hat{\sigma}_x$ interaction ($\alpha_1 = 1$ and $\alpha_2 = 0$):

$$\begin{pmatrix} c_{\uparrow,n}(t) \\ c_{\downarrow,n}(t) \end{pmatrix} = \hat{R}(\vartheta,\varphi)\begin{pmatrix} c_{\uparrow,n}(0) \\ c_{\downarrow,n}(0) \end{pmatrix}, \tag{3.29}$$

where

$$\hat{R}(\vartheta,\varphi) := \begin{pmatrix} \cos(\vartheta/2) & -\mathrm{i}\mathrm{e}^{\mathrm{i}\varphi}\sin(\vartheta/2) \\ -\mathrm{i}\mathrm{e}^{-\mathrm{i}\varphi}\sin(\vartheta/2) & \cos(\vartheta/2) \end{pmatrix}, \tag{3.30}$$

$\vartheta := 2\Omega_{n,n}t$ and $\varphi := \varphi_\mathrm{I}$. The rotation matrix $\hat{R}(\pi/2,\varphi)$ describes a $\pi/2$-pulse and $\hat{R}(\pi,\varphi)$ a $\pi$-pulse with phase $\varphi$.

### 3.3. *Effective $\hat{\sigma}_z \otimes \hat{\sigma}_z$ interaction*

We will now discuss the case of equation (3.16) with $\alpha_1 = \alpha_2 = 0$. Hence, we omit the superscript of the Hamiltonian indicating an RWA. In the Lamb–Dicke regime, $\eta^{(i)}_m\langle(\hat{a}_m + \hat{a}^\dagger_m)^2\rangle^{1/2} \ll 1$, the Hamiltonian can be expanded to first

The interaction described by equation (3.33) can be interpreted as follows: the first exponential function has the form of a displacement operator $\hat{D}(\lambda) = \mathrm{e}^{\lambda\hat{a}^\dagger - \lambda^*\hat{a}}$, which leads to a displacement of a coherent state by $\lambda$ in phase space. Due to the $(\mathrm{e}^{-\mathrm{i}\delta_m(t-t_0)} - 1)$ proportionality of the exponent, the trajectory for a coherent state of each mode describes a circle in phase space (or a straight line in the limit $\delta_m = 0$). The coherent state returns to its initial position at times $T_m = 2\pi l/\delta_m$ with $l \in \mathbb{N}$, where the exponent vanishes. The second exponential can be expanded into a $\hat{\sigma}_z \otimes \hat{\sigma}_z$ interaction, a $\hat{\sigma}_z$ interaction and a global phase. The $\hat{\sigma}_z \otimes \hat{\sigma}_z$ terms give rise to a geometric phase, which increases in time $t$, and the $\hat{\sigma}_z$ terms lead to a dynamic phase [112, 113]. The area in phase space enclosed by the trajectory is proportional to these phases.

### 3.4. *Geometric phase gates*

The collective interaction of multiple ions with the same laser(s) has been proposed for the implementation of quantum

gates [85, 114–117]. These gates are described in the $z$-basis by equation (3.33) and have been first implemented in [110, 118]. Mølmer–Sørensen gates can be mathematically treated analogously in a rotated basis and are described in detail in [86, 87]. Implementations are reported in [119–122].

We will exemplarily discuss geometric phase gates based on the $\hat{\sigma}_z \otimes \hat{\sigma}_z$ terms in equation (3.33) in the following. They offer excellent tools to investigate a pure $\hat{\sigma}_z \otimes \hat{\sigma}_z$ interaction required for the simulation of more involved Hamiltonians such as quantum spin Hamiltonians. The geometric phase gates also allow the discussion of the $\hat{\sigma}_z \otimes \hat{\sigma}_z$ interaction in a familiar frame, while for the quantum Ising Hamiltonian a canonical transformation is introduced, which leads to a more involved dressed-state picture (see section 3.5).

The interaction according to the Hamiltonian can be implemented [47, 110, 123] by stimulated-Raman transitions driven by two beams with wavevectors $\vec{k}_1, \vec{k}_2$ and difference frequency close to a (several) motional mode(s) (see figure 5(*b*)). On average the differential ac Stark shift between the levels $|\downarrow\rangle$ and $|\uparrow\rangle$ caused by the two beams can be compensated by choosing appropriate polarizations of the beams. Still, on short timescales $\sim 2\pi/\delta_m$ the ions experience a state-dependent force that leads to the above displacement in the phase spaces of the corresponding modes.

In the original implementation of the geometric phase gate [110] two $^9Be^+$ ions are used. The state-dependent forces amount to $\vec{F}_\downarrow = -2\vec{F}_\uparrow$. This means that the operators $(\alpha_0 \hat{\mathbb{1}}^{(i)} + \alpha_3 \hat{\sigma}_z^{(i)})$ have diagonal elements 1 and $-2$, which is fulfilled for $\alpha_0 = -1/2$ and $\alpha_3 = 3/2$. The effective wavevectors $\vec{k}_\mathrm{I}^{(1)} = \vec{k}_\mathrm{I}^{(2)} = \vec{k}_1 - \vec{k}_2$ point along the axis of the linear trap and the laser beams are detuned by $\delta_\mathrm{STR} = 2\pi \times 26\,\mathrm{kHz}$ from the stretch (STR) mode. The effect of the centre-of-mass (COM) mode can be neglected ($\delta_\mathrm{COM} \approx 100\delta_\mathrm{STR}$). The ions are placed at the same phase of the stimulated-Raman interaction ($\varphi_\mathrm{I}^{(1)} = \varphi_\mathrm{I}^{(2)} = 0$).

For $t = T_\mathrm{g} = 2\pi/\delta_\mathrm{STR}$ the time evolution operator equation (3.33) simplifies to

$$\hat{U}_\mathrm{I}'^{(\mathrm{LDR})(\mathrm{RWA})}(T_\mathrm{g}, 0) \approx \exp\left( -2\pi \mathrm{i} \sum_{i=1}^{2}\sum_{j=1}^{2} \frac{(-1)^{i-j}\Omega_\mathrm{I}^2 \eta_\mathrm{STR}^2}{\delta_\mathrm{STR}^2} \times \left[\alpha_3^2 \hat{\sigma}_z^{(i)} \otimes \hat{\sigma}_z^{(j)} + \alpha_0\alpha_3 \left(\hat{\sigma}_z^{(i)} + \hat{\sigma}_z^{(j)}\right)\right]\right), \tag{3.34}$$

where we have used $\eta_\mathrm{STR} := \eta_\mathrm{STR}^{(1)} = -\eta_\mathrm{STR}^{(2)}$ and neglected the global phase arising from the $\hat{\mathbb{1}}^{(i)} \otimes \hat{\mathbb{1}}^{(j)}$ terms. The sequence of the gate is similar to the one in figure 7, but without the second displacement pulse $\hat{D}_2$. Ideally, the initial state $|\psi\rangle = |\downarrow\downarrow\rangle|n_\mathrm{COM} = 0, n_\mathrm{STR} = 0\rangle$ is rotated to $1/2(|\downarrow\downarrow\rangle + |\downarrow\uparrow\rangle + |\uparrow\downarrow\rangle + |\uparrow\uparrow\rangle)|n_\mathrm{COM} = 0, n_\mathrm{STR} = 0\rangle$ by the first $\hat{R}(\pi/2, \pi/2)$ pulse (the phase $\varphi$ of the first pulse can be chosen arbitrarily). The only non-vanishing contributions arise from the $\hat{\sigma}_z \otimes \hat{\sigma}_z$ terms for the $|\downarrow\uparrow\rangle$ and $|\uparrow\downarrow\rangle$ states, which gain a geometric phase

$$\Phi_{\mathrm{STR}\downarrow\uparrow/\uparrow\downarrow} = -2\pi \times 4 \frac{\Omega_\mathrm{I}^2 \eta_\mathrm{STR}^2}{\delta_\mathrm{STR}^2} \alpha_3^2. \tag{3.35}$$

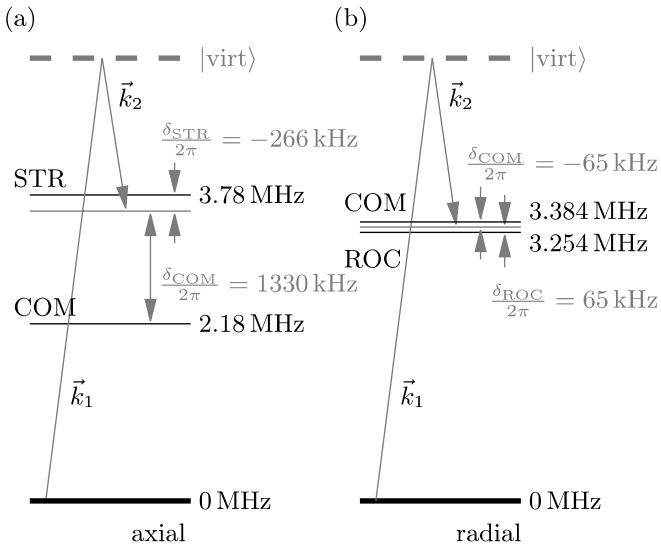


**Figure 6.** Comparison between parameters of geometric phase gates [110] with two ions using the axial motional modes and radial motional modes. (*a*) The parameters correspond to the gate from [123]. The axial centre-of-mass (COM) and stretch (STR) mode have a large frequency difference ($2\pi \times 1.6\,\mathrm{MHz}$). The detuning of the Raman beams from the STR mode amounts to $\delta_\mathrm{STR} = -2\pi \times 266\,\mathrm{MHz}$. That is why the main contribution to the differential geometric phase between $|\downarrow\downarrow\rangle/|\uparrow\uparrow\rangle$ and $|\downarrow\uparrow\rangle/|\uparrow\downarrow\rangle$ is due to a (single) loop in the phase space of the STR mode. However, as already suggested in [110], the detuning from the COM mode is chosen to be an integer multiple of the detuning from the STR mode ($\delta_\mathrm{COM} = -5 \times \delta_\mathrm{STR}$). Hence, there is no entanglement left between the electronic and motional modes at the gate duration $T_\mathrm{g} = |2\pi/\delta_\mathrm{STR}| = 3.75\,\mu\mathrm{s}$. (Note that the spin-echo sequence is not included in $T_\mathrm{g}$.) (*b*) The parameters correspond to a phase gate on two of the radial motional modes. The radial centre-of-mass (COM) and rocking (ROC) mode have a comparatively small frequency difference of only $2\pi \times 130\,\mathrm{kHz}$. The detunings from both modes are chosen to have the same absolute values resulting in (approximately) equal contributions to the acquired geometric phase from both modes. The gate duration according to the original implementation would amount to $T_\mathrm{g} = |2\pi/\delta_\mathrm{STR}| = 15.4\,\mu\mathrm{s}$. As the displacement pulse is repeated in the second gap of the spin-echo sequence (compare figure 7) to cancel dynamic phases (compare [118] and see text), the duration increases by an additional factor of two.

By choosing appropriate beam intensities and thus $\Omega_\mathrm{I}$, these phases equal $\Phi_{\mathrm{STR}\downarrow\uparrow/\uparrow\downarrow} = -\pi/2$. The subsequent $\hat{R}(\pi, \pi/2)$ and $\hat{R}(\pi/2, \pi/2)$ pulses lead to the final Bell state $|\tilde{\psi}\rangle = 1/\sqrt{2}(|\downarrow\downarrow\rangle + \mathrm{i}|\uparrow\uparrow\rangle)$, which is achieved experimentally with a fidelity of $F = 97\%$ [110].

A similar implementation of the geometric phase gate is reported in [123] based on two $^{25}Mg^+$ ions. The state-dependent forces amount to $\vec{F}_\downarrow = -3/2\vec{F}_\uparrow$ ($\alpha_0 = -1/4$ and $\alpha_3 = 5/4$). Furthermore, the detuning from the STR mode amounts to $\delta_\mathrm{STR} = -2\pi \times 266\,\mathrm{kHz}$ and simultaneously the detuning from the COM mode $\delta_\mathrm{COM} = -2\pi \times 1330\,\mathrm{kHz}$ (compare figure 6(*a*)). Hence, the effect of the COM mode is also exploited for the gate. As the detuning from the COM mode is chosen to be an integer multiple of the detuning from the STR mode ($\delta_\mathrm{COM} = -5\delta_\mathrm{STR}$), the first exponential in equation (3.33) still becomes unity for the gate duration of $T_\mathrm{g} = |2\pi/\delta_\mathrm{STR}|$. (In other words, all circular trajectories in

all phase spaces return to their initial position for $T_g$.) As a result, there is no entanglement left between the electronic and motional states.

Analogous to equation (3.35), but considering $\delta_{STR} < 0$ and $\delta_{COM} > 0$ for the detunings and $\eta^{(1)}_{COM} = \eta^{(2)}_{COM}$ for the Lamb-Dicke parameters of the COM mode, the geometric phases yield

$$\Phi_{STR\downarrow\uparrow/\uparrow\downarrow} = 2\pi \times 4\frac{\Omega_I^2\eta_{STR}^2}{\delta_{STR}^2}\alpha_3^2, \tag{3.36}$$

$$\Phi_{COM\downarrow\downarrow/\uparrow\uparrow} = -2\pi\left|\frac{\delta_{COM}}{\delta_{STR}}\right| \times 4\frac{\Omega_I^2\eta_{COM}^2}{\delta_{COM}^2}\alpha_3^2. \tag{3.37}$$

By adjusting the beam intensities appropriately the differential phase between $|\downarrow\downarrow\rangle/|\uparrow\uparrow\rangle$ and $|\downarrow\uparrow\rangle/|\uparrow\downarrow\rangle$ can be adjusted to fulfil $\Phi_{STR\downarrow\uparrow/\uparrow\downarrow} - \Phi_{COM\downarrow\downarrow/\uparrow\uparrow} = \pi/2$. As $\Phi_{STR\downarrow\uparrow/\uparrow\downarrow}$ has the opposite sign compared with $\Phi_{COM\downarrow\downarrow/\uparrow\uparrow}$, the geometric phase gate makes use of two motional modes simultaneously.

However, some of the dynamic phases from the COM mode do not vanish:

$$\tilde{\Phi}_{COM\downarrow\downarrow/\uparrow\uparrow} = \pm 2\pi\left|\frac{\delta_{COM}}{\delta_{STR}}\right| \times 8\frac{\Omega_I^2\eta_{COM}^2}{\delta_{COM}^2}\alpha_0\alpha_3. \tag{3.38}$$

These phases have an absolute value of $2\alpha_0/\alpha_3$ of the geometric phase from the COM mode and lead to a small deviation from the ideal state at the end of the gate.

Compared with the original implementation in [110], the gate is speeded up by approximately a factor of 10 and the fidelity $F$ for the Bell state exceeds 95%. (Note that the duration of the spin-echo sequence is not included in $T_g$, because its rotations could be much faster and empty gaps can in principle be removed.)

The radial motional modes are interesting, because they are similar to the normal modes in systems of individual traps for each ion (compare section 6), which are promising candidates for scalable systems in quantum simulations. To investigate the differences between the axial and radial modes of motion the geometric phase gate with $^{25}Mg^+$ is performed on a pair of radial modes (see also [122] for a Mølmer–Sørensen gate performed on the radial modes).

The detunings from the COM and ROC mode (abbreviation for 'rocking' mode, the equivalent to the STR mode in terms of the axial motional modes) are chosen to have the same absolute values $\delta_{COM} = -\delta_{ROC} = 2\pi \times 65$ kHz (see figure 6). The geometric phases acquired on each motional mode are basically the same as in equation (3.36), where 'STR' has to be replaced by 'ROC', and equation (3.37). (However, the signs change due to a change of the signs of the detunings.) The contributions to the total differential geometric phase between $|\downarrow\downarrow\rangle/|\uparrow\uparrow\rangle$ and $|\downarrow\uparrow\rangle/|\uparrow\downarrow\rangle$ due to the COM and ROC mode are (approximately) equal now. However, the dynamic phase (analogous to equation (3.38)) arising from the COM mode can no longer be neglected.

The pulse scheme of the geometric phase gate is modified by adding a second displacement pulse in the second gap of the spin-echo sequence (see figure 7 and compare [118]). The intensities of the beams are now adjusted for differential geometric phases due to each displacement pulse of

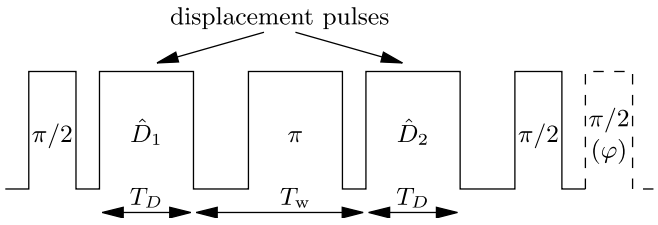


**Figure 7.** Pulse scheme of the geometric phase gate. It consists of a spin-echo sequence ($\hat{R}(\pi/2, \pi/2)$, $\hat{R}(\pi, \pi/2)$, $\hat{R}(\pi/2, \pi/2)$ pulses) with a displacement pulse (labelled '$\hat{D}_1$') in the first gap of the spin-echo sequence for the original implementation of the phase gate [110]. For the gate on the radial modes of motion a second displacement pulse (labelled '$\hat{D}_2$') is introduced to cancel dynamic phases from $\hat{D}_1$ due to different absolute values of the forces on $|\uparrow\rangle$ and $|\downarrow\rangle$ (compare [118]). For all gates the duration of each displacement pulse is chosen to be $T_D = |2\pi/\delta_{STR/ROC}|$ such that each displacement pulse leads to a closed loop in each phase space. Hence, the total gate duration amounts to $T_g = T_D$ for the original implementation and $T_g = 2T_D$ for the gate on the radial modes of motion. (Note that the spin-echo sequence is not included in $T_g$.) The dashed $\hat{R}(\pi/2, \pi/2 + \varphi)$ analysis pulse is added for the measurement of the gate fidelity (see figure 9).

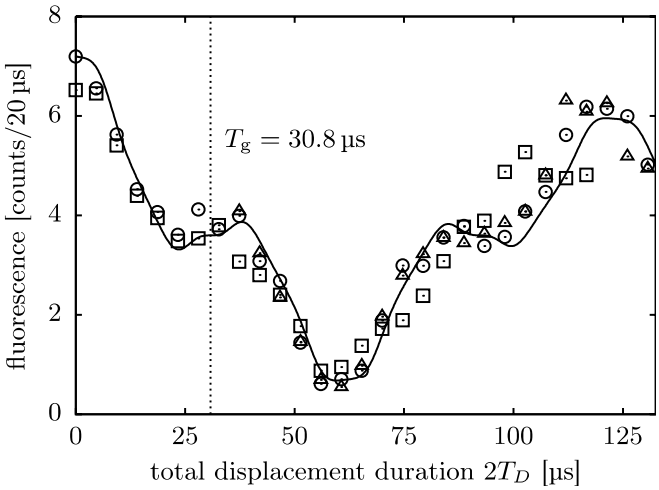


**Figure 8.** Total fluorescence from the two ions as a function of the total displacement duration $2T_D$ (compare figure 7). The detected fluorescence signal from both ions amounts to approximately 7 counts/20 $\mu$s for state $|\downarrow\downarrow\rangle$ and close to zero for $|\uparrow\uparrow\rangle$. The duration between the displacement pulses is chosen to be $T_w = |2\pi/\delta_{COM/ROC}|$ in the experiment (compare figure 7). At $T_g \approx 30.8\,\mu$s the state $|\psi\rangle \approx (|\uparrow\uparrow\rangle + i|\downarrow\downarrow\rangle)|n_{COM} = 0, n_{ROC} = 0\rangle$ is prepared. Each data point represents the average of 400 measurements (squares and triangles) and 200 measurements (circles), respectively. The statistical errors are on the order of the size of the symbols. The curve is based on a fit of the time evolution of equation (3.33) with an additional empirical exponential decay to mimic decoherence effects. The only fit parameters are the fluorescence for $|\downarrow\downarrow\rangle$ amounting to 7.2 counts/20 $\mu$s and the decay constant $\tau \approx 290\,\mu$s. The gate serves as an experimental reference for the isolated interaction strength and is not optimized to provide the highest gate fidelity.

$\Phi_{COM\downarrow\downarrow/\uparrow\uparrow} - \Phi_{ROC\downarrow\uparrow/\uparrow\downarrow} = \pi/4$. While the geometric phases of both displacement pulses add up to $\pi/2$, the dynamic phases cancel each other, as the $\pi$ pulse of the spin-echo sequence interchanges $|\downarrow\downarrow\rangle \leftrightarrow |\uparrow\uparrow\rangle$ (and $|\downarrow\uparrow\rangle \leftrightarrow |\uparrow\downarrow\rangle$). Additionally, the more symmetric pulse scheme enhances the robustness

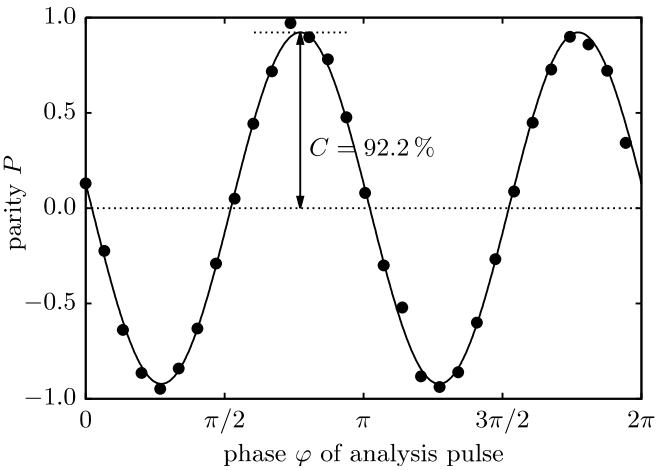


**Figure 9.** Parity measurement after the geometric phase gate on two radial modes of motion with two ions. The parity is defined as $P := P_{\downarrow\downarrow} + P_{\uparrow\uparrow} - (P_{\uparrow\downarrow} + P_{\downarrow\uparrow})$, where $P_{s,s'}$ denotes the population of the electronic state $|s, s'\rangle$ with $s, s' \in \{\downarrow, \uparrow\}$. It is measured as a function of the phase $\varphi$ of the analysis pulse $\hat{R}(\pi/2, \pi/2 + \varphi)$ (compare figure 7). Each data point represents the mean of 2500 measurements. The contrast $C = 92.2\%$ is determined from the fitted curve. Considering the populations $P_{\downarrow\downarrow} + P_{\uparrow\uparrow} > 98\%$ for the entangled state we obtain a Bell state fidelity $F > 95\%$.

of the gate against uncompensated differential ac Stark shifts between $|\downarrow\rangle$ and $|\uparrow\rangle$.

The total fluorescence from the two ions as a function of the total duration of the displacements $2T_D$ is shown in figure 8. The gate duration due to the smaller detunings and the second displacement pulse is more than a factor of eight longer than for the gate in [123]. Still, the fidelity exceeds 95% (see figure 9).

### 3.5. *Quantum Ising Hamiltonian*

Above we have introduced $\hat{\sigma}_z \otimes \hat{\sigma}_z$ interactions that are used in quantum gates. In the following we will present a slightly different approach, in which Ising spin–spin interactions are continuously induced by means of optical forces.

The spin–spin interaction as proposed in [21] and experimentally realized in the simulation of a quantum Ising Hamiltonian in [47] is identical to the interaction $\hat{\mathcal{H}}_\mathrm{I}$ described in section 3.3. (Note that a similar proposal involving the same mathematics is given in [23].) However, the quantum Ising Hamiltonian contains an additional (simulated) magnetic field pointing in the $x$-direction. We will adapt our notation in this section and split the total interaction Hamiltonian into the following terms: $\hat{\mathcal{H}}_\mathrm{S}$ denotes the term that generates the spin–spin interaction and $\hat{\mathcal{H}}_\mathrm{M}$ denotes the term leading to the simulated magnetic field. The index 'I' of the frequencies $\Omega_\mathrm{I}$ and $\omega_\mathrm{I}$, etc is changed to 'S' or 'M' accordingly in the respective terms. The complete interaction is described by the Hamiltonian $\hat{\mathcal{H}}_\mathrm{I} = \hat{\mathcal{H}}_\mathrm{S} + \hat{\mathcal{H}}_\mathrm{M}$. In the following, we will first derive the spin–spin interaction Hamiltonian from $\hat{\mathcal{H}}_\mathrm{S}$ focusing on an Ising interaction ($\hat{\sigma}_z \otimes \hat{\sigma}_z$ only). Afterwards, we will discuss the magnetic field term $\hat{\mathcal{H}}_\mathrm{M}$ and its effect.

The derivation of the quantum Ising Hamiltonian [21, 124] involves a slightly different interaction picture compared with section 3.1 by substituting $\hat{\mathcal{H}}_0$ with $\hat{\mathcal{H}}_\emptyset$:

$$\begin{aligned}\hat{\mathcal{H}}_0 &= \hat{\mathcal{H}}_\mathrm{e} + \hat{\mathcal{H}}_\mathrm{m} \\ &= \underbrace{\hat{\mathcal{H}}_\mathrm{e} + \sum_{m=1}^{3N} \hbar\omega_\mathrm{S} \hat{a}_m^\dagger \hat{a}_m}_{=:\hat{\mathcal{H}}_\emptyset} \underbrace{- \sum_{m=1}^{3N} \hbar\delta_m \hat{a}_m^\dagger \hat{a}_m}_{=:\hat{\mathcal{H}}_\delta}. \end{aligned} \tag{3.39}$$

The term $\hat{\mathcal{H}}_\delta$ is added to the interaction Hamiltonian.

To retrieve the representation of $\hat{\mathcal{H}}_\mathrm{S}$ in the newly defined interaction picture,

$$\hat{\mathcal{H}}'_\mathrm{S} := \hat{U}_\emptyset^\dagger \hat{\mathcal{H}}_\mathrm{S} \hat{U}_\emptyset \qquad \text{with} \quad \hat{U}_\emptyset := \mathrm{e}^{-\mathrm{i}\hat{\mathcal{H}}_\emptyset t/\hbar}, \tag{3.40}$$

we adapt the calculations from sections 3.1 and 3.3 accordingly: the frequencies in the transformation equation (3.14) are changed to $\omega_m \to \omega_\mathrm{S}$. As a result, the substitution $\mathrm{e}^{\pm\mathrm{i}\omega_m t} \to \mathrm{e}^{\pm\mathrm{i}\omega_\mathrm{S} t}$ has to be applied to equation (3.15) (and subsequent equations) and $\mathrm{e}^{\pm\mathrm{i}\delta_m t} \to 1$ to equation (3.32). Hence, $\hat{\mathcal{H}}_\mathrm{S}$ reads in the new interaction picture (including the expansion to first order in the Lamb–Dicke parameters and the RWA):

$$\begin{aligned}\hat{\mathcal{H}}_\mathrm{S}^{\prime(\mathrm{LDR})(\mathrm{RWA})} &= \sum_{i=1}^{N} \sum_{m=1}^{3N} \mathrm{i}\hbar\Omega_\mathrm{S}^{(i)} \eta_m^{(i)} \mathrm{e}^{\mathrm{i}\varphi_\mathrm{S}^{(i)}} \hat{a}_m^\dagger \\ &\quad \times \left(\alpha_0 \hat{\mathbb{1}}^{(i)} + \alpha_3 \hat{\sigma}_z^{(i)}\right) + \mathrm{h.c.} \end{aligned} \tag{3.41}$$

However, the full Hamiltonian in the interaction picture now also involves

$$\hat{\mathcal{H}}'_\delta = \hat{U}_\emptyset^\dagger \hat{\mathcal{H}}_\delta \hat{U}_\emptyset = \hat{\mathcal{H}}_\delta, \tag{3.42}$$

where the transformation is the identity, because trivially $[\hat{\mathcal{H}}_\emptyset, \hat{\mathcal{H}}_\delta] = 0$.

To gain the form of a spin–spin interaction, we apply a canonical transformation (compare [21]) to the Hamiltonian. We want to note that an adiabatic elimination of phonons would yield the same effective description of the system; however, the canonical transformation provides a systematic method to also calculate the corrections to the ideal quantum Ising model:

$$\hat{\mathcal{H}}_\mathrm{S}^{\prime\prime(\mathrm{LDR})(\mathrm{RWA})} + \hat{\mathcal{H}}''_\delta := \hat{U}_\mathrm{c} \left(\hat{\mathcal{H}}_\mathrm{S}^{\prime(\mathrm{LDR})(\mathrm{RWA})} + \hat{\mathcal{H}}_\delta\right) \hat{U}_\mathrm{c}^\dagger \tag{3.43}$$

with

$$\hat{U}_\mathrm{c} := \exp\left(-\sum_{i=1}^{N} \sum_{m=1}^{3N} \frac{1}{\hbar\delta_m} \left[\hat{\xi}_m^{(i)} \hat{a}_m^\dagger - \hat{\xi}_m^{(i)\dagger} \hat{a}_m\right]\right) \tag{3.44}$$

and

$$\hat{\xi}_m^{(i)} := \mathrm{i}\hbar\Omega_\mathrm{S}^{(i)} \eta_m^{(i)} \mathrm{e}^{\mathrm{i}\varphi_\mathrm{S}^{(i)}} \left(\alpha_0 \hat{\mathbb{1}}^{(i)} + \alpha_3 \hat{\sigma}_z^{(i)}\right). \tag{3.45}$$

Using the calculations from appendix G, the transformed Hamiltonian reads

$$\begin{aligned}\hat{\mathcal{H}}_\mathrm{S}^{\prime\prime(\mathrm{LDR})(\mathrm{RWA})} + \hat{\mathcal{H}}''_\delta &= \sum_{i=1}^{N} \sum_{j=1}^{N} \sum_{m=1}^{3N} \frac{1}{\hbar\delta_m} \hat{\xi}_m^{(i)} \otimes \hat{\xi}_m^{(j)\dagger} + \hat{\mathcal{H}}_\delta \\ &= \hbar \sum_{i=1}^{N} \sum_{j=1}^{N} \sum_{m=1}^{3N} \frac{\Omega_\mathrm{S}^{(i)} \Omega_\mathrm{S}^{(j)} \eta_m^{(i)} \eta_m^{(j)}}{\delta_m} \mathrm{e}^{\mathrm{i}\left(\varphi_\mathrm{S}^{(i)} - \varphi_\mathrm{S}^{(j)}\right)} \\ &\quad \times \left(\alpha_0 \hat{\mathbb{1}}^{(i)} + \alpha_3 \hat{\sigma}_z^{(i)}\right) \otimes \left(\alpha_0 \hat{\mathbb{1}}^{(j)} + \alpha_3 \hat{\sigma}_z^{(j)}\right) + \hat{\mathcal{H}}_\delta. \end{aligned} \tag{3.46}$$

The Hamiltonian can be expanded into a pure $\hat{\sigma}_z \otimes \hat{\sigma}_z$ interaction, a 'bias' term with $\hat{\sigma}_z$ interaction, and a constant term that can be neglected. The 'bias' term acts as a longitudinal magnetic field and leads to a deviation from the quantum Ising model. At first glance, this is not desired and it will be treated as an error in the following discussion. However, by including a 'bias' term in a controlled way we could also explore an extended phase diagram with the longitudinal field as an additional parameter.

We want to stress the similarity between the spin–spin interaction according to equation (3.46) and the $\hat{\sigma}_z \otimes \hat{\sigma}_z$ interaction discussed in section 3.3. The canonical transformation has the form of a displacement operator and looks very similar to the first exponential function in equation (3.33) (except for the time dependence of the latter). The similarity to the geometric phase term in equation (3.33) can be best seen comparing the time evolution operators. As the Hamiltonian in equation (3.46) is time-independent, the time evolution simply reads

$$\begin{aligned}\hat{U}_{\mathrm{S}}^{\prime\prime(\mathrm{LDR})(\mathrm{RWA})}(t,t_0) &\times \hat{U}_{\delta}(t,t_0)\\ &= \exp\Bigg(-\mathrm{i}\sum_{i=1}^{N}\sum_{j=1}^{N}\sum_{m=1}^{3N}\frac{\Omega_{\mathrm{S}}^{(i)}\Omega_{\mathrm{S}}^{(j)}\eta_m^{(i)}\eta_m^{(j)}}{\delta_m^2}\left(\alpha_0\hat{\mathbb{1}}^{(i)}+\alpha_3\hat{\sigma}_z^{(i)}\right)\\ &\quad\otimes\left(\alpha_0\hat{\mathbb{1}}^{(j)}+\alpha_3\hat{\sigma}_z^{(j)}\right)\times\delta_m(t-t_0)\mathrm{e}^{\mathrm{i}\left(\varphi_{\mathrm{S}}^{(i)}-\varphi_{\mathrm{S}}^{(j)}\right)}\Bigg)\\ &\quad\times\exp\left(\mathrm{i}\sum_{m=1}^{3N}\delta_m(t-t_0)\hat{a}_m^{\dagger}\hat{a}_m\right). \end{aligned}\tag{3.47}$$

Before we can apply the easier time evolution of equation (3.47), in which electronic states are decoupled from motional states, the state vector $|\psi\rangle$ has to be transformed from the original picture to $|\psi\rangle'' := \hat{U}_{\mathrm{c}}|\psi\rangle$. As $\hat{U}_{\mathrm{c}}$ depends on the electronic state, the transformation will in general lead to an entangled state and the canonical transformation can be interpreted as dressed-state picture (electronic states 'dressed' with motional states). As the states for the simulation of the quantum Ising Hamiltonian are prepared in the original (undressed) picture, but the Hamiltonian acts in the dressed picture, an error is introduced into the simulation (see, for example, [125]). However, as long as the effect due to $\hat{U}_{\mathrm{c}}$ is small ($|\Omega_{\mathrm{S}}^{(i)}\eta_m^{(i)}\alpha_l/\delta_m| \ll 1$), we can use the approximation $|\psi\rangle'' \approx |\psi\rangle$. In terms of the geometric phase gate this corresponds to the case when the circles in phase space are small and the entanglement between electronic and motional states can be neglected at any time.

The same holds for the measurements of observables: they are performed in the original (undressed) picture, in which electronic states are entangled with the motional states, and in general a further error is introduced in the simulation. However, the measurement of the states is typically insensitive to the motional states and involves a projection to one of the electronic states, for example, the $|\downarrow\rangle$ state: $\hat{P}^{(i)} := |\downarrow\rangle^{(i)}\langle\downarrow|^{(i)}$. As $[\hat{U}_{\mathrm{c}}, \hat{P}^{(i)}] = 0$, the projector does not change under the canonical transformation and the readout of $\hat{\sigma}_z$ eigenstates (without any rotations of the bases applied beforehand) does not introduce further errors.

The form of the 'bias' term proportional to $\hat{\sigma}_z$ can be simplified in the case of a linear Paul trap with equal Rabi frequencies $\Omega_{\mathrm{S}}^{(i)}$ and equal phases $\varphi_{\mathrm{S}}^{(i)}$ for all ions: The sum over $j$ extends over the Lamb-Dicke parameters $\eta_m^{(j)}$ only. This sum is non-zero only for centre-of-mass modes, for which the $\eta_m^{(j)}$ are additionally independent of the site $j$. Hence, the three sums simplify to a sum over $\hat{\sigma}_z^{(i)}$ with constant prefactor [21]:

$$2\Omega_{\mathrm{S}}^2\hbar N\alpha_0\alpha_3\left(\sum_{m\in\{\mathrm{c.m.}\}}\frac{\eta_m^2}{\delta_m}\right)\sum_{i=1}^{N}\hat{\sigma}_z^{(i)}. \tag{3.48}$$

However, this simplification does not necessarily hold for two-dimensional arrays of individual traps for each ion.

In the following, we will discuss the magnetic field term, which originates from a $\hat{\sigma}_x$ interaction described by equation (3.17) (with $\alpha_1 = 1$ and $\alpha_2 = 0$). In principle, we have to apply the substitution $\mathrm{e}^{\pm\mathrm{i}\omega_m t} \rightarrow \mathrm{e}^{\pm\mathrm{i}\omega_{\mathrm{S}} t}$ due to the new interaction picture here, too. However, we consider a magnetic field term without motional dependence in the following ($\eta_m^{(i)} = 0$, compare section 3.2) and thus the terms containing the motional creation/annihilation operators vanish:

$$\hat{\mathcal{H}}_{\mathrm{M}}^{\prime(\mathrm{RWA})} = \sum_{i=1}^{N}\frac{\hbar}{2}\Omega_{\mathrm{M}}^{(i)}\mathrm{e}^{\mathrm{i}\left(-\left(\omega_{\mathrm{M}}-\omega_{\uparrow\downarrow}\right)t+\varphi_{\mathrm{M}}^{(i)}\right)}\hat{\sigma}_+^{(i)}+\mathrm{h.c.} \tag{3.49}$$

The canonical transformation can be rewritten as

$$\hat{U}_{\mathrm{c}} = \exp\left(\mathrm{i}\sum_{i=1}^{N}\hat{h}^{(i)}\left(\alpha_0\hat{\mathbb{1}}^{(i)}+\alpha_3\hat{\sigma}_z^{(i)}\right)\right) \tag{3.50}$$

with the Hermitian operator

$$\hat{h}^{(i)} := \sum_{m=1}^{3N}\left[\zeta_m^{(i)}\hat{a}_m^{\dagger}+\zeta_m^{(i)\dagger}\hat{a}_m\right] \tag{3.51}$$

and

$$\zeta_m^{(i)} := -\frac{\hbar\Omega_{\mathrm{S}}^{(i)}\eta_m^{(i)}\mathrm{e}^{\mathrm{i}\varphi_{\mathrm{S}}^{(i)}}}{\hbar\delta_m}. \tag{3.52}$$

Trivially, the commutator $[\hat{h}^{(i)}, \hat{\sigma}_+^{(i)}] = 0$. The canonical transformation of $\hat{\mathcal{H}}_{\mathrm{M}}^{\prime(\mathrm{RWA})}$ (see equation (3.49)) is thus equivalent to a transformation of the $\hat{\sigma}_{\pm}^{(i)}$ operator as in equations (B.16) and (B.17):

$$\begin{aligned}\hat{\mathcal{H}}_{\mathrm{M}}^{\prime\prime(\mathrm{RWA})} &= \hat{U}_{\mathrm{c}}\hat{\mathcal{H}}_{\mathrm{M}}^{\prime(\mathrm{RWA})}\hat{U}_{\mathrm{c}}^{\dagger}\\ &= \sum_{i=1}^{N}\frac{\hbar}{2}\Omega_{\mathrm{M}}^{(i)}\mathrm{e}^{\mathrm{i}\left(-\left(\omega_{\mathrm{M}}-\omega_{\uparrow\downarrow}\right)t+\varphi_{\mathrm{M}}^{(i)}\right)}\mathrm{e}^{2\mathrm{i}\alpha_3\hat{h}^{(i)}}\hat{\sigma}_+^{(i)}+\mathrm{h.c.}\end{aligned}\tag{3.53}$$

The expansion to first order in $\zeta_m^{(i)}$ (and thus to first order in $\hat{\eta}_m^{(i)}$) yields

$$\begin{aligned}\hat{\mathcal{H}}_{\mathrm{M}}^{\prime\prime(\mathrm{RWA})} &\approx \sum_{i=1}^{N}\frac{\hbar}{2}\Omega_{\mathrm{M}}^{(i)}\mathrm{e}^{\mathrm{i}\left(-\left(\omega_{\mathrm{M}}-\omega_{\uparrow\downarrow}\right)t+\varphi_{\mathrm{M}}^{(i)}\right)}\\ &\quad\times\left(1+2\mathrm{i}\alpha_3\sum_{m=1}^{3N}\left[\zeta_m^{(i)}\hat{a}_m^{\dagger}+\zeta_m^{(i)\dagger}\hat{a}_m\right]\right)\hat{\sigma}_+^{(i)}+\mathrm{h.c.}\\ &=: \hat{\mathcal{H}}_{\mathrm{M}}^{\prime(\mathrm{RWA})}+\hat{\mathcal{H}}_{\mathrm{E}}^{\prime\prime}.\end{aligned}\tag{3.54}$$

The magnetic field term after the canonical transformation deviates to order $\Omega_S^{(i)}\eta_m^{(i)}\alpha_3/\delta_m$ due to $\hat{\mathcal{H}}_E''$ from the pure $\hat{\sigma}_x$ interaction $\hat{\mathcal{H}}_M'^{(RWA)}$. This introduces an additional error in the simulation. If the condition $|\Omega_S^{(i)}\eta_m^{(i)}\alpha_l/\delta_m| \ll 1$ is met, it can be small or even negligible and we, effectively, will obtain the desired magnetic field term.

To summarize, the complete Hamiltonian is obtained by adding equation (3.46) and equation (3.54). It consists of a spin–spin interaction term and a simulated magnetic field pointing in the $x$-direction, which add up to the ideal quantum Ising Hamiltonian. Assuming a resonant interaction for the simulated magnetic field ($\omega_M - \omega_{\uparrow\downarrow} = 0$) and neglecting the phases ($\varphi_S^{(i)} = \varphi_M^{(i)} = 0$), the quantum Ising part can be written as

$$\hat{\mathcal{H}}_{QIsing} := \hat{\mathcal{H}}_B + \hat{\mathcal{H}}_J = \sum_{i=1}^{N} B_x^{(i)}\hat{\sigma}_x^{(i)} + \sum_{i=1}^{N}\sum_{\substack{j=1\\ j\neq i}}^{N} J^{(i,j)}\hat{\sigma}_z^{(i)} \otimes \hat{\sigma}_z^{(j)}, \quad (3.55)$$

where

$$B_x^{(i)} := \hbar\Omega_M^{(i)} \quad \text{and} \quad J^{(i,j)} := \hbar \sum_{m=1}^{3N} \frac{\Omega_S^{(i)}\Omega_S^{(j)}\eta_m^{(i)}\eta_m^{(j)}}{\delta_m}\alpha_3^2. \quad (3.56)$$

(Note that the superscripts of $B_x^{(i)}$ and $J^{(i,j)}$ indicating the site will be omitted in the following sections, if the interaction strengths for all ions are equal.)

Depending on the sign of the detunings $\delta_m$, the effective spin–spin interaction can be of ferromagnetic ($J^{(i,j)} < 0$) or antiferromagnetic ($J^{(i,j)} > 0$) nature. The range and spatial structure of the spin–spin interactions can be partially controlled by choosing the absolute values of the detunings $\delta_m$. There are two different limits in which the interaction can be shaped in a very controlled way. On the one hand, if the laser is tuned close to the frequency of a given mode $m'$ ($|\delta_{m\neq m'}| \gg |\delta_{m'}|\ \forall\ m$), then $J^{(i,j)}$ is a long-range interaction, whose spatial dependence is governed by the phonon wavefunction corresponding to $m'$, as can be seen directly in equation (3.56). On the other hand, if all the motional modes contribute to the spin–spin coupling ($|\delta_m - \delta_{m'}| \ll |\delta_{m'}| \forall m, m'$), the interaction shows a power-law decay $J^{(i,j)} \propto 1/|i-j|^3$ [21, 124]. This can be understood by the partial interference between the contributions from each mode's wavefunction.

Furthermore, the freedom in the choice of the coupling strengths $\Omega_S^{(i)}$ for the individual ions as well as the trapping geometry and laser direction going into $\eta_m^{(i)}$ allows us to shape the individual coupling strengths $J^{(i,j)}$. This opens up the possibility of simulating a rich variety of models beyond the quantum Ising Hamiltonian, such as spin-frustrated systems [48] (see section 5.1). An illustration of the normal modes of motion and an example of the effective spin–spin couplings in a surface-electrode trap similar to the traps discussed in section 6 is given in figure 10.

In addition to the quantum Ising part discussed above the complete Hamiltonian consists of the following terms that lead to a deviation from the ideal model (constant terms are omitted):

$$\hat{\mathcal{H}}_{Error} = 2\sum_{i=1}^{N}\sum_{j=1}^{N} \frac{\alpha_0}{\alpha_3} J^{(i,j)}\hat{\sigma}_z^{(i)} + \hat{\mathcal{H}}_\delta + \hat{\mathcal{H}}_E''. \quad (3.57)$$

The first 'bias' term is further discussed in the context of the experimental realization, see [47] and section 5.1. The second term $\hat{\mathcal{H}}_\delta$ can be interpreted as an energy offset, which cancels by applying an appropriate redefinition of the energy scale. As mentioned above, the last term leads to only a small or even negligible error for $|\Omega_S^{(i)}\eta_m^{(i)}\alpha_l/\delta_m| \ll 1$. For a more detailed discussion of the errors in the simulation of quantum spin Hamiltonians we refer the reader to [125].

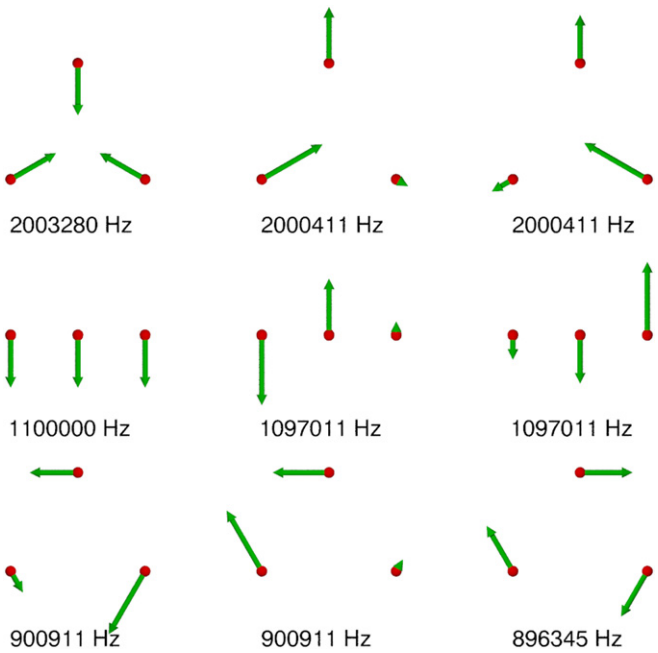


**Figure 10.** Example for normal modes in a surface-electrode trap geometry similar to the one discussed in section 6. It consists of three trapping zones (red spheres) arranged in a triangle at mutual distances of 40 $\mu$m. Each trapping zone has a (bare) frequency of $2\pi \times 2$ MHz corresponding to the vibration towards the centre of the triangle, $2\pi \times 1.1$ MHz for the out-of-plane vibration and $2\pi \times 0.9$ MHz for the third, perpendicular direction. The eigenvectors (green arrows) of the nine normal modes for an ion of mass $m = 25$ amu in each potential minimum are shown (first and last row: top view for in-plane modes; middle row: side view for out-of-plane modes; see appendix A for details of the calculation). The labels denote the frequencies corresponding to the modes. The (coupled) frequencies make up three triplets close to each bare frequency; two frequencies in each triplet are degenerate. For $\hat{k}_I^{(i)} = \hat{k}_I$ pointing in the direction corresponding to the (bare) $2\pi \times 2$ MHz vibration of one of the trapping zones, $\omega_I \approx 2\pi \times 1.725$ MHz, and equal $\Omega_I^{(i)} = \Omega_I$ we can obtain effective spin–spin couplings $J^{(1,2)} = J^{(1,3)} = -J^{(2,3)} \sim 2\pi \times 1$ kHz, which would allow for the evolution to a frustrated spin state. We want to note that the out-of-plane modes must be tilted in an implementation to allow for three-dimensional Doppler cooling. This can, for example, be achieved by applying dc voltages to appropriate electrodes (compare section 6). These dc fields could also be used to achieve/raise the degeneracy of the bare frequencies in the individual potential minima and, hence, switch on/off motional couplings between the ions.

We want to emphasize that $[\hat{\mathcal{H}}_B, \hat{\mathcal{H}}_J] \neq 0$, such that the time evolution of the total quantum Ising Hamiltonian $\hat{\mathcal{H}}_{QIsing}$ cannot be simply described by the time evolutions of $\hat{\mathcal{H}}_B$ and $\hat{\mathcal{H}}_J$ separately.

## 4. Operations interpreted for experimental quantum simulations

To realize a QS for a quantum spin Hamiltonian, we have to (1) simulate the spin, provide (2) its initialization and (3) the interaction of this 'spin' with a simulated magnetic field, (4) realize an interaction between several spins (spin–spin interaction) and (5) allow for efficient detection of the final spin state. Additional diversity for QS arises by the capability of precise initialization, control and readout of the motional states.

The mathematical derivation and description of the individual operations have been described in section 3. In this section, we explain in a simplified pictorial way the related generic building blocks in terms of an adiabatic QS of a quantum spin Hamiltonian within a linear chain of ions. No specific ion species or trapping concept are required. A well-suited system to illustrate the generic requirements and to investigate the feasibility of QS in ion traps is given by the quantum Ising Hamiltonian (see equation (3.55)). We want to note that the building blocks already suffice to implement a whole family of quantum spin Hamiltonians.

However, the toolbox for QS is substantially larger (see also section 5.2). (1) Phonons do not have to be restricted to mediate interactions in QC and QS: they were also proposed to simulate bosons, for example atoms in the Bose–Hubbard model [22] or charged particles [126]. (2) Topological defects in the zigzag structure of two-dimensional Coulomb crystals (see figure 13) are proposed to simulate solitons [127].

### *4.1. Simulating the spin*

The mutual distance between the ions/spins in linear RF traps is typically of the order of several micrometres (see figure 3). Therefore, the direct interaction between their electronic states remains negligible, which is advantageous, because the related interaction strength could hardly be tuned or even switched off. Therefore, the spin-1/2 states are implemented like qubit states (see section 2.2).

### *4.2. Simulating the magnetic field*

Implementing an artificial spin allows us to shape artificial fields to implement a precisely controllable interaction and related dynamics between the 'spin' and the 'field'. To simulate an effective magnetic field, the two electronic states $|\downarrow\rangle$ and $|\uparrow\rangle$ are coupled via electro-magnetic radiation (see section 2.3, operation (a)). The related coherent oscillation of the state population between the two levels can be described in terms of Rabi flopping. In the Bloch sphere picture, the tip of the electronic state vector rotates during one flop continuously from state $|\downarrow\rangle$ to $|\uparrow\rangle$ and vice versa. For continuous coupling this can be interpreted as the precession of a spin exposed to a perpendicular magnetic field.

The rotation matrix in equation (3.30) exactly describes this interaction with a single spin (see also sections 3.2 and 3.4). For example, if we start with $|\downarrow\rangle$ and apply a pulsed rotation $\hat{R}(\pi/2, \pi/2)$, we will obtain an eigenstate of $\hat{\sigma}_x$, which is abbreviated by $|\rightarrow\rangle := 1/\sqrt{2}(|\downarrow\rangle + |\uparrow\rangle)$. In the Bloch picture, this corresponds to a 90° rotation of the Bloch vector around the $y$-axis, such that it will point in the direction of the $x$-axis. Continuing with a second identical rotation we just flip the spin to $|\uparrow\rangle$ as if we applied $\hat{R}(\pi, \pi/2)$ or a 180° rotation around the $y$-axis, respectively. However, we can replace the second operation by $\hat{R}(\pi/2, 0)$, which corresponds to a rotation around the $x$-axis. As the state $|\rightarrow\rangle$ is an eigenstate of $\sigma_x$ it will not be affected.

Stroboscopic rotations have been introduced in section 3.4 to implement single-qubit gates for a QC. Continuous versions of these single-qubit operations can be interpreted in the context of analogue QS as simulated magnetic field (first term of equation (3.55)).

### *4.3. Simulating the spin–spin interaction*

Let us first discuss the implementation of a basic spin–spin interaction close to the original proposal in [21]: two ions are confined in a linear RF trap and a standing wave provides state-dependent dipole forces. The ions are located at the same phases ($\varphi^{(i)} = 0$), such that ions in different spin states are pulled/pushed in opposite directions.

If both ions are in the same spin state, they will be pulled in the same direction. Hence, their mutual distance and mutual Coulomb energy, respectively, remain unchanged. However, if the two spins are in different states, one ion will be pulled and the other one pushed. Their mutual distance and as a result their mutual Coulomb energy will change. This is exactly the essence of a spin–spin interaction, where the energy corresponding to a spin state depends on the states of its neighbours. To interpret interactions as ferromagnetic or antiferromagnetic it is advantageous to consider the mutual Coulomb energy in longer chains of spins (see figure 11).

The technical realization in [47] avoids the difficulties arising from standing waves and resonantly enhances the interaction strengths by implementing the spin–spin interactions with stimulated-Raman transitions as in the case of quantum gates [124] (see section 3.4). In a pictorial interpretation, the standing waves are replaced by 'walking' waves and instead of static displacements we obtain driven oscillations of the ions. However, the mathematical description yields exactly the same spin model in an appropriately chosen frame (see section 3.5). The sign of $J$ can additionally be changed by choosing a different sign for the detunings $\delta_m$ from the modes (see equation (3.56)).

### *4.4. Geometric phase gate versus adiabatic quantum simulations*

It might be helpful to emphasize the differences and similarities of the interactions in QC and analogue QS: to realize a

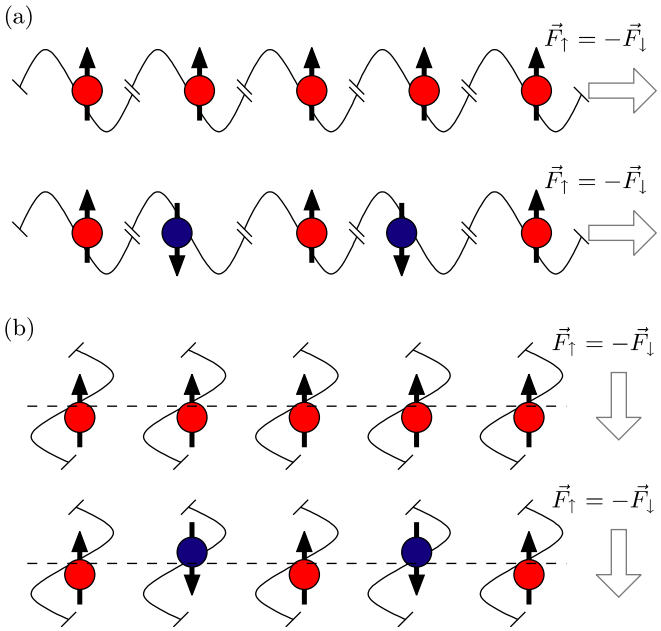


**Figure 11.** Ion chains superimposed by standing waves providing state-dependent forces in the (*a*) axial direction and (*b*) radial direction. All ions are placed at the same phases of the standing waves. (*a*) If all spins are in the same state, the ions will all be shifted in the same direction without changing their mutual Coulomb energy. However, if every second spin is in the opposite spin state, distances between neighbouring ions will be alternately increased and decreased and the mutual Coulomb energy is increased due to its $1/d$ dependence. Here $d$ denotes the distance between neighbouring spins. The ferromagnetic order is energetically preferred, such that $J < 0$ for this interaction. (*b*) A chain of ions with the same spin states will again only be displaced and the mutual Coulomb energy will not change. For alternating spin states the distances between neighbouring ions will increase, such that the mutual Coulomb energy will be decreased. (Note that this should not to be confused with the structural zigzag phase-transition (see figure 3), where the radial displacements are typically orders of magnitude larger and spin-independent.) The antiferromagnetic order is energetically preferred, such that $J > 0$.

phase gate operation on the radial modes of two qubits, as described in section 3.4, typically one or two isolated modes of motion are selected. The small detuning from the modes is chosen to obtain comparatively large interaction strengths and thus motional excitations. For ions being initialized in the motional ground state the displacements in the respective phase space(s) lead to an average phonon number $\bar{n} \sim 1$ at the point of maximal motional excitation and to a significant entanglement between electronic and motional states. However, this entanglement vanishes at the end of the gate and there will be an (maximal) entanglement between the qubit states only (see section 3.4).

In contrast, we consider an adiabatic evolution according to the quantum Ising Hamiltonian in the case of analogue QS (see section 5.1 for the experimental protocol). We have to make sure that the entanglement between electronic and motional states remains small at any time during the simulation (see discussion of errors in section 3.5). Additionally, running the simulation on many spins simultaneously will result in contributions from many motional modes simultaneously. As a result, a large detuning from all modes has to be chosen, such that the difference of the radial frequencies can be neglected and a net effect from all modes remains. Choosing the right parameters allows the simulation of spin–spin interactions of different strength, different signs and even range of interaction [21].

Furthermore, a scan of the duration of the displacement pulses $T_\mathrm{D}$ in geometric phase gates leads to a periodic evolution from $|\downarrow\downarrow\rangle$ to $|\uparrow\uparrow\rangle$ and vice versa (see figure 8).

In contrast, the distinct contributions ($\hat{\mathcal{H}}_\mathrm{B}$ and $\hat{\mathcal{H}}_\mathrm{J}$) of the quantum Ising Hamiltonian are not stroboscopically alternated but applied simultaneously. As mentioned in section 3.5, the time evolution according to the quantum Ising Hamiltonian is not simply the time evolution according to $\hat{\mathcal{H}}_\mathrm{B}$ and $\hat{\mathcal{H}}_\mathrm{J}$ separately. As a consequence, applying the spin–spin interaction for a longer duration and/or increasing its strength does not alter the state anymore.

## 5. Towards simulating many-body physics

In the first part of this section we want to assemble the building blocks described above to illustrate how an analogue QS of a quantum spin Hamiltonian can be implemented. For this purpose, we will describe the realization of first proof-of-principle experiments on the quantum Ising Hamiltonian (see equation (3.55)). In the second part we aim to summarize, to the best of our knowledge, the existing proposals addressing many-body physics with the described and available toolbox.

### *5.1. Proof-of-principle experiments on quantum spin Hamiltonians*

First, we will describe the basic implementation of the experimental protocol on the axial modes for the case of two spins [47], as illustrated in figure 12. Subsequently, we will emphasize the differences and additional information explored in [48, 49]. For the details on the individual experimental parameters we refer to these references.

For the case of two spins, the protocol has been realized following five steps. (1) The two ions are initialized by Doppler cooling, sideband cooling and optical pumping (see section 2.4) in the state $|\downarrow\downarrow\rangle|n_\mathrm{STR} = 0\rangle$. (2) Both spins are prepared by a common $\hat{R}(\pi/2, \pi/2)$ rotation in the $\hat{\sigma}_x^{(i)}$ eigenstate $|\rightarrow\rightarrow\rangle|n_\mathrm{STR} = 0\rangle$. (3) An effective magnetic field of amplitude $B_x$ is applied equivalent to a continuous $\hat{R}(2\Omega_\mathrm{M}t, 0)$ rotation (see equations (3.55) and (3.56)). At this step, the state $|\rightarrow\rightarrow\rangle|n_\mathrm{STR} = 0\rangle$ represents the ground state of the first term of the quantum Ising Hamiltonian in equation (3.55) that can be 'easily' prepared. Note that the rotation is slightly off-resonant to mimic an additional $\hat{\sigma}_z$ interaction counteracting the 'bias' field (see also [47]). (4) The effective spin–spin interaction $J$ is ramped up adiabatically with respect to the timescale $1/\Omega_\mathrm{M}$ defined by the simulated magnetic field, until $|J| \gg B_x$. The system adiabatically evolves into its new ground state, which is an equal superposition of the two energetically preferred states of the ferromagnetic order: $1/\sqrt{2}(|\downarrow\downarrow\rangle + |\uparrow\uparrow\rangle)$. (5) Finally, both interactions are switched off. The readout of the final spin state is performed by state-dependent detection. This

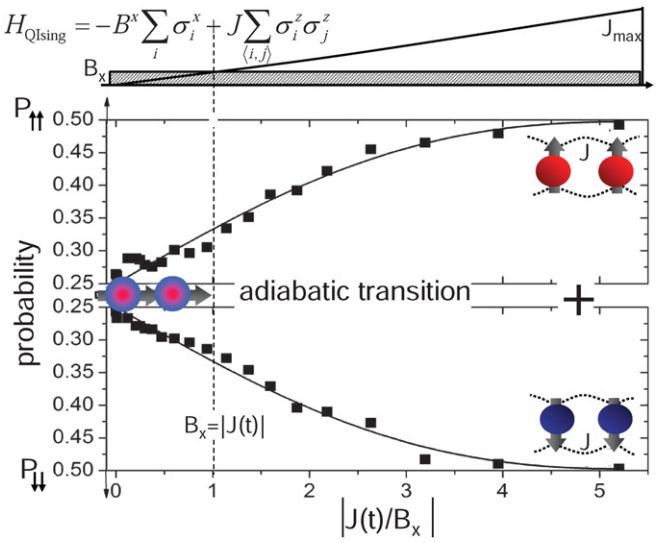


**Figure 12.** Probability of finding two spins in either of the states $|\downarrow\downarrow\rangle$ or $|\uparrow\uparrow\rangle$ after an adiabatic QS of the quantum Ising Hamiltonian as a function of $|J/B_x|$, starting within paramagnetic order. The experimental protocol (top) consists of the interactions applied simultaneously including an adiabatic increase in $|J|$ to transfer the system from the former ground state $|\rightarrow\rightarrow\rangle$ to the new one (bottom). We achieve a maximal probability of $P_{\uparrow\uparrow} = P_{\downarrow\downarrow} = (49 \pm 1)\%$ to observe one of the states $|\downarrow\downarrow\rangle$ and $|\uparrow\uparrow\rangle$ corresponding to a ferromagnetic order and define the quantum magnetization to be equal to $P_{\uparrow\uparrow} + P_{\downarrow\downarrow} = (98 \pm 2)\%$. We derive the fidelity for the entangled state $1/\sqrt{2}(|\downarrow\downarrow\rangle + |\uparrow\uparrow\rangle)$ to approximately $F = 0.88$ by a parity measurement (compare [47] and section 3.4).

projects the spin state to one out of the four eigenstates of the measurement basis ($|\downarrow\downarrow\rangle$, $|\downarrow\uparrow\rangle$, $|\uparrow\downarrow\rangle$, $|\uparrow\uparrow\rangle$). Steps (1)–(5) are repeated many times to obtain the populations related to these states.

To investigate the degree of entanglement of the final spin state, an additional parity measurement is performed as in the case of the geometric phase gates (see section 3.4). The populations of $|\downarrow\downarrow\rangle$ and $|\uparrow\uparrow\rangle$ as a function of $|J|/B_x$ and the entanglement fidelity are summarized in figure 12.

The experimentally observed entanglement of the final states confirms that the transition from paramagnetic to ferromagnetic order is not caused by thermal fluctuations that drive thermal phase transitions, but by the so-called quantum fluctuations [45, 128] driving QPTs in the thermodynamic limit at zero temperature. In this picture tunnelling processes induced by $B_x$ coherently couple the degenerate states $|\uparrow\rangle$ and $|\downarrow\rangle$ with an amplitude $\propto B_x/|J|$. For $N$ spins the amplitude for the tunnelling process between $|\Psi_{N\uparrow}\rangle = |\uparrow\uparrow \ldots \uparrow\rangle$ and $|\Psi_{N\downarrow}\rangle = |\downarrow\downarrow \ldots \downarrow\rangle$ is proportional to $(B_x/|J|)^N$, since all $N$ spins must be flipped. In the thermodynamic limit ($N \rightarrow \infty$) the system is predicted to undergo a QPT at $|J| = B_x$. At values $|J| > B_x$ the tunnelling between $|\Psi_{\infty\uparrow}\rangle$ and $|\Psi_{\infty\downarrow}\rangle$ is completely suppressed. In our case of a finite system $|\Psi_{2\uparrow}\rangle$ and $|\Psi_{2\downarrow}\rangle$ remain coupled and the sharp QPT is smoothed into a gradual change from paramagnetic to ferromagnetic order (see figure 12).

It has to be noted that the performance of such a simulation on a large number of spins in a one-dimensional chain requires several technical improvements. Recently, a group at the University of Maryland pioneered a substantial step for scaling by investigating the emergence of magnetism in the quantum Ising model using up to nine ions [49]. To achieve these results they mediated the interactions via the radial modes of motion [21, 122] (see also section 3.4). Furthermore, they implemented the effective spin–spin interactions in a rotated frame using Mølmer–Sørensen interactions [85, 87] on robust hyperfine clock states. Thereby, they do not depend on the phases $\varphi^{(i)}$ of the laser beams at the sites of the ions. To perform an adiabatic transition, the simulated magnetic field has been adiabatically turned off, while the effective spin–spin interaction remains constant.

Their results allow much more than simply increasing the number of spins: they enter a new regime of intriguing questions. The crossover of the quantum magnetization [47] from paramagnetic to ferromagnetic order is sharpening as the number of ions is increased from two to nine, 'prefacing the expected QPT in the thermodynamic limit' [49]. Even though the results can still be calculated on a classical computer, they provide a possibility to critically benchmark QS aiming for only slightly larger systems.

Increasing the number of ions to three and adapting the individual spin–spin interactions including their signs allows spin frustration to be addressed in the smallest possible magnetic network [48]. Spin frustration of the ground state can be pictorially understood in a two-dimensional triangular spin lattice featuring antiferromagnetic spin–spin interactions. Here, it becomes impossible for neighbouring ions to have pairwise opposite states. Classically, two ions will adopt different states, while the state of the third one is undetermined. During an adiabatic evolution of the quantum mechanical system (starting from the paramagnetic order) nature will choose a superposition of all degenerate states, leading to massive entanglement in a spin-frustrated system. In the realization of the experiment, the three ions are still trapped in a one-dimensional chain. However, almost complete control over the amplitudes and signs of $J^{(1,2)}$, $J^{(2,3)}$, $J^{(3,1)}$ is gained by coupling to particular collective modes of motion and choosing appropriate detunings [48].

It has to be mentioned that for an increased number of spins the energetic gap between ground and excited states further shrinks and the requirement on adiabaticity enforces longer simulation durations related to a longer exposure to decohering disturbances. Still, as mentioned in section 1, the influence of decoherence might destroy the entanglement within the system, but this might not be relevant for the observable of interest. Here it will be crucial to investigate the role of the decoherence effects with respect to the specific analogue QS.

With respect to digital (stroboscopic) QS it should be emphasized that no quantum error correction is required for proof-of-principle experiments on a few ions. Promising results of a stroboscopic version of the simulation of the quantum Ising Hamiltonian with two spins have been shown recently [129].

### *5.2. Systems featuring many-body physics proposed for analogue quantum simulations*

Condensed matter met atomic, molecular and optical physics not so long ago, when trapping techniques for ultracold neutral atoms and ions allowed experimentalists to generate lattices and crystals, where models from solid-state physics may be implemented. Combining the fields has led to a very rich interdisciplinary research activity, as well as to several misunderstandings between scientists looking at the same system from different points of view. In the particular case of trapped ion experiments, the outlook for quantum simulation of many-body models is very exciting, but some knowledge on the details of this physical system is required to understand both the limitations and the amazing possibilities of this setup.

In the following we review many-body models that have the potential to be simulated with trapped ions. There have been several contributions both from theory and experiments to this research line. Most of them share the common feature that they are inspired by known models from condensed matter physics, but their implementation with trapped ions turns out to lead to a rich variety of new physical phenomena, which may even require new theoretical paradigms that go beyond the conventional ones in the solid state. The three main reasons for this are (1) trapped ion experiments are naturally performed in a non-equilibrium regime, whereas solid-state physics typically deals with thermal equilibrium, (2) trapped ion systems may in principle be controlled and measured at the single particle level, (3) ion crystals are typically mesoscopic systems, in the sense that they may reach a number of particles (spins, phonons, etc) large enough to show emergent many-body physics, but still finite size effects are important. All those peculiarities have to be kept in mind, since they provide us with unique features for analogue QS.

*5.2.1. Quantum spin models.* Following the experimental advances in QIP, the most natural degree of freedom to be used for QS seems to be the electronic states for spins and the phonons to mediate their mutual interactions. However, one has to identify conditions where interesting phenomena arise, such as, for example, quantum critical phases. This has already lead to the promising proof-of-principle experiments discussed above.

A unique feature that we can exploit with trapped ions is the fact that the effective spin–spin interactions can be implemented showing a dipolar decay, $J^{(i,j)} \propto 1/|i-j|^3$. In the case of the Ising interaction, the cubic dependence does not change the critical universality class of the model, as shown, for example, by the numerical calculations in [125]. However, even in this case, long-range entanglement is induced by the long-range interaction, which is absent in conventional nearest-neighbour quantum Ising chains. On the other hand, when considering other interacting schemes, such as the $XXZ$-Hamiltonian, the dipolar interaction may lead to the formation of quasi-crystalline phases of spin excitations [130]. Furthermore, the simulation of the hexagonal Kitaev model with ions in an optimized, two-dimensional surface-electrode trap has been proposed [131].

Moreover, intrinsic properties of the trapped ion crystal, such as the linear–zigzag transition, have been demonstrated to be a QPT of the universality class of the Ising model in a transverse field [132, 133].

Several pieces have been added to the toolbox of quantum simulation, which definitely allow us to explore physics beyond conventional solid-state paradigms. For example, a theoretical proposal has been presented to implement models, whose ground states show topological features [134]. Also, methods to implement three-body spin–spin interactions have been designed, see [135]. Finally, dissipation in trapped ion systems has been proved to be useful to engineer quantum phases that arise as steady-state of dissipative processes [136]. The many-body physics of dissipative systems is a much more unexplored area than equilibrium properties, even for theorists. For that reason, adding dissipation to quantum magnetism opens an exciting perspective for trapped ions.

*5.2.2. Interacting boson models.* A variety of exciting quantum many-body systems may also be simulated using the collective motional degrees of freedom (phonons) to realize models of interacting bosons. In particular, whenever the motional coupling between ions is small compared with the trapping frequency, the phonon number is conserved and becomes a good quantum number to characterize the quantum state of the system. This principle was introduced and exploited in [22] to show that the physics of radial modes in Coulomb chains is effectively described by a Bose–Hubbard model. Vibrational couplings between two ions, say 1 and 2, induced by the Coulomb interaction, have a typical form $\propto \hat{x}^{(1)}\hat{x}^{(2)}$, where $\hat{x}^{(i)}$ is the ion displacement operator. Under the approximation of phonon number conservation, those terms become tunnelling couplings of the form $(\hat{a}_1^\dagger \hat{a}_2 + \text{h.c.})$. The same idea applies to quartic anharmonicities of the trap, which yield Hubbard interactions, $(\hat{a}_m^\dagger \hat{a}_m)^2$. Anharmonicities may be induced and controlled with optical forces, as shown in [22]. This analogy between phonons and interacting bosons opens an exciting avenue of research, where experiments might be relevant even with a single ion, realizing a single anharmonic quantum oscillator.

The ground state of those phonon-Hubbard models in Coulomb chains was extensively studied in [137], where it was shown that phonon Luttinger liquid phases may arise. Very recent experiments indeed show the tunnelling of phonons between ions trapped by different potentials, realizing thus an important step towards the use of phonons for quantum simulation [138, 139]. Exploiting phonon tight-binding models has also been shown to allow the implementation of models with disorder showing Anderson localization [140], as well as synthetic gauge potentials using periodic driving of the trap frequencies, see [126]. Using dipole forces acting on ions confined in a microtrap array (see section 6), motional couplings can be controlled such that phonons simulating charged particles experience synthetic gauge fields.

*5.2.3. Spin–boson models.* The natural convergence of the proposals presented above leads to the quantum simulation of

spin–boson models. This is a paradigmatic model for quantum impurities in solids, which typically describes a single spin coupled to a continuous bath of harmonic oscillators with a power-law spectral density. Surprisingly, the coupling of the electronic levels of a single ion to the axial phonons of a Coulomb chain yields a spin–boson model with a quasi-ohmic spectral density [44]. The physics to be simulated here is equivalent to some celebrated models in condensed matter physics, such as the Kondo effect. The finite size effects that are intrinsic of trapped ion systems turn out to yield features beyond the conventional physics of these models, in particular quantum revivals associated with the reflection of vibrational waves along the chain. Quite recently, it has been proposed to study a situation in which spins and phonons are coupled, in such a way that a Jaynes–Cummings–Hubbard model is simulated [141]. In this model phonons follow a tight-binding Hamiltonian and, in addition, they are locally coupled to spins. The system has been shown to undergo a superfluid–Mott insulator QPT.

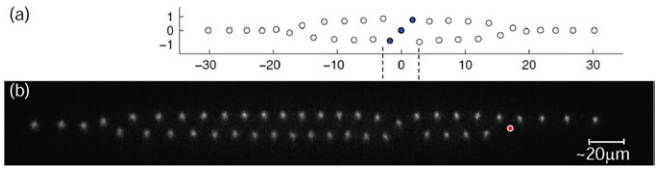


**Figure 13.** Topological defects in two-dimensional Coulomb crystals (compare figure 3(*c*) for a comparable crystal without defects). Changing the experimental parameters non-adiabatically during a structural phase transition from a linear chain of ions to a zigzag structure, the order within the crystal breaks up in domains, framed by topologically protected defects that are suited to simulate solitons. (*a*) Numerical simulations for 33 ions predicting a localized topological defect at the position of the marked (blue) ions. (Courtesy of Benni Reznik and Haggai Landa.) (*b*) CCD image of 45 laser cooled $Mg^+$ ions providing clear evidence of the topological defect indicated by the zigzag–zagzig transition. The crystal contains a non-fluorescing molecular ion ($MgH^+$) at the red mark. (Courtesy of Günther Leschhorn and Steffen Kahra of the group at MPQ.)

*5.2.4. Inhomogeneous many-body models: impurities and topological defects.* The tools for QS in ion traps are not restricted to electronic and motional degrees of freedom only. It has been proposed to exploit impurities in the Coulomb crystal. On the one hand, for example, by embedding ion(s) of a different species (different mass) into the crystal and taking advantage of the altered spectrum of the modes and scattering of phonons [142] and the option to include larger simulated spins ($S > 1/2$) [143]. On the other hand, by creating localized topological defects within the more dimensional structure of the Coulomb crystal (see figure 13). In [127] it was suggested to induce a structural phase transition from a linear chain of ions (see figure 3(*b*)) to a zigzag structure (see figure 3(*c*)), for example, by lowering the radial confinement. Changing the parameters in a non-adiabatic way (fast compared with the phonons mediating information within the crystal) should cause independent domains of 'zigzag' and 'zagzig' structure, respectively. At their clash, topological defects were predicted and have recently been observed (see figure 13). The number of the created defects should scale according to the Kibble–Zurek prediction [144–146]. The defects themselves can be interpreted as solitons [127]. Solitons are defined as localized solutions of nonlinear systems, which depend essentially on nonlinearity. Such solitons have a unique spectrum of frequencies with modes which are localized to the soliton and whose frequency is separated by a gap from the other phonons. A quantum mechanical time evolution of these modes was calculated numerically and it is expected to remain coherent for hundreds of oscillations [147]. QS could allow us to explore their potential applications for QIP [127] as well as the quantum behaviour of these 'objects' themselves. Solitons appear in all branches of the natural sciences and have been extensively investigated in solid-state systems [148]. Among others, classical solitons were observed in waveguide arrays [149, 150] and Bose–Einstein condensates (BECs) [151], where they are mean field solutions. Discrete solitons were investigated in the Frenkel–Kontorova (FK) model [152, 153], which describes chains of coupled particles interacting with a local nonlinear potential. In a different realization, a variant of the FK model can also be realized in the ion trap by adding an optical lattice to a linear chain [154–156].

The important requirement to address any of these intriguing models will be to increase the number of ions and the dimensionality of the system. Trapping ions in two-dimensional arrays would allow the study of hard-core boson phases, showing the effect of frustration, quantum spin liquid phases and quantum states with chiral ordering [157]. Two approaches for scaling will be described in more detail in the following sections.

## 6. Scaling analogue quantum simulations in arrays of radio-frequency surface-electrode traps

One possible way to overcome the limitations on scalability of trapped ions in a common potential well (see section 2.1) is to store them in an array of individual RF traps.

### *6.1. One-dimensional radio-frequency surface-electrode traps*

Conventional RF traps with their three-dimensional geometry of electrodes (see figure 2) individually fabricated with conventional machining were unique 'masterpieces' with unique characteristics.

In 2005 and 2006, a group at NIST pioneered the miniaturization of RF traps by projecting the electrodes onto a surface [73, 74] (see figure 14(*a*)), very similar to chip traps for neutral atoms [158]. Introducing photolithographic techniques for the trap fabrication opened up exceptional precision and the production of small series of identical traps, see for example [159, 160]. Within these linear RF surface-electrode traps, motional ground state cooling was achieved at a height of the ion over the electrode surface of $h = 40\,\mu$m and with a comparatively small motional heating rate of the order of 1 quantum $\mathrm{ms}^{-1}$ [74].

Motional heating rates scale with $\sim h^{-4}$ [161]. The exact heating mechanisms are not yet fully understood and the groups

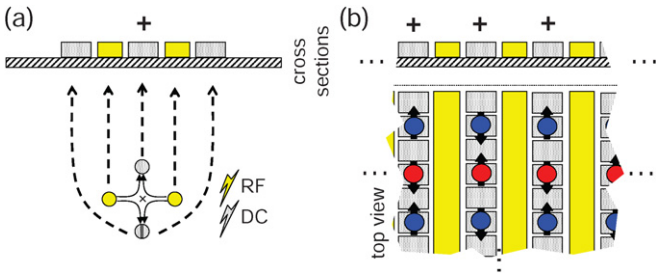


**Figure 14.** Schematic to illustrate the projection of the electrodes of the RF (yellow) and dc (shaded) electrodes on a surface as a way to scale towards two-dimensional arrays of ions. The black crosses indicate the positions of the minima of the pseudopotentials. (*a*) Cross section of the electrodes of a conventional linear RF trap with three-dimensional geometry and the electrode structures projected onto a surface. The dashed arrows point at the new location of the electrodes, the white areas represent isolating gaps. (*b*) Cross section (upper part) and top view (lower part) of the stripe electrodes. It has been proposed to concatenate several linear RF surface-electrode traps as depicted in (*a*) as a basic unit to span a two-dimensional array of ions [164] (red and blue disks representing ions in opposite spin states). For sufficiently small mutual ion distances and decoherence rates of the ions, this is an approach to scale analogue QS.

at NIST, in Berkeley, at MIT and others are currently putting a lot of effort into further investigations. However, the groups at MIT [162], NIST and the University of Maryland demonstrated a significant reduction of the heating rates in cryogenic (surface electrode) traps for QC purposes (see also [50]). The inverse of these heating rates has long been compared with typical operational durations of a QC of tens of microseconds (see also section 3.4).

For scaling towards a universal QC it might suffice to interconnect linear ion traps via junctions on a two-dimensional surface to a network of one-dimensional traps [163], realizing the 'multiplex ion trap architecture' [75]. That is, ions are proposed to be shuttled between processor and memory traps only interacting in the processor traps. This would allow the subdivision of the large total number of ions into small groups in many individual traps and to reduce the local requirements to a technically manageable effort. One-dimensional RF surface-electrode traps with more than 150 individual dc electrodes and several junctions have been realized [163], allowing ions at moderate heating rates to be shuttled.

In addition, the opportunity arose to deliver identical traps to different groups. One example is the linear RF surface-electrode trap (denoted by 'Sandia Linear Trap' in the following) [159], which was designed by the groups in Oxford, Innsbruck and Sandia National Laboratories. The latter fabricated a small series of identical replicas. The traps have been tested in several laboratories and the individually measured trapping parameters are in good agreement with the design values. Publications are in preparation by the groups at Oxford and Sandia (see also [159]).

It has to be emphasized that pursuing the multiplex approach for scaling universal QC is not applicable to the proposed analogue QS, where the ensemble of spins is supposed to evolve uniformly as a whole.

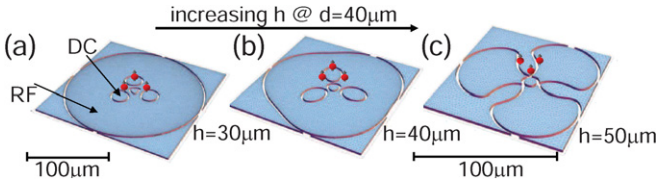


**Figure 15.** Illustration of the optimization results for the electrode structure for a basic triangular lattice with respect to the height of the ions above the traps at constant mutual ion distance. The white gap isolates RF and dc patches. The three red disks symbolize three ions at a constant distance of $d = 40\,\mu$m, hovering above the surface at a height of (*a*) $h = 30\,\mu$m, (*b*) $h = 40\,\mu$m and (*c*) $h = 50\,\mu$m. (Courtesy of Roman Schmied.)

### *6.2. Optimized two-dimensional arrays of radio-frequency surface-electrode traps*

Shortly after the invention of RF surface-electrode traps it was proposed to concatenate linear traps sufficiently close, such that the ions experience mutual Coulomb interaction in two dimensions [164] (see figure 14(*b*)). However, for a real two-dimensional lattice at sufficiently small and uniform ion distances of $d \leqslant 40\,\mu$m in two dimensions, this proposal requires the ions to approach the disturbing surface to $h \leqslant d/2 = 20\,\mu$m [73].

Schmied *et al* implemented a method to calculate the global optimum of the electrode shapes for arbitrary trap locations and curvatures (originally only for periodic boundary conditions) [165]. The gaps between neighbouring electrodes were neglected. The authors exemplarily optimized a trap array with comparatively stiff horizontal confinement.

The idea of optimizing electrode structures can also be used for designing traps for analogue QSs with partially converse requirements. In a collaboration of R. Schmied, NIST, Sandia National Laboratories, and us, such a surface-electrode trap has been designed and is currently in fabrication. The trap will provide three trapping zones arranged in a triangle (similar to figure 15) and is intended as a first step towards larger arrays of ions. For this purpose, the optimization method was extended to finite-sized traps.

It has to be emphasized that there are currently several proposals and approaches for arrays of surface-electrode traps mainly for QC. Groups in Berkeley and Innsbruck aim at trap arrays with individually controlled RF electrodes. They have the advantage of selectively lowerable trap frequencies for individual traps and thus increasable interaction strengths between ions in different traps, while especially the height of the ions above the surface can be larger and the trap depth of other traps can be sustained [166] (see also the discussion in the following subsections). This approach can in principle be extended to quasi-micromotion-free shuttling of ions in arrays of RF traps [167] at the expense of precise control of the RF voltage for each RF electrode. Another proposal suggests individual coils to be included for each trap to allow for laser-less interactions mainly for QS [168]. Different trap geometries specifically for QSs have been designed by a group in Sussex [169]. Arrays of Penning traps with surface electrodes are advanced by the groups at Imperial College [170] and the University of Mainz [171].

In the following subsections we discuss the optimization goals for a surface-electrode trap for an analogue QS, their implications and the perspectives for scalability of this approach.

*6.2.1. Maximization of interaction strengths.* The crucial prerequisite for QSs is to maximize the interaction strength (see section 3). As opposed to the QC case with multiple ions in a common potential, this has to be achieved in QS for ions in individual potentials. The increased mutual ion distances in arrays of individual traps substantially reduces the strength of the effective spin–spin interaction. It has be taken into account that the conditional forces have a limited strength, for example, because the laser power is limited or the assumptions in the theoretical model impose constraints as for the quantum Ising Hamiltonian (see section 3.5). However, a reduced stiffness of the individual potentials compared with the example [165] (trap frequencies on the order of $2\pi \times 20$ MHz) results in larger displacements of the ions by the same forces. This is related to an increased mutual Coulomb energy and thus larger interaction strengths. Still, a lower bound for the trap frequencies (on the order of $2\pi \times 1$ MHz for $Mg^+$) is imposed by the constraints for efficient ground state cooling.

*6.2.2. Minimization of decoherence.* The ions will inevitably approach the disturbing electrode surfaces, if the distance between the individual traps is reduced. We now reinvest the reduced requirements on the stiffness of the horizontal confinement to increase the height of the ions above the surface $h$ keeping the mutual ion distances $d$ constant. Some results for the scenario of a basic triangular lattice are depicted in figure 15, which demonstrates the adapted shape of the electrodes due to different optimization goals. Note that the influence from electrodes of neighbouring traps increases for an increased height $h$. The optimization allows for an increase in the height by more then a factor of 2, still maintaining realistic trapping parameters (see below). Hence, the related motional heating rates (in units of energy per time) are expected to be reduced by more than an order of magnitude. In addition, the increased $h$ should help to protect the electrodes from the high intensity of the laser beams parallel to the electrode surfaces.

We additionally include required isolating gaps between electrodes into subsequent simulations to deduce deviations in the resulting trapping potential [172] (see figure 15). The influence of the gaps turned out to be negligible for the example shown in figure 15, however, for further miniaturized traps these influences will grow in importance due to technically limited gap sizes.

*6.2.3. Maximization of the lifetime of trapped ions.* The reduced frequencies and increased height above the surface come at the price of a reduced trap depth. First, sufficiently deep potentials have to be provided to assure adequate loading rates out of thermal atomic beams, preferably via efficient photoionization [173, 174]. Second, sufficient lifetimes for many ions within the potentials of scaled traps have to be achieved. Currently, the average lifetime in a room temperature surface-electrode trap exceeds one hour (for the Sandia Linear Trap operated in our laboratory).

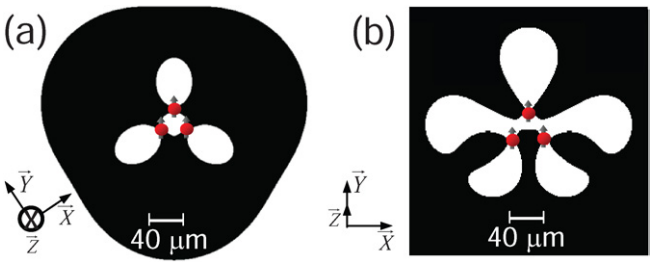


**Figure 16.** Electrode structures for basic triangular lattices with different orientation and tilt of the principal axes. Red disks symbolize ions trapped in the potential minima for parameters comparable to those in figure 15(*b*). (*a*) One principal axis points in the vertical direction with the $X$- and $Y$-axis lying in the horizontal plane of the electrodes. The $X$-principal axis of each trap points towards the centre of the triangle. (*b*) The respective principal axes of all traps point in the same direction and additionally the $Z$-axis is tilted with respect to the surface by more than 10°, which results in a different symmetry of the electrodes. The tilt of the $Z$-axis is essential to reach all spatial degrees of freedom with laser beams restricted to a plane parallel to the electrodes. (Courtesy of Roman Schmied.)

Deeper trapping potentials for surface traps were already achieved by a conductive mesh with controlled voltage (85% light transmittance) a few millimetres above the electrode surface [175]. It has also been successfully tested for the Sandia Linear Trap. The mesh shields the ions from charges on the camera viewport and provides a wavelength-independent alternative to a conductive coating (see, for example [176]).

*6.2.4. Control of the symmetry of interaction.* We additionally gain control over the individual orientations of trap axes or the relative orientations of axes of different traps, respectively (see figure 16). This allows the interaction to be shaped for a given direction of motional excitation between ions in different traps (see section 3). It also allows cooling of all spatial degrees of freedom with laser beams, which have to propagate parallel to the trap surface to minimize scattering off the surface. We can rotate the individual trap axes from pointing towards the centre of the structure (see figure 16(*a*)) into a parallel alignment and additionally include the required tilt of the vertical ($Z$) axes, which will result in a different symmetry of the electrodes (see figure 16(*b*)).

*6.2.5. Control of the potential in individual traps.* First, splitting dc electrodes into several separately controllable segments allows for the individual compensation of displacements of the ions from the minima of the pseudopotential due to stray fields and space charge effects (compare section 2.1 and see [176, 177] for schemes of micromotion compensation). Second, for further scaling, these electrodes can be used to compensate boundary effects. Due to the larger number of inner ions, outer ones would be shifted to larger mutual distances. The further increased density of electrodes on the surface requires their connections in a multilayer structure with vertical wiring (vias) [159, 160].

*6.2.6. Estimation of parameters.* We estimate the strength of simulated spin–spin interactions for the case of $Mg^+$ ions in such devices with currently available laser equipment. We assume a typical laser power of 400 mW (max. 600 mW are available) at 280 nm from an all solid-state laser source [178]. We further assume the beam to have a cylindrical profile with waists of 10 $\mu$m × 100 $\mu$m and an electrode structure as depicted in figure 16(*b*) ($d = h = 40\,\mu$m). For a trap depth of 100 meV and a minimal oscillation frequency of the ions of $2\pi \times 2$ MHz, the interaction strengths by far exceed $2\pi\hbar \times 1$ kHz.

In a different approach, we could think of using the motional degrees of freedom for QSs. This scheme would have the advantage that bare motional couplings are already in the $2\pi \times 5$ kHz regime. In that sense, they are stronger than effective spin–spin interactions, since the latter are slowed down with respect to the original motional couplings by the requirement of adiabaticity. A recent theoretical proposal by some of us has shown that using periodic modulations of the trapping frequencies, some phenomena from solid-state physics may be simulated, such as photon assisted tunnelling [126] (see section 5.2).

### 6.3. Perspectives of our approach

As depicted in figure 16(*b*), in a first step three ions will reside on the vertices of a triangle and the interaction between the spins can be simulated as in [47, 48] (compare section 3.5) or [126] (compare section 5.2). The above parameter estimates should already suffice for proof-of-principle experiments and mesoscopically scaled QS. Motional modes in two-dimensional trap arrays will behave similarly to radial modes in linear RF traps for all three dimensions [21, 124] and the effective spin–spin interaction will prefer antiferromagnetic order for far, red detuning from all modes. Thus, the systems should give us the possibility to study spin frustrations in a spatial, triangular configuration (see also section 5.1).

Based on the results of these investigations further scaling of the surface-trap architecture to large-scale (triangular) lattices of tens or even hundreds of spins might be pursued (see figure 17). In addition to the optimization of the trapping parameters, further technical difficulties have to be considered.

Decoherence due to motional heating as a result of the vicinity to the electrode surfaces could be mitigated within a cryogenic setup [50, 162]. The reduced vacuum pressure could additionally help to increase the lifetime of $Mg^+$, which is currently limited by photochemical reactions with hydrogen (mostly $H_2 + Mg^{+*} \rightarrow MgH^+ + H^*$) and collisions with heavy components of the rest gas. The reaction can also be inverted by pulsed laser beams [179]. However, scaling the system to tens or hundreds of ions will still require frequent and efficient reloading. Increasing the loading efficiency and preserving the vacuum conditions could be achieved by photoionizing cold atoms from a magneto-optical trap (MOT) [180].

Currently, the available laser power should not impose any restrictions on the realization of systems of few tens of ions (see [178] currently providing up to 600 mW). Higher laser powers for magnesium are in reach [181–183] and could allow for even larger arrays of simultaneously coupled ions. In addition to that, efforts in optics, for example arrays of lenses [184, 185], fibres integrated into the trap [186] or integrated mirrors [187–189], could provide individual addressing and high light intensities at the position of the ions. To further mitigate the problem of scattered light from surfaces, one could think of realizing surface traps on partially transparent substrates [74]. Alternatively, laser-less coupling could be used as mentioned in section 2.3 [88, 89, 91–93, 168].

Last but not least, it still has to be identified how to measure observables that permit the verification of frustration effects without the need for full (exponentially complex) state tomography.

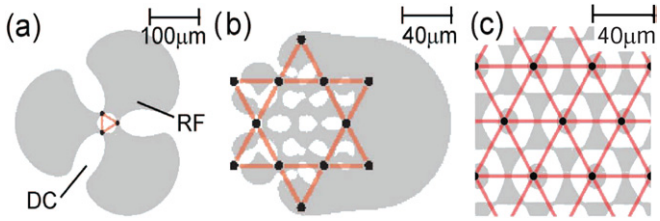


**Figure 17.** Electrode structures for RF surface-electrode traps scaled for analogue QSs. Black dots symbolize the RF minima, red lines serve as a guide to the eye to emphasize the lattice structures for (*a*) three, (*b*) 12 and (*c*) an infinite number of ions/spins. The identical orientation of the principal axes of each RF minimum and non-vanishing components parallel to the trap surfaces (see figure 16) are considered for the latter two. (Courtesy of Roman Schmied.)

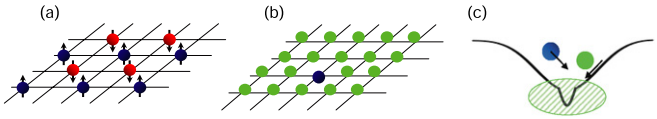


**Figure 18.** Illustration of new options for analogue QS based on ions (red and blue) and atoms (green) in optical potentials (black lines as a guide to the eye). (*a*) Ions populate an optical lattice on well separated sites. The Coulomb force still provides a large strength of dipolar (long-ranging) interaction allowing for analogue QS on many-body effects, similar to the proposed approach in arrays of RF surface-electrode traps (see section 6). (*b*) An ion and atoms populate a common optical lattice and, for example, share the charge via tunnelling electrons. (*c*) An ion could be cooled sympathetically by cold atoms (for example, a BEC indicated by the green ellipse) [192, 199]. Since the micromotion of the ion and the related differential motion between atoms and ion becomes negligible in the common optical trap [60], deep equilibrium temperatures are predicted to be achievable, down to a regime where ultra-cold chemistry might dominate the collisions.

## 7. Scaling quantum simulations based on ions in optical lattices

Some groups aim to merge the two fields of QS based on ions in RF traps and atoms confined in optical lattices. It has already been proposed to combine Coulomb crystals in a harmonic confinement of a common RF trap of three-dimensional geometry with (commensurate) optical lattices to shape anharmonic trapping potentials providing new possibilities to simulate interactions [157]. Another proposal deals with the

simulation of the Frenkel–Kontorova model using a standing wave aligned with the trap axis [156]. Kollath *et al* suggested exploiting a trapped ion to coherently couple (such as a scanning microscope) to the atoms confined in an optical lattice [190].

Optical ion trapping was realized with a single $Mg^+$ ion trapped in a dipole trap [80]. We can now dream of spanning an array of ions (even simultaneously with neutral atoms) within an optical lattice. It has to be emphasized that the smaller trap depth of optical traps (see figure 1) renders it highly unlikely that optically trapping charged atoms will allow us to outperform the achievable trapping parameters or coherence times of both, ions in RF traps and of optically trapped neutral atoms. However, in our opinion, this is not required. The advantage of equally and closely spaced traps might be combined with individual addressability and, most importantly, the long-range interaction provided by Coulomb forces between the ions.

In the following, we will first describe how trapping of an ion in a dipole trap was achieved. Still facing a huge variety of challenges, the new possibilities will be discussed afterwards.

### *7.1. Trapping of an ion in a dipole trap*

The procedure used in [80] to load a magnesium ion ($^{24}Mg^+$) into a dipole trap consists of the following steps: an atom is photoionized out of a thermal beam and trapped and Doppler cooled in a conventional RF trap. Next, stray electric fields are minimized at the site of the ion using the ion as a sensor. Then a Gaussian laser beam providing the dipole trap is focused onto the ion and the RF drive of the RF trap is switched off. From that time on, the ion is confined in the dipole trap in the directions perpendicular to the beam propagation. The depth of the dipole trap potential amounts to $U_0 \approx 2\pi\hbar \times 800\,\mathrm{MHz}$ or $U_0 \approx k_\mathrm{B} \times 38\,\mathrm{mK}$, respectively, and the detuning of the dipole trap beam from the relevant transition ($S_{1/2} \leftrightarrow P_{3/2}$) to $\Delta \approx -6600\Gamma$, where $1/\Gamma$ determines the lifetime of the $|P_{3/2}\rangle$ state. Static electric fields provide the confinement in the direction of beam propagation. After a few milliseconds the RF drive is switched on again and the presence of the ion can be verified via its fluorescence during Doppler cooling.

For the given parameters a half-life of approximately 2.5 ms is achieved. This value is in very good agreement with the theoretical predictions, assuming exclusively the heating process related to off-resonant scattering of the trapping light by the ion, the so-called recoil heating. It can be concluded that the heating and subsequent loss of ions from the optical potential is not dominated by heating effects related to the charge of the ion, for example, due to the vicinity of electrodes or fluctuating stray electric fields. Thus, state-of-the-art techniques for neutral atoms should allow effective enhancement of the lifetime and coherence times [191].

### *7.2. Lifetime and coherence times of optically trapped ions*

We aim to increase the lifetime by cooling the ion in the dipole trap. Due to the large ac Stark shift and its large position dependence, simple Doppler cooling within the existing setup is challenging. Possibilities of cooling the ions directly towards the ground state of motion within the dipole potential are currently being investigated theoretically and experimentally.

An alternative approach suggests to use cold atoms or even a BEC to sympathetically cool ions [192]. On longer timescales the approach of cavity assisted cooling of ions in conventional RF traps reported in [193] might also provide long lifetimes without affecting the electronic state of the ion.

Currently, the coherence time of the electronic state of the ion is limited to a few microseconds due to the high spontaneous emission rate. If longer coherence times are required (which is not necessarily the case for every scenario), they can be achieved in two ways. (1) As for two-photon stimulated-Raman transitions the spontaneous emission rate can be reduced by increasing the detuning. A larger beam intensity could sustain the potential depth. (2) Another option would be to work with blue detuned light, where the potential depths can remain identical, however, the ions seek low intensity and exhibit less spontaneous emission.

### *7.3. Towards ions and atoms in a common optical lattice*

It has still to be demonstrated that one or several ions can be confined within one- or more-dimensional optical lattices. With currently available laser sources a mutual ion distance within each dimension of the order of tens of micrometres could be achieved, which corresponds to one ion at approximately every 40th to 50th lattice site (see methods in [80]). Therefore the mutual ion distance could be smaller than the currently envisioned distances between neighbouring traps in the RF surface-electrode trap approach (see section 6).

Since the photoionization scheme applied so far ionizes out of a thermal beam of magnesium atoms, the average kinetic energy of the atoms is much larger than the depth of the optical potential and, in addition, the local vacuum is severely affected. The loading efficiency for RF traps could be largely enhanced by ionizing Mg atoms from a MOT [194], which would also allow direct loading of atoms into an optical trap. In addition, after loading neutral atoms into the lattice, some of them could be photoionized on site.

Ions and atoms confined in a common optical lattice could offer an approach to exploit the physics of charge transfer reactions. This might allow for a complete new class of QS, for example, of solid-state systems, where atoms in a completely occupied lattice (at an initially small density of ions) share electrons by tunnelling causing highly entangled states of the compound system. The resulting quantum many-body dynamics should be governed by the interplay of the quantum state of the trapped neutral atoms and the electron tunnelling from neutrals to ions.

## 8. Conclusions

In the last few years the basic building blocks for a scalable architecture of a quantum information processor (QC) with trapped ions have been demonstrated for a few qubits. Additionally, a large variety of new techniques have already been tested that might considerably extend the available

toolbox. For example, interactions based on magnetic field gradients and RF fields, fibre-coupled optical support on chip or economically and technologically facilitated cryogenic environments. Despite the fact that it will be a non-trivial challenge to scale the system to approximately $10^5$ qubits, no fundamental limitations have been identified so far.

On a shorter timescale, intriguing problems might be studied by realizing analogue quantum simulators (QS), by far exceeding the capabilities of classical computers. They can be based on similar techniques as a potential QC, but with less severe constraints on the fidelity of operations and the number of required ions.

Currently available operational fidelities are predicted to allow for studying many-body physics, for example in systems described by quantum spin Hamiltonians, the Bose–Hubbard and the spin–boson models. First proof-of-principle experiments simulating Ising type interactions with a few ions have already been successfully demonstrated.

The required increase of the number of ions and the accessible dimensions is proposed within two-dimensional arrays of RF surface-electrode traps. However, the approach is still at the level of proof-of-principle experiments and further challenges might arise during its development. Alternative approaches include Penning traps or optical lattices.

Even though the enthusiasm within this quickly growing field seems to be justified, it has to be emphasized that efficient analogue QS still require more than simply scaling. Examples of other important challenges are (1) to investigate carefully the influence of different sources of decoherence on the fidelity of the simulation. Thus, it must be distinguished for the dedicated application, which decoherence the simulation will be robust against, which decoherence can be considered in the simulation and which decoherence is even essential to be included. (2) To identify possibilities to cross-check the validity of the output or to benchmark it against other QS approaches, as soon as the achieved output is not accessible with a classical computer anymore.

In the future it might be beneficial to combine advantages of several systems for hybrid QS. On longer timescales, the experiences gained by developing an analogue QS based on trapped ions might culminate in approaches incorporating solid-state devices that might allow for 'easier' scaling. With the realization of a universal QC, universal QS will also become accessible.

## Acknowledgments

CS and TS acknowledge support by the Max-Planck-Institut für Quantenoptik (MPQ), Max-Planck-Gesellschaft (MPG), Deutsche Forschungsgemeinschaft (DFG) (SCHA 973/1-6), the European Commission (The Physics of Ion Coulomb Crystals: FP7 2007–2013. grant no. 249958) and the DFG Cluster of Excellence 'Munich Centre for Advanced Photonics'. DP acknowledges support from C.A.M. Project QUITEMAD, RyC Contract Y200200074, and MICINN FIS2009-10061. Martin Enderlein, Thomas Huber, and Hector Schmitz have participated in the measurements of the geometric phase gate utilizing the radial modes of motion presented in section 3.4. Günther Leschhorn and Steffen Kahra have observed and taken the picture of the structural defect in a Coulomb crystal of $Mg^+$ ions (see figure 13(*b*)). Benni Reznik and Haggai Landa provided the corresponding simulation (see figure 13(*a*)). Roman Schmied kindly provided several simulation results and illustrations of optimized electrode structures of surface-electrode traps (see section 6). We want to thank Geza Giedke and Alex Retzker for discussions and Martin Enderlein, Thomas Huber, and Dietrich Leibfried for comments on the manuscript. We also thank Ignacio Cirac and Gerhard Rempe for their intellectual and financial support.

## Appendix A. Normal modes and frequencies

This section describes a more general derivation of the normal modes and frequencies compared with the one-dimensional treatment for the linear Paul trap as in [195]. The equations are extended to three dimensions and an arbitrary trap potential, as long as the potential at the equilibrium position $\vec{x}_0^{(i)}$ of each ion can be well approximated by a harmonic potential.

The position of the $i$th ion is expressed in the Cartesian coordinates of the laboratory frame

$$\vec{r}^{(i)} = r_i\vec{e}_X + r_{i+N}\vec{e}_Y + r_{i+2N}\vec{e}_Z. \tag{A.1}$$

The decomposition into the equilibrium position $\vec{x}_0^{(i)}$ and displacements $\vec{x}^{(i)}$ yields

$$\vec{r}^{(i)} = \vec{x}_0^{(i)} + \vec{x}^{(i)} \tag{A.2}$$

$$= (x_{0,i} + x_i)\vec{e}_X + (x_{0,i+N} + x_{i+N})\vec{e}_Y + (x_{0,i+2N} + x_{i+2N})\vec{e}_Z. \tag{A.3}$$

The Lagrangian for $N$ ions takes the form

$$\mathcal{L} = \frac{1}{2}M\left[\sum_{k=1}^{3N}\dot{x}_k^2 - \sum_{k=1}^{3N}\sum_{l=1}^{3N}\underbrace{\frac{1}{M}\left(\frac{\partial^2 V}{\partial r_k \partial r_l}\right)_{x_k=x_l=0}}_{=:a_{kl}} x_k x_l\right], \tag{A.4}$$

where $M$ denotes the mass of an ion, the index of the partial derivatives signifies its evaluation at the equilibrium positions and $V$ denotes the potential consisting of the trap potential $V_0$ and the Coulomb potentials of the ions:

$$V = V_0 + \frac{Q^2}{8\pi\epsilon_0}\sum_{i=1}^{N}\sum_{\substack{j=1\\ j\neq i}}^{N}\frac{1}{|\vec{r}^{(i)} - \vec{r}^{(j)}|}. \tag{A.5}$$

Here, $Q$ denotes the charge and $\epsilon_0$ the electric constant.

For practical purposes the trap potential can be expressed by the harmonic terms corresponding to each ion:

$$V_0 = \frac{1}{2}M\sum_{i=1}^{N}\sum_{j=1}^{3}\omega_j^{(i)2}\left(\vec{r}^{(i)} - \vec{p}^{(i)}\right)^{\mathrm{T}}\vec{d}_j^{(i)} \otimes \vec{d}_j^{(i)}(\vec{r}^{(i)} - \vec{p}^{(i)}). \tag{A.6}$$

Here, $\omega_j^{(i)}$ denotes the $j$th frequency of the harmonically approximated potential of the $i$th ion, $\vec{d}_j^{(i)}$ the unity vector of the principle axis corresponding to $\omega_j^{(i)}$ and $\vec{p}^{(i)}$ the position of

the local minimum of the potential for the $i$th ion. Note that the frequencies, the vectors of the principle axes, and the minima of the potentials become equal for all ions in the special case of a linear Paul trap.

The eigenvalues of the Hessian $A := (a_{kl})$ (see equation (A.4)) yield the squares of the frequencies $\omega_m$ of the normal modes and its eigenvectors $\vec{b}_m$ determine the ions' motion of the $m$th mode:

$$q_m = \vec{b}_m \cdot \vec{x} \qquad \text{with} \quad \vec{x} := (x_1, \ldots, x_{3N}) . \tag{A.7}$$

With the abbreviations $\vec{q} := (q_1, \ldots, q_{3N})$ and $B := (\vec{b}_1, \ldots, \vec{b}_{3N})^{\mathrm{T}}$, where the $\vec{b}_m$ shall be understood as rows of $B$, we can express the relation in a more compact way:

$$\vec{q} = B\vec{x} \quad \Leftrightarrow \quad \vec{x} = B^{\mathrm{T}}\vec{q}. \tag{A.8}$$

Typically, the eigenvalues and eigenvectors of $A$ have to be determined numerically.

## Appendix B. Transformations of Pauli operators

The definitions of the Pauli operators are repeated here to avoid confusions concerning their normalization:

$$\hat{\sigma}_x := \begin{pmatrix} 0 & 1 \\ 1 & 0 \end{pmatrix}, \quad \hat{\sigma}_y := \begin{pmatrix} 0 & -\mathrm{i} \\ \mathrm{i} & 0 \end{pmatrix}, \quad \hat{\sigma}_z := \begin{pmatrix} 1 & 0 \\ 0 & -1 \end{pmatrix}. \tag{B.1}$$

The Pauli operators obey the relations

$$[\hat{\sigma}_i, \hat{\sigma}_j] = 2\mathrm{i}\epsilon_{ijk}\hat{\sigma}_k, \tag{B.2}$$

$$\{\hat{\sigma}_i, \hat{\sigma}_j\} = 2\delta_{ij}, \tag{B.3}$$

$$\hat{\sigma}_i^2 = \hat{\mathbb{1}}. \tag{B.4}$$

A more convenient notation in some contexts is

$$\hat{\sigma}_+ := \hat{\sigma}_x + \mathrm{i}\hat{\sigma}_y = \begin{pmatrix} 0 & 2 \\ 0 & 0 \end{pmatrix}, \tag{B.5}$$

$$\hat{\sigma}_- = \hat{\sigma}_x - \mathrm{i}\hat{\sigma}_y = \begin{pmatrix} 0 & 0 \\ 2 & 0 \end{pmatrix} \tag{B.6}$$

with the normalization as in [50]. They fulfil the following relations:

$$[\hat{\sigma}_\pm, \hat{\sigma}_\mp] = \pm 4\hat{\sigma}_z, \tag{B.7}$$

$$[\hat{\sigma}_z, \hat{\sigma}_\pm] = \pm 2\hat{\sigma}_\pm. \tag{B.8}$$

The transformations of the Pauli operators into the interaction picture involve terms of the form

$$\hat{\sigma}_i' := \mathrm{e}^{\mathrm{i}\kappa\hat{\sigma}_z}\hat{\sigma}_i\mathrm{e}^{-\mathrm{i}\kappa\hat{\sigma}_z}. \tag{B.9}$$

The transformation leaves $\hat{\mathbb{1}}$ and $\hat{\sigma}_z$ unchanged. The non-trivial cases $i = x$ and $i = y$ can be calculated using the Baker–Campbell–Hausdorff formula

$$\begin{aligned} \mathrm{e}^{-\hat{B}}\hat{A}\mathrm{e}^{\hat{B}} &= \sum_n \frac{1}{n!}[\hat{A}, \hat{B}]^{\{n\}} \\ &= \hat{A} + [\hat{A}, \hat{B}] + \frac{1}{2}[[\hat{A}, \hat{B}], \hat{B}] + \cdots \end{aligned} \tag{B.10}$$

with $\hat{B} = -\mathrm{i}\kappa\hat{\sigma}_z$, $\hat{A} = \hat{\sigma}_{x/y} = \frac{\hat{\sigma}_+ \pm \hat{\sigma}_-}{m_\pm}$, $m_+ := 2$ and $m_- := 2\mathrm{i}$.

The commutators are given by

$$[\hat{\sigma}_+ \pm \hat{\sigma}_-, -\mathrm{i}\kappa\hat{\sigma}_z] = \mathrm{i}2\kappa\left(\hat{\sigma}_+ \mp \hat{\sigma}_-\right), \tag{B.11}$$

$$\begin{aligned} [\hat{\sigma}_+ \pm \hat{\sigma}_-, -\mathrm{i}\kappa\hat{\sigma}_z]^{\{2\}} &= \mathrm{i}2\kappa[\left(\hat{\sigma}_+ \mp \hat{\sigma}_-\right), -\mathrm{i}\kappa\hat{\sigma}_z] \\ &= (\mathrm{i}2\kappa)^2\left(\hat{\sigma}_+ \pm \hat{\sigma}_-\right), \end{aligned} \tag{B.12}$$

$$[\hat{\sigma}_+ \pm \hat{\sigma}_-, -\mathrm{i}\kappa\hat{\sigma}_z]^{\{2n-1\}} = (\mathrm{i}2\kappa)^{2n-1}\left(\hat{\sigma}_+ \mp \hat{\sigma}_-\right), \tag{B.13}$$

$$[\hat{\sigma}_+ \pm \hat{\sigma}_-, -\mathrm{i}\kappa\hat{\sigma}_z]^{\{2n\}} = (\mathrm{i}2\kappa)^{2n}\left(\hat{\sigma}_+ \pm \hat{\sigma}_-\right). \tag{B.14}$$

Hence, the Pauli operators in the interaction picture read

$$\begin{aligned} \mathrm{e}^{\mathrm{i}\kappa\hat{\sigma}_z}\hat{\sigma}_{x/y}\mathrm{e}^{-\mathrm{i}\kappa\hat{\sigma}_z} &= \mathrm{e}^{\mathrm{i}\kappa\hat{\sigma}_z}\frac{\hat{\sigma}_+ \pm \hat{\sigma}_-}{m_\pm}\mathrm{e}^{-\mathrm{i}\kappa\hat{\sigma}_z} \\ &= \frac{1}{m_\pm}\sum_n \frac{(\mathrm{i}2\kappa)^{2n+1}}{(2n+1)!}\left(\hat{\sigma}_+ \mp \hat{\sigma}_-\right) \\ &\quad + \frac{1}{m_\pm}\sum_n \frac{(\mathrm{i}2\kappa)^{2n}}{(2n)!}\left(\hat{\sigma}_+ \pm \hat{\sigma}_-\right) \\ &= \frac{1}{m_\pm}\sum_n \frac{(\mathrm{i}2\kappa)^n}{n!}\hat{\sigma}_+ \\ &\quad \pm \frac{1}{m_\pm}\sum_n \frac{(-\mathrm{i}2\kappa)^n}{n!}\hat{\sigma}_- \\ &= \frac{1}{m_\pm}\left(\mathrm{e}^{\mathrm{i}2\kappa}\hat{\sigma}_+ \pm \mathrm{e}^{-\mathrm{i}2\kappa}\hat{\sigma}_-\right). \end{aligned} \tag{B.15}$$

The operators $\hat{\sigma}_+$ and $\hat{\sigma}_-$ transform:

$$\mathrm{e}^{\mathrm{i}\kappa\hat{\sigma}_z}\hat{\sigma}_+\mathrm{e}^{-\mathrm{i}\kappa\hat{\sigma}_z} = \mathrm{e}^{\mathrm{i}2\kappa}\hat{\sigma}_+, \tag{B.16}$$

$$\mathrm{e}^{\mathrm{i}\kappa\hat{\sigma}_z}\hat{\sigma}_-\mathrm{e}^{-\mathrm{i}\kappa\hat{\sigma}_z} = \mathrm{e}^{-\mathrm{i}2\kappa}\hat{\sigma}_-. \tag{B.17}$$

## Appendix C. Transformations of motional operators

The creation operator $\hat{a}$ and the annihilation operator $\hat{a}^\dagger$ fulfil the relations

$$\hat{a}|n\rangle = \sqrt{n}|n-1\rangle, \tag{C.1}$$

$$\hat{a}^\dagger|n\rangle = \sqrt{n+1}|n+1\rangle, \tag{C.2}$$

$$[\hat{a}, \hat{a}^\dagger] = \hat{\mathbb{1}}. \tag{C.3}$$

The transformation of the Hamiltonians into the interaction picture requires the knowledge of the transformation of $\mathrm{e}^{\mathrm{i}\xi(\hat{a}+\hat{a}^\dagger)}$.

It can be performed using the special case of the Baker–Campbell–Hausdorff formula from appendix B again. The commutators appearing in the formula are

$$[\hat{a} + \hat{a}^\dagger, -\mathrm{i}\lambda\hat{a}^\dagger\hat{a}] = -\mathrm{i}\lambda\left(\hat{a} - \hat{a}^\dagger\right), \tag{C.4}$$

$$\begin{aligned} [\hat{a} + \hat{a}^\dagger, -\mathrm{i}\lambda\hat{a}^\dagger\hat{a}]^{\{2\}} &= -\mathrm{i}\lambda[\hat{a} - \hat{a}^\dagger, -\mathrm{i}\lambda\hat{a}^\dagger\hat{a}] \\ &= (-\mathrm{i}\lambda)^2\left(\hat{a} + \hat{a}^\dagger\right), \end{aligned} \tag{C.5}$$

$$[\hat{a} + \hat{a}^\dagger, -\mathrm{i}\lambda\hat{a}^\dagger\hat{a}]^{\{n\}} = (-\mathrm{i}\lambda)^n\left(\hat{a} + (-1)^n\hat{a}^\dagger\right). \tag{C.6}$$

(C.7)

Hence, the full transformation reads

$$\begin{aligned} \mathrm{e}^{\mathrm{i}\lambda\hat{a}^\dagger\hat{a}}\left(\hat{a} + \hat{a}^\dagger\right)\mathrm{e}^{-\mathrm{i}\lambda\hat{a}^\dagger\hat{a}} &= \sum_n \frac{(-\mathrm{i}\lambda)^n}{n!}\left(\hat{a} + (-1)^n\hat{a}^\dagger\right) \\ &= \hat{a}\mathrm{e}^{-\mathrm{i}\lambda} + \hat{a}^\dagger\mathrm{e}^{\mathrm{i}\lambda}. \end{aligned} \tag{C.8}$$

From this relation we can immediately derive

$$\begin{aligned} \mathrm{e}^{\mathrm{i}\lambda\hat{a}^\dagger\hat{a}}\left(\hat{a}+\hat{a}^\dagger\right)^n\mathrm{e}^{-\mathrm{i}\lambda\hat{a}^\dagger\hat{a}} &= \left[\mathrm{e}^{\mathrm{i}\lambda\hat{a}^\dagger\hat{a}}\left(\hat{a}+\hat{a}^\dagger\right)\mathrm{e}^{-\mathrm{i}\lambda\hat{a}^\dagger\hat{a}}\right]^n \\ &= \left[\hat{a}\mathrm{e}^{-\mathrm{i}\lambda}+\hat{a}^\dagger\mathrm{e}^{\mathrm{i}\lambda}\right]^n \end{aligned} \tag{C.9}$$

by making use of the unitarity of $\mathrm{e}^{\mathrm{i}\lambda\hat{a}^\dagger\hat{a}}$. We obtain for the transformation

$$\begin{aligned} \mathrm{e}^{\mathrm{i}\lambda\hat{a}^\dagger\hat{a}}\mathrm{e}^{\mathrm{i}\xi\left(\hat{a}+\hat{a}^\dagger\right)}\mathrm{e}^{-\mathrm{i}\lambda\hat{a}^\dagger\hat{a}} &= \mathrm{e}^{\mathrm{i}\lambda\hat{a}^\dagger\hat{a}}\sum_n\frac{(\mathrm{i}\xi)^n}{n!}\left(\hat{a}+\hat{a}^\dagger\right)^n\mathrm{e}^{-\mathrm{i}\lambda\hat{a}^\dagger\hat{a}} \\ &= \sum_n\frac{(\mathrm{i}\xi)^n}{n!}\left[\hat{a}\mathrm{e}^{-\mathrm{i}\lambda}+\hat{a}^\dagger\mathrm{e}^{\mathrm{i}\lambda}\right]^n \\ &= \exp\left(\mathrm{i}\xi\left[\hat{a}\mathrm{e}^{-\mathrm{i}\lambda}+\hat{a}^\dagger\mathrm{e}^{\mathrm{i}\lambda}\right]\right). \end{aligned} \tag{C.10}$$

## Appendix D. Matrix elements of displacement operator

The following derivation is based on [95]. A difference is that we do not restrict the displacement to purely imaginary $\lambda$ in the following. A similar derivation can be found in appendix B of [111].

The simple Baker–Campbell–Hausdorff formula

$$\mathrm{e}^{A+B} = \mathrm{e}^A\mathrm{e}^B\mathrm{e}^{-[A,B]/2} \tag{D.1}$$

holds for $[A,[A,B]] = [B,[B,A]] = 0$.

We obtain for the annihilation operator

$$\hat{a}^m|n\rangle = \begin{cases}\sqrt{\frac{n!}{(n-m)!}}|n-m\rangle & \text{for } m\leqslant n,\\ 0 & \text{else.}\end{cases} \tag{D.2}$$

Using the above form of the Baker–Campbell–Hausdorff formula, we can rewrite the displacement operator as

$$\hat{D}(\lambda) = \mathrm{e}^{\lambda\hat{a}^\dagger-\lambda^*\hat{a}} = \mathrm{e}^{-|\lambda|^2/2}\mathrm{e}^{\lambda\hat{a}^\dagger}\mathrm{e}^{-\lambda^*\hat{a}}. \tag{D.3}$$

With

$$\begin{aligned} \mathrm{e}^{-\lambda^*\hat{a}}|n\rangle &= \sum_m\frac{(-\lambda^*)^m}{m!}\hat{a}^m|n\rangle \\ &= \sum_m\frac{(-\lambda^*)^m}{m!}\sqrt{\frac{n!}{(n-m)!}}|n-m\rangle, \end{aligned} \tag{D.4}$$

this yields for $n'\geqslant n$

$$\begin{aligned} \langle n'|\hat{D}(\lambda)|n\rangle &= \mathrm{e}^{-|\lambda|^2/2}\langle n'|\mathrm{e}^{\lambda\hat{a}^\dagger}\mathrm{e}^{-\lambda^*\hat{a}}|n\rangle \\ &= \mathrm{e}^{-|\lambda|^2/2}\sum_{m'}\sum_m\langle n'-m'|n-m\rangle\frac{\lambda^{m'}}{m'!} \\ &\quad\times\frac{(-\lambda^*)^m}{m!}\sqrt{\frac{n'!}{(n'-m')!}}\sqrt{\frac{n!}{(n-m)!}} \\ &= \mathrm{e}^{-|\lambda|^2/2}\lambda^{n'-n}\sum_{m=0}^{n}\frac{(-1)^m|\lambda|^{2m}}{m!(n'-n+m)!} \\ &\quad\times\frac{\sqrt{n'!n!}}{(n-m)!} \\ &= \mathrm{e}^{-|\lambda|^2/2}\lambda^{n'-n}\sqrt{\frac{n!}{n'!}}L_n^{(n'-n)}\left(|\lambda|^2\right), \end{aligned} \tag{D.5}$$

where $L_n^{(\alpha)}(x)$ denotes the generalized Laguerre polynomials [196]. Analogously, we obtain for $n'\leqslant n$

$$\langle n'|\hat{D}(\lambda)|n\rangle = \mathrm{e}^{-|\lambda|^2/2}\left(-\lambda^*\right)^{n-n'}\sqrt{\frac{n'!}{n!}}L_{n'}^{(n-n')}\left(|\lambda|^2\right). \tag{D.6}$$

For values $\lambda = \mathrm{i}\eta\mathrm{e}^{\mathrm{i}\omega t}$ with $\eta\in\mathbb{R}$, we can write equations (D.5) and (D.6) as

$$\begin{aligned} \langle n'|\hat{D}\left(\mathrm{i}\eta\mathrm{e}^{\mathrm{i}\omega t}\right)|n\rangle &= \mathrm{e}^{-\eta^2/2}(\mathrm{i}\eta)^{|n'-n|}\,\mathrm{e}^{\mathrm{i}\omega(n'-n)t} \\ &\quad\times\sqrt{\frac{n_<!}{n_>!}}L_{n_<}^{|n'-n|}\left(\eta^2\right), \end{aligned} \tag{D.7}$$

where $n_< := \min(n',n)$ and $n_> := \max(n',n)$.

## Appendix E. System of differential equations of the Rabi problem

The Rabi problem consists of the following system of differential equations:

$$\left|\begin{aligned}\dot{c}_2 &= \lambda\mathrm{e}^{-\mathrm{i}\omega t}c_1\\ \dot{c}_1 &= -\lambda^*\mathrm{e}^{\mathrm{i}\omega t}c_2\end{aligned}\right|. \tag{E.1}$$

It can be solved by differentiating with respect to $t$

$$\left|\begin{aligned}\ddot{c}_2 &= \lambda\mathrm{e}^{-\mathrm{i}\omega t}\dot{c}_1 - \mathrm{i}\omega\lambda\mathrm{e}^{-\mathrm{i}\omega t}c_1\\ \ddot{c}_1 &= -\lambda^*\mathrm{e}^{\mathrm{i}\omega t}\dot{c}_2 - \mathrm{i}\omega\lambda^*\mathrm{e}^{\mathrm{i}\omega t}c_2\end{aligned}\right| \tag{E.2}$$

and inserting equation (E.1):

$$\ddot{c}_2 = -\mathrm{i}\omega\dot{c}_2 - |\lambda|^2c_2, \tag{E.3}$$

$$\ddot{c}_1 = \mathrm{i}\omega\dot{c}_1 - |\lambda|^2c_1. \tag{E.4}$$

Using the ansatz $c_i = a_i\mathrm{e}^{\mathrm{i}\kappa_i t}$ we obtain the characteristic equations

$$-\kappa_2^2 = \omega\kappa_2 - |\lambda|^2, \tag{E.5}$$

$$-\kappa_1^2 = -\omega\kappa_1 - |\lambda|^2, \tag{E.6}$$

which have the solutions

$$\kappa_{2,\pm} = -\frac{\omega}{2}\pm\sqrt{\frac{\omega^2}{4}+|\lambda|^2} := -\frac{\omega}{2}\pm\kappa', \tag{E.7}$$

$$\kappa_{1,\pm} = \frac{\omega}{2}\pm\sqrt{\frac{\omega^2}{4}+|\lambda|^2} := \frac{\omega}{2}\pm\kappa' = -\kappa_{2,\mp}. \tag{E.8}$$

Here, we introduced the abbreviation $\kappa' := \sqrt{(\omega^2/4)+|\lambda|^2}$. The solutions of equations (E.3) and (E.4) read

$$\begin{aligned} c_2 &= a_{2,+}\mathrm{e}^{\mathrm{i}\kappa_{2,+}t} + a_{2,-}\mathrm{e}^{\mathrm{i}\kappa_{2,-}t}\\ &= \left(a_{2,+}\mathrm{e}^{\mathrm{i}\kappa' t} + a_{2,-}\mathrm{e}^{-\mathrm{i}\kappa' t}\right)\mathrm{e}^{-\mathrm{i}\omega t/2}, \end{aligned} \tag{E.9}$$

$$\begin{aligned} c_1 &= a_{1,+}\mathrm{e}^{\mathrm{i}\kappa_{1,+}t} + a_{1,-}\mathrm{e}^{\mathrm{i}\kappa_{1,-}t}\\ &= \left(a_{1,+}\mathrm{e}^{\mathrm{i}\kappa' t} + a_{1,-}\mathrm{e}^{-\mathrm{i}\kappa' t}\right)\mathrm{e}^{\mathrm{i}\omega t/2}. \end{aligned} \tag{E.10}$$

Inserting them into the original system of differential equations equation (E.1), we obtain the following relations for the constants $a_{i,\pm}$:

$$\mathrm{i}\kappa_{2,\pm}a_{2,\pm} = \lambda a_{1,\pm}, \tag{E.11}$$

$$\mathrm{i}\kappa_{1,\pm}a_{1,\pm} = -\lambda^*a_{2,\pm}. \tag{E.12}$$

We replace $a_{1,\pm}$ by $a_{2,\pm}$ using equation (E.11) and obtain

$$c_2 = \left(a_{2,+}\mathrm{e}^{\mathrm{i}\kappa' t} + a_{2,-}\mathrm{e}^{-\mathrm{i}\kappa' t}\right)\mathrm{e}^{-\mathrm{i}\omega t/2}, \tag{E.13}$$

$$c_1 = \left(\mu_+ a_{2,+}\mathrm{e}^{\mathrm{i}\kappa' t} + \mu_- a_{2,-}\mathrm{e}^{-\mathrm{i}\kappa' t}\right)\mathrm{e}^{\mathrm{i}\omega t/2}, \tag{E.14}$$

where we introduced the (temporary) abbreviation $\mu_\pm := \mathrm{i}\kappa_{2,\pm}/\lambda$.

The constants $a_{2,\pm}$ can now be expressed in terms of the initial values $c_{20} := c_2(t=0)$ and $c_{10} := c_1(t=0)$. Setting $t = 0$ in equations (E.13) and (E.14), we obtain a system of linear equations with the solutions

$$a_{2,+} = \frac{\mu_- c_{20} - c_{10}}{\mu_- - \mu_+}, \tag{E.15}$$

$$a_{2,-} = -\frac{\mu_+ c_{20} - c_{10}}{\mu_- - \mu_+}. \tag{E.16}$$

Hence,

$$c_2 = \frac{(\mu_- c_{20} - c_{10})\mathrm{e}^{\mathrm{i}\kappa' t} - (\mu_+ c_{20} - c_{10})\mathrm{e}^{-\mathrm{i}\kappa' t}}{\mu_- - \mu_+}\mathrm{e}^{-\mathrm{i}\omega t/2}, \tag{E.17}$$

$$c_1 = \frac{\mu_+(\mu_- c_{20} - c_{10})\mathrm{e}^{\mathrm{i}\kappa' t} - \mu_-(\mu_+ c_{20} - c_{10})\mathrm{e}^{-\mathrm{i}\kappa' t}}{\mu_- - \mu_+}\mathrm{e}^{\mathrm{i}\omega t/2}, \tag{E.18}$$

and by expressing $\mu_\pm$ in terms of $\omega$, $\kappa'$, and $\lambda$ we obtain

$$c_2(t) = \left(\cos(\kappa' t) + \frac{\omega}{2}\frac{\mathrm{i}}{\kappa'}\sin(\kappa' t)\right)\mathrm{e}^{-\mathrm{i}\omega t/2}c_2(0) + \frac{\lambda}{\kappa'}\sin(\kappa' t)\mathrm{e}^{-\mathrm{i}\omega t/2}c_1(0), \tag{E.19}$$

$$c_1(t) = -\frac{\lambda^*}{\kappa'}\sin(\kappa' t)\mathrm{e}^{\mathrm{i}\omega t/2}c_2(0) + \left(\cos(\kappa' t) - \frac{\omega}{2}\frac{\mathrm{i}}{\kappa'}\sin(\kappa' t)\right)\mathrm{e}^{\mathrm{i}\omega t/2}c_1(0). \tag{E.20}$$

## Appendix F. Time evolution operator

The calculation of the time evolution operator involves terms of the form

$$\hat{\mathcal{H}}_m^{(i)}(t) = \mathrm{i}\xi_m^{(i)}\mathrm{e}^{\mathrm{i}(-\delta_m t + \varphi^{(i)})}\hat{a}_m^\dagger + \mathrm{h.c.}, \tag{F.1}$$

where $\xi_m^{(i)} \in \mathbb{R}$ and the total Hamiltonian reads $\hat{\mathcal{H}}(t) =: \sum_{i=1}^{N}\sum_{m=1}^{3N}\hat{\mathcal{H}}_m^{(i)}(t)$. (More generally, the constants $\xi_m^{(i)}$ represent Hermitian operators $\hat{\xi}_m^{(i)}$ with $[\hat{\xi}_m^{(i)}, \hat{\xi}_n^{(j)}] = 0 \forall i, j, m, n$.)

The commutator of two of these terms will trivially vanish for all $i$, $j$ and all times $t'$, $t''$, if both terms belong to different modes $m \neq n$:

$$[\hat{\mathcal{H}}_m^{(i)}(t'), \hat{\mathcal{H}}_n^{(j)}(t'')] = 0 \qquad \text{for} \quad m \neq n. \tag{F.2}$$

However, for $m = n$, the commutators do not vanish. Using the relation

$$\begin{aligned}[\mathrm{e}^{\mathrm{i}\lambda}\hat{a}^\dagger - \mathrm{e}^{-\mathrm{i}\lambda}\hat{a}, \mathrm{e}^{\mathrm{i}\lambda'}\hat{a}^\dagger - \mathrm{e}^{-\mathrm{i}\lambda'}\hat{a}] &= \mathrm{e}^{\mathrm{i}(\lambda-\lambda')}(\hat{a}\hat{a}^\dagger - \hat{a}^\dagger\hat{a}) - \mathrm{e}^{-\mathrm{i}(\lambda-\lambda')}(\hat{a}\hat{a}^\dagger - \hat{a}^\dagger\hat{a}) \\ &= 2\mathrm{i}\sin(\lambda - \lambda')\hat{\mathbb{1}}\end{aligned} \tag{F.3}$$

yields

$$\begin{aligned}&[\hat{\mathcal{H}}_m^{(i)}(t'), \hat{\mathcal{H}}_m^{(j)}(t'')] \\ &\quad = 2\mathrm{i}\xi_m^{(i)}\xi_m^{(j)}\sin(\delta_m(t' - t'') - (\varphi^{(i)} - \varphi^{(j)})).\end{aligned} \tag{F.4}$$

The time evolution operator can be calculated using a Magnus expansion [197, 198]. As commutators with higher 'nesting level' trivially vanish, the expansion simplifies to

$$\begin{aligned}\hat{U}(t, t_0) = \exp\Bigg(&-\frac{\mathrm{i}}{\hbar}\int_{t_0}^{t}\mathrm{d}t'\hat{\mathcal{H}}(t') \\ &- \frac{1}{2\hbar^2}\int_{t_0}^{t}\mathrm{d}t'\int_{t_0}^{t'}\mathrm{d}t''[\hat{\mathcal{H}}(t'), \hat{\mathcal{H}}(t'')]\Bigg).\end{aligned} \tag{F.5}$$

The single integrals yield

$$\int_{t_0}^{t}\mathrm{d}t'\hat{\mathcal{H}}_m^{(i)}(t') = -\frac{\xi_m^{(i)}}{\delta_m}\left(\mathrm{e}^{-\mathrm{i}\delta_m(t-t_0)} - 1\right)\mathrm{e}^{-\mathrm{i}\delta_m t_0}\mathrm{e}^{\mathrm{i}\varphi^{(i)}}\hat{a}_m^\dagger + \mathrm{h.c.} \tag{F.6}$$

and the double integrals of the commutators yield

$$\begin{aligned}\int_{t_0}^{t}\mathrm{d}t'\int_{t_0}^{t'}\mathrm{d}t''[\hat{\mathcal{H}}_m^{(i)}(t'), \hat{\mathcal{H}}_m^{(j)}(t'')] &= 2\mathrm{i}\xi_m^{(i)}\xi_m^{(j)} \\ &\quad\times\int_{t_0}^{t}\mathrm{d}t'\int_{t_0}^{t'}\mathrm{d}t''\sin\left(\delta_m(t' - t'') - \left(\varphi^{(i)} - \varphi^{(j)}\right)\right) \\ &= \frac{2\mathrm{i}\xi_m^{(i)}\xi_m^{(j)}}{\delta_m}\int_{t_0}^{t}\mathrm{d}t'\left[\cos\left(\varphi^{(i)} - \varphi^{(j)}\right)\right. \\ &\quad\left.- \cos\left(\delta_m(t' - t_0) - \left(\varphi^{(i)} - \varphi^{(j)}\right)\right)\right] \\ &= \frac{2\mathrm{i}\xi_m^{(i)}\xi_m^{(j)}}{\delta_m^2}\left[\delta_m(t - t_0)\cos\left(\varphi^{(i)} - \varphi^{(j)}\right)\right. \\ &\quad\left.- \sin\left(\delta_m(t - t_0) - (\varphi^{(i)} - \varphi^{(j)})\right) - \sin(\varphi^{(i)} - \varphi^{(j)})\right].\end{aligned} \tag{F.7}$$

Note that in the time evolution operator corresponding to $\hat{\mathcal{H}}(t)$ the terms $\sin(\varphi^{(i)} - \varphi^{(j)}) = -\sin(\varphi^{(j)} - \varphi^{(i)})$ cancel each other.

## Appendix G. Canonical transformation

The unitary operator of the canonical transformation has the form

$$\hat{U}_\mathrm{c} := \mathrm{e}^{-(\lambda\hat{a}^\dagger - \lambda^*\hat{a})} \qquad \text{with} \quad \lambda := \frac{\xi}{\kappa} \tag{G.1}$$

and is applied to

$$\hat{\mathcal{H}} := \underbrace{\left(\xi\hat{a}^\dagger + \xi^*\hat{a}\right)}_{:=\hat{\mathcal{H}}_1} + \underbrace{\left(-\kappa\hat{a}^\dagger\hat{a}\right)}_{:=\hat{\mathcal{H}}_2} \quad \rightarrow \quad \hat{\mathcal{H}}' := \hat{U}_\mathrm{c}\hat{\mathcal{H}}\hat{U}_\mathrm{c}^\dagger. \tag{G.2}$$

Here, the constants $\xi \in \mathbb{C}$ and $\kappa \in \mathbb{R}$.

We use the Baker–Campbell–Hausdorff formula from appendix B to do the transformation. The commutators for $\hat{\mathcal{H}}_1$ yield

$$\begin{aligned}[\xi\hat{a}^\dagger + \xi^*\hat{a}, \lambda\hat{a}^\dagger - \lambda^*\hat{a}] &= \xi\lambda^*\left(-\hat{a}^\dagger\hat{a} + \hat{a}\hat{a}^\dagger\right) \\ &\quad - \xi^*\lambda\left(\hat{a}^\dagger\hat{a} - \hat{a}\hat{a}^\dagger\right) \\ &= \left(\xi\lambda^* + \xi^*\lambda\right)\hat{\mathbb{1}} \\ &= \frac{2\xi\xi^*}{\kappa}\hat{\mathbb{1}}.\end{aligned} \tag{G.3}$$

Commutators with higher 'nesting levels' trivially vanish. Hence, the complete transformation of $\hat{\mathcal{H}}_1$ reads

$$\hat{\mathcal{H}}_1' := \hat{U}_c \hat{\mathcal{H}}_1 \hat{U}_c^\dagger = \left(\xi \hat{a}^\dagger + \xi^* \hat{a}\right) + \frac{2\xi\xi^*}{\kappa}\hat{\mathbb{1}}. \tag{G.4}$$

The commutators for $\hat{\mathcal{H}}_2$ read

$$\begin{aligned}[-\kappa \hat{a}^\dagger \hat{a}, \lambda \hat{a}^\dagger - \lambda^* \hat{a}] &= -\kappa \left(\hat{a}^\dagger [\hat{a}, \lambda \hat{a}^\dagger - \lambda^* \hat{a}] \right. \\ &\quad \left. + [\hat{a}^\dagger, \lambda \hat{a}^\dagger - \lambda^* \hat{a}]\hat{a}\right) \\ &= -\kappa \left(\lambda \hat{a}^\dagger + \lambda^* \hat{a}\right) \\ &= -\left(\xi \hat{a}^\dagger + \xi^* \hat{a}\right)\end{aligned} \tag{G.5}$$

and

$$\begin{aligned}[-\kappa \hat{a}^\dagger \hat{a}, \lambda \hat{a}^\dagger - \lambda^* \hat{a}]^{\{2\}} &= [-\left(\xi \hat{a}^\dagger + \xi^* \hat{a}\right), \lambda \hat{a}^\dagger - \lambda^* \hat{a}] \\ &= -\frac{2\xi\xi^*}{\kappa}\hat{\mathbb{1}},\end{aligned} \tag{G.6}$$

where we used equation (G.3). Higher order terms in the expansion trivially vanish again. The complete transformation of $\hat{\mathcal{H}}_2$ reads

$$\hat{\mathcal{H}}_2' := \hat{U}_c \hat{\mathcal{H}}_2 \hat{U}_c^\dagger = -\kappa \hat{a}^\dagger \hat{a} - \left(\xi \hat{a}^\dagger + \xi^* \hat{a}\right) - \frac{\xi\xi^*}{\kappa}\hat{\mathbb{1}}. \tag{G.7}$$

Hence, the transformation of the full Hamiltonian reads

$$\hat{\mathcal{H}}' = \hat{\mathcal{H}}_1' + \hat{\mathcal{H}}_2' = \frac{\xi\xi^*}{\kappa}\hat{\mathbb{1}} - \kappa \hat{a}^\dagger \hat{a}. \tag{G.8}$$

We want to stress that the canonical transformation is exact in this case.

## References


[1] Lloyd S 1996 Universal quantum simulators *Science* **273** 1073–8

[2] Schinarakis K 2011 Weltrekord: Jülicher Supercomputer simuliert Quantencomputer *Press release* http://www2.fz-juelich.de/portal/index.php?cmd=show&mid=760&index=163

[3] De Raedt K, Michielsen K, De Raedt H, Trieu B, Arnold G, Richter M, Lippert Th, Watanabe H and Ito N 2007 Massively parallel quantum computer simulator *Comput. Phys. Commun.* **176** 121–36

[4] Moore G E 1965 Cramming more components onto integrated circuits *Electronics* **38** 114–7

[5] Feynman R 1982 Simulating physics with computers *Int. J. Theor. Phys.* **21** 467–88

[6] diVincenzo D P 1995 Two-bit gates are universal for quantum computation *Phys. Rev.* A **51** 1015–22

[7] diVincenzo D P 2000 The physical implementation of quantum computation *Fortschr. Phys.* **48** 771–83

[8] Ladd T D, Jelezko F, Laflamme R, Nakamura Y, Monroe C and O'Brien J L 2010 Quantum computers *Nature* **464** 45–53

[9] Nielsen M A and Chuang I L 2000 *Quantum Computation and Quantum Information* (*Cambridge Series on Information and the Natural Sciences*) (Cambridge: Cambridge University Press)

[10] Knill E 2005 Quantum computing with realistically noisy devices *Nature* **434** 39–44

[11] Home J P, Hanneke D, Jost J D, Amini J M, Leibfried D and Wineland D J 2009 Complete methods set for scalable ion trap quantum information processing *Science* **325** 1227–30

[12] Buluta I and Nori F 2009 Quantum simulators *Science* **326** 108–111

[13] Hauke P, Cucchietti F M, Tagliacozzo L, Lewenstein M and Deutsch I 2011 On the robustness of quantum simulations arXiv:1109.6457v1

[14] Engel G S, Calhoun T R, Read E L, Ahn T-K, Mančal T, Cheng Y-C, Blankenship R E and Fleming G R 2007 Evidence for wavelike energy transfer through quantum coherence in photosynthetic systems *Nature* **446** 782–6

[15] Mohseni M, Rebentrost P, Lloyd S and Aspuru-Guzik A 2008 Environment-assisted quantum walks in photosynthetic energy transfer *J. Chem. Phys.* **129** 174106

[16] Leibfried D 2010 Could a boom in technologies trap Feynman's simulator? *Nature* **463** 608

[17] Jaksch D and Zoller P 2005 The cold atom Hubbard toolbox *Ann. Phys.* **315** 52–79

[18] Lewenstein M, Sanpera A, Ahufinger V, Damski B, Sen(De) A and Sen U 2007 Ultracold atomic gases in optical lattices: mimicking condensed matter physics and beyond *Adv. Phys.* **56** 243–379

[19] Bloch I, Dalibard J and Zwerger W 2008 Many-body physics with ultracold gases *Rev. Mod. Phys.* **80** 885–964

[20] Simon J, Bakr W S, Ma R, Tai M E, Preiss P M and Greiner M 2011 Quantum simulation of antiferromagnetic spin chains in an optical lattice *Nature* **472** 307–12

[21] Porras D and Cirac J I 2004 Effective quantum spin systems with trapped ions *Phys. Rev. Lett.* **92** 207901

[22] Porras D and Cirac J I 2004 Bose–Einstein condensation and strong-correlation behavior of phonons in ion traps *Phys. Rev. Lett.* **93** 263602

[23] Wunderlich C 2002 Conditional spin resonance with trapped ions *Laser Physics at the Limits* ed Figger H *et al* (Berlin: Springer) pp 261–73

[24] Cirac J I and Zoller P 1995 Quantum computations with cold trapped ions *Phys. Rev. Lett.* **74** 4091–4

[25] Chou C W, Hume D B, Koelemeij J C J, Wineland D J and Rosenband T 2010 Frequency comparison of two high-accuracy $Al^+$ optical clocks *Phys. Rev. Lett.* **104** 070802

[26] Schützhold R, Uhlmann M, Petersen L, Schmitz H, Friedenauer A and Schätz T 2007 Analogue of cosmological particle creation in an ion trap *Phys. Rev. Lett.* **99** 201301

[27] Horstmann B, Reznik B, Fagnocchi S and Cirac J I 2010 Hawking radiation from an acoustic black hole on an ion ring *Phys. Rev. Lett.* **104** 250403

[28] Horstmann B, Schützhold R, Reznik B, Fagnocchi S and Cirac J I 2011 Hawking radiation on an ion ring in the quantum regime *New J. Phys.* **13** 045008

[29] Lamata L, León J, Schätz T and Solano E 2007 Dirac equation and quantum relativistic effects in a single trapped ion *Phys. Rev. Lett.* **98** 253005

[30] Gerritsma R, Kirchmair G, Zahringer F, Solano E, Blatt R and Roos C F 2010 Quantum simulation of the Dirac equation *Nature* **463** 68–71

[31] Casanova J, García-Ripoll J J, Gerritsma R, Roos C F and Solano E 2010 Klein tunneling and Dirac potentials in trapped ions *Phys. Rev.* A **82** 020101

[32] Gerritsma R, Lanyon B P, Kirchmair G, Zähringer F, Hempel C, Casanova J, García-Ripoll J J, Solano E, Blatt R and Roos C F 2011 Quantum simulation of the Klein paradox with trapped ions *Phys. Rev. Lett.* **106** 060503

[33] Casanova J, Sabín C, León J, Egusquiza I L, Gerritsma R, Roos C F, García-Ripoll J J and Solano E 2011 Quantum simulation of the Majorana equation and unphysical operations arXiv:1102.1651v2

[34] Lamata L, Casanova J, Gerritsma R, Roos C F, García-Ripoll J-J and Solano E 2011 Relativistic quantum mechanics with trapped ions *New J. Phys.* **13** 095003

[35] Casanova J, Lamata L, Egusquiza I L, Gerritsma R, Roos C F, García-Ripoll J J and Solano E 2011 Quantum simulation of quantum field theories in trapped ions arXiv:1107.5233v2

[36] Leibfried D *et al* 2002 Trapped-ion quantum simulator: experimental application to nonlinear interferometers *Phys. Rev. Lett.* **89** 247901

[37] Travaglione B C and Milburn G J 2002 Implementing the quantum random walk *Phys. Rev.* A **65** 032310

[38] Schmitz H, Matjeschk R, Schneider Ch, Glueckert J, Enderlein M, Huber T and Schaetz T 2009 Quantum walk of a trapped ion in phase space *Phys. Rev. Lett.* **103** 090504

[39] Zähringer F, Kirchmair G, Gerritsma R, Solano E, Blatt R and Roos C F 2010 Realization of a quantum walk with one and two trapped ions *Phys. Rev. Lett.* **104** 100503

[40] Matjeschk R, Schneider C, Enderlein M, Huber T, Schmitz H, Glueckert J and Schaetz T 2011 Experimental simulation and limitations of quantum walks with trapped ions arXiv:1108.0913v1

[41] Cai J, Guerreschi G G and Briegel H J 2010 Quantum control and entanglement in a chemical compass *Phys. Rev. Lett.* **104** 220502

[42] Cai J, Popescu S and Briegel H J 2010 Dynamic entanglement in oscillating molecules and potential biological implications *Phys. Rev.* E **82** 021921

[43] Plenio M B and Huelga S F 2008 Dephasing-assisted transport: quantum networks and biomolecules *New J. Phys.* **10** 113019

[44] Porras D, Marquardt F, von Delft J and Cirac J I 2008 Mesoscopic spin-boson models of trapped ions *Phys. Rev.* A **78** 010101

[45] Sachdev S 1999 *Quantum Phase Transitions* (Cambridge: Cambridge University Press)

[46] Johanning M, Varón A and Wunderlich C 2009 Quantum simulations with cold trapped ions *J. Phys. B: At. Mol. Opt. Phys.* **42** 154009

[47] Friedenauer A, Schmitz H, Glueckert J T, Porras D and Schaetz T 2008 Simulating a quantum magnet with trapped ions *Nature Phys.* **4** 757–61

[48] Kim K, Chang M-S, Korenblit S, Islam R, Edwards E E, Freericks J K, Lin G-D, Duan L-M and Monroe C 2010 Quantum simulation of frustrated Ising spins with trapped ions *Nature* **465** 590–3

[49] Islam R, Edwards E E, Kim K, Korenblit S, Noh C, Carmichael H, Lin G-D, Duan L-M, Wang C-C J, Freericks J K and Monroe C 2011 Onset of a quantum phase transition with a trapped ion quantum simulator *Nature Commun.* **2** 377

[50] Wineland D J, Monroe C, Itano W M, Leibfried D, King B E and Meekhof D M 1998 Experimental issues in coherent quantum-state manipulation of trapped atomic ions *J. Res. Natl Inst. Stand. Technol.* **103** 259–328

[51] Leibfried D, Blatt R, Monroe C and Wineland D 2003 Quantum dynamics of single trapped ions *Rev. Mod. Phys.* **75** 281–324

[52] Biercuk M J, Uys H, VanDevender A P, Shiga N, Itano W M and Bollinger J J 2009 High-fidelity quantum control using ion crystals in a Penning trap *Quantum Inform. Comput.* **9** 0920–0949

[53] Bollinger J and Britton J 2011 private communication

[54] Paul W 1990 Electromagnetic traps for charged and neutral particles *Rev. Mod. Phys.* **62** 531–40

[55] Dehmelt H 1990 Experiments with an isolated subatomic particle at rest *Rev. Mod. Phys.* **62** 525–30

[56] Phillips W D 1998 Nobel lecture: laser cooling and trapping of neutral atoms *Rev. Mod. Phys.* **70** 721–41

[57] Paul W and Steinwedel H 1953 Ein neues massenspektrometer ohne magnetfeld *Z. Naturf.* a **8** 448–50

[58] Paul W, Osberghaus O and Fischer E 1958 Ein Ionenkäfig *Forschungsber. Wirtsch. Verkehrsministeriums Nordrhein-Westfalen* **415** 1–42

[59] Ashkin A 1970 Acceleration and trapping of particles by radiation pressure *Phys. Rev. Lett.* **24** 156–9

[60] Cormick C, Schaetz T and Morigi G 2011 Trapping ions with lasers *New J. Phys.* **13** 043019

[61] Wineland D J and Dehmelt H 1975 Proposed $10^{14}\delta\nu < \nu$ laser fluorescence spectroscopy on $T1^+$ mono-ion oscillator III *Bull. Am. Phys. Soc.* **20** 637

[62] Hänsch T W and Schawlow A L 1975 Cooling of gases by laser radiation *Opt. Commun.* **13** 68–9

[63] Wineland D J, Drullinger R E and Walls F L 1978 Radiation-pressure cooling of bound resonant absorbers *Phys. Rev. Lett.* **40** 1639–42

[64] Neuhauser W, Hohenstatt M, Toschek P and Dehmelt H 1978 Optical-sideband cooling of visible atom cloud confined in parabolic well *Phys. Rev. Lett.* **41** 233–6

[65] Waki I, Kassner S, Birkl G and Walther H 1992 Observation of ordered structures of laser-cooled ions in a quadrupole storage ring *Phys. Rev. Lett.* **68** 2007–10

[66] Birkl G, Kassner S and Walther H 1992 Multiple-shell structures of laser-cooled $^{24}Mg^+$ ions in a quadrupole storage ring *Nature* **357** 310–13

[67] Monz T, Schindler P, Barreiro J T, Chwalla M, Nigg D, Coish W A, Harlander M, Hänsel W, Hennrich M and Blatt R 2011 14-qubit entanglement: creation and coherence *Phys. Rev. Lett.* **106** 130506

[68] Lin G-D, Zhu S-L, Islam R, Kim K, Chang M-S, Korenblit S, Monroe C and Duan L-M 2009 Large-scale quantum computation in an anharmonic linear ion trap *Europhys. Lett.* **86** 60004

[69] Schätz T, Schramm U and Habs D 2001 Crystalline ion beams *Nature* **412** 717–20

[70] Schramm U, Schätz T and Habs D 2001 Bunched crystalline ion beams *Phys. Rev. Lett.* **87** 184801

[71] Schramm U, Schätz T and Habs D 2002 Three-dimensional crystalline ion beams *Phys. Rev.* E **66** 036501

[72] Moehring D L 2011 private communication

[73] Chiaverini J, Blakestad R B, Britton J, Jost J D, Langer C, Leibfried D, Ozeri R and Wineland D J 2005 Surface-electrode architecture for ion-trap quantum information processing *Quantum Inform. Comput.* **5** 419–39

[74] Seidelin S *et al* 2006 Microfabricated surface-electrode ion trap for scalable quantum information processing *Phys. Rev. Lett.* **96** 253003

[75] Kielpinski D, Monroe C and Wineland D J 2002 Architecture for a large-scale ion-trap quantum computer *Nature* **417** 709–11

[76] Tan J N, Bollinger J J, Jelenkovic B and Wineland D J 1995 Long-range order in laser-cooled, atomic-ion Wigner crystals observed by Bragg scattering *Phys. Rev. Lett.* **75** 4198–201

[77] Itano W M, Bollinger J J, Tan J N, Jelenković B, Huang X-P and Wineland D J 1998 Bragg diffraction from crystallized ion plasmas *Science* **279** 686–9

[78] Mitchell T B, Bollinger J J, Dubin D H E, Huang X-P, Itano W M and Baughman R H 1998 Direct observations of structural phase transitions in planar crystallized ion plasmas *Science* **282** 1290–3

[79] Porras D and Cirac J I 2006 Quantum manipulation of trapped ions in two dimensional Coulomb crystals *Phys. Rev. Lett.* **96** 250501

[80] Schneider Ch, Enderlein M, Huber T and Schaetz T 2010 Optical trapping of an ion *Nature Photon.* **4** 772–5

[81] Trapped Ion Quantum Information Group; University of Maryland. Ion periodic table (http://www.iontrap.umd.edu/research_info/ioncatalog/index.html)

[82] Saffman M and Mølmer K 2008 Scaling the neutral-atom Rydberg gate quantum computer by collective encoding in holmium atoms *Phys. Rev.* A **78** 012336

[83] Bollinger J J, Heizen D J, Itano W M, Gilbert S L and Wineland D J 1991 A 303-Mhz frequency standard based on trapped $Be^+$ ions *IEEE Trans. Instrum. Meas.* **40** 126–8

[84] Fisk P T H, Sellars M J, Lawn M A, Coles C, Mann A G and Blair D G 1995 Very high Q microwave spectroscopy on trapped $^{171}Yb^+$ ions: application as a frequency standard *IEEE Trans. Instrum. Meas.* **44** 113–6

[85] Sørensen A and Mølmer K 1999 Quantum computation with ions in thermal motion *Phys. Rev. Lett.* **82** 1971–4

[86] Roos C F 2008 Ion trap quantum gates with amplitude-modulated laser beams *New J. Phys.* **10** 013002

[87] Lee P J, Brickman K-A, Deslauriers L, Haljan P C, Duan L-M and Monroe C 2005 Phase control of trapped ion quantum gates *J. Opt.* B **7** S371–83

[88] Mintert F and Wunderlich C 2001 Ion-trap quantum logic using long-wavelength radiation *Phys. Rev. Lett.* **87** 257904

[89] Johanning M, Braun A, Timoney N, Elman V, Neuhauser W and Wunderlich C 2009 Individual addressing of trapped ions and coupling of motional and spin states using rf radiation *Phys. Rev. Lett.* **102** 073004

[90] Timoney N, Elman V, Glaser S, Weiss C, Johanning M, Neuhauser W and Wunderlich C 2008 Error-resistant single-qubit gates with trapped ions *Phys. Rev.* A **77** 052334

[91] Ospelkaus C, Langer C E, Amini J M, Brown K R, Leibfried D and Wineland D J 2008 Trapped-ion quantum logic gates based on oscillating magnetic fields *Phys. Rev. Lett.* **101** 090502

[92] Brown K R, Wilson A C, Colombe Y, Ospelkaus C, Meier A M, Knill E, Leibfried D and Wineland D J 2011 Single-qubit-gate error below $10^{-4}$ in a trapped ion *Phys. Rev.* A **84** 030303

[93] Ospelkaus C, Warring U, Colombe Y, Brown K R, Amini J M, Leibfried D and Wineland D J 2011 Microwave quantum logic gates for trapped ions *Nature* **476** 181–4

[94] Happer W 1972 Optical pumping *Rev. Mod. Phys.* **44** 169–250

[95] Wineland D J and Itano W M 1979 Laser cooling of atoms *Phys. Rev.* A **20** 1521–40

[96] Diedrich F, Bergquist J C, Itano W M and Wineland D J 1989 Laser cooling to the zero-point energy of motion *Phys. Rev. Lett.* **62** 403–6

[97] Monroe C, Meekhof D M, King B E, Jefferts S R, Itano W M, Wineland D J and Gould P 1995 Resolved-sideband Raman cooling of a bound atom to the 3D zero-point energy *Phys. Rev. Lett.* **75** 4011–4

[98] Morigi G, Eschner J and Keitel C H 2000 Ground state laser cooling using electromagnetically induced transparency *Phys. Rev. Lett.* **85** 4458–61

[99] Roos C F, Leibfried D, Mundt A, Schmidt-Kaler F, Eschner J and Blatt R 2000 Experimental demonstration of ground state laser cooling with electromagnetically induced transparency *Phys. Rev. Lett.* **85** 5547–50

[100] Wineland D J, Bergquist J C, Itano W M and Drullinger R E 1980 Double-resonance and optical-pumping experiments on electromagnetically confined, laser-cooled ions *Opt. Lett.* **5** 245–7

[101] Nagourney W, Sandberg J and Dehmelt H 1986 Shelved optical electron amplifier: observation of quantum jumps *Phys. Rev. Lett.* **56** 2797–9

[102] Sauter Th, Neuhauser W, Blatt R and Toschek P E 1986 Observation of quantum jumps *Phys. Rev. Lett.* **57** 1696–8

[103] Bergquist J C, Hulet R G, Itano W M and Wineland D J 1986 Observation of quantum jumps in a single atom *Phys. Rev. Lett.* **57** 1699–702

[104] Myerson A H, Szwer D J, Webster S C, Allcock D T C, Curtis M J, Imreh G, Sherman J A, Stacey D N, Steane A M and Lucas D M 2008 High-fidelity readout of trapped-ion qubits *Phys. Rev. Lett.* **100** 200502

[105] Burrell A H, Szwer D J, Webster S C and Lucas D M 2010 Scalable simultaneous multiqubit readout with 99.99% single-shot fidelity *Phys. Rev.* A **81** 040302

[106] Schaetz T, Barrett M D, Leibfried D, Britton J, Chiaverini J, Itano W M, Jost J D, Knill E, Langer C and Wineland D J 2005 Enhanced quantum state detection efficiency through quantum information processing *Phys. Rev. Lett.* **94** 010501

[107] Hume D B, Rosenband T and Wineland D J 2007 High-fidelity adaptive qubit detection through repetitive quantum nondemolition measurements *Phys. Rev. Lett.* **99** 120502

[108] Schmidt P O, Rosenband T, Langer C, Itano W M, Bergquist J C and Wineland D J 2005 Spectroscopy using quantum logic *Science* **309** 749–52

[109] Meekhof D M, Monroe C, King B E, Itano W M and Wineland D J 1996 Generation of nonclassical motional states of a trapped atom *Phys. Rev. Lett.* **76** 1796–9

[110] Leibfried D *et al* 2003 Experimental demonstration of a robust, high-fidelity geometric two ion-qubit phase gate *Nature* **422** 412–5

[111] Cahill K E and Glauber R J 1969 Ordered expansions in boson amplitude operators *Phys. Rev.* **177** 1857–81

[112] Berry M V 1984 Quantal phase factors accompanying adiabatic changes *Proc. R. Soc. Lond.* A **392** 45–57

[113] Aharonov Y and Anandan J 1987 Phase change during a cyclic quantum evolution *Phys. Rev. Lett.* **58** 1593–6

[114] Solano E, de Matos Filho R L and Zagury N 1999 Deterministic Bell states and measurement of the motional state of two trapped ions *Phys. Rev.* A **59** R2539–R2543

[115] Milburn G J, Schneider S and James D F V 2000 Ion trap quantum computing with warm ions *Fortschr. Phys.* **48** 801–10

[116] Sørensen A and Mølmer K 2000 Entanglement and quantum computation with ions in thermal motion *Phys. Rev.* A **62** 022311

[117] Wang X, Sørensen A and Mølmer K 2001 Multibit gates for quantum computing *Phys. Rev. Lett.* **86** 3907–10

[118] Home J P, McDonnell M J, Lucas D M, Imreh G, Keitch B C, Szwer D J, Thomas N R, Webster S C, Stacey D N and Steane A M 2006 Deterministic entanglement and tomography of ion-spin qubits *New J. Phys.* **8** 188

[119] Sackett C A *et al* 2000 Experimental entanglement of four particles *Nature* **404** 256–9

[120] Haljan P C, Lee P J, Brickman K-A, Acton M, Deslauriers L and Monroe C 2005 Entanglement of trapped-ion clock states *Phys. Rev.* A **72** 062316

[121] Benhelm J, Kirchmair G, Roos C F and Blatt R 2008 Towards fault-tolerant quantum computing with trapped ions *Nature Phys.* **4** 463–6

[122] Kim K, Chang M-S, Islam R, Korenblit S, Duan L-M and Monroe C 2009 Entanglement and tunable spin-spin couplings between trapped ions using multiple transverse modes *Phys. Rev. Lett.* **103** 120502

[123] Schmitz H, Friedenauer A, Schneider C, Matjeschk R, Enderlein M, Huber T, Glueckert J, Porras D and Schaetz T 2009 The 'arch' of simulating quantum spin systems with trapped ions *Appl. Phys.* B **95** 195–203

[124] Porras D and Cirac J I 2008 Quantum manipulation of trapped ions in two dimensional Coulomb crystals arXiv:quant-ph/0601148v3

[125] Deng X-L, Porras D and Cirac J I 2005 Effective spin quantum phases in systems of trapped ions *Phys. Rev.* A **72** 063407

[126] Bermudez A, Schaetz T and Porras D 2011 Synthetic gauge fields for vibrational excitations of trapped ions *Phys. Rev. Lett.* **107** 150501

[127] Landa H, Marcovitch S, Retzker A, Plenio M B and Reznik B 2010 Quantum coherence of discrete kink solitons in ion traps *Phys. Rev. Lett.* **104** 043004

[128] Sachdev S 2000 Quantum criticality: competing ground states in low dimensions *Science* **288** 475–80

[129] Blatt R 2011 private communication

[130] Hauke P, Cucchietti F M, Müller-Hermes A, Bañuls M-C, Cirac J I and Lewenstein M 2010 Complete devil's staircase and crystal–superfluid transitions in a dipolar *XXZ* spin chain: a trapped ion quantum simulation *New J. Phys.* **12** 113037

[131] Schmied R, Wesenberg J H and Leibfried D 2011 Quantum simulation of the hexagonal Kitaev model with trapped ions *New J. Phys.* **13** 115011

[132] Shimshoni E, Morigi G and Fishman S 2011 Quantum zigzag transition in ion chains *Phys. Rev. Lett.* **106** 010401

[133] Shimshoni E, Morigi G and Fishman S 2011 Quantum structural phase transition in chains of interacting atoms *Phys. Rev.* A **83** 032308

[134] Milman P, Maineult W, Guibal S, Guidoni L, Douçot B, Ioffe L and Coudreau T 2007 Topologically decoherence-protected qubits with trapped ions *Phys. Rev. Lett.* **99** 020503

[135] Bermudez A, Porras D and Martin-Delgado M A 2009 Competing many-body interactions in systems of trapped ions *Phys. Rev.* A **79** 060303

[136] Barreiro J T, Müller M, Schindler P, Nigg D, Monz T, Chwalla M, Hennrich M, Roos C F, Zoller P and Blatt R 2011 An open-system quantum simulator with trapped ions *Nature* **470** 486–91

[137] Deng X-L, Porras D and Cirac J I 2008 Quantum phases of interacting phonons in ion traps *Phys. Rev.* A **77** 033403

[138] Brown K R, Ospelkaus C, Colombe Y, Wilson A C, Leibfried D and Wineland D J 2011 Coupled quantized mechanical oscillators *Nature* **471** 196–9

[139] Harlander M, Lechner R, Brownnutt M, Blatt R and Hänsel W 2011 Trapped-ion antennae for the transmission of quantum information *Nature* **471** 200–3

[140] Bermudez A, Martin-Delgado M A and Porras D 2010 The localization of phonons in ion traps with controlled quantum disorder *New J. Phys.* **12** 123016

[141] Ivanov P A, Ivanov S S, Vitanov N V, Mering A, Fleischhauer M and Singer K 2009 Simulation of a quantum phase transition of polaritons with trapped ions *Phys. Rev.* A **80** 060301

[142] Ivanov P A, Vitanov N V, Singer K and Schmidt-Kaler F 2010 Dynamical control and novel quantum phases in impurity doped linear ion crystals arXiv:1002.3033v2

[143] Ivanov P A and Schmidt-Kaler F 2011 Simulation of quantum magnetism in mixed spin systems with impurity doped ion crystal arXiv:1105.0598v1

[144] Kibble T W B 1976 Topology of cosmic domains and strings *J. Phys. A: Math. Gen.* **9** 1387–98

[145] Zurek W H 1985 Cosmological experiments in superfluid helium? *Nature* **317** 505–8

[146] del Campo A, De Chiara G, Morigi G, Plenio M B and Retzker A 2010 Structural defects in ion chains by quenching the external potential: the inhomogeneous Kibble–Zurek mechanism *Phys. Rev. Lett.* **105** 075701

[147] Marcovitch S and Reznik B 2008 Entanglement of solitons in the Frenkel–Kontorova model *Phys. Rev.* A **78** 052303

[148] Kartashov Y V, Malomed B A and Torner L 2011 Solitons in nonlinear lattices *Rev. Mod. Phys.* **83** 247–305

[149] Eisenberg H S, Silberberg Y, Morandotti R, Boyd A R and Aitchison J S 1998 Discrete spatial optical solitons in waveguide arrays *Phys. Rev. Lett.* **81** 3383–6

[150] Fleischer J W, Segev M, Efremidis N K and Christodoulides D N 2003 Observation of two-dimensional discrete solitons in optically induced nonlinear photonic lattices *Nature* **422** 147–150

[151] Trombettoni A and Smerzi A 2001 Discrete solitons and breathers with dilute Bose–Einstein condensates *Phys. Rev. Lett.* **86** 2353–6

[152] Frenkel J and Kontorowa T 1938 On the theory of plastic deformation and twinning *Phys. Z. Sowjetunion* **13** 1–10

[153] Kivshar Y S and Braun O M 2004 *The Frenkel–Kontorova Model* (Berlin: Springer)

[154] García-Mata I, Zhirov O V and Shepelyansky D L 2007 Frenkel–Kontorova model with cold trapped ions *Eur. Phys. J.* D **41** 325–30

[155] Benassi A, Vanossi A and Tosatti E 2011 Nanofriction in cold ion traps *Nature Commun.* **2** 236

[156] Pruttivarasin T, Ramm M, Talukdar I, Kreuter A and Häffner H 2011 Trapped ions in optical lattices for probing oscillator chain models *New J. Phys.* **13** 075012

[157] Schmied R, Roscilde T, Murg V, Porras D and Cirac J I 2008 Quantum phases of trapped ions in an optical lattice *New J. Phys.* **10** 045017

[158] Folman R, Krüger P, Cassettari D, Hessmo B, Maier T and Schmiedmayer J 2000 Controlling cold atoms using nanofabricated surfaces: atom chips *Phys. Rev. Lett.* **84** 4749–52

[159] Stick D, Fortier K M, Haltli R, Highstrete C, Moehring D L, Tigges C and Blain M G 2010 Demonstration of a microfabricated surface electrode ion trap arXiv:1008.0990v2

[160] Moehring D L, Highstrete C, Stick D, Fortier K M, Haltli R, Tigges C and Blain M G 2011 Design, fabrication and experimental demonstration of junction surface ion traps *New J. Phys.* **13** 075018

[161] Turchette Q A *et al* 2000 Heating of trapped ions from the quantum ground state *Phys. Rev.* A **61** 063418

[162] Labaziewicz J, Ge Y, Antohi P, Leibrandt D, Brown K R and Chuang I L 2008 Suppression of heating rates in cryogenic surface-electrode ion traps *Phys. Rev. Lett.* **100** 013001

[163] Wineland D J and Leibfried D 2011 Quantum information processing and metrology with trapped ions *Laser Phys. Lett.* **8** 175–88

[164] Schaetz T, Friedenauer A, Schmitz H, Petersen L and Kahra S 2007 Towards (scalable) quantum simulations in ion traps *J. Mod. Opt.* **54** 2317–25

[165] Schmied R, Wesenberg J H and Leibfried D 2009 Optimal surface-electrode trap lattices for quantum simulation with trapped ions *Phys. Rev. Lett.* **102** 233002

[166] Kumph M, Brownnutt M and Blatt R 2011 Two-dimensional arrays of radio-frequency ion traps with addressable interactions *New J. Phys.* **13** 073043

[167] Karin T, Le Bras I, Kehlberger A, Singer K, Daniilidis N and Häffner H 2012 Transport of charged particles by adjusting rf voltage amplitudes *Appl. Phys.* B at press (arXiv:1011.6116v5)

[168] Chiaverini J and Lybarger W E 2008 Laserless trapped-ion quantum simulations without spontaneous scattering using microtrap arrays *Phys. Rev.* A **77** 022324

[169] Hennsinger W 2011 private communication

[170] Castrejón-Pita J R, Ohadi H, Crick D R, Winters D F A, Segal D M and Thompson R C 2007 Novel designs for Penning ion traps *J. Mod. Opt.* **54** 1581–94
[171] Hellwig M, Bautista-Salvador A, Singer K, Werth G and Schmidt-Kaler F 2010 Fabrication of a planar micro Penning trap and numerical investigations of versatile ion positioning protocols *New J. Phys.* **12** 065019
[172] Schmied R 2010 Electrostatics of gapped and finite surface electrodes *New J. Phys.* **12** 023038
[173] Hurst G S, Payne M G, Kramer S D and Young J P 1979 Resonance ionization spectroscopy and one-atom detection *Rev. Mod. Phys.* **51** 767–819
[174] Kjærgaard N, Hornekær L, Thommesen A M, Videsen Z and Drewsen M 2000 Isotope selective loading of an ion trap using resonance-enhanced two-photon ionization *Appl. Phys.* B **71** 207–10
[175] Pearson C E, Leibrandt D R, Bakr W S, Mallard W J, Brown K R and Chuang I L 2006 Experimental investigation of planar ion traps *Phys. Rev.* A **73** 032307
[176] Allcock D T C *et al* 2010 Implementation of a symmetric surface-electrode ion trap with field compensation using a modulated Raman effect *New J. Phys.* **12** 053026
[177] Berkeland D J, Miller J D, Bergquist J C, Itano W M and Wineland D J 1998 Minimization of ion micromotion in a Paul trap *J. Appl. Phys.* **83** 5025–33
[178] Friedenauer A, Markert F, Schmitz H, Petersen L, Kahra S, Herrmann M, Udem T, Hänsch T W and Schätz T 2006 High power all solid state laser system near 280 nm *Appl. Phys.* B **84** 371–3
[179] Bertelsen A, Vogelius I S, Jørgensen S, Kosloff R and Drewsen M 2004 Photo-dissociation of cold $MgH^+$ *Eur. Phys. J.* D **31** 403–8
[180] Cetina M, Grier A, Campbell J, Chuang I and Vuletić V 2007 Bright source of cold ions for surface-electrode traps *Phys. Rev.* A **76** 041401
[181] Feng Y, Taylor L R and Calia D B 2009 150 W highly-efficient Raman fiber laser *Opt. Express* **17** 23678–83
[182] Feng Y, Taylor L R and Calia D B 2009 25 W Raman-fiber-amplifier-based 589 nm laser for laser guide star *Opt. Express* **17** 19021–6
[183] Toptica Photonics AG 2010 private communication
[184] Dumke R, Volk M, Müther T, Buchkremer F B J, Birkl G and Ertmer W 2002 Micro-optical realization of arrays of selectively addressable dipole traps: a scalable configuration for quantum computation with atomic qubits *Phys. Rev. Lett.* **89** 097903
[185] Streed E W, Norton B G, Jechow A, Weinhold T J and Kielpinski D 2011 Imaging of trapped ions with a microfabricated optic for quantum information processing *Phys. Rev. Lett.* **106** 010502
[186] VanDevender A P, Colombe Y, Amini J, Leibfried D and Wineland D J 2010 Efficient fiber optic detection of trapped ion fluorescence *Phys. Rev. Lett.* **105** 023001
[187] Shu G, Kurz N, Dietrich M R and Blinov B B 2010 Efficient fluorescence collection from trapped ions with an integrated spherical mirror *Phys. Rev.* A **81** 042321
[188] Noek R, Knoernschild C, Migacz J, Kim T, Maunz P, Merrill T, Hayden H, Pai C S and Kim J 2010 Multiscale optics for enhanced light collection from a point source *Opt. Lett.* **35** 2460–2
[189] Herskind P F, Wang S X, Shi M, Ge Y, Cetina M and Chuang I L 2011 Microfabricated surface ion trap on a high-finesse optical mirror *Opt. Lett.* **36** 3045–7
[190] Kollath C, Köhl M and Giamarchi T 2007 Scanning tunneling microscopy for ultracold atoms *Phys. Rev.* A **76** 063602
[191] Grimm R, Weidemüller M and Ovchinnikov Y B 2000 Optical dipole traps for neutral atoms *Adv. At. Mol. Opt. Phys.* **42** 95–170
[192] Zipkes C, Palzer S, Sias C and Köhl M 2010 A trapped single ion inside a Bose-Einstein condensate *Nature* **464** 388–91
[193] Leibrandt D R, Labaziewicz J, Vuletić V and Chuang I L 2009 Cavity sideband cooling of a single trapped ion *Phys. Rev. Lett.* **103** 103001
[194] Rehbein N *et al* 2007 Optical quenching of metastable magnesium *Phys. Rev.* A **76** 043406
[195] James D F V 1998 Quantum dynamics of cold trapped ions with application to quantum computation *Appl. Phys.* B **66** 181–90
[196] Abramowitz M and Stegun I A (ed) 1972 *Handbook of Mathematical Functions with Formulas, Graphs, and Mathematical Tables* (Washington, DC: GPO)
[197] Magnus W 1954 On the exponential solution of differential equations for a linear operator *Commun. Pure Appl. Math.* **7** 649–73
[198] Blanes S, Casas F, Oteo J A and Ros J 2009 The Magnus expansion and some of its applications *Phys. Rep.* **470** 151–238
[199] Schmid S, Härter A and Hecker Denschlag J 2010 Dynamics of a cold trapped ion in a Bose–Einstein condensate *Phys. Rev. Lett.* **105** 133202

# Designer Spin Pseudomolecule Implemented with Trapped Ions in a Magnetic Gradient

A. Khromova, Ch. Piltz, B. Scharfenberger, T. F. Gloger, M. Johanning, A. F. Varón, and Ch. Wunderlich*

*Department Physik, Naturwissenschaftlich-Technische Fakultät, Universität Siegen, 57068 Siegen, Germany*

(Received 3 February 2012; published 1 June 2012)

We report on the experimental investigation of an individual pseudomolecule using trapped ions with adjustable magnetically induced $J$-type coupling between spin states. Resonances of individual spins are well separated and are addressed with high fidelity. Quantum gates are carried out using microwave radiation in the presence of thermal excitation of the pseudomolecule's vibrations. Demonstrating controlled-NOT gates between non-nearest neighbors serves as a proof-of-principle of a quantum bus employing a spin chain. Combining advantageous features of nuclear magnetic resonance experiments and trapped ions, respectively, opens up a new avenue toward scalable quantum information processing.

DOI: 10.1103/PhysRevLett.108.220502 PACS numbers: 03.67.Lx, 03.65.Ud, 37.10.Ty, 42.50.Dv

Successful experiments with molecules using nuclear magnetic resonance (NMR) [1–7] and with trapped ions [8–12] have been an important driving force for quantum information science. Early on during the development of quantum information science, NMR was successfully applied to carry out sophisticated quantum logic operations and complete quantum algorithms based on the so-called $J$-coupling between nuclear spins in molecules. In molecules used for NMR, the direct dipole-dipole interaction between nuclear spins is usually negligible. However, nuclear spins interact indirectly via $J$-coupling which is mediated by bonding electrons. This $J$-coupling provides a mechanism to implement conditional quantum dynamics with nuclear spins that are characterized by long coherence times and are manipulated using rf radiation. Scalability of NMR is hampered mainly by the use of ensembles of molecules making it difficult to prepare pure spin states. Also, nuclear spin resonances and $J$-coupling between spins in molecules are given by nature, and thus often are not well suited for quantum computing.

Here, effective spin-1/2 systems are realized by using long-lived hyperfine states of trapped atomic ions. The vibrational modes of this individual ion pseudomolecule [13] mediate an effective $J$-type coupling when exposing trapped ions to a spatially varying magnetic field [14–16]. The constants $J_{ij}$ arising from magnetic gradient induced coupling (MAGIC) of such an individual spin-pseudomolecule can be adjusted through variation of the trapping potential that determines the frequencies $\nu_n$ of the ion crystal's vibrational modes. In addition, the range of interactions can be tuned by applying local static potentials [16,17]. Single spins can be addressed in frequency space, since the magnetic field gradient leads to a position dependent shift of an ion's resonance frequency [18,19]. A further useful feature of spin-pseudomolecules is the use of radio-frequency and microwave radiation for conditional quantum dynamics as opposed to laser light [18–21], a feature that substantially reduces experimental complexity and contributed to the rapid success of NMR in quantum information science. In addition, this eliminates spontaneous emission that otherwise may destroy coherences [22]. Moreover, $J$-type coupling in a spin-pseudomolecule is tolerant against thermal excitation of vibrational motion. This substantially reduces the necessity for cooling trapped ions in order to achieve high fidelity gates.

Exposing a trapped ion Coulomb crystal to a spatially varying magnetic field induces a spin-spin interaction mediated by the common vibrational motion of the ion crystal [14,15],

$$H = -\frac{\hbar}{2}\sum_{i<j}^{N} J_{ij}\sigma_z^{(i)}\sigma_z^{(j)}, \tag{1}$$

where $\sigma_z$ is a Pauli matrix and the coupling constants $J_{ij} = \sum_{n=1}^{N} \nu_n \kappa_{ni}\kappa_{nj}$. This sum extends over all vibrational modes with angular frequency $\nu_n$, and $\kappa_{nl} \equiv \frac{\Delta z \partial_z \omega_l}{\nu_n} S_{nl}$ indicates how strongly ion $l$ couples to the vibrational mode $n$, when the spin of ion $l$ is flipped. Here, $\Delta z = \sqrt{\hbar/2m\nu_n}$ is the extension of the ground state wave function of vibrational mode $n$, and $\Delta z \partial_z \omega_l = g_F \mu_B b_l/\hbar$ gives the change of the ion's resonance frequency $\omega_l$ when moving it by $\Delta z$ ($b_l$ is the magnetic field gradient at the position of ion $l$, $\hbar$ is the reduced Planck's constant, $\mu_B$ the Bohr magneton, and $g_F$ the Landé factor, e.g., $g_F = 1$ for $^{171}Yb^+$ ions in the electronic ground state). The dimensionless matrix elements $S_{nl}$ give the scaled deviation of ion $l$ from its equilibrium positions when vibrational mode $n$ is excited. Such magnetic gradient induced coupling may also be implemented using electrons confined in a Penning trap [23]. Tunable spin-spin coupling based on optical dipole forces was proposed in [24] and demonstrated in [25,26].

After outlining how individual spins can be addressed with high fidelity in what follows, the measurement of the coupling matrix $\{J_{ij}\}$ for a three-spin–pseudomolecule is described. In addition, it is shown how coupling constants can be adjusted by variation of the ion trapping potential. Then, the experimental realization of controlled-NOT gates between any pair of spins is described, including a CNOT

 

gate between non-neighboring ions. The entanglement of spins is proven by measuring the parity (defined below) of a two-spin state.

Hyperfine levels of the $^2S_{1/2}$ ground state of $^{171}Yb^+$ serve as an effective spin-1/2 system [15], namely $|\downarrow_i\rangle \equiv {}^2S_{1/2}$ $(F = 0)$ and $|\uparrow_i\rangle \equiv {}^2S_{1/2}$ $(F = 1, m_F = +1)$, where $i = 1, 2, 3$ refers to ion $i$. These states are coherently controlled by microwave radiation near 12.65 GHz in resonance with the $|\downarrow_i\rangle \leftrightarrow |\uparrow_i\rangle$ transition. For the experiments presented here, we load three $^{171}Yb^+$ ions in a linear Paul trap where the effective harmonic trapping potential is characterized by the secular radial frequency $\nu_r = 2\pi \times 502(2)$ kHz and axial frequency $\nu_1 = 2\pi \times 123.5(2)$ kHz. Initial preparation in state $|\downarrow\rangle$ is achieved by optical pumping on the $^2S_{1/2}$ $(F = 1) \leftrightarrow {}^2P_{1/2}$ $(F = 1)$ transition near 369 nm, and state-selective detection is done by registering resonance fluorescence scattered on the $^2S_{1/2}$ $(F = 1) \leftrightarrow {}^2P_{1/2}$ $(F = 0)$ electronic transition. This ionic resonance serves at the same time for Doppler cooling of the ion crystal. The population of the center-of-mass (c.m.) mode after Doppler cooling along the axial direction is $\langle n_1\rangle \approx 150$. Microwave sideband cooling is applied to attain $\langle n_1\rangle = 23(7)$ (details will be published elsewhere).

The ions are exposed to a magnetic field gradient along the $z$ direction that is created by two hollow cylindrical SmCo permanent magnets plated with nickel and mounted at each end-cap electrode of the trap with identical poles facing each other. The total magnetic field amplitude is given by $B(z) = \sqrt{(B_{0\|} + b_{\rm pm} z)^2 + B_{0\perp}^2}$, where $B_{0\|} = 3.4 \times 10^{-4}$ T and $B_{0\perp} = 6.2 \times 10^{-5}$ T are longitudinal and radial components of the bias field at the coordinate origin defined by the position of the center ion, and $b_{\rm pm} = 19.0(1)$ T/m is the magnetic field gradient created by the permanent magnets in the absence of a perpendicular bias field. The magnetic field gradient $b_l = \partial_z B(z)|_{z=z_l}$ defined at the position $z_l$ of ion $l$ is smaller than $b_{\rm pm}$ and not constant due to the nonzero radial component $B_{0\perp}$ of the bias field.

The state $|\uparrow\rangle$ is magnetically sensitive and undergoes an energy shift $\Delta E = g_F \mu_B B$ due to the linear Zeeman effect, while state $|\downarrow\rangle$ to first order is insensitive to the magnetic field. Because of the gradient of the magnetic field, three ions with an inter-ion spacing of 11.9 $\mu$m [Fig. 1(a)] are subject to different energy shifts resulting in a frequency shift of the resonance $|\downarrow\rangle \leftrightarrow |\uparrow\rangle$ of approximately $\Delta f \simeq 3$ MHz between adjacent ions [Fig. 1(b)]. This energy shift makes it possible to address the ions independently in frequency space by using microwave radiation (or laser light [27]). The probability amplitude of exciting a neighboring ion decreases with the square of the detuning. Here, it is less than $4 \times 10^{-4}$ (see Supplemental Material [28]).

In addition, the magnetic gradient induces the spin-spin interaction, Eq. (1), between the ions' internal states mediated by their common vibrational modes. Not only nearest neighbors interact but also the outer ions 1 and 3. The

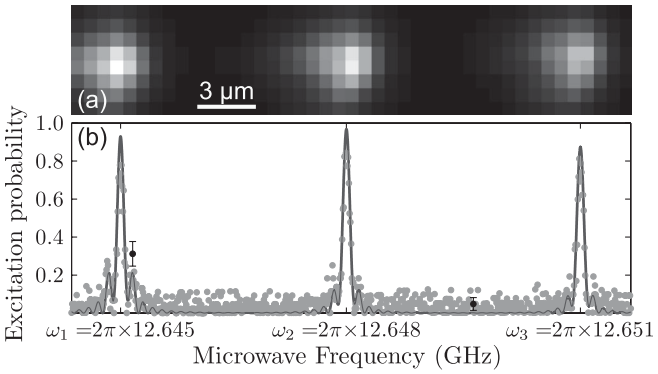


FIG. 1. Individual addressing of spins. (a) Spatially resolved resonance fluorescence (near 369 nm) of three $^{171}Yb^+$ ions recorded with an intensified CCD camera is shown. Neighboring ions are separated by 11.9 $\mu$m. (b) Microwave-optical double resonance spectrum of the above ions. The spectrum was recorded by applying a microwave frequency pulse of 8 $\mu$s to the ions initially prepared in the state $|\downarrow\rangle$. The probability to find an ion in $|\uparrow\rangle$ was determined from counting resonance fluorescence photons while probing with laser light near 369 nm. In a magnetic gradient of $\approx 18.2$ T/m, the qubit transitions $|\downarrow\rangle \leftrightarrow |\uparrow\rangle$ of different ions are nondegenerate. The solid line is a fit to the data. Each data point accounts for 50 repetitions. Two points with error bars are displayed representing the typical statistical standard deviations.

coupling constants $J_{12}$, $J_{23}$, and $J_{13}$ have been measured in a Ramsey-type experiment and are displayed in Fig. 2(a) together with their calculated values. For these measurements, first all three ions are initialized in state $|\downarrow\downarrow\downarrow\rangle$. After a microwave $\pi/2$ pulse has been applied to ion $j$, this spin's precession will depend on the state of ion $i$ which can be left in state $|\downarrow_i\rangle$ or set to $|\uparrow_i\rangle$ by a microwave $\pi$ pulse. After time $\tau$, a second $\pi/2$ pulse with variable phase $\phi$ is applied and the population $P(\phi)$ of $|\uparrow_j\rangle$ is measured with ion $i$ initially prepared in state $|\downarrow_i\rangle$ or in $|\uparrow_i\rangle$, respectively. The coupling between ions $i$ and $j$ is then deduced from the phase difference $\Delta\phi_{ij}$ between these two sinusoidal signals $P(\phi)$: $J_{ij} = \Delta\phi_{ij}/2\tau$. In order to extend the coherence time of the spin states, which is limited by ambient magnetic field fluctuations, a multipulse spin-echo sequence is applied to ions $i$ and $j$ between the $\pi/2$-Ramsey pulses [28]. The third ion (labeled $k$) has no active role and is left in state $|\downarrow_k\rangle$ during the whole sequence. Its interaction with the other ions via $J$-coupling is canceled by the applied spin-echo sequence (which is true independent of its internal state).

It is possible to encode quantum information in two sets of states, where one set is magnetically sensitive (as is used in this work), and the other set is not [e.g., $^2S_{1/2}$ $(F = 1, m_F = 0)$ and $(F = 0)$]. This allows for temporal storage of quantum information in magnetically insensitive states that do not couple to other spins and provide a memory intrinsically robust against ambient field fluctuations.

Figure 2(b) shows the dependence of $J$-type coupling on the c.m. frequency $\nu_1$, that is, on the strength of the axial

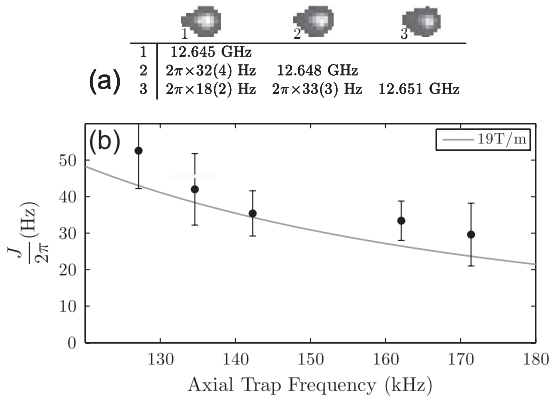


FIG. 2. $J$-type coupling of a three-spin pseudomolecule. In (a), the table lists the measured $J$-type coupling constants (below the diagonal) for a three-spin pseudomolecule together with the resonance frequencies of the microwave transitions (on the diagonal). For the nonuniform magnetic gradient present in our setup ($b_1 = 16.8$ T/m, $b_2 = 18.7$ T/m, $b_3 = 18.9$ T/m) and the axial trap frequency ($\nu_1 = 2\pi \times 123.5$ kHz), the calculated values are $J_{12} = 2\pi \times 32.9$ Hz, $J_{23} = 2\pi \times 37.0$ Hz, $J_{13} = 2\pi \times 23.9$ Hz. (b) Dependence of the coupling strength on the trapping potential. For a pseudomolecule consisting of two ions, the coupling strength $J$ has been measured for varying c.m. frequency $\nu_1$. A calculated curve for a uniform magnetic gradient of 19 T/m is represented by a solid line. These measurements demonstrate how $J$-type coupling can be varied by adjusting the trapping potential [16,17].

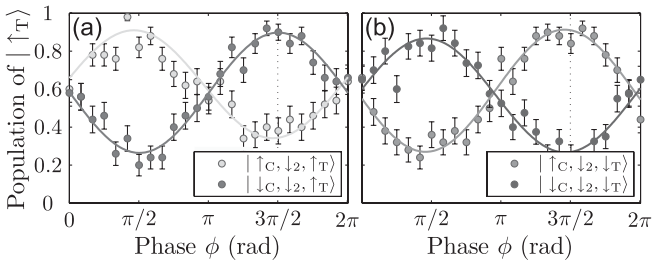


FIG. 3. Conditional quantum dynamics and CNOT gate between non-neighboring ions. The probability to find the target spin (ion 3) in state $|\uparrow\rangle$ at the end of a Ramsey-type sequence is shown as a function of the phase $\phi$ of the second $\pi/2$ pulse applied to the target. The inset shows the input state prepared before the Ramsey experiment. In (a) the target is initially prepared in $|\uparrow\rangle$ while in (b) it is prepared in $|\downarrow\rangle$. $J$-type coupling between the control qubit (ion 1) and the target qubit (ion 3) produces a phase shift on the target population as a function of the control qubit's state (different shades of gray). A free evolution time of $\tau = 11$ ms yields a phase shift of approximately $\pi$ (3.1(2) radians) between the pairwise displayed curves. For $\phi = 3\pi/2$, a CNOT gate results. The middle ion, prepared in state $|\downarrow\rangle$, does not interact with other ions. Each data point represents 50 repetitions, the error bars correspond to mean standard deviations, and solid lines are fits to the data.

trapping potential. These data were taken with two trapped ions with the measurements carried out analogous to those described above, except that only a single spin-echo pulse was used here. This leads to shorter accessible precession times and thus smaller phase shifts which in turn yields a larger statistical error as compared to the data in Fig. 2(a). The data are in agreement with the calculated dependence of $J$ on $\nu_1$ ($J \propto (b/\nu_1)^2$).

$J$-type coupling between two spins is employed to implement a CNOT gate between ion 1 (control qubit) and ion 3 (target qubit). The evolution time $\tau = 11$ ms is chosen to achieve a phase shift of $\Delta\phi_{13} = \pi$. Figures 3(a) and 3(b) show the resulting state population of the target qubit as a function of phase $\phi$ of the last $\pi/2$-Ramsey pulse which is applied to the target qubit. The CNOT operation is achieved when selecting $\phi = 3\pi/2$. The four measured sets of data are in agreement with the truth table of the CNOT gate which induces a flip of the target qubit or leaves it unchanged depending on the initial state $|\uparrow\rangle$ or $|\downarrow\rangle$ of the control qubit.

The quantum nature of the conditional gate is verified by creation of entanglement in the outcome $|\psi_B\rangle = \frac{1}{\sqrt{2}} \times (|\downarrow_C\downarrow_2\downarrow_T\rangle + e^{i\alpha}|\uparrow_C\downarrow_2\uparrow_T\rangle)$ if the input is a superposition state. Only the correlations of the control and target qubit determine the parity $\Pi = P_{\uparrow\uparrow} + P_{\downarrow\downarrow} - (P_{\uparrow\downarrow} + P_{\downarrow\uparrow})$ of the resulting bipartite entangled Bell state ($P_{ij}$, $i, j = \downarrow, \uparrow$ denotes the probability to find the control and target qubits in the state $|ij\rangle$). When measuring in the $\sigma_z$ basis, we observe a parity $\Pi_z = 0.43(13)$. To prove that the correlations are nonclassical, the parity $\Pi(\phi)$ was measured in addition along different bases [10] by applying additional $\pi/2$ pulses with phase $\phi$ to both ions. Figure 4 shows the resulting signal $\Pi(\phi)$ that oscillates with twice the phase variation, as one would expect for a bipartite entangled state. From the visibility of $V = 0.42(6)$ of the signal shown in Fig. 4 we evaluate the fidelity [10] of a Bell state $F = \frac{\Pi_z+1}{4} + \frac{V}{2}$ to be 0.57(4) which exceeds the Bell limit of 0.5 and thus proves the existence of entanglement. This shows that a conditional quantum gate between two non-neighboring ions is achieved.

In a similar manner, a CNOT gate was achieved between the first and the second ion with a fidelity of $F = 0.64(5)$ showing that it is possible to carry out on demand entangling operations between two ions at desired positions of the ion chain. For neighboring ions the coupling constants are higher, allowing for shorter evolution times (in this case 8 ms) and therefore reducing the effect of decoherence. In future experiments, microwave dressed states will be employed to extend the coherence time of magnetic sensitive states by several orders of magnitude [21], and thus the fidelity of quantum gates will be improved.

The entanglement procedure shown here can be applied to longer ion chains with minimal modifications. A large-scale quantum processor would be made up of an array of traps [11] each containing a spin-pseudomolecule allowing for simultaneous conditional quantum dynamics with more than two spins (multiqubit gates). This could substantially speed up the execution of quantum algorithms [29] and would be an alternative to a processor that contains zones for conditional quantum dynamics with two or three ions

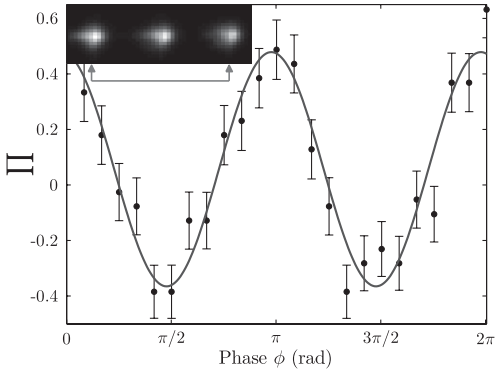


FIG. 4. Parity signal $\Pi(\phi)$ showing the quantum nature of the observed correlations of ion 1 and 3. The Bell state $|\psi_B\rangle = \frac{1}{\sqrt{2}} \times (|{\downarrow_C}{\downarrow_2}{\downarrow_T}\rangle + e^{i\alpha}|{\uparrow_C}{\downarrow_2}{\uparrow_T}\rangle)$ is the result of a CNOT operation applied to the superposition input state $|\psi_i\rangle = \frac{1}{\sqrt{2}}(|{\downarrow_C}{\downarrow_2}{\downarrow_T}\rangle + |{\uparrow_C}{\downarrow_2}{\downarrow_T}\rangle)$. In order to measure the correlations along different bases [10], microwave $\pi/2$ pulses with phase $\phi$ are applied to both ions followed by state-selective detection resulting in $\Pi(\phi)$ oscillating as $\cos(2\phi)$. The fidelity of creating the bipartite entangled state $|\psi_B\rangle$ is evaluated as $F = 0.57(4)$ (see text). Each data point represents 50 repetitions and error bars indicate 1 standard deviation.

[11]. Importantly, physical relocation (''shuttling'') of ions could be avoided during the processing of quantum information within a given spin-pseudomolecule [29]. The possibility to directly perform logic gates between distant qubits (e.g., the endpoints of a spin chain as demonstrated here) makes spin-pseudomolecules suitable as a quantum bus connecting different processor regions [30]. In that case, shuttling would be restricted to a pair of messenger ions which enable communication between different spin-pseudomolecules. In addition, a spin-pseudomolecule could serve as a versatile tool for quantum simulations of otherwise intractable physical systems [24–26,31,32].

It is desirable to increase the $J$-type constants due to MAGIC. This will be attained in microstructured ion traps [33,34] and trap arrays that allow for the application of larger magnetic gradients, or by using magnetic field gradients oscillating near the trap frequency [35]. In addition, segmented traps will allow for shaping $J$-coupling matrices by applying local electrostatic potentials [16,17], for example, to create cluster states [36], or to perform quantum simulations.

Assistance in data-taking by Th. Collath and D. Kaufmann and discussions with O. Gühne are gratefully acknowledged, as well as financial support by the Bundesministerium für Bildung und Forschung (FK 01BQ1012), Deutsche Forschungsgemeinschaft, and the European Commission under STREP PICC and iQIT.

*wunderlich@physik.uni-siegen.de

[1] D. G. Cory, A. F. Fahmy, and T. F. Havel, Proc. Natl. Acad. Sci. U.S.A. **94**, 1634 (1997).
[2] I. L. Chuang, L. M. K. Vandersypen, X. Zhou, D. W. Leung, and S. Lloyd, Nature (London) **393**, 143 (1998).
[3] J. A. Jones, M. Mosca, and R. H. Hansen, Nature (London) **393**, 344 (1998).
[4] R. Marx, A. F. Fahmy, J. M. Myers, W. Bermel, and S. J. Glaser, Phys. Rev. A **62**, 012310 (2000).
[5] E. Knill, R. Laflamme, R. Martinez, and C.-H. Tseng, Nature (London) **404**, 368 (2000).
[6] L. M. K. Vandersypen, M. Steffen, G. Breyta, C. S. Yannoni, M. H. Sherwood, and I. L. Chuang, Nature (London) **414**, 883 (2001).
[7] D. Suter and T. S. Mahesh, J. Chem. Phys. **128**, 052206 (2008).
[8] J. I. Cirac and P. Zoller, Phys. Rev. Lett. **74**, 4091 (1995).
[9] R. Blatt and D. Wineland, Nature (London) **453**, 1008 (2008).
[10] C. A. Sackett *et al.*, Nature (London) **404**, 256 (2000).
[11] D. Kielpinski, C. Monroe, and D. J. Wineland, Nature (London) **417**, 709 (2002).
[12] G. Kirchmair, J. Benhelm, F. Zähringer, R. Gerritsma, C. F. Roos, and R. Blatt, New J. Phys. **11**, 023002 (2009).
[13] D. J. Wineland, J. C. Bergquist, W. M. Itano, J. J. Bollinger, and C. H. Manney, Phys. Rev. Lett. **59**, 2935 (1987).
[14] Ch. Wunderlich, in *Laser Physics at the Limit*, edited by D. Meschede, C. Zimmermann, and H. Figger (Springer, New York, 2002), p. 261.
[15] Ch. Wunderlich and Ch. Balzer, Adv. At. Mol. Phys., **49**, 293 (2003).
[16] D. Mc Hugh and J. Twamley, Phys. Rev. A **71**, 012315 (2005).
[17] H. Wunderlich, Ch. Wunderlich, K. Singer, and F. Schmidt-Kaler, Phys. Rev. A **79**, 052324 (2009).
[18] F. Mintert and Ch. Wunderlich, Phys. Rev. Lett. **87**, 257904 (2001).
[19] M. Johanning, A. Braun, N. Timoney, V. Elman, W. Neuhauser, and Ch. Wunderlich, Phys. Rev. Lett. **102**, 073004 (2009).
[20] C. Ospelkaus, U. Warring, Y. Colombe, K. R. Brown, J. M. Amini, D. Leibfried, and D. J. Wineland, Nature (London) **476**, 181 (2011).
[21] N. Timoney, I. Baumgart, M. Johanning, A. F. Varón, M. B. Plenio, A. Retzker, and Ch. Wunderlich, Nature (London) **476**, 185 (2011).
[22] N. Akerman, S. Kotler, Y. Glickman, and R. Ozeri, arXiv:1111.1622v1.
[23] G. Ciaramicoli, F. Galve, I. Marzoli, and P. Tombesi, Phys. Rev. A **72**, 042323 (2005).
[24] D. Porras and J. I. Cirac, Phys. Rev. Lett. **92**, 207901 (2004).
[25] A. Friedenauer, H. Schmitz, J. T. Glueckert, D. Porras, and T. Schaetz, Nature Phys. **4**, 757 (2008).
[26] K. Kim, M. S. Chang, R. Islam, S. Korenblit, L.-M. Duan, and C. Monroe, Phys. Rev. Lett. **103**, 120502 (2009).
[27] S. X. Wang, J. Labaziewicz, Y. Ge, R. Shewmon, and I. L. Chuang, Appl. Phys. Lett. **94**, 094103 (2009).
[28] See Supplemental Material at http://link.aps.org/supplemental/10.1103/PhysRevLett.108.220502 for information about the experiment and its imperfections that presently limit the fidelity of conditional quantum gates.
[29] T. Schulte-Herbrüggen, A. Spörl, N. Khaneja, and S. J. Glaser, Phys. Rev. A **72**, 042331 (2005).

[30] D. Gottesman and I. L. Chuang, Nature (London) **402**, 390 (1999).
[31] Z. Li, M.-H. Yung, H. Chen, D. Lu, J. D. Whitfield, X. Peng, A. Aspuru-Guzik, and J. Du, Sci. Rep. **1**, 88 (2011).
[32] P. A. Ivanov and F. Schmidt-Kaler, New J. Phys. **13**, 125008 (2011).
[33] M. D. Hughes, B. Lekitsch, J. A. Broersma, and W. K. Hensinger, Contemp. Phys. **52**, 505 (2011).
[34] D. Kaufmann, T. Collath, M. T. Baig, P. Kaufmann, E. Asenwar, M. Johanning, and Ch.Wunderlich, arXiv:1107.4082 [Appl. Phys. B (to be published)].
[35] J. Welzel, A. Bautista-Salvador, C. Abarbanel, V. Wineman-Fisher, Ch. Wunderlich, R. Folman, and F. Schmidt-Kaler, Eur. Phys. J. D **65**, 285 (2011).
[36] H. J. Briegel, D. E. Browne, W. Dur, R. Raussendorf, and M. Van den Nest, Nature Phys. **5**, 19 (2009).

# Synthetic Gauge Fields for Vibrational Excitations of Trapped Ions

Alejandro Bermudez,[1,2] Tobias Schaetz,[3,4] and Diego Porras[2]

[1]*Institut für Theoretische Physik, Albert-Einstein Allee 11, Universität Ulm, 89069 Ulm, Germany*
[2]*Departamento de Física Teórica I, Universidad Complutense, 28040 Madrid, Spain*
[3]*Max-Planck-Institut für Quantenoptik, Hans-Kopfermann-Strasse 1, D-85748 Garching, Germany*
[4]*Albert-Ludwigs-Universität Freiburg, Physikalisches Institut, Hermann-Herder-Straße 3, 79104 Freiburg, Germany*

(Received 9 May 2011; published 3 October 2011)

The vibrations of a collection of ions in a microtrap array can be described in terms of tunneling phonons. We show that the vibrational couplings may be tailored by using a gradient of the trap frequencies together with a periodic driving of the trapping potentials. These ingredients allow us to induce effective gauge fields on the vibrational excitations, such that phonons mimic the behavior of charged particles in a magnetic field. In particular, microtrap arrays are well suited to realize a quantum simulator of the famous Aharonov-Bohm effect and observe the paradigmatic edge states typical from quantum-Hall samples and topological insulators.

DOI: 10.1103/PhysRevLett.107.150501 PACS numbers: 03.67.Ac, 37.10.Ty, 37.10.Vz

*Introduction.*—The ultimate goal of quantum simulation (QS) is to provide an alternative way of exploring the physics of quantum many-body systems [1]. This challenge requires efficient methods to prepare quantum states, an exquisite control of the interactions, and precise measurement techniques. Quantum-information technologies have an important application in this context, since they provide us with a powerful toolbox for the manipulation of quantum systems. In particular, trapped ions [2] are an interesting candidate, their main advantage being an unrivaled efficiency in preparing and measuring quantum states at the single-particle level. In addition, the strong long-range Coulomb interactions make them suitable for the QS of a variety of collective phenomena, from quantum magnetism [3] to dissipative models [4]. So far there have been experiments with up to 9 ions [5], and a lot of effort is being focused on scaling them up. A promising avenue are the so-called two-dimensional arrays of microtraps (2DAM) [6], which may open new routes towards the many-body regime. Unfortunately, this setup still faces some obstacles, such as the large distances between ions ($d_x \approx 40$ $\mu$m) leading to weak spin-spin interactions. In order to realize QS schemes based on vibration-mediated interactions, it is fundamental to overcome these issues. Alternatively, focusing directly on the vibrational modes [7] yields a significant speed-up with respect to decoherence rates. In fact, the transfer of vibrational excitations between two aligned traps was recently observed [8].

In this Letter, we show how to tailor the vibrational couplings in a 2DAM, such that this speed-up is exploited. This opens the possibility of building a QS of lattice bosons under synthetic gauge fields. We note that laser-based methods for neutral atoms might also lead to effective gauge fields [9]. Our proposal, however, relies on the different concept of photon-assisted tunneling [10,11], and requires a gradient of the individual trapping frequencies, together with a periodic driving of the trapping potentials that can be achieved by an optical force. This Letter is structured as follows. (i) We show that the amplitude and phase of the vibrational couplings between ions can be tuned by inducing resonances that correspond to the absorption or emission of photons from a classical driving field (photon-assisted tunneling). (ii) We extend this result to 2D and show how it leads to the implementation of synthetic gauge fields, where phonons move like charged particles in a lattice. (iii) We present an implementation of the required drivings by means of optical forces, such that the optical phase can be interpreted as an effective gauge field. (iv) We propose a proof of principle of our ideas with four ions in a plaquette displaying a discrete version of the celebrated Aharonov-Bohm effect [12]. (v) We suggest to concatenate those plaquettes in ladders, leading to Aharonov-Bohm cages [13] and allowing us to observe the edge states characteristic of quantum-Hall samples and topological insulators [14].

*(i) Photon-assisted tunneling.*—We introduce our scheme for two ions with mass $M$ and charge $e$, trapped by independent potentials with frequencies $\omega_{1,2}$ [Figs. 1(a) and 1(b)]. The equilibrium positions, separated by $d_x$, lie along the $x$ direction, and the axial vibrational modes are periodically driven. The Hamiltonian is $H(\tau) = H_0(\tau) + H_c$, with ($\hbar = 1$),

$$H_0(\tau) = \sum_{j=1,2} \omega_j a_j^\dagger a_j + H_d(\tau),$$
$$H_c = \frac{e^2}{d_x^3}(\delta x_1 - \delta x_2)^2. \quad (1)$$

$H_c$ is the Coulomb coupling to second order in the ion displacements, $\delta x_j = (a_j + a_j^\dagger)/\sqrt{2M\omega_j}$, with $a_j^\dagger(a_j)$ phonon creation (annihilation) operators. The periodic driving is

 

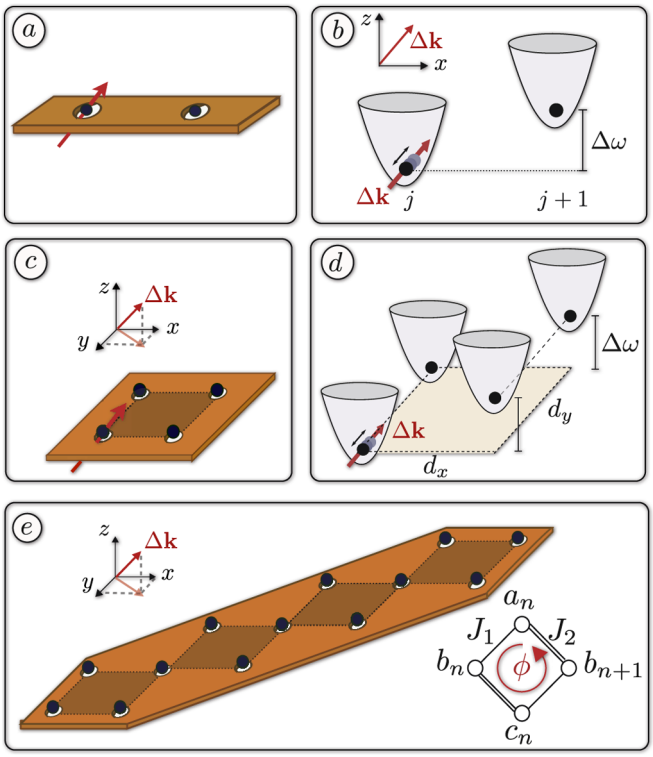


FIG. 1 (color online). Arrangement of ion microtraps: Schematic representation of the microtrap layout for (a) two-ion link, (c) four-ion plaquette, (e) many-ion rhombic ladder [the relevant parameters of the effective Hamiltonian (13) are also shown]. Requirements for the photon-assisted tunneling of phonons: (b) The frequencies of two adjacent traps $\omega_1, \omega_2$ are shifted by $\Delta\omega$. By shining a pair of Raman lasers, one assists the phonon transfer. (d) For a plaquette, the gradient is along $x$ and the $\Delta\mathbf{k}$ has a component along the $x$-$y$-$z$ axes.

$$H_d(\tau) = \sum_{j=1,2} \eta_d \omega_d \cos(\omega_d \tau + \phi_j) a_j^\dagger a_j, \tag{2}$$

where $\tau$ represents the time dependence, $\omega_d$ ($\eta_d \omega_d$) is the driving frequency (strength), and $\phi_j$ a site-dependent phase. We assume that $\omega_1 = \omega$, $\omega_2 = \omega + \Delta\omega$, and $\{\Delta\omega, \eta_d\omega_d\} \ll \omega$; namely, both the frequency difference and driving strength are small perturbations to the trapping frequency. In the absence of driving, the vibrational coupling is

$$H_c = J_c a_2^\dagger a_1 + \text{H.c.}, \tag{3}$$

where $J_c = -\beta\omega$ and $\beta = e^2/M\omega^2 d_x^3$. Equation (3) holds for $|J_c| \ll \omega$, such that the cross terms, $a_1 a_2$, $a_1^\dagger a_2^\dagger$, can be neglected in a rotating-wave approximation (RWA). This condition, which is met for the experiments in [8], allows us to interpret the dynamics as the tunneling of phonons [7].

To understand the effects of driving, we express Eq. (3) in the interaction picture with respect to $H_0(\tau)$, where $a_i(\tau) = a_i e^{-i\omega_i\tau} e^{-i\eta_d \sin(\omega_d\tau+\phi_i)} e^{i\eta_d \sin(\phi_i)}$. After the trivial transformation $a_i e^{i\eta_d \sin(\phi_i)} \to a_i$, one writes $H_c(\tau)$ by replacing the bare Coulomb coupling $J_c$ by a time-dependent dressed coupling

$$J(\tau) = J_c e^{i\Delta\omega\tau} \sum_{s,s'=-\infty}^{\infty} \mathcal{J}_s(\eta_d)\mathcal{J}_{s'}(\eta_d) \times e^{is(\omega_d\tau+\phi_2)} e^{-is'(\omega_d\tau+\phi_1)}, \tag{4}$$

where $\mathcal{J}_s(\eta_d)$ are Bessel functions of the first kind. By choosing the driving frequencies $r\omega_d = \Delta\omega$, with $r = 1, 2, \ldots$, one selects resonant processes that correspond to the absorption or emission of $r$ photons from the classical driving field. If $\Delta\omega \gg J_c$, only the resonant terms must be considered after a RWA, and the effective vibrational coupling can be written as

$$J_{[r]}(\eta_d, \{\phi_n\}) = J_c \mathcal{F}_r(\eta_d, \Delta\phi) e^{-i(r/2)(\phi_1+\phi_2)},$$
$$\mathcal{F}_r(\eta_d, \Delta\phi) = \sum_{s=-\infty}^{\infty} \mathcal{J}_s(\eta_d)\mathcal{J}_{s+r}(\eta_d) e^{i(s+r/2)\Delta\phi}, \tag{5}$$

where $\Delta\phi = \phi_2 - \phi_1$. Since no perturbative assumption is required on the driving strength, the dressed coupling $J_{[r]}$ may be close to the bare one $J_c$. Figure 2(a) shows a calculation of the dressed coupling under different conditions. By tuning $\eta_d$ and $\{\phi_j\}$, one controls the amplitude and phase of the tunneling, which may be enhanced or even completely suppressed. We note that the coherent control of tunneling is interesting on its own [10], and can now be investigated with trapped ions.

*(ii) Synthetic magnetic fields.*—We extend this scheme to different geometries given by the ion equilibrium positions in a 2DAM, separated by $d_x$, $d_y$, and labeled by vectors of integers, $\mathbf{i} = (i_x, i_y)$. In the most general situation, trapping frequencies $\omega_{\alpha,\mathbf{i}}$ depend on the site $\mathbf{i}$ and the spatial direction $\alpha = x, y, z$. The trap potentials, together with a driving term, are

$$H_0(\tau) = \sum_{\mathbf{i},\alpha} \omega_{\alpha,\mathbf{i}} a_{\alpha,\mathbf{i}}^\dagger a_{\alpha,\mathbf{i}} + H_d(\tau). \tag{6}$$

The vibrational couplings between ions in the array arise due to the Coulomb interaction

$$V_c = \frac{e^2}{2} \sum_{\mathbf{i}\neq\mathbf{j}} \frac{1}{|\mathbf{r}_\mathbf{i}^0 - \mathbf{r}_\mathbf{j}^0 + \delta\mathbf{r}_\mathbf{i} - \delta\mathbf{r}_\mathbf{j}|}, \tag{7}$$

where $\mathbf{r}_\mathbf{i}^0$ and $(\delta\mathbf{r}_\mathbf{i})_\alpha = (a_{\alpha,\mathbf{i}} + a_{\alpha,\mathbf{i}}^\dagger)/\sqrt{2M\omega_{\alpha,\mathbf{i}}}$ are the equilibrium positions and relative ion displacements. We assume that the vibrational modes in different directions are not coupled and the phonon number is conserved. The validity of this approximation is quantified below. In the harmonic approximation, that is, up to second order in $\delta\mathbf{r}_\mathbf{i}$, we find

$$H_c = \sum_{\mathbf{i}>\mathbf{j},\alpha} J^{\alpha}_{c;\mathbf{i},\mathbf{j}}(a^{\dagger}_{\alpha,\mathbf{i}}a_{\alpha,\mathbf{j}} + a^{\dagger}_{\alpha,\mathbf{j}}a_{\alpha,\mathbf{i}}),$$

$$J^{\alpha}_{c;\mathbf{i},\mathbf{j}} = -\frac{e^2}{2M\sqrt{\omega_{\alpha,\mathbf{i}}\omega_{\alpha,\mathbf{j}}}}\frac{3(\mathbf{r}^0_{\mathbf{i}-\mathbf{j}})_{\alpha}(\mathbf{r}^0_{\mathbf{i}-\mathbf{j}})_{\alpha} - |\mathbf{r}^0_{\mathbf{i}-\mathbf{j}}|^2}{|\mathbf{r}^0_{\mathbf{i}-\mathbf{j}}|^5}, \quad (8)$$

where $\mathbf{r}^0_{\mathbf{i}-\mathbf{j}} = \mathbf{r}^0_{\mathbf{i}} - \mathbf{r}^0_{\mathbf{j}}$. The assumption of independent vibrations in each direction holds for $|\omega_{\alpha,\mathbf{i}} - \omega_{\beta,\mathbf{j}}|_{\alpha\neq\beta} \gg |J^{\alpha}_{c;\mathbf{i},\mathbf{j}}|$, whereas phonon number conservation is valid if $\omega_{\alpha,\mathbf{i}} \gg |J^{\alpha}_{c;\mathbf{i},\mathbf{j}}|$.

In quantum mechanics, charged particles under electromagnetic fields acquire a phase that depends on the field background. To make a QS of this phenomenon, we focus on the ion motion in direction $\bar{\alpha}$ and choose a linear gradient along $x$, $\omega_{\bar{\alpha},\mathbf{i}} = \omega_{\bar{\alpha}} + \Delta\omega i_x$, together with phases that depend linearly on the position, $\phi_{\mathbf{i}} = \phi_x i_x + \phi_y i_y$. Equation (2) is generalized to $H_d(\tau) = \sum_{\mathbf{i}} \eta_d \omega_d \cos(\omega_d\tau + \phi_{\mathbf{i}})a^{\dagger}_{\bar{\alpha},\mathbf{i}}a_{\bar{\alpha},\mathbf{i}}$. In analogy to the two-ion case, we find that the effective vibrational couplings to leading order in $\eta_d$ [15] are the following:

$$J^{\bar{\alpha}}_{[r];\mathbf{i},\mathbf{j}} = J^{\bar{\alpha}}_{c;\mathbf{i},\mathbf{j}}\mathcal{F}_r(\eta_d, \Delta\phi_{\mathbf{i},\mathbf{j}})e^{-i(r/2)(\phi_{\mathbf{i}}+\phi_{\mathbf{j}})}\delta_{i_x,j_x+1} + J^{\bar{\alpha}}_{c;\mathbf{i},\mathbf{j}}\delta_{i_x,j_x}, \quad (9)$$

where $\Delta\phi_{\mathbf{i},\mathbf{j}} = \phi_{\mathbf{i}} - \phi_{\mathbf{j}}$, and $\delta_{i_x,j_x}$ is the Kronecker delta. The first term describes the photon-assisted tunneling along $x$, whereas the second one is the bare coupling along $y$. A crucial result is that the amplitude of tunneling around a plaquette,

$$W^{\bar{\alpha}}_{\circlearrowleft} = J^{\bar{\alpha}}_{[r];\mathbf{i},\mathbf{i}+\hat{\mathbf{y}}}J^{\bar{\alpha}}_{[r];\mathbf{i}+\hat{\mathbf{y}},\mathbf{i}+\hat{\mathbf{x}}+\hat{\mathbf{y}}}J^{\bar{\alpha}}_{[r];\mathbf{i}+\hat{\mathbf{x}}+\hat{\mathbf{y}},\mathbf{i}+\hat{\mathbf{x}}}J^{\bar{\alpha}}_{[r];\mathbf{i}+\hat{\mathbf{x}},\mathbf{i}} = |W^{\bar{\alpha}}_{\circlearrowleft}|e^{i\phi_{\circlearrowleft}},$$

yields an accumulated phase that depends on the laser parameters $\phi_{\circlearrowleft} = -r\phi_y$ and can be recast in terms of the celebrated Aharonov-Bohm phase [12], $\phi_{\circlearrowleft} = e\oint_{\circlearrowleft} d\mathbf{x}\cdot\mathbf{A}$, where $\oint_{\circlearrowleft}$ is the line integral along the plaquette and $\mathbf{A} = r\phi_y y/(ed_x d_y)\hat{\mathbf{x}}$ is a synthetic vector potential. Accordingly, phonons move as charged particles subjected to a magnetic field perpendicular to the microtrap array and yield a bosonic counterpart of the Azbel-Harper-Hofstadter model [16]. We stress that arbitrary fluxes $\phi_{\circlearrowleft} \in [0, 2\pi)$ can be attained, even reaching one flux quantum per unit cell; a regime inaccessible in solid-state materials for realistic magnetic fields. This opens the possibility to observe a dipolar version of the fractal Hofstadter butterfly, among other interesting effects presented in (iv) and (v).

*(iii) Realization of the periodic driving.*—The simplest setup to realize Eq. (2) would consist of an array of microtraps, where the driving fields are provided by the local control of the electrodes. Since this scheme is yet to be realized and scaled [6,17], we base our alternative approach on state-of-the-art optical forces. We focus on the vibrational modes transverse to the microtrap plane, $\bar{\alpha} = z$, although other schemes along the $x$-$y$ plane are equally valid [18]. We consider lasers that drive two-photon stimulated Raman transitions between the electronic levels of the ions $|0\rangle_{\mathbf{i}}$, $|1\rangle_{\mathbf{i}}$. The lasers are detuned by $\omega_L$ and provide a Raman wave vector $\Delta\mathbf{k}$,

$$H_L = \frac{\Omega_L}{2}\sum_{\mathbf{i}} O_{\mathbf{i}}(e^{i\Delta\mathbf{k}(\mathbf{r}^0_{\mathbf{i}}+\delta\mathbf{r}_{\mathbf{i}})-i\omega_L\tau} + \text{H.c.}), \quad (10)$$

where $\Omega_L$ is the Rabi frequency and $O_{\mathbf{i}}$ is an operator acting on the electronic levels. By a proper choice of the laser detunings and polarizations, one may realize $O_{\mathbf{i}} = \mathbf{1}_{\mathbf{i}}$, or other operators like $O_{\mathbf{i}} = \sigma^z_{\mathbf{i}}$ that widen the applicability of our QS (see the section on outlook). The effect of the ion-laser interaction can be understood as a periodic driving of the microtrap frequencies under the assumptions below. We consider a gradient along $x$, $\omega_{z,\mathbf{i}} = \omega_z + \Delta\omega i_x$, such that the following conditions are fulfilled: $\{\Delta\omega, \omega_L\} \ll \{\omega_{\alpha}, |\omega_{\alpha} - \omega_{\beta}|_{\alpha\neq\beta}\}$. Let us define the Lamb-Dicke parameter along $\alpha$, $\eta_{\alpha} = |\Delta\mathbf{k}_{\alpha}|/\sqrt{2M\omega_{\alpha}}$. In the limit $\eta_{\alpha} \ll 1$, we perform a Taylor expansion of (10) up to second order in $\eta_{\alpha}$, $H_L = H_{L,0} + H_{L,1} + H_{L,2}$. Note that $H_{L,0}$ does not affect the vibrational modes, and $H_{L,1}$ can be neglected if $\Omega_L\eta_{\alpha} \ll \omega_{\alpha}$ in a RWA. This leads to

$$H_{L,2} \approx -\Omega_L\sum_{\alpha,\beta,\mathbf{i}}\eta_{\alpha}\eta_{\beta}O_{\mathbf{i}}\cos(\Delta\mathbf{k}\cdot\mathbf{r}^0_{\mathbf{i}} - \omega_L\tau)a^{\dagger}_{\alpha,\mathbf{i}}a_{\beta,\mathbf{i}}. \quad (11)$$

Finally, by considering $|\omega_{\alpha} - \omega_{\beta}|_{\alpha\neq\beta} \gg \Omega_L\eta^2_{\alpha}$ [18], we neglect the coupling between different directions and get the announced periodic driving presented in Eq. (2) with the following identifications: $\omega_d = \omega_L$, $\eta_d\omega_d = -\Omega_L\eta^2_z$, and $\phi_{\mathbf{i}} = -\Delta\mathbf{k}\cdot\mathbf{r}^0_{\mathbf{i}}$.

Current microtrap design [6,17] is consistent with the above requirements, $\{\omega_{\alpha}, |\omega_{\alpha} - \omega_{\beta}|_{\alpha\neq\beta}\} \gg \{\omega_L, \Delta\omega\} \gg J_{\mathbf{i},\mathbf{j}}$. Typically, $\omega_{\alpha}/2\pi \approx 1$–$10$ MHz, $J/2\pi \approx 5$ kHz. To fit the inequality, we can take $\omega_L/2\pi \approx 50$ kHz. With a typical Lamb-Dicke parameter of $\eta_{\alpha} \approx 0.2$, the condition $\eta_{\alpha}\Omega_L \ll |\omega_{\alpha} - \omega_{\beta}|$ is still fulfilled [18]. In Fig. 2(b), we compare the effective description (5) to the exact optical forces (10) for a two-ion array, with parameters $\Delta\omega = 0.05\omega_z$, $\eta_z = 0.2$, $\Omega_L = 0.75\omega_z$, $\beta = 0.002$, $r = 1$, where the phonon Hilbert space is truncated to $n_{\max} = 4$. We observe an excellent agreement between both descriptions, yielding assisted tunneling for $\Delta\phi \approx \pi$ [10].

*(iv) and (v) Aharonov-Bohm physics in lattices.*—We apply our ideas to a square lattice and set $r = 1$, $|\Delta\mathbf{k}_x|d_x = 2\pi n_x + \phi_x$, $|\Delta\mathbf{k}_y|d_y = 2\pi n_y + \phi_y$, with $n_x, n_y \in \mathbb{Z}$. The latter are introduced because typical ion distances are larger than optical wavelengths. From Eq. (9), we get the tight-binding model,

$$H_{\text{eff}} = \sum_{\mathbf{i}} J^z_{[1];\mathbf{i},\mathbf{i}+\hat{\mathbf{x}}}a^{\dagger}_{\mathbf{i}}a_{\mathbf{i}+\hat{\mathbf{x}}}e^{-i\phi_{\circlearrowleft}i_y} + \sum_{\mathbf{i},m>0} J^z_{c;\mathbf{i},\mathbf{i}+m\hat{\mathbf{y}}}a^{\dagger}_{\mathbf{i}}a_{\mathbf{i}+m\hat{\mathbf{y}}} + \text{H.c.}, \quad (12)$$

where $\phi_\circlearrowleft = \phi_y$ [19]. Note that photon-assisted tunneling along the diagonals has been neglected, since for $\phi_x = 2\pi - \phi_y$ that tunneling amplitude vanishes $\mathcal{F}(\eta_d, 2\pi) = 0$ [Fig. 2(a)]. Additionally, the remaining diagonal terms, $J^z_{[1];\mathbf{i},\mathbf{i}+\hat{\mathbf{x}}+m\hat{\mathbf{y}}}$, are negligible for $m > 1$ due to the fast dipolar decay.

*(iv) Discrete Aharonov-Bohm effect.*—The simplest realization of this tight-binding model consists of a single plaquette [Figs. 1(c) and 1(d)]. In Figs. 2(c) and 2(d), we test the validity of the effective dynamics in (12) by comparing with an exact numerical calculation of the complete driven Hamiltonian (10). These results describe a realization of the discrete Aharonov-Bohm effect with minimal required resources. In Fig. 2(d), we observe that an initial excitation can follow two possible paths, either $1 \leftrightarrow 2 \leftrightarrow 3$ or $1 \leftrightarrow 4 \leftrightarrow 3$, enclosing a net flux $\phi_\circlearrowleft = \pi$. The paths interfere destructively and forbid the phonon to tunnel to site 3. Conversely, in Fig. 2(c), phonons tunnel around the plaquette for $\phi_\circlearrowleft = 0$.

*(v) Aharonov-Bohm cages and flatband physics.*—Let us consider an interesting route beyond the single plaquette, which is the rhombic 3-leg ladder presented in Fig. 1(d). This system is described by the Hamiltonian

$$H = \sum_j J_1(b_j^\dagger a_j + c_j^\dagger b_{j+1}) + J_2(b_j^\dagger c_j + e^{i\phi} a_j^\dagger b_{j+1}) + \text{H.c.}, \tag{13}$$

where we have labeled the boson operators for each leg as $a_j$, $b_j$, $c_j$ [Fig. 1(e)]. This Hamiltonian follows directly from Eq. (12), when the plaquettes are arranged along a diagonal, with $J_1 = e^2/(2md_y^3)$, $J_2 = J_1\mathcal{F}_r(\eta_d, \Delta\phi) \times (d_y/d_x)^3$, and $\phi = \phi_y$, $\phi_x = 2\pi - \phi_y$. This model yields two effects. Because of the Aharonov-Bohm interference for $\phi = \pm\pi$, all the modes of the system are localized and one obtains flat vibrational bands [Fig. 2(e)]. In particular, the nonzero energy modes correspond to the so-called Aharonov-Bohm cages, where phonons are not allowed to tunnel two plaquettes apart [13]. Additionally, one finds the so-called edge states, which are midgap modes exponentially localized around the boundaries. By tuning $\phi$ and $J_2/J_1$, one can explore a transition between two topologically nonequivalent phases [Fig. 2(f)].

Finally, let us consider the experimental requirements for the implementation of our ideas. The duration of a QS to observe the effects of the synthetic gauge fields is of the order of $1/J_{[r]}$, with $J_{[r]}$ being of the order of the bare

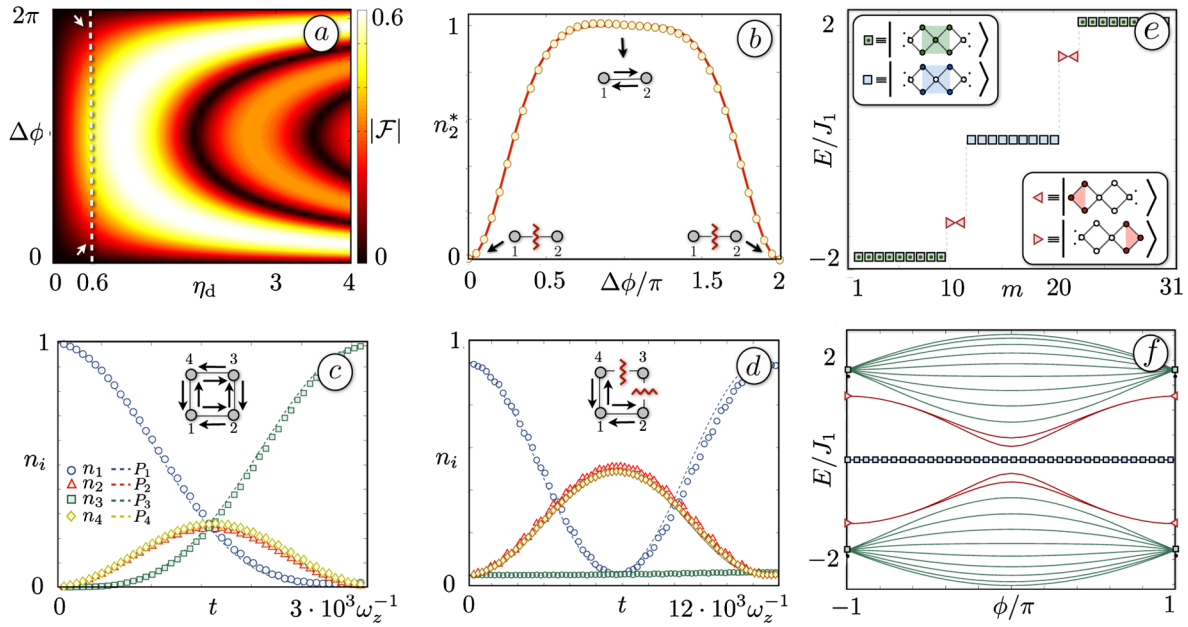


FIG. 2 (color online). Photon-assisted tunneling and Aharonov-Bohm cages. (a) Effective hopping amplitude $|\mathcal{F}_{r=1}|$ as a function of $(\eta_d, \Delta\phi)$. The values of the dashed line at $\eta_d \approx 0.6$ are used in (b). (b) Photon-assisted hopping for a two-ion link of a single vibrational excitation $|\psi_0\rangle = a_1^\dagger|0\rangle$ under the effective description (5) (solid red line) and the complete Hamiltonian (3) with the driving term (10) (yellow dots). We plot the vibrational population $n_2^*$ transferred to site 2 after time $t^* = \pi/|J_{[r]}(0.6, \phi)|$. Maximum phonon transfer occurs at $\Delta\phi = \pi$. (c),(d) Evolution of the phonon excitation in a rectangular plaquette. We plot the phonon populations under approximation (9) $[P_i(t)]$, and under the exact Hamiltonian Eqs. (6)–(8) driven by (10) $[n_i(t)]$. In (c) $\phi_\circlearrowleft = 0$, $\phi_x = \pi$, $\phi_y = 0$, $d_x = d_y|\mathcal{F}_1(\eta_d, \pi)|^{2/3}$, $n_{\max} = 2$, and other parameters same as (b). In (d), $\phi_\circlearrowleft = \pi$, and there is an Aharonov-Bohm destructive interference that inhibits tunneling to site 3. $\phi_x = \pi$, $\phi_y = \pi$, $\Omega_L = 0.25\omega_z$, and other values same as (c). (e) Energy spectrum $E$ for the $\pi$-flux regime of Hamiltonian (13) for $N = 31$ microtraps. Flat bands appear at $E \approx \pm 2J_1$ (Aharonov-Bohm cages) (see also the schematic description of the eigenstates), and also at $E = 0$ (which arise solely due to the geometry of the lattice). Also, in the middle of the gaps, single edge states localized to the boundaries of the ladder arise. (f) Energy level spectrum as a function of the effective flux, which displays a gap-vanishing point at $\phi = 0$.

couplings $J_c$, which are in the range 1–2 kHz [8]. This can be increased to 5 kHz following the trap design [17], and even enhanced by orders of magnitude by further miniaturizing the electrode structure and storing more than one ion per lattice site [8]. The main competing decoherence mechanism is heating of the motional modes [2]. Heating rates as low as 0.07 phonons/ms have been reported in cryogenic traps [8], in principle allowing us to implement our ideas. Even when heating rates are comparable to couplings $J_{[r]}$, they may induce a thermal background over which propagation of vibrational excitations may still be observed [8]. Note that experimental techniques are available for preparation and measurement of phonon states [20]. Also, the vibrational spectrum can be measured without local addressing in the ions' fluorescence sidebands [2].

*Conclusions and outlook.*—We have presented a proposal to induce synthetic gauge fields for ions in microtrap arrays, which is based on the photon-assisted tunneling of vibrational excitations. By considering trap designs with anharmonicities, effective phonon-phonon interactions can be included [7], which may allow us to study strongly correlated phases. Inducing electronic state-dependent drivings, one gets effective spin-orbit couplings that induce disorder [21]. Also, by adding dissipation, i.e., motional heating, one may study quantum effects in energy transport in the presence of noise [22]. These ingredients make a versatile QS of many-body physics, which would outperform classical computers for $\approx 10$ ions and $\approx 4$ phonons per ion. That size seems feasible in the near future in view of current experimental progress [6]. Finally, our scheme could be extended to other systems such as photons in arrays of cavities in circuit QED [23].

This work was partially supported by EU STREPs (HIP, PICC), and by QUITEMAD S2009-ESP-1594, FIS2009-10061, CAM-UCM/910758, and RyC Contract No. Y200200074.

[1] R. Feynman, Int. J. Theor. Phys. **21**, 467 (1982).
[2] D. Leibfried *et al.*, Rev. Mod. Phys. **75**, 281 (2003).
[3] D. Porras and J. I. Cirac, Phys. Rev. Lett. **92**, 207901 (2004); A. Friedenauer *et al.*, Nature Phys. **4**, 757 (2008); K. Kim *et al.*, Nature (London) **465**, 590 (2010); E. E. Edwards *et al.*, Phys. Rev. B **82**, 060410 (2010).
[4] J. T. Barreiro *et al.*, Nature (London) **470**, 486 (2011).
[5] R. Islam *et al.*, Nature Commun. **2**, 377 (2011).
[6] T. Schaetz *et al.*, J. Mod. Opt. **54**, 2317 (2007); J. Chiaverini and W. E. Lybarger, Phys. Rev. A **77**, 022324 (2008); J. Labaziewicz *et al.*, Phys. Rev. Lett. **100**, 013001 (2008).
[7] D. Porras and J. I. Cirac, Phys. Rev. Lett. **93**, 263602 (2004).
[8] K. R. Brown *et al.*, Nature (London) **471**, 196 (2011); M. Harlander *et al.*, Nature (London) **471**, 200 (2011).
[9] D. Jaksch *et al.*, New J. Phys. **5**, 56 (2003); see also J. Dalibard *et al.*, arXiv:1008.5378 [Rev. Mod. Phys. (to be published)], and references therein.
[10] M. Grifoni *et al.*, Phys. Rep. **304**, 229 (1998).
[11] A. Eckardt, C. Weiss, and M. Holthaus, Phys. Rev. Lett. **95**, 260404 (2005); C. E. Creffield and T. S. Monteiro, Phys. Rev. Lett. **96**, 210403 (2006); H. Lignier *et al.*, Phys. Rev. Lett. **99**, 220403 (2007); E. Kierig *et al.*, Phys. Rev. Lett. **100**, 190405 (2008).
[12] Y. Aharonov *et al.*, Phys. Rev. **115**, 485 (1959).
[13] J. Vidal, R. Mosseri, and B. Doucot, Phys. Rev. Lett. **81**, 5888 (1998); J. Vidal *et al.*, Phys. Rev. Lett. **85**, 3906 (2000).
[14] M. Z. Hasan *et al.*, Rev. Mod. Phys. **82**, 3045 (2010).
[15] This can be extended straightforwardly to any order of the driving parameter $\eta_d$. See A. Bermudez *et al.* (to be published).
[16] M. Ya. Azbel', Zh. Eksp. Teor. Fiz. **46**, 929 (1964) [Sov. Phys. JETP **19**, 634 (1964)].P. G. Harper, Proc. Phys. Soc. London Sect. A **68**, 874 (1955); D. R. Hofstadter, Phys. Rev. B **14**, 2239 (1976).
[17] R. Schmied, J. H. Wesenberg, and D. Leibfried, Phys. Rev. Lett. **102**, 233002 (2009); C. Schneider *et al.*, arXiv:1106.2597.
[18] An effective Raman wave vector along $\hat{z}$ may be obtained without illuminating the trap surface by choosing the trapping axis $\hat{z}$ to be tilted with respect to the surface.
[19] We ignore the $x$ dependence of $\mathbf{A}$ since it may be gauged away by the transformation $a_{\mathbf{i}} \rightarrow a_{\mathbf{i}} e^{-i\chi_{\mathbf{i}}}$, with $\chi_{\mathbf{i}} = \phi_x i_x^2/2$.
[20] D. M. Meekhof *et al.*, Phys. Rev. Lett. **77**, 2346(E) (1996).
[21] A. Bermudez *et al.*, New J. Phys. **12**, 123016 (2010).
[22] M. B. Plenio *et al.*, New J. Phys. **10**, 113019 (2008).
[23] S. Schmidt *et al.*, Phys. Rev. B **82**, 100507(R) (2010).

New Journal of Physics
The open-access journal for physics

# Photon-assisted-tunneling toolbox for quantum simulations in ion traps

**Alejandro Bermudez**[1,5], **Tobias Schaetz**[2,3] **and Diego Porras**[4]

[1] Institut für Theoretische Physik, Albert-Einstein Allee 11, Universität Ulm, 89069 Ulm, Germany
[2] Max-Planck-Institut für Quantenoptik, Hans-Kopfermann-Strasse 1, D-85748 Garching, Germany
[3] Physikalisches Institut, Albert-Ludwigs-Universität Freiburg, Hermann-Herder-Strasse 3, 79104 Freiburg, Germany
[4] Departamento de Física Teórica I, Universidad Complutense, 28040 Madrid, Spain
E-mail: bermudez.carballo@gmail.com

*New Journal of Physics* **14** (2012) 053049 (31pp)
Received 28 January 2012
Published 31 May 2012
Online at http://www.njp.org/
doi:10.1088/1367-2630/14/5/053049

**Abstract.** We describe a versatile toolbox for the quantum simulation of many-body lattice models, capable of exploring the combined effects of background Abelian and non-Abelian gauge fields, bond and site disorder and strong on-site interactions. We show how to control the quantum dynamics of particles trapped in lattice potentials by the photon-assisted tunneling induced by periodic drivings. This scheme is general enough to be applied to either bosons or fermions with the additional advantage of being non-perturbative. It finds an ideal application in microfabricated ion trap arrays, where the quantized vibrational modes of the ions can be described by a quantum lattice model. We present a detailed theoretical proposal for a quantum simulator in that experimental setup, and show that it is possible to explore phases of matter that range from the fractional quantum Hall effect, to exotic strongly correlated glasses or flux-lattice models decorated with arbitrary patterns of localized defects.

[5] Author to whom any correspondence should be addressed.

## Contents



## 1. Introduction

In general, quantum many-body systems cannot be understood by extrapolating the properties of their individual constituents [1], but rather by considering their rich collective behavior. A prototypical example is that of sound waves in solids [2], where the atoms do not move individually but vibrate collectively and give rise to propagating quasiparticles, the so-called phonons. This particular many-body problem is exceptional since the properties of the phonons can be calculated exactly, something that rarely occurs in quantum many-body systems. The usual paradigm is that the complexity of the model grows very fast with the number of particles, making both analytical and numerical methods more involved and less efficient. A radically different approach is based on the so-called *experimental quantum simulations*, which were envisaged several decades ago by R P Feynman [3] and have now evolved into a discipline that merges concepts from atomic physics, quantum optics, quantum-information science and condensed-matter physics. The central idea of a quantum simulation is to manipulate the microscopic properties of a particular experimental setup in a way that it faithfully reproduces a quantum many-body model under study. In this way, nature itself computes the properties of the model, and our measurements yield the answer to questions such as the nature of the ground-state and collective excitations, determining whether a dedicated model is sufficient for describing the relevant properties of a particular system. Accordingly, quantum simulations have the potential for solving fundamental open problems in physics, ranging from high-temperature superconductivity, to the thermalization of closed quantum systems or the properties of spin glasses.

Imagine for a moment that the phonons in a solid were controllable to such an extent that their Hamiltonian could be engineered to target a many-body model of interest. For instance, by shaping the crystal anharmonicities, one could tune the phonon–phonon interactions and reproduce the physics of strongly correlated models. Unfortunately, it is hard to develop techniques that allow such microscopic control in solid-state materials, and it might be beneficial to search for different experimental platforms. This exotic idea may become realized in

experiments with Coulomb crystals of cold atomic ions in radio-frequency traps [4]. Current experimental tools allow for a promising control of the vibrational excitations at the quantum level, such that phonon-based quantum simulations of many-body physics may become a reality [5, 6].

So far, the most exploited property of the vibrational excitations of trapped ions is their ability to transfer information between distant ions, which encode quantum bits (qubits) in their electronic states. This provides a mechanism to perform quantum logic operations between distant qubits, a fundamental building block of quantum-information protocols [7] (for a review, see [8] and references therein). This type of two-qubit couplings can be interpreted as a spin–spin interaction where the qubit plays the role of a pseudospin (henceforth referred to as spin) [9] and can be exploited for quantum-simulation purposes. From this perspective, the phonons act as mediators of the interaction and give rise to a wide range of spin models [10], which are familiar in the field of quantum magnetism. The experimental success of these spin-based quantum simulations, either in an analogue [11] or digital version [12], has motivated a variety of proposals that range from neural networks [13], to three-body interactions [14], frustrated magnetism [15], mixed-spin models [16] or topologically ordered spin models [17].

Instead of using the phonons as a gadget to obtain the desired quantum-spin simulator, one can substantially enhance the capabilities by reclaiming phonons as the building blocks for the quantum simulation of many-body models [5]. The local vibrational excitations of each atomic ion, considered to be trapped individually, correspond to bosonic quasiparticles, and the Coulomb interaction is responsible for the interchange of these bosons between distant ions. To build interesting bosonic quantum simulators, one must complement the aforementioned scheme with additional ingredients, such as strong trapping nonlinearities that lead to Mott insulating [5] and frustrated phases [18], or incommensurate trapping potentials leading to different quantum-phase transitions [19]. Besides, the spins of the ions can be used as a tool to widen the applicability of this quantum simulator, which can potentially target the spin-boson model [20], the lattice Jaynes–Cummings model [21] or the phenomenon of Anderson localization due to disorder [22]. In addition to these many-body quantum simulations, there has also been a recent activity in building analogues of single-particle phenomena with a special emphasis on relativistic effects (see, e.g., [23]). In this case, even if the models are tractable on a classical computer, the predicted effects are hard to access in the original experiments and thus justify the effort at building a trapped-ion analogue.

In this paper, we introduce a versatile toolbox for the quantum simulation of many-body lattice models. This toolbox is based on the phenomenon of *photon-assisted tunneling* (PAT) of phonons in ion traps [24], but can also be applied to different systems of bosons, and even fermions, in a lattice. As shown in the present paper, the PAT effect has a variety of facets that can be exploited to provide new paradigms for the aforementioned many-body quantum simulation. The idea underlying the PAT is that the tunneling of particles between the wells of a periodic lattice can be assisted by inducing resonances that correspond to the absorption/emission of photons out of an electromagnetic (EM) field providing a periodic driving force. Even though this idea was initially introduced for condensed-matter systems [25] (see [26] and references therein), it has also been applied in the field of ultracold atoms in optical lattices [27]. Here, the analogy is straightforward since the neutral atoms can tunnel between the adjacent wells of a driven periodic potential created by light. In this work, we show how to exploit the PAT to induce synthetic gauge fields in the aforementioned many-body lattice models.

In the context of trapped ions, a possibility of controlling the tunneling of the vibrational excitations between ions stored in two separate potential minima, aligned within a linear radio-frequency trap, has recently been demonstrated [28]. The exchange of phonons between two ions can be controlled and optimized by matching their individual trapping frequencies. Building on these seminal experiments, we have demonstrated theoretically that driving the trapping frequencies in/out of resonance realizes a novel version of the PAT paradigm [24]. Rather than relying on a periodic force [25, 27] scaled to a larger number of ions, which may be quite demanding in trapped-ion experiments, our scheme relies on the periodic modulation of the trapping frequencies. In particular, it requires an additional relative phase between the individual modulations that can be experimentally tuned. This allows for the full control of both the amplitude and the phase of the tunneling of phonons, a result that becomes especially interesting for two-dimensional (2D) arrays of micro-fabricated traps [29]. Here, the technology of ion-trap micro-fabrication provides a means of assembling arrays of ion traps in any desired geometry [30]. The combination of the capabilities for the design and fabrication of arrays of microtraps with the tool of PAT [24] opens up a great deal of possibilities for a quantum simulator of many-body physics. These range from the realization of bosonic models subjected to *Abelian and non-Abelian synthetic gauge field*s, to bond and site disorder leading to *glassy phases* or to decorated flux lattices that can be related to *anyonic excitations*. In this paper, we provide a detailed analysis of such PAT in arrays of microtraps.

The paper is organized as follows. The main results are summarized in section 4, so this section can be consulted for a general overview. The general scheme of PAT for any lattice model is introduced in section 2, where we demonstrate how the synthetic gauge field arises from the assisted tunneling. Its application as a toolbox for quantum simulations with trapped ions is presented in section 3. Here, we present a thorough description of the different many-body models that can be explored by exploiting the peculiarities of trapped ions, which widen the versatility of our quantum simulator.

## 2. Photon-assisted tunneling (PAT) and synthetic gauge fields

In this section, we describe the concept of PAT for a general system, and discuss how it can be exploited for the quantum simulation of lattice models incorporating synthetic gauge fields. Once the main ingredients are identified, we focus on the case of ions in micro-fabricated traps in section 3 and show how to implement the PAT for the vibrational excitations. Let us remark that the generality of this section may also find applications in different platforms, such as photons in arrays of cavities in circuit quantum electrodynamics (QED) [31] or ultracold atoms in optical lattices [32]. We also note that the PAT scheme is not restricted to bosons, but works equally well for fermions. This may alleviate some of the difficulties that arise in the simulation of synthetic gauge fields via Raman-assisted tunneling of fermionic atoms in spin-dependent optical lattices ([33] and references therein).

We consider a tight-binding model describing the tunneling of particles, either bosons or fermions, between the sites of an underlying 2D lattice. The lattice sites are characterized by a vector of integer numbers $\mathbf{i} = (i_1, i_2)$, such that $\mathbf{r}_{\mathbf{i}}^0 = i_1 d_1 \mathbf{e}_1 + i_2 d_2 \mathbf{e}_2$, where $\{\mathbf{e}_\alpha\}$ are the unit vectors spanning the lattice, and $\{d_\alpha\}$ are the corresponding lattice constants. The particles are represented by bosonic or fermionic creation–annihilation operators $a^\dagger_{\sigma,\mathbf{i}}$, $a_{\sigma,\mathbf{i}}$, where $\sigma$ labels some additional degrees of freedom. The dynamics of the system is described by the following

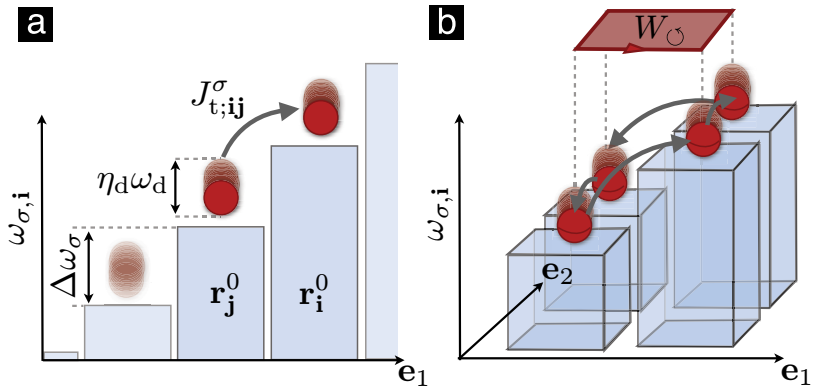


**Figure 1.** PAT scheme. (a) Scheme for the driven 1D tight-binding model in equations (1) and (4). The tunneling of the particles between neighboring sites $\mathbf{r}^0_{\mathbf{j}} \to \mathbf{r}^0_{\mathbf{i}}$, which is initially suppressed by the large gradient $\Delta\omega_{\sigma} \gg J^{\sigma}_{\mathrm{t};\mathbf{ij}}$, gets assisted by a resonant periodic modulation of the on-site energies with amplitude $\eta_{\mathrm{d}}\omega_d$. (b) 2D scheme giving rise to a synthetic gauge field such that the path around an elementary plaquette $W_{\circlearrowleft} \propto \mathrm{e}^{\mathrm{i}\phi_{\circlearrowleft}}$ mimics the Aharonov–Bohm phase, which is picked up by a charged particle following the path around a plaquette pierced by an external magnetic field orthogonal to the lattice.

Hamiltonian:

$$H = H_0 + H_{\mathrm{t}} = \sum_{\sigma,\mathbf{i}} \omega_{\sigma,\mathbf{i}} a^{\dagger}_{\sigma,\mathbf{i}} a_{\sigma,\mathbf{i}} + \sum_{\sigma} \sum_{\mathbf{i}>\mathbf{j}} (J^{\sigma}_{\mathrm{t};\mathbf{ij}} a^{\dagger}_{\sigma,\mathbf{i}} a_{\sigma,\mathbf{j}} + \mathrm{H.c.}), \tag{1}$$

where $\omega_{\sigma,\mathbf{i}}$ stands for the on-site energy ($\hbar = 1$), and $J^{\sigma}_{\mathrm{t};\mathbf{ij}}$ is the tunneling amplitude of the particles between different lattice sites $\mathbf{j} \to \mathbf{i}$, which usually depends on the distance between sites such that $J^{\sigma}_{\mathrm{t};\mathbf{ij}} = J^{\sigma}_{t}(|\mathbf{r}^0_{\mathbf{i}} - \mathbf{r}^0_{\mathbf{j}}|)$. The tunneling constraint $\mathbf{i} > \mathbf{j}$ refers to an ordering of the sites, such that $i_1 > j_1$ or $i_2 > j_2$ if $i_1 = j_1$. Two additional ingredients are required:

(i) Gradient of the on-site energies: the on-site energies have the following expression: $\omega_{\sigma,\mathbf{i}} = \omega_{\sigma} + \Delta\omega_{\sigma} i_1$. Here, $\omega_{\sigma}$ is a constant energy offset, and $\Delta\omega_{\sigma}$ results due to a gradient along one of the lattice principal axes satisfying

$$J^{\sigma}_{\mathrm{t};\mathbf{ij}} \ll \Delta\omega_{\sigma}. \tag{2}$$

(ii) Periodic modulation of the on-site energies: the on-site energies must be supplemented with the periodic modulation $\omega_{\sigma,\mathbf{i}} \to \omega_{\sigma,\mathbf{i}} + \eta_{\mathrm{d}}\omega_{\mathrm{d}} \cos(\omega_{\mathrm{d}} t + \phi_{\mathbf{i}})$, where $\omega_{\mathrm{d}}$ is the driving frequency and $\eta_{\mathrm{d}}\omega_d$ the driving amplitude. Note that the periodic driving incorporates a site-dependent phase $\phi_{\mathbf{i}}$ that shall play a crucial role in the PAT and is described by

$$\phi_{\mathbf{i}} = \phi_1 i_1 + \phi_2 i_2. \tag{3}$$

These two ingredients, schematically represented in figure 1(a), are incorporated into the above description by modifying the Hamiltonian $H_0 \to H_0(t)$ as follows:

$$H_0(t) = \sum_{\sigma,\mathbf{i}} (\omega_{\sigma} + \Delta\omega_{\sigma} i_1 + \eta_{\mathrm{d}}\omega_{\mathrm{d}} \cos(\omega_{\mathrm{d}} t + \phi_{\mathbf{i}})) a^{\dagger}_{\sigma,\mathbf{i}} a_{\sigma,\mathbf{i}}. \tag{4}$$

Let us emphasize again that the standard formulation of the PAT relies on a periodic force acting on the particles residing on the lattice sites [25, 27]. In contrast, our scheme considers a periodic modulation of the on-site energies, which turns out to be better suited for tailoring the tunneling amplitudes in analogy with a background synthetic gauge field. In section 2.1, we present an analytical model, which is contrasted with numerical simulations in section 2.2.

### *2.1. Analytical description*

*2.1.1. Dressed tunneling.* In this subsection, we derive a compact expression for the PAT strength and study its dependence on the periodic-driving parameters. Let us express the tunneling Hamiltonian $H_{\rm t}$ in the interaction picture with respect to $H_0(t)$, namely $H_{\rm t}(t) = U(t)^{\dagger} H_t U(t)$, where $U(t) = {\rm e}^{-{\rm i}\int_0^t {\rm d}\tau H_0(\tau)}$. In this picture, the annihilation operators fulfill

$$ {\rm i}\frac{{\rm d}a_{\sigma,\mathbf{i}}}{{\rm d}t} = (\omega_\sigma + \Delta\omega_\sigma i_1 + \eta_{\rm d}\omega_{\rm d}\cos(\omega_{\rm d}t + \phi_{\mathbf{i}}))a_{\sigma,\mathbf{i}}, \tag{5} $$

which leads to the following relation between both pictures:

$$ a_{\sigma,\mathbf{i}}(t) = {\rm e}^{-{\rm i}(\omega_\sigma + \Delta\omega i_1)t}{\rm e}^{-{\rm i}\eta_{\rm d}\sin(\omega_{\rm d}t+\phi_{\mathbf{i}})}{\rm e}^{+{\rm i}\eta_{\rm d}\sin(\phi_{\mathbf{i}})}a_{\sigma,\mathbf{i}}. \tag{6} $$

At this point, we note that the tunneling Hamiltonian $H_{\rm t}$ is invariant under U(1) gauge transformations, and thus, the last term in the above expression can be trivially gauged away $a_{\sigma,\mathbf{i}} \to {\rm e}^{-{\rm i}\eta_d sin(\phi_{\mathbf{i}})}a_{\sigma,\mathbf{i}}$. Accordingly, the Hamiltonian becomes $H_{\rm t}(t) = \sum_{\mathbf{i}>\mathbf{j}} J^{\sigma}_{{\rm d};\mathbf{ij}}(t)a^{\dagger}_{\sigma,\mathbf{i}}a_{\sigma,\mathbf{j}} + {\rm H.c.}$, where $J^{\sigma}_{{\rm d};\mathbf{ij}}(t) = J^{\sigma}_{t;\mathbf{ij}}\Theta(t)$, and the time dependence is encoded in the function

$$ \Theta(t) = \begin{cases} {\rm e}^{{\rm i}\eta_{\rm d}(\sin(\omega_{\rm d}t+\phi_{\mathbf{i}})-\sin(\omega_{\rm d}t+\phi_{\mathbf{j}}))}{\rm e}^{{\rm i}\Delta\omega_\sigma(i_1-j_1)t} & \text{if } i_1 > j_1, \\ {\rm e}^{{\rm i}\eta_{\rm d}(\sin(\omega_{\rm d}t+\phi_{\mathbf{i}})-\sin(\omega_{\rm d}t+\phi_{\mathbf{j}}))} & \text{if } i_1 = j_1. \end{cases} \tag{7} $$

In this expression, one readily observes that the tunneling amplitude becomes dressed by the photons of the periodic driving $J^{\sigma}_{{\rm t};\mathbf{ij}} \to J^{\sigma}_{{\rm d};\mathbf{ij}}(t)$. Besides, the fundamental role of the phase of the periodic driving also becomes apparent: only when $\phi_{\mathbf{i}} \neq \phi_{\mathbf{j}}$, the tunneling becomes assisted $J^{\sigma}_{{\rm d};\mathbf{ij}}(t) \neq J^{\sigma}_{t;\mathbf{ij}}$. In order to proceed with this analytical treatment, we use the identity

$$ {\rm e}^{{\rm i}\eta_{\rm d}\sin(\omega_{\rm d}t+\phi_{\mathbf{i}})} = \sum_{s\in\mathbb{Z}} J_s(\eta_{\rm d}){\rm e}^{{\rm i}s(\omega_{\rm d}t+\phi_{\mathbf{i}})}, \tag{8} $$

where $J_s(\eta_{\rm d})$ are Bessel functions of the first class [34]. Hence, the dressed tunneling becomes a sum of terms with different time dependences. Let us first focus on the tunneling along the gradient, $i_1 > j_1$, which can be expressed as follows:

$$ J^{\sigma}_{{\rm d};\mathbf{ij}}(t) = J^{\sigma}_{{\rm t};\mathbf{ij}}\sum_{s,s'\in\mathbb{Z}} J_s(\eta_{\rm d})J_{s'}(\eta_{\rm d}){\rm e}^{{\rm i}\Delta\omega_\sigma(i_1-j_1)t}{\rm e}^{{\rm i}\left((s-s')\omega_{\rm d}t+s\phi_{\mathbf{i}}-s'\phi_{\mathbf{j}}\right)}. \tag{9} $$

By tuning the driving frequency to $\omega_{\rm d} = \Delta\omega_\sigma/r$, where $r$ is some positive integer, the above expression contains two different types of terms. There are resonant terms fulfilling

$$ s' = s + r(i_1 - j_1), \tag{10} $$

whereas the remaining terms are far off-resonance. By applying a rotating-wave approximation (RWA) for $J^{\sigma}_{{\rm t};\mathbf{ij}} \ll \Delta\omega_\sigma$ (2), we neglect the rapidly oscillating terms yielding

$$ J^{\sigma}_{{\rm d};\mathbf{ij}} = J^{\sigma}_{{\rm t};\mathbf{ij}}\sum_{s\in\mathbb{Z}} J_s(\eta_{\rm d})J_{s+r(i_1-j_1)}(\eta_{\rm d}){\rm e}^{{\rm i}\left(s\phi_{\mathbf{i}}-(s+r(i_1-j_1))\phi_{\mathbf{j}}\right)}. \tag{11} $$

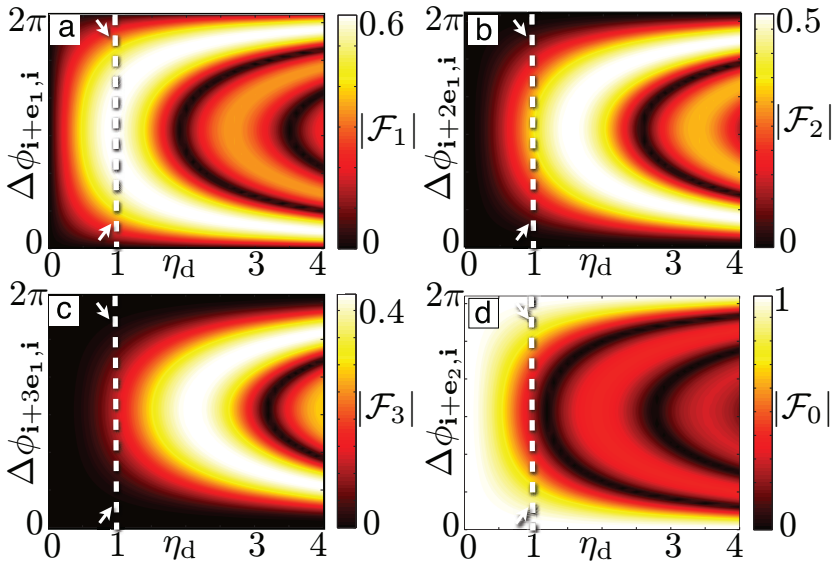


**Figure 2.** Photon-assisted modulation of the tunneling amplitude: contour plot of the modulation amplitude $|\mathscr{F}_{r(i_1-j_1)}|$ for the tunneling between sites $\mathbf{i}\to\mathbf{j}$, such that $i_1 > j_1$, as a function of the driving parameters $\eta_d$, $\Delta\phi_{\mathbf{ij}}$ for $r = 1$. (a) First-neighbor-assisted tunneling ($\mathbf{i}\to\mathbf{i}+\mathbf{e}_1$). (b) Second-neighbor-assisted tunneling ($\mathbf{i}\to\mathbf{i}+2\mathbf{e}_1$). (c) Third-neighbor-assisted tunneling ($\mathbf{i}\to\mathbf{i}+3\mathbf{e}_1$). (d) First-neighbor-assisted tunneling orthogonal to the gradient $\mathbf{i}\to\mathbf{i}+\mathbf{e}_2$.

According to this expression, both the amplitude and the phase of the tunneling are controlled by the periodic driving parameters. As shown in section 3, the periodic driving can be achieved by means of optical dipole forces on the ions, and the tunneling along the $\mathbf{e}_1$-axis is thus assisted by the absorption/emission of $r(i_1 - j_1)$ photons from the EM field providing the driving force, hence the name PAT. A similar analysis for the tunneling orthogonal to the gradient, $i_1 = j_1$, shows that the resonant terms satisfy $s' = s$.

The complete assisted-tunneling Hamiltonian becomes

$$H_{\text{eff}} = \sum_{\sigma}\sum_{\mathbf{i}>\mathbf{j}} J^{\sigma}_{\text{d};\mathbf{ij}} a^{\dagger}_{\sigma,\mathbf{i}} a_{\sigma,\mathbf{j}} + \text{H.c.}, \tag{12}$$

with the dressed couplings expressed as follows:

$$J^{\sigma}_{\text{d};\mathbf{ij}} = J^{\sigma}_{\text{t};\mathbf{ij}} \mathscr{F}_{f(\mathbf{i},\mathbf{j})}(\eta_d, \eta_d, \Delta\phi_{\mathbf{ij}}) e^{-i\frac{f(\mathbf{i},\mathbf{j})}{2}(\phi_{\mathbf{i}}+\phi_{\mathbf{j}})}, \tag{13}$$

where the function $\mathscr{F}$ is responsible for the modulation of the tunneling amplitude

$$\mathscr{F}_{\chi}(\zeta,\xi,\theta) = \sum_{s\in\mathbb{Z}} J_s(\zeta) J_{s+\chi}(\xi) e^{i(s+\frac{\chi}{2})\theta}, \tag{14}$$

and we have defined the phase difference $\Delta\phi_{\mathbf{ij}} = \phi_{\mathbf{i}} - \phi_{\mathbf{j}}$ and the function $f(\mathbf{i},\mathbf{j}) = r(i_1 - j_1)$.

Let us emphasize one of the important properties of this photon-assisted scheme, namely its non-perturbative character. So far, we have not used any restriction on the values of $\eta_d$ or $\phi_{\mathbf{i}}$, so that the dressed tunneling $J_d$ may be of the same order as the bare one $J_t$. In figure 2, we

represent the modulation function $\mathscr{F}_{f(\mathbf{i},\mathbf{j})}(\eta_d, \eta_d, \Delta\phi_{\mathbf{ij}})$ for different periodic-driving parameters, and different ranges of tunneling. In particular, figures 2(a)–(c) represent the tunneling along the direction of the gradient for $r = 1$, whereas figure 2(d) stands for the tunneling orthogonal to the gradient. As derived from figure 2(a), for $\eta_d \approx 1$, $\Delta\phi = \pi$, one gets the maximal amplitude for the assisted tunneling between nearest neighbors. In particular, we find $|\mathscr{F}_1| \approx 0.6$ for these optimal values, which thus supports our previous claim about the non-perturbative nature of the scheme (i.e. $|J^{\sigma}_{d;\mathbf{i}+\mathbf{e}_1,\mathbf{i}}| \approx 0.6|J^{\sigma}_{t;\mathbf{i}+\mathbf{e}_1,\mathbf{i}}|$). It is also interesting to note that, as we consider longer-range terms, their amplitude gets gradually diminished, as shown in figures 2(b)–(c). In figure 2(d), we represent the modulation amplitude in the direction perpendicular to the gradient, which taking the same parameters as above leads to $|J^{\sigma}_{d;\mathbf{i}+\mathbf{e}_2,\mathbf{i}}| \approx 0.2|J^{\sigma}_{t;\mathbf{i}+\mathbf{e}_2,\mathbf{i}}|$.

Before concluding this subsection, we briefly comment on another interesting property of this scheme. Let us consider that the original Hamiltonian (1) also contains on-site particle–particle interactions $H + V$, where

$$V = \sum_{\sigma\sigma'} \sum_{\mathbf{i}} U_{\sigma\sigma'} a^{\dagger}_{\sigma,\mathbf{i}} a^{\dagger}_{\sigma',\mathbf{i}} a_{\sigma',\mathbf{i}} a_{\sigma,\mathbf{i}}, \tag{15}$$

and the dependence of the interaction strengths $U_{\sigma\sigma'}$ on the internal indices depends on the bosonic/fermionic nature of the particles. It is straightforward to see that the gradient and periodic driving do not modify $V$. Therefore, the PAT also works in the presence of on-site interactions. It would be interesting to study how the scheme can be used to modify long-range interactions, but this is beyond the scope of the present work.

*2.1.2. Synthetic gauge fields.* In this subsection, we demonstrate that it is possible to interpret the phase of the dressed tunneling (13) as if it was originated by a background gauge field. In particular, we show that whenever particles tunnel along a closed path in the lattice, they pick up a non-vanishing phase analogous to the celebrated Aharonov–Bohm phase for charged particles in electromagnetic fields [35]. The consecutive tunneling of a particle around a unit plaquette of the lattice $\mathbf{i} \to \mathbf{i}+\mathbf{e}_1 \to \mathbf{i}+\mathbf{e}_1+\mathbf{e}_2 \to \mathbf{i}+\mathbf{e}_2 \to \mathbf{i}$ (figure 1(b)) is formally given by

$$W^{(1)}_{\circlearrowleft} = J^{\sigma}_{d;\mathbf{i},\mathbf{i}+\mathbf{e}_2} J^{\sigma}_{d;\mathbf{i}+\mathbf{e}_2,\mathbf{i}+\mathbf{e}_1+\mathbf{e}_2} J^{\sigma}_{d;\mathbf{i}+\mathbf{e}_1+\mathbf{e}_2,\mathbf{i}+\mathbf{e}_1} J^{\sigma}_{d;\mathbf{i}+\mathbf{e}_1,\mathbf{i}}. \tag{16}$$

By using equations (7) and (13), it can be expressed as

$$W^{(1)}_{\circlearrowleft} = |J^{\sigma}_{t}(d_2) J^{\sigma}_{t}(d_1) \mathscr{F}_0(\eta_d, \eta_d, \phi_2) \mathscr{F}_r(\eta_d, \eta_d, \phi_1)|^2 e^{ir\phi_2}, \tag{17}$$

which leads to $W^{(1)}_{\circlearrowleft} = |W^{(1)}_{\circlearrowleft}| e^{i\phi_{\circlearrowleft}}$, where $\phi_{\circlearrowleft} = r\phi_2$ only depends on the component of the periodic-driving phase that is orthogonal to the gradient. This quantity is a gauge-invariant observable proportional to the so-called Wilson loop in lattice gauge theories [36], which can be expressed as follows:

$$W^{(1)}_{\circlearrowleft} \propto e^{ie^* \oint_{\circlearrowleft} d\mathbf{r}\cdot\mathbf{A}_s} = e^{ie^* \int_{\square} \mathbf{B}_s \cdot d\mathbf{S}}. \tag{18}$$

Here, we have introduced an effective charge $e^*$ independent of the charged/neutral character of the particles, the synthetic gauge potential $\mathbf{A}_s$ and the synthetic gauge field $\mathbf{B}_s$. Independently of how we rearrange the phases of the tunneling strengths locally, the enclosed phase $\phi_{\circlearrowleft} = e^* \int_{\square} \mathbf{B}_s \cdot d\mathbf{S}$ shall always be left invariant and can be thus interpreted as the magnetic flux of a synthetic magnetic field $\mathbf{B}_s$ that pierces the lattice. In order for this analogy to be complete, one should consider carefully the long-range character of the tunneling, according to which

particles can follow different closed paths. We shall explore the two possible paths around the second smallest plaquettes, namely

$$W^{(2)}_{\circlearrowleft} = J^{\sigma}_{\mathrm{d};\mathbf{i},\mathbf{i}+2\mathbf{e}_2} J^{\sigma}_{\mathrm{d};\mathbf{i}+2\mathbf{e}_2,\mathbf{i}+\mathbf{e}_1+2\mathbf{e}_2} J^{\sigma}_{\mathrm{d};\mathbf{i}+\mathbf{e}_1+2\mathbf{e}_2,\mathbf{i}+\mathbf{e}_1} J^{\sigma}_{\mathrm{d};\mathbf{i}+\mathbf{e}_1,\mathbf{i}},$$
$$W'^{(2)}_{\circlearrowleft} = J^{\sigma}_{\mathrm{d};\mathbf{i},\mathbf{i}+\mathbf{e}_2} J^{\sigma}_{\mathrm{d};\mathbf{i}+\mathbf{e}_2,\mathbf{i}+2\mathbf{e}_1+\mathbf{e}_2} J^{\sigma}_{\mathrm{d};\mathbf{i}+2\mathbf{e}_1+\mathbf{e}_2,\mathbf{i}+2\mathbf{e}_1} J^{\sigma}_{\mathrm{d};\mathbf{i}+2\mathbf{e}_1,\mathbf{i}}. \tag{19}$$

Repeating the above calculations, we find that $W^{(2)}_{\circlearrowleft}/|W^{(2)}_{\circlearrowleft}| = W'^{(2)}_{\circlearrowleft}/|W'^{(2)}_{\circlearrowleft}| = \mathrm{e}^{\mathrm{i}2\phi_{\circlearrowleft}}$. Hence, the Aharonov–Bohm phase is doubled with respect to the unit plaquette, which is consistent with the fact that the enclosed area is also doubled for these paths. The same occurs for any other closed path and thus the analogy to a background gauge field is consistent with the possible long-range of tunneling.

At this point, it is worth emphasizing the generality of the scheme proposed here. It works for both bosons and fermions, for any range of the tunneling $J^{\sigma}_{\mathrm{t};\mathbf{ij}} = J^{\sigma}_{\mathrm{t}}(|\mathbf{r}^0_{\mathbf{i}} - \mathbf{r}^0_{\mathbf{j}}|)$, it can incorporate local particle–particle interactions and it is non-perturbative. In the second part of this paper, we shall specify this scheme for trapped-ion experiments, which provide an ideal platform where to realize a bosonic PAT (i.e. vibrational excitations). Before moving onto the numerical verification of these results, let us introduce an alternative and more compact formulation of the synthetic gauge fields. It is possible to rewrite the PAT Hamiltonian in analogy to the so-called Peierls substitution [37], which yields

$$H_{\mathrm{eff}} = \sum_{\sigma} \sum_{\mathbf{i}>\mathbf{j}} \tilde{J}^{\sigma}_{\mathrm{d};\mathbf{ij}} \mathrm{e}^{\mathrm{i}e^* \int_{\mathbf{j}}^{\mathbf{i}} \mathrm{d}\mathbf{r}\cdot\mathbf{A}_{\mathrm{s}}} a^{\dagger}_{\sigma,\mathbf{i}} a_{\sigma,\mathbf{j}} + \mathrm{H.c.}, \tag{20}$$

where we have introduced the dressed-tunneling amplitude $\tilde{J}^{\sigma}_{\mathrm{d};\mathbf{ij}} = J^{\sigma}_{\mathrm{t};\mathbf{ij}} \mathscr{F}_{f(\mathbf{i},\mathbf{j})}(\eta_{\mathrm{d}}, \eta_{\mathrm{d}}, \Delta\phi_{\mathbf{ij}})$ and the synthetic gauge potential $\mathbf{A}_{\mathrm{s}}(\mathbf{x}) = -B_0 y \mathbf{e}_1$, where $B_0 = r\phi_2/e^* d_1 d_2$. This gauge potential, which corresponds to the famous Landau gauge for electrons in a constant magnetic field, is obtained after the following U(1) gauge transformation $a_{\sigma,\mathbf{i}} \to a_{\sigma,\mathbf{i}} \mathrm{e}^{-\mathrm{i}\chi_{\mathbf{i}}}$, where $\chi_{\mathbf{i}} = \phi_1 i_1^2/2$. We note that this transformation is also consistent with the long-range character of the tunneling. This compact formulation (20) condenses the main result of this section: a gradient and a periodic modulation of the on-site energies give us full access to the amplitude and phase of the tunneling, such that the effects of background synthetic gauge fields can be mimicked even for neutral particles or quasiparticles.

### 2.2. Numerical simulations

In this subsection, we confront the analytical model for the PAT in equation (20) with numerical simulations for the tunneling Hamiltonian (1) subjected to the gradient and periodic driving (4). We analyze in detail some basic realizations of the PAT, which allow us to carry out a thorough numerical study considering even the effects of finite temperatures.

*2.2.1. PAT along one link.* Let us initially focus on the simplest situation to test the accuracy of the analytical model, namely a lattice consisting of only two sites populated by spinless bosons. We consider the following parameters of the driven Hamiltonian in equations (1) and (4): the bare tunneling is $J_{\mathrm{t};12} = 10^{-2}\omega$, the gradient $\Delta\omega = 0.5\omega$ and the periodic driving parameters correspond to $\eta_{\mathrm{d}} = 1$, and $\omega_{\mathrm{d}} = \Delta\omega$. Note that we do not consider additional degrees of freedom, avoiding thus the index $\sigma$ in the following. In figure 3, we represent the expectation values $\langle n_i(t)\rangle = \langle\Psi(t)|a_i^{\dagger}(a)_i|\Psi(t)\rangle$ that result from the numerical integration of the

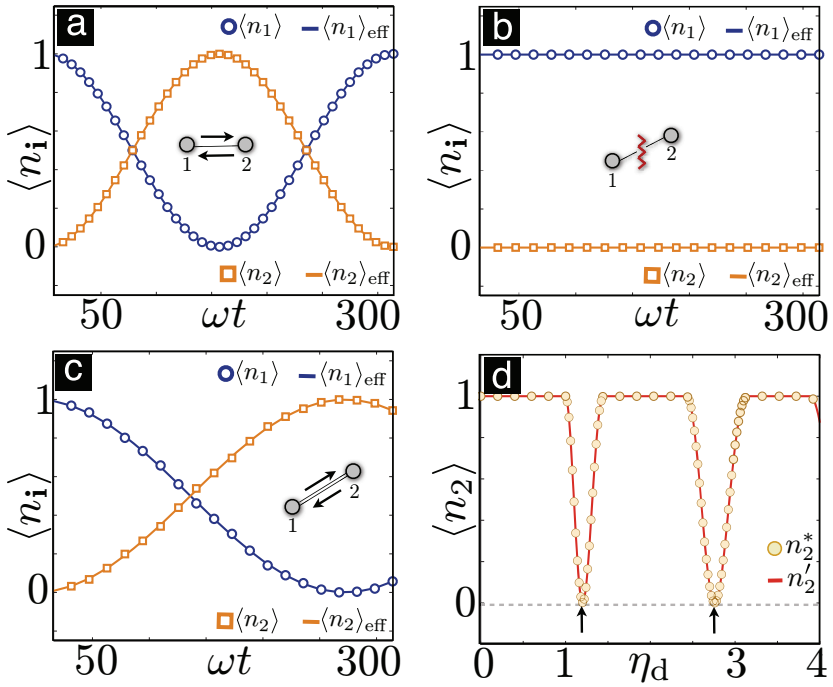


**Figure 3.** PAT along a link. (a) Bare tunneling for an initial state $|\Psi_0\rangle = a_1^\dagger|\text{vac}\rangle$ with a single particle occupying the first site. The numerical expectation values $\langle n_1(t)\rangle$ (blue circle) and $\langle n_2(t)\rangle$ (orange squares) are compared to the effective description $\langle n_1(t)\rangle_{\rm eff}$ (blue lines) and $\langle n_2(t)\rangle_{\rm eff}$ (orange lines) described in equation (21). (b) Suppressed tunneling due to the gradient and in the absence of periodic driving. (c) Assisted tunneling in the presence of periodic driving for $\Delta\phi_{12} = \pi$. (d) Coherent destruction of tunneling (black arrows) due to periodic driving in the absence of the gradient. The yellow circles represent the maximum population transferred to site 2 $n_2^* = \max\{\langle n_2(t)\rangle : t \leqslant t^*\}$, such that $t^* = 100\pi/|\mathscr{F}_0(\eta_{\rm d}, \pi)|\omega$, as obtained from the numerical integration of equations (1) and (4). The red line represents the predictions for the same magnitude $n_2'$ according to the effective Hamiltonian (12).

Schrödinger equation $\mathrm{i}\mathrm{d}|\Psi(t)\rangle/dt = (H_0(t) + H_t)|\Psi(t)\rangle$, and compare them with the effective analytical description $|\Psi(t)\rangle_{\rm eff} = e^{-\mathrm{i}H_{\rm eff}t}|\Psi_0\rangle$. We consider an initial state with a single bosonic particle in the first site $|\Psi_0\rangle = a_1^\dagger|\text{vac}\rangle$, where $|\text{vac}\rangle$ stands for vacuum. In this case, the effective description (12) can be integrated exactly, yielding the following periodic oscillations of the particle between the two lattice sites:

$$\begin{aligned}\langle n_1(t)\rangle_{\rm eff} &= \tfrac{1}{2}(1+\cos\omega_{\rm eff}t),\\ \langle n_2(t)\rangle_{\rm eff} &= \tfrac{1}{2}(1-\cos\omega_{\rm eff}t),\end{aligned} \tag{21}$$

where $\omega_{\rm eff} = 2|J_{\rm d;12}|$ is the frequency of oscillations. In the absence of any gradient or periodic driving, $\omega_{\rm eff} = 2|J_{\rm t;12}| = 0.02\omega$, and thus the particle exchange undergoes oscillations with a period of $T_{\rm t;12} = \pi/|J_{t;12}| = 100\pi/\omega$, which coincides exactly with the scale shown in figure 3(a). In this figure, we reveal that the effective description (circles and squares) agrees

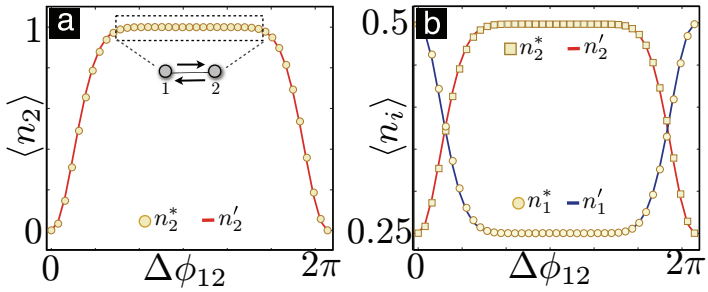


**Figure 4.** Phase dependence and thermal photon-assisted tunneling. (a) Dependence of the PAT on the relative driving phase $\Delta\phi_{12}$. The yellow circles represent the maximum population transfer to site 2, $n_2^*$, for a particle initially located at site 1, $|\Psi_0\rangle = a_1^\dagger|\text{vac}\rangle$, as obtained from the numerical integration of the full time-dependent Hamiltonian $H_0(t) + H_t$. The red line corresponds to the same quantity evaluated for the effective description $H_{\text{eff}}$, referred to as $n_2'$. Marked by the dotted frame is the region of optimal assisted tunneling. (b) Phase dependence of the PAT for an initial thermal state with $\bar{n}_1 = 0.5$, $\bar{n}_2 = 0.25$. We also represent the particle transfer to site 1.

with the numerical results (solid lines). Note that in order to carry out the numerical integration, we truncate the bosonic Hilbert space to $n_{\text{trunc}} = 4$. We have confirmed that the truncation error after changing $n_{\text{trunc}} \to \tilde{n}_{\text{trunc}} = n_{\text{trunc}} + 1$ lies below $|\langle n_i(t)\rangle_{n_{\text{trunc}}} - \langle n_i(t)\rangle_{\tilde{n}_{\text{trunc}}}| < 10^{-4}$. The same occurs in figure 3(b), where we switch on the gradient. As a consequence of the mismatch between the on-site energies, the tunneling is completely inhibited. In order to assist it, we switch on the periodic driving in figure 3(c) for $\phi_1 = \phi_2 + \pi$, which activates again the periodic oscillations but with a different period $T_{t;12} = \pi/|J_{d;12}| = 100\pi/|\mathscr{F}_1(\eta_d, \eta_d, \pi)|\omega$. For the parameters used, we obtain $|\mathscr{F}_1(\eta_d, \eta_d, \pi)| \approx 0.6$ (figure 2(a)), which explains the slightly longer oscillation period. However, we remark that both dynamics occur on the same time scale as a consequence of the non-perturbative character of the scheme.

In figure 3(d), we study the maximal population transfer to site 2 due to the periodic driving $\eta_d \neq 0$, but in the absence of the gradient $\Delta\omega = 0$. We set the phases to $\phi_1 = 0, \phi_2 = \pi$, and study the maximal transfer $n_2^* = \max\{\langle n_2(t)\rangle : t \leqslant t^*\}$, such that $t^* = 100\pi/|\mathscr{F}_0(\eta_d, \eta_d, \pi)|\omega$ for a range of driving strengths $\eta_d \in [0, 4]$. As shown in this figure, there are certain values of the driving strength, marked by black arrows, where the tunneling gets completely suppressed, a phenomenon known as coherent destruction of tunneling [25] or dynamic localization. Let us remark that this scheme leads to a perfect localization of the particles also in a longer 1D chain, since the dressed tunneling cancels for all pairs of nearest-neighboring lattice sites simultaneously. Once we set $\phi_{i_1} = \pi i_1/2$, such that $\Delta\phi_{i_1 i_1+1} = \pi$, it is possible to find a zero of the modulating function $\mathscr{F}_0(\eta_d^0, \eta_d^0, \pm\pi) = 0$, which is related to the particular values of the Bessel functions. In this limit, the particles shall not diffuse through the lattice.

In figure 4(a), we study the photon-assisted process for different driving phases $\Delta\phi_{12} \in [0, 2\pi]$, considering the same parameters and initial state as before. We represent the maximum population transferred to site 2 $n_2^* = \max\{\langle n_2(t)\rangle : t \leqslant t^*\}$, such that $t^* = 50\pi/|\mathscr{F}_1(\eta_d, \eta_d, \pi)|\omega$ corresponds to the optimal PAT with $\Delta\phi_{12} = \pi$. The yellow dots correspond to the numerical integration of the truncated Hamiltonian (1) and (4), whereas the solid line corresponds

to the analytical prediction evaluated at the related exchange period $n_2' = \langle n_2(t')\rangle_{\rm eff}$ for the different phases, namely $t' = 50\pi/|\mathscr{F}_1(\eta_{\rm d}, \eta_{\rm d}, \Delta\phi_{12})|\omega$. In this figure, we reveal the agreement between both descriptions for any of the driving phases. Note that this agreement will not be compromised by going to larger arrays. As announced previously, we can interpolate between the optimally assisted and the completely suppressed tunneling regimes by modifying the driving phase.

It is also interesting to consider an initial state that does not correspond to a single particle, but rather to a thermal ensemble. We focus now on bosons with independent mean numbers of particles $\bar{n}_1, \bar{n}_2$. This state corresponds to $\rho_0 = \rho_1 \otimes \rho_2$ with

$$\rho_i = \frac{1}{\mathscr{Z}_i} \mathrm{e}^{-\beta_i \omega_i a_i^\dagger a_i}, \qquad \mathscr{Z}_i = \mathrm{tr}(\mathrm{e}^{-\beta_i \omega_i a_i^\dagger a_i}), \tag{22}$$

such that the parameters $\beta_i$ are implicitly defined through the mean number of particles following a Bose–Einstein distribution $\bar{n}_i = 1/(\mathrm{e}^{\beta_i \omega_i} - 1)$. In this case, we must integrate numerically the Liouville–Von Neumann equation $\mathrm{i}\mathrm{d}\rho(t)/\mathrm{d}t = [H_0(t) + H_t, \rho(t)]$, and compare the result to the effective description $\rho_{\rm eff}(t) = e^{-\mathrm{i}H_{\rm eff}t}\rho_0 e^{+\mathrm{i}H_{\rm eff}t}$. In particular, we consider the same parameters as before, and set $\bar{n}_1 = 0.5, \bar{n}_2 = 0.25$ after truncating the particle Hilbert space to $n_{\rm trunc} = 7$. Note that due to the thermal effects, the truncation parameter has been increased with respect to the previous simulations. Again, we have checked the convergence of the results by increasing $n_{\rm trunc}$. In figure 4(b), we represent the expectation values $n_2^*, n_2'$ introduced above, together with those of site 1, $n_1^* = \min\{\langle n_1(t)\rangle : t \leqslant t^*\}$ and $n_1' = \langle n_1(t')\rangle_{\rm eff}$ for $t' = 50\pi/|\mathscr{F}_1(\eta_{\rm d}, \eta_{\rm d}, \Delta\phi_{12})|\omega$. We conclude from the perfect agreement shown in the figure that the scheme also works for thermal states. In fact, in the absence of interactions, the equations of motion do not depend on whether the state is pure or a mixed thermal state. For the latter, there is a background over which the PAT phenomena will occur. The role of the additional interactions, and its interplay with the thermal states, is a very interesting topic that deserves a separate study.

The suitability of the PAT scheme for thermal states will turn out to be essential in section 3, where we discuss a realistic implementation of the quantum simulator of gauge fields with phonons in microtrap arrays. In this case, it means that cooling to the vibrational ground state is not necessary for observing the nontrivial effects of the PAT. Another interesting topic is the occurrence of motional heating in the microtraps. In case this motional heating is global, it should not interfere with the PAT effects. However, if this heating has a local nature, it may lead to very interesting effects that mimic the role played by a reservoir providing electrons to local regions of a metallic conductor. This effect can be complemented by the controlled engineering of dephasing in the phonon dynamics by introducing noisy potentials in the trap electrodes [38]. Hence, the applicability of the PAT quantum simulator could be widened and used to study how transport phenomena are affected by an environment that induces decoherence effects such as motional heating or dephasing.

*2.2.2. PAT around a plaquette.* Let us now apply our formalism to a 2D setup to test the application of PAT for the quantum simulation of synthetic gauge fields. We consider a model of spinless bosons in a square plaquette, and set the parameters of the total Hamiltonian in equations (1) and (4) to $J_{\mathrm{t};12} = 10^{-2}\omega$, $\Delta\omega = 0.5\omega$, $\eta_{\rm d} = 1$, $r = 1$ and $\omega_{\rm d} = \Delta\omega$. Our aim is to test the accuracy of the effective description (20), trying to find clear-cut evidence for the

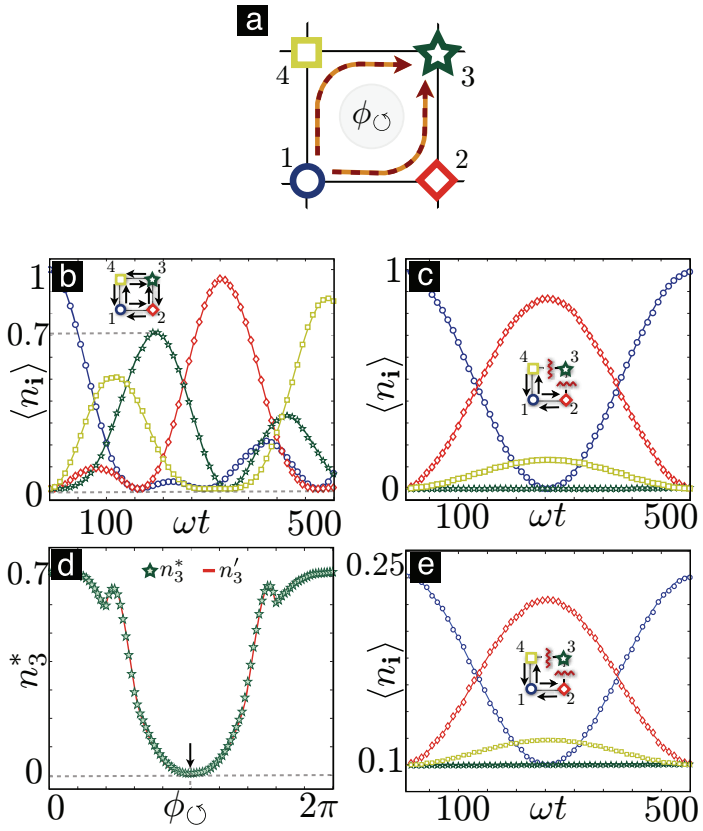


**Figure 5.** PAT around a plaquette. (a) Schematic representation of the plaquette, highlighting the two possible paths connecting sites 1 and 3. (b) PAT for an initial state $|\Psi_0\rangle = a_1^\dagger|\text{vac}\rangle$, such that the periodic-driving phase is $\phi_1 = \pi$, and $\phi_{\circlearrowleft} = r\phi_2 = 0$ with $r = 1$. The numerical expectation values $\langle n_1(t)\rangle$ (blue circles), $\langle n_2(t)\rangle$ (red diamonds), $\langle n_3(t)\rangle$ (green stars) and $\langle n_4(t)\rangle$ (yellow squares) are compared to the effective description in equation (20) (solid lines with the same colors). For vanishing $\phi_{\circlearrowleft} = 0$, the particle can tunnel anywhere in the lattice. (c) The same as above, but setting $\phi_{\circlearrowleft} = \pi$, where one clearly observes the Aharonov–Bohm interference $\langle n_3(t)\rangle = 0$. (d) Maximum population transfer to site 3 as a function of the enclosed phase $\phi_{\circlearrowleft} \in [0, 2\pi]$. The yellow dots correspond to the exact numerical integration $n_3^*$, and the solid red line to the effective description $n_3'$. A black arrow marks the perfect Aharonov–Bohm interference. (e) Aharonov–Bohm interference for an initial thermal state $\bar{n}_1 = 0.25$ and $\bar{n}_2 = \bar{n}_3 = \bar{n}_4 = 0.1$.

underlying synthetic gauge field. In order to do so, we study a discrete version of the celebrated Aharonov–Bohm effect [35].

Let us briefly recall the underlying interference effect (figure 5(a)). A particle initially localized at site 1 can tunnel to site 3 following two different paths, namely $\gamma_1 : 1 \to 2 \to 3$ or $\gamma_2 : 1 \to 4 \to 3$. Due to the gauge field, each path leads to a different phase $|\Psi_f\rangle \propto e^{ie^* \int_{\gamma_1} \mathbf{dr}\cdot\mathbf{A}_s}(a)_3^\dagger|\text{vac}\rangle + e^{ie^* \int_{\gamma_2} \mathbf{dr}\cdot\mathbf{A}_s} a_3^\dagger|\text{vac}\rangle$, such that the probability of performing such a trajectory

is $P_3 \propto 2+2\cos(e^*\int_{\gamma_1} d\mathbf{r}\cdot\mathbf{A}_s - e^*\int_{\gamma_2} d\mathbf{r}\cdot\mathbf{A}_s) = 2(1+\cos\phi_{\circlearrowleft})$, where $\phi_{\circlearrowleft} = e^*\oint_{\circlearrowleft} d\mathbf{r}\cdot\mathbf{A}_s$ was defined in equation (18). From this expression, one finds a perfect destructive interference that forbids the particle to tunnel to site 3 when the enclosed phase $\phi_{\circlearrowleft} = \pi$. This Aharonov–Bohm interference will serve us as a test bed for the validity of the gauge-field analogy (20).

We now compare the dynamics obtained from the numerical integration of the driven Hamiltonian (1) and (4) to the effective description in equation (20). In figures 5(b) and (c), we consider $|\Psi_0\rangle = a_1^\dagger|\text{vac}\rangle$ and study the propagation of the particle along the square plaquette for different driving phases. In figure 5(b), we observe that for the phases $\phi_1 = \pi, \phi_2 = 0$, the particle is allowed to tunnel to every lattice site. This is consistent with the fact that for $\phi_{\circlearrowleft} = \phi_2 = 0$, there is no interference. Conversely, we set $\phi_1 = \pi, \phi_2 = \pi$ in figure 5(c), where one readily observes that the tunneling to site 3 is forbidden by the aforementioned Aharonov–Bohm interference. We note that for the trapped ion case (see the sections below), the diagonal path going from sites $1 \to 3$ and $2 \to 4$ must also be accounted for since the tunneling amplitude need not be small. In [24], we discussed how to cancel it by playing with the phases, so that the analogy with the Aharonov–Bohm effect is valid. In figure 5(e), we corroborate that the effect also holds for thermal states. Finally, we check in figure 5(d) that the perfect destructive interference only occurs for the so-called $\pi$-flux phase. In this figure, we represent the maximal transferred population to site 3, $n_3^* = \max\{\langle n_3(t)\rangle, 0 < t < t^*\}$, where $t^* = 100\pi/|\mathscr{F}_1(\eta_d, \eta_d, \pi)|\omega$, and show that the perfect interference only occurs when the enclosed phase $\phi_{\circlearrowleft} = \pi$. This allows us to rule out other possible sources of interference, and conclude that it is only due to the synthetic gauge field.

Let us close this subsection by highlighting the accuracy of our analytical treatment, which has been contrasted with a numerical survey of different setups with a wide range of parameters. The rest of this paper will be devoted to analyzing the experimental setups in the field of quantum optics, ions in microtrap arrays, where the necessary ingredients for this PAT are within reach using state-of-the-art technologies. Besides, we shall also introduce novel methods to exploit additional aspects of PAT phenomenology.

## 3. PAT toolbox for trapped ions

In this section, we apply the above scheme to arrays of micro-fabricated ion traps, and show that one can achieve PAT of the vibrational excitations between distant microtraps. In order to set the notation, we start by showing in section 3.1 that the vibrations of an ensemble of ions in a microtrap array can be described in terms of tunneling phonons [5]. Then, we describe in section 3.2 how the gradient and periodic driving of the trapping frequencies can be achieved using the tools of state-of-the-art experiments in ion traps (see the reviews [46]). In particular, the gradient can be implemented by the local control of dc voltages applied to the trap electrodes, whereas the periodic driving stems from an optical dipole force. We derive a set of constraints that this dipole force must fulfill, and discuss how these requirements can be met for realistic experimental parameters. In section 3.3, we incorporate phonon–phonon interactions in the phonon-based quantum simulator of bosonic particles exposed to synthetic gauge fields. Finally, in sections 3.4–3.6, we describe how to extend the PAT scheme beyond the applications discussed so far, reaching more involved models where the spin of the ion can be exploited as an additional tool.

### 3.1. Tunneling of phonons in microtrap arrays

Let us consider an ensemble of $N$ ions with charge $e$ and mass $m$, labeled by integer numbers $\mathbf{i} = (i_x, i_y)$. Each ion is subjected to the electric potential energy created by a planar micro-fabricated trap $V_\mathrm{t}$ and the Coulomb energy potential $V_\mathrm{c}$, causing repulsion between the remaining ions, such that the total Hamiltonian is

$$H = H_0 + H_\mathrm{c} = \sum_{\mathbf{i}} \left( \frac{\mathbf{p}_\mathbf{i}^2}{2m} + V_\mathrm{t}(\mathbf{r}_\mathbf{i}) \right) + \frac{e^2}{2} \sum_{\mathbf{i}\neq\mathbf{j}} \frac{1}{|\mathbf{r}_\mathbf{i} - \mathbf{r}_\mathbf{j}|}. \tag{23}$$

Here, the trap is designed in such a way that the ion equilibrium positions, which are given by $\nabla(V_\mathrm{t} + V_\mathrm{c})|_{\mathbf{r}_\mathbf{i}^0} = \mathbf{0}$, form a regular lattice $\mathbf{r}_\mathbf{i}^0 = i_1 d_1 \mathbf{e}_1 + i_2 d_2 \mathbf{e}_2$, where $\mathbf{e}_1, \mathbf{e}_2$ are the unit vectors and $d_1, d_2$ the lattice spacings. At sufficiently small temperatures, the excursions of the ions from these equilibrium positions $\mathbf{r}_\mathbf{i} = \mathbf{r}_\mathbf{i}^0 + \delta\mathbf{r}_\mathbf{i}$ are small with respect to the lattice spacing. Thus, for our purpose, we are allowed to consider the above Hamiltonian up to second order only [2, 47]. This approximation yields a system of coupled harmonic oscillators

$$H = \sum_{\mathbf{i}} \frac{\mathbf{p}_\mathbf{i}^2}{2m} + \sum_{\mathbf{i}\neq\mathbf{j}} \sum_{\alpha,\gamma} (\mathscr{V}_{\mathrm{t};\mathbf{ij}}^{\alpha\gamma} + \mathscr{V}_{\mathrm{c};\mathbf{ij}}^{\alpha\gamma}) \delta r_{\alpha,\mathbf{i}} \delta r_{\gamma,\mathbf{j}}, \tag{24}$$

with the following couplings:

$$\begin{aligned} \mathscr{V}_{\mathrm{t};\mathbf{ij}}^{\alpha\gamma} &= \frac{1}{2} \frac{\partial^2 V_\mathrm{t}}{\partial r_{\alpha,\mathbf{i}} \partial r_{\gamma,\mathbf{j}}} \bigg|_{\{\mathbf{r}_\mathbf{l}^0\}} = \frac{m}{2} \omega_{\alpha,\mathbf{i}}^2 \delta_{\mathbf{ij}} \delta_{\alpha\gamma}, \\ \mathscr{V}_{\mathrm{c};\mathbf{ij}}^{\alpha\gamma} &= \frac{1}{2} \frac{\partial^2 V_\mathrm{c}}{\partial r_{\alpha,\mathbf{i}} \partial r_{\gamma,\mathbf{j}}} \bigg|_{\{\mathbf{r}_\mathbf{l}^0\}} \\ &= \frac{e^2}{2} \sum_{\mathbf{l}\neq\mathbf{i}} (\delta_{\mathbf{lj}} - \delta_{\mathbf{ij}}) \left( \frac{\delta_{\alpha\gamma}}{|\mathbf{r}_{\mathbf{i}-\mathbf{l}}^0|^3} - \frac{3(\mathbf{r}_{\mathbf{i}-\mathbf{l}}^0)_\alpha (\mathbf{r}_{\mathbf{i}-\mathbf{l}}^0)_\gamma}{|\mathbf{r}_{\mathbf{i}-\mathbf{l}}^0|^5} \right), \end{aligned} \tag{25}$$

where $\mathbf{r}_{\mathbf{i}-\mathbf{l}}^0 = \mathbf{r}_\mathbf{i}^0 - \mathbf{r}_\mathbf{l}^0$, $\delta_{\mathbf{il}}$ stands for the Kronecker delta, and $\alpha, \gamma = x, y, z$ refer to the main axes of the trapping potential. Note that the micro-fabricated trap gives rise to a confinement that can be considered to be harmonic for the motional amplitudes considered here and is therefore characterized by the frequencies $\omega_{\alpha,\mathbf{i}}$ that may depend on the axis and the ion position within the lattice. The Hamiltonian (24) can be expressed in the basis of local quantized vibrations

$$\begin{aligned} \delta r_{\alpha,\mathbf{i}} &= \sqrt{\frac{1}{2m\omega_{\alpha,\mathbf{i}}}} \left( b_{\alpha,\mathbf{i}}^\dagger + b_{\alpha,\mathbf{i}} \right), \\ p_{\alpha,\mathbf{i}} &= i \sqrt{\frac{m\omega_{\alpha,\mathbf{i}}}{2}} \left( b_{\alpha,\mathbf{i}}^\dagger - b_{\alpha,\mathbf{i}} \right), \end{aligned} \tag{26}$$

where $b_{\alpha,\mathbf{i}}^\dagger$, $b_{\alpha,\mathbf{i}}$ are the bosonic creation–annihilation operators, and we set $\hbar = 1$. In this local basis, the vibrational Hamiltonian becomes $H = H_0 + H_\mathrm{c}$,

$$H = \sum_{\alpha,\mathbf{i}} \omega_{\alpha,\mathbf{i}} b_{\alpha,\mathbf{i}}^\dagger b_{\alpha,\mathbf{i}} + \sum_{\mathbf{ij}} \sum_{\alpha,\gamma} J_{\mathrm{c};\mathbf{ij}}^{\alpha\gamma} \left( b_{\alpha,\mathbf{i}}^\dagger + b_{\alpha,\mathbf{i}} \right) \left( b_{\gamma,\mathbf{j}}^\dagger + b_{\gamma,\mathbf{j}} \right), \tag{27}$$

where the Coulomb couplings $J_{\mathrm{c};\mathbf{ij}}^{\alpha\gamma} = \mathscr{V}_{\mathrm{c};\mathbf{ij}}^{\alpha\gamma} / (2m\sqrt{\omega_{\alpha,\mathbf{i}}\omega_{\gamma,\mathbf{j}}})$ describe the exchange of vibrational excitations between different ions $\mathbf{i}, \alpha \leftrightarrow \mathbf{j}, \gamma$, and yield the aforementioned collective phonons

once diagonalized. Let us express $H_c$ in the interaction picture with respect to $H_0$, namely $H_c' = e^{iH_0 t} H_c e^{-iH_0 t}$,

$$H_c' = \sum_{\mathbf{ij}\alpha\gamma} J^{\alpha\gamma}_{c;\mathbf{ij}} (b^\dagger_{\alpha,\mathbf{i}} b_{\gamma,\mathbf{j}} e^{i(\omega_{\alpha,\mathbf{i}} - \omega_{\gamma,\mathbf{j}})t} + b^\dagger_{\alpha,\mathbf{i}} b^\dagger_{\gamma,\mathbf{j}} e^{i(\omega_{\alpha,\mathbf{i}} + \omega_{\gamma,\mathbf{j}})t}) + \text{H.c.} \tag{28}$$

In this work, we consider that the microtraps fulfill

$$\alpha \neq \gamma,\ J^{\alpha\gamma}_{c;\mathbf{ij}} \ll |\omega_{\alpha,\mathbf{i}} - \omega_{\gamma,\mathbf{j}}|, \quad \alpha = \gamma,\ J^{\alpha\alpha}_{c;\mathbf{ij}} \ll |\omega_{\alpha,\mathbf{i}} + \omega_{\alpha,\mathbf{j}}|, \tag{29}$$

which allow us to neglect the rapidly oscillating terms of the above Hamiltonian using a standard RWA. The first condition allows us to consider independent vibrations along each of the trapping axes, whereas the second one allows us to neglect the terms that do not conserve the number of vibrational excitations. Accordingly,

$$H = H_0 + H_c = \sum_{\mathbf{i},\alpha} \omega'_{\alpha,\mathbf{i}} b^\dagger_{\alpha,\mathbf{i}} b_{\alpha,\mathbf{i}} + \sum_{\alpha} \sum_{\mathbf{i}>\mathbf{j}} \left( J^{\alpha}_{c;\mathbf{ij}} b^\dagger_{\alpha,\mathbf{i}} b_{\alpha,\mathbf{j}} + \text{H.c.} \right), \tag{30}$$

where the trapping frequency of each ion is slightly modified by the electrostatic interaction with its neighboring ions $\omega'_{\alpha,\mathbf{i}} = (\omega^2_{\alpha,\mathbf{i}} + \mathscr{V}^{\alpha\alpha}_{c;\mathbf{ii}}/2m)^{1/2}$, and we have defined $J^{\alpha}_{c;\mathbf{ij}} = 2J^{\alpha\alpha}_{c;\mathbf{ij}}$. This Hamiltonian can be interpreted as a tight-binding model for the local phonons, which tunnel between distant microtraps according to the dipolar tunneling strengths $J^{\alpha}_{c;\mathbf{ij}}$. By a direct comparison to the general tight-binding model in equation (1), we can identify the index $\sigma$ with the vibrational axis, the tunneling strength $J^{\sigma}_{t;\mathbf{ij}}$ with the aforementioned dipolar Coulomb couplings and the on-site energies $\omega_{\sigma,\mathbf{i}}$ with the microtrap trapping frequencies. In the following subsection, we describe how to obtain the gradient and the periodic driving using state-of-the-art tools in trapped-ion experiments.

### *3.2. Gradient and periodic driving of the trapping frequencies*

In microtrap arrays, it is possible to design the individual trapping frequencies $\{\omega_{\alpha,\mathbf{i}}\}$ by the control of dc voltages applied to local micro-fabricated electrodes. In fact, the experiments [28] have made explicit use of this property in a conventionally segmented linear rf trap, in order to switch on/off the phonon tunneling by tuning the trapping frequencies of two neighboring traps in/out of common resonance [29]. We chose the trapping frequencies distributed according to a gradient $\omega_{\alpha,\mathbf{i}} = \omega_\alpha + \Delta\omega_\alpha i_1$. Considering mutual trap and mutual ion distances $>10\,\mu$m due to current constraints in fabrication, the correction to the trapping frequency due to the electrostatic interaction can be neglected, and we get the desired gradient of the on-site energies $\omega'_{\alpha,\mathbf{i}} \approx \omega_{\alpha,\mathbf{i}} = \omega_\alpha + \Delta\omega_\alpha i_1$ which must be incorporated into the tight-binding Hamiltonian (30).

We now turn to the periodic driving of the trapping frequencies, which shall be implemented by an optical dipole force [46]. We consider a pair of laser beams with frequencies $\omega_1, \omega_2$ and wavevectors $\mathbf{k}_1, \mathbf{k}_2$, which couple to the electronic states $|{\downarrow_\mathbf{i}}\rangle, |{\uparrow_\mathbf{i}}\rangle, |a_\mathbf{i}\rangle$ (see the energy-level scheme of figure 6 for the particular case of $^{25}Mg^+$ ions). Encoding the spin degree of freedom into a pair of electronic ground states by exploiting their hyperfine or Zeeman splitting, the energy difference $\omega_0/2\pi$ between the states $|{\downarrow_\mathbf{i}}\rangle, |{\uparrow_\mathbf{i}}\rangle$ lies in the microwave range 1 GHz, whereas the energy splitting $\omega_a/2\pi$ to an auxiliary state $|a_\mathbf{i}\rangle$ is much larger $\omega_a \gg \omega_0$, and typically lies in the optical domain 100–1000 THz. By tuning the beatnote of the phase-locked laser beams to a particular value, it is possible to choose from a variety of couplings. For instance, when $\omega_1 - \omega_2 \approx \omega_0$, such that $\omega_1, \omega_2 \ll \omega_a$, one speaks of a stimulated two-photon Raman transition between the ground and excited states (figure 6(b)). Conversely, when

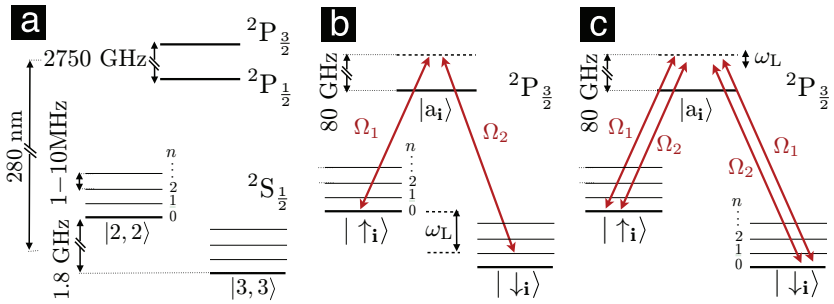


**Figure 6.** Energy-level scheme and laser-beam arrangement. (a) Reduced diagram for the hyperfine energy levels $|F, M\rangle$ of $^{25}Mg^+$. The ground-state manifold $^2S_{1/2}$ is split into the hyperfine levels $F = 2, 3$, such that an additional magnetic field allows us to isolate two magnetic sublevels $|\uparrow_i\rangle = |2, 2\rangle_i$, $|\downarrow_i\rangle = |3, 3\rangle_i$ with an energy difference of $\omega_0/2\pi \approx 1.8$ GHz. Note also that these levels are dressed by a vibrational ladder with equidistant spacing $\omega_\alpha/2\pi \approx 1$–$10$ MHz. The excited manifold $^2P_{3/2}$ contains an auxiliary level to implement a stimulated Raman scheme with two laser beams and a beatnote $\omega_L = \omega_1 - \omega_2$. (b) Raman scheme for two laser beams with Rabi frequencies $\Omega_1, \Omega_2$ in the so-called red-sideband regime $\omega_L \approx \omega_0 - \omega_\alpha$. In this regime, excitations are exchanged between the electronic and vibrational states of the ions. (c) Raman scheme for the periodic modulation of the trapping frequencies $\omega_L \ll \omega_\alpha$. In this limit, only negligible coupling between the internal or vibrational states takes place during the transition, but rather a periodic modulation of the trapping frequencies is realized.

$\omega_1 - \omega_2 \approx \omega_\alpha \ll \omega_0$, one obtains a running-wave realization of the so-called spin-dependent dipole forces. In this work, we are interested in another different regime $\omega_1 - \omega_2 \ll \omega_\alpha$ (figure 6(c)), where we get the desired periodic driving by the laser dipole force. We consider the ion–laser interaction in the dipolar approximation

$$H_L = \sum_{l=1,2}\sum_{\mathbf{i}} \frac{1}{2}\Omega^{(l)}_{a\uparrow}|a_\mathbf{i}\rangle\langle\uparrow_\mathbf{i}|e^{-i(\mathbf{k}_l\mathbf{r}_\mathbf{i}-\omega_l t)} + \text{H.c.} + \sum_{l=1,2}\sum_{\mathbf{i}} \frac{1}{2}\Omega^{(l)}_{a\downarrow}|a_\mathbf{i}\rangle\langle\downarrow_\mathbf{i}|e^{-i(\mathbf{k}_l\mathbf{r}_\mathbf{i}-\omega_l t)} + \text{H.c.}, \tag{31}$$

where $\Omega^{(l)}_{a\uparrow}$, $\Omega^{(l)}_{a\downarrow}$ are the Rabi frequencies for each of the transitions to the auxiliary level induced by each of the laser beams. Since we are assuming that the laser frequencies are far off-resonant with respect to the auxiliary state, it is possible to perform an adiabatic elimination of this state to simplify the dynamics between $|\uparrow_i\rangle, |\downarrow_i\rangle$. Furthermore, for sufficiently small Rabi frequencies and considering that $\omega_1 - \omega_2 \ll \omega_0$, it is possible to obtain

$$H_L = -\sum_{\mathbf{i}}\left[\frac{(\Omega^{(1)}_{a\downarrow})^*\Omega^{(2)}_{a\downarrow}}{4\Delta}e^{i(\Delta\mathbf{k}\cdot\mathbf{r}_\mathbf{i}-\omega_L t)} + \text{H.c.}\right]|\downarrow_\mathbf{i}\rangle\langle\downarrow_\mathbf{i}|$$

$$-\sum_{\mathbf{i}}\left[\frac{(\Omega^{(1)}_{a\uparrow})^*\Omega^{(2)}_{a\uparrow}}{4\Delta}e^{i(\Delta\mathbf{k}\cdot\mathbf{r}_\mathbf{i}-\omega_L t)} + \text{H.c.}\right]|\uparrow_\mathbf{i}\rangle\langle\uparrow_\mathbf{i}|, \tag{32}$$

where we have defined the beatnote $\omega_L = \omega_1 - \omega_2$, $\Delta\mathbf{k} = \mathbf{k}_1 - \mathbf{k}_2$ and $\Delta = \omega_a - \omega_0 - \omega_1$ such that $|\Delta| \gg \omega_0$. Note that we have neglected the ac-Stark shifts arising from each single laser beam, since they do not play any role in the periodic driving of the trapping frequencies. By a proper choice of the laser intensities, detunings and polarizations, one finds a regime where the two-photon Rabi frequency is $\Omega_L = -(\Omega_{a\downarrow}^{(1)})^*\Omega_{a\downarrow}^{(2)}/2\Delta = -(\Omega_{a\uparrow}^{(1)})^*\Omega_{a\uparrow}^{(2)}/2\Delta$, and thus the laser–ion interaction becomes

$$H_L = \tfrac{1}{2}\Omega_L \sum_{\mathbf{i}} e^{i(\Delta\mathbf{k}\cdot\mathbf{r}_i - \omega_L t)} + \text{H.c.} \tag{33}$$

This expression corresponds to a Stark shift that acts equally on both electronic states, and is caused by crossed laser beams of different frequencies.

To obtain the desired periodic driving from the ion–laser Hamiltonian (33), we express the ion position in terms of the local phonon operators $\mathbf{r}_\mathbf{i} = \mathbf{r}_\mathbf{i}^0 + \sum_\alpha \mathbf{e}_\alpha (b_{\alpha,\mathbf{i}}^\dagger + b_{\alpha,\mathbf{i}})/\sqrt{2m\omega_\alpha}$. By introducing the so-called Lamb–Dicke parameter $\eta_\alpha = \mathbf{e}_\alpha \cdot \Delta\mathbf{k}/\sqrt{2m\omega_\alpha} \ll 1$, we can Taylor expand the Hamiltonian $H_L \approx H_L^{(0)} + H_L^{(1)} + H_L^{(2)}$, whereby

$$\begin{aligned}
H_L^{(0)} &= \frac{\Omega_L}{2} \sum_{\mathbf{i}} e^{i\Delta\mathbf{k}\cdot\mathbf{r}_\mathbf{i}^0 - i\omega_L t} + \text{H.c.},\\
H_L^{(1)} &= \frac{i\Omega_L}{2} \sum_{\mathbf{i}\alpha} e^{i\Delta\mathbf{k}\cdot\mathbf{r}_\mathbf{i}^0 - i\omega_L t} \eta_\alpha (b_{\alpha,\mathbf{i}} + b_{\alpha,\mathbf{i}}^\dagger) + \text{H.c.},\\
H_L^{(2)} &= \frac{-\Omega_L}{4} \sum_{\mathbf{i}\alpha\gamma} e^{i\Delta\mathbf{k}\cdot\mathbf{r}_\mathbf{i}^0 - i\omega_L t} \eta_\alpha \eta_\gamma \left(b_{\alpha,\mathbf{i}} + b_{\alpha,\mathbf{i}}^\dagger\right)\left(b_{\gamma,\mathbf{i}} + b_{\gamma,\mathbf{i}}^\dagger\right) + \text{H.c.}
\end{aligned} \tag{34}$$

Note that the first term corresponds to an irrelevant $c$-number that does not modify the phonon dynamics. In order to find the relevant contribution of the two remaining terms $H_L^{(1)}$, $H_L^{(2)}$, we switch to the interaction picture with respect to $H_0 = \sum_{\alpha,\mathbf{i}} \omega_{\alpha,\mathbf{i}} b_{\alpha,\mathbf{i}}^\dagger b_{\alpha,\mathbf{i}}$. If we consider that both, the frequency gradient and the laser frequency, fulfill $\Delta\omega_\alpha, \omega_L \ll \omega_\alpha$, $|\omega_\alpha - \omega_\gamma|_{\alpha\neq\gamma}$, an RWA for $\eta_\alpha\Omega_L \ll \omega_\alpha$ allows us to neglect the rapidly oscillating terms and leads to the desired periodic driving of the trapping frequencies

$$H_L \approx -\Omega_L \sum_{\alpha,\mathbf{i}} \eta_\alpha^2 \cos(\Delta\mathbf{k}\cdot\mathbf{r}_\mathbf{i}^0 - \omega_L t) b_{\alpha,\mathbf{i}}^\dagger b_{\alpha,\mathbf{i}}. \tag{35}$$

By direct comparison with equation (4), we find the following, individually tunable, mapping between the parameters of the periodic driving and the laser beams: $\omega_d = \omega_L$, $\omega_d\eta_d = -\Omega_L\eta_\alpha^2$, and $\phi_\mathbf{i} = -\Delta\mathbf{k}\cdot\mathbf{r}_\mathbf{i}^0$. Let us also note that in order to neglect the higher order terms that rotate with the laser frequency $\omega_L$, we impose that $\Omega_L\eta_\alpha^4 \ll \omega_L$. It is important to remark that even if we are considering small Lamb–Dicke parameters $\eta_\alpha \ll 1$, the periodic driving $|\eta_d| = \Omega_L\eta_\alpha^2/\omega_L$ need not be small by selecting the appropriate laser and Rabi frequencies, so that the non-perturbative character of the PAT can be exploited.

The task remaining in order to demonstrate that the scheme of PAT works for phonons in microtrap arrays is to consider the typical values for the experimental parameters and discuss whether they satisfy the constraints imposed during the above derivation. The orders of magnitude of all the relevant parameters are listed in table 1, which satisfy the different constraints made along this derivation, namely

$$\eta_\alpha\Omega_L \ll \omega_\alpha, \quad \Delta\omega_\alpha, \omega_L \ll \omega_\alpha, \quad |\omega_\alpha - \omega_\gamma|_{\alpha\neq\gamma}. \tag{36}$$

For the last inequality, it suffices to focus on the phonon modes transverse to the microtrap plane, $\alpha = z$, such that $|\omega_z - \omega_\gamma|_{\gamma\neq z}/2\pi \approx 1$ MHz. If the in-plane vibrational modes are to be

**Table 1.** Typical parameters for ion microtrap arrays.

| $\omega_\alpha/2\pi$ | $\Delta\omega_\alpha/2\pi$ | $\omega_L/2\pi$ | $J^\alpha_{c;12}/2\pi$ | $\Omega_L/2\pi$ | $\eta_\alpha$ |
|---|---|---|---|---|---|
| 1–10 MHz | 50–500 kHz | 50–500 kHz | 1–10 kHz | 0.1–1 MHz | 0.1–0.4 |

used, the anisotropy of the trapping frequencies $\omega_x \neq \omega_y$ should be considered in the microtrap design. Finally, table 1 allows us to estimate the parameters of the model Hamiltonian, and reveal whether the constraints for the PAT in equations (2) and (3) are fulfilled. We find that $J^\alpha_{c;12}/2\pi \approx$ 1–10 kHz$\ll \Delta\omega_\alpha/2\pi \approx$ 50–500 kHz, which thus satisfies the constraint in equation (2). Besides, we find that $\phi_{\mathbf{i}} = \phi_1 i_1 + \phi_2 i_2$, where $\phi_\alpha = -(\Delta\mathbf{k}\cdot\mathbf{e}_\alpha)d_\alpha$, and thus the constraint (3) is also satisfied. Therefore, we can conclude that the required ingredients for the PAT introduced in section 2 can already be met with the current technology of microtrap arrays if the tunneling rates outrun the decoherence rates. Note that if motional heating turns out to degrade the results severely, we could mitigate this problem by using a cryogenic setup.

Let us finally comment on two additional constraints different from (2) and (3), which are particular to the trapped-ion setup. Both the gradient and the the periodic driving should not modify the stability of the ion crystal and thus must be smaller than the trapping frequencies

$$\Delta\omega_\alpha, \quad \eta_d\omega_d \ll \omega_\alpha. \tag{37}$$

This is also fulfilled for the parameters in table 1. Let us note that this condition sets a limit to the scalability of our proposal. For gradients $\Delta\omega_\alpha/2\pi \approx 50$ kHz and trapping frequencies $\omega_\alpha/2\pi \approx$ 1 MHz, an array of $10 \times 10$ microtraps is still consistent with the maximum attainable trapping frequency. We note that the gradient can be reduced further (10 kHz) without compromising the efficiency of the PAT scheme and leading to larger systems with $N = 2500$ microtraps. Finally, we would like to remark that the scheme could be scaled even further by considering a local gradient that only affects a few sites and repeats periodically along one axis of the microtrap array. In order to assist the tunneling between the sites where the gradient is changed, while maintaining a homogeneous synthetic flux, an additional periodic driving with a suitable frequency and phase must also be introduced.

### *3.3. Synthetic gauge fields and phonon–phonon interactions*

The discussion of the PAT of phonons has focused on the quadratic Hamiltonians corresponding to the Coulomb-induced tunneling (30) and the periodic driving of the trap frequencies (36). However, as discussed in section 2, nonlinearities corresponding to the on-site interactions in equation (15) can be incorporated without modifying the assisted-tunneling scheme. In fact, this broadens the applicability of our many-body quantum simulator, since it also targets models of strongly interacting particles. To obtain such phonon–phonon interactions [5], strong nonlinearities in the trapping potential are required. Remarkably, one can exploit a different realization of the above dipole forces (33) in order to give rise to such nonlinearities. We denote the parameters of these new dipole forces by a wiggled bar in order to differentiate them from the dipole forces leading to periodic driving.

We consider that two additional laser beams leading to a dipole force have the same frequency, in a way that the beatnote $\tilde{\omega}_L = 0$, and equation (33) corresponds to a standing wave. In analogy to the previous expansion (34), we consider that $\tilde{\Omega}_L\tilde{\eta}_\alpha \ll \omega_\alpha$ so that all the terms that

**Table 2.** Mapping of microtrap phonons onto the PAT model.

| | | | | | | | |
|---|---|---|---|---|---|---|---|
| Equations (1), (15): | $a_{\sigma,\mathbf{i}}$ | $\sigma$ | $J^{\sigma}_{\mathrm{t};\mathbf{ij}}$ | $\omega_{\mathrm{d}}$ | $\eta_{\mathrm{d}}\omega_{\mathrm{d}}$ | $\phi_{\mathbf{i}}$ | $\tilde{U}_{\sigma\sigma'}$ |
| Equations (30), (38): | $b_{\alpha,\mathrm{i}}$ | $\alpha$ | $J^{\alpha}_{\mathrm{c};\mathbf{ij}}$ | $\omega_{\mathrm{L}}$ | $-\Omega_{\mathrm{L}}\eta_{\alpha}^2$ | $\Delta\mathbf{k}\cdot\mathbf{r}_{\mathrm{i}}^0$ | $\frac{1}{2}\tilde{\Omega}_{\mathrm{L}}\tilde{\eta}_{\alpha}^2\tilde{\eta}_{\gamma}^2\cos\tilde{\phi}_{\mathbf{i}}$ |

do not conserve the number of phonons can be neglected. However, since $\tilde{\omega}_{\mathrm{L}} = 0$, the quadratic terms now correspond to a small shift of the trapping frequencies, which has no effect since $\tilde{\Omega}_{\mathrm{L}}\tilde{\eta}_{\alpha}^2 \ll \Delta\omega_{\sigma} \ll \omega_{\alpha}$. The most relevant contribution is due to the quartic terms

$$\tilde{H}_{\mathrm{L}} \approx \sum_{\mathbf{i},\alpha,\gamma} \tilde{U}_{\mathbf{i},\alpha\gamma} b^{\dagger}_{\alpha,\mathbf{i}} b^{\dagger}_{\gamma,\mathbf{i}} b_{\gamma,\mathbf{i}} b_{\alpha,\mathbf{i}}, \quad \tilde{U}_{\mathbf{i},\alpha\gamma} = \frac{1}{2}\tilde{\Omega}_{\mathrm{L}}\tilde{\eta}_{\alpha}^2\tilde{\eta}_{\gamma}^2 \cos(\Delta\tilde{\mathbf{k}}\cdot\mathbf{r}_{\mathbf{i}}^0), \tag{38}$$

which corresponds exactly to the on-site interactions introduced in equation (15). In table 2, we summarize the mapping of the phonon Hamiltonian onto the original periodically driven tunneling Hamiltonian of section 2. As discussed there, since this interaction is purely local, it shall not be modified by the scheme of PAT. Therefore, the effective phonon Hamiltonian becomes $H_{\mathrm{eff}} = K_{\mathrm{eff}} + V_{\mathrm{eff}}$, where

$$\begin{aligned} K_{\mathrm{eff}} &= \sum_{\alpha} \sum_{\mathbf{i}>\mathbf{j}} \tilde{J}^{\alpha}_{\mathrm{d};\mathbf{ij}} \mathrm{e}^{\mathrm{i}e^* \int_{\mathbf{j}}^{\mathbf{i}} \mathrm{d}\mathbf{r}\cdot\mathbf{A}_{\mathrm{s}}} b^{\dagger}_{\alpha,\mathbf{i}} b_{\alpha,\mathbf{j}} + \mathrm{H.c.}, \\ V_{\mathrm{eff}} &= \sum_{\mathbf{i},\alpha,\gamma} \tilde{U}_{\mathbf{i},\alpha\gamma} b^{\dagger}_{\alpha,\mathbf{i}} b^{\dagger}_{\gamma,\mathbf{i}} b_{\gamma,\mathbf{i}} b_{\alpha,\mathbf{i}}, \end{aligned} \tag{39}$$

where the tunneling is $\tilde{J}^{\alpha}_{\mathrm{d};\mathbf{ij}} = J^{\alpha}_{\mathrm{t};\mathbf{ij}} \mathscr{F}_{f(\mathbf{i},\mathbf{j})}(\eta_{\mathrm{d}}, \eta_{\mathrm{d}}, \Delta\phi_{\mathbf{ij}})$, and the gauge field can be expressed as $\mathbf{A}_{\mathrm{s}}(\mathbf{x}) = -B_0 y \mathbf{e}_1$, such that $B_0 = (r\phi_2/e^* d_1 d_2)$. Equation (39) incorporates the central result of this section, which shows that the PAT in microtrap arrays leads to a quantum simulator of a long-range Bose–Hubbard model [42] under additional gauge fields [43].

There are several interesting regimes for this quantum simulator. In the non-interacting limit for a square microtrap array, it yields a bosonic *dipolar* version of the so-called *Azbel–Harper–Hofstadter model* [39]. The nearest-neighbor model has been studied thoroughly during the last few decades, and contains several interesting properties that range from its relation to topological numbers, to the fractal and self-similar properties of its energy spectrum and wavefunctions, the existence of gapless edge excitations or the so-called $\pi$-flux phases [40]. The addition of the long-range dipolar tunneling introduces a new feature in the model that, to the best of our knowledge, has not been studied previously and may modify the above phenomena. Besides, most of these effects rely on a magnetic flux per plaquette of the order of the flux quantum, which cannot be achieved in solid-state materials assuming realistic magnetic fields. In contrast, our proposal has the potential to reach these regimes since it is non-perturbative and the flux can attain arbitrary values $\phi_{\circlearrowleft} \in [0, 2\pi]$.

Since it is possible to build any desired microtrap geometry [30], our quantum simulator can explore the physics of *bosonic ladders* subjected to synthetic gauge fluxes. Besides, the capability of tuning the fluxes, together with the independent control of the tunneling strength along/across the ladder rungs, dives into the phenomena of *flat-band physics* and *edge states* [41], which is typical for fermionic topological insulators that break the time-reversal symmetry [45].

Another interesting regime corresponds to $|J^{\alpha}_{\mathrm{d};\mathbf{ij}}| \approx \tilde{U}_{\mathbf{i},\alpha\gamma}$, where the interactions compete with the kinetic energy and induce strong correlations in the Bose–Hubbard model [42]. With

respect to the neutral-atom realizations [44], the phonon model includes the effects of longer-range tunnelings, and the possibility of addressing site-dependent interactions. Besides, thanks to the tunability of the functions $\mathscr{F}_{f(\mathbf{i},\mathbf{j})}$ (figure 2), the strongly correlated regime can be reached, in principle, regardless of how small the on-site interactions are. Let us note, however, that there is a fundamental limit to this approach, which is imposed by external sources of decoherence and heating. Accordingly, the dynamics must always be faster than the time scale imposed by these sources of noise.

For vibrational modes transverse to the microtrap array $\alpha = z$, the condition $\tilde{\Omega}_{\mathrm{L}}\tilde{\eta}_{\alpha} \ll \omega_{\alpha}$ can be relaxed for ions in the node of the standing wave. It then suffices to set $\tilde{\Omega}_{\mathrm{L}}\tilde{\eta}_{\alpha}^{2} \ll \omega_{\alpha}$, which allows us to reach interaction strengths in the $\tilde{U} \sim 1$–$10\,\mathrm{kHz}$ regime, which are directly of the order of bare tunneling. Finally, including the gauge fields in this strongly correlated regime further enhances the versatility of our quantum simulator. Even if the particles are bosonic and the interactions are local, one can target *fractional quantum Hall states* and *composite-fermion fluids* [43].

### 3.4. Non-Abelian synthetic gauge fields

The synthetic gauge fields discussed so far (39) correspond to standard electromagnetism. In this theory, they are formally introduced to restore the invariance with respect to local unitary transformations in the gauge group U(1). A natural question that arises is whether these synthetic fields can be generalized to different gauge groups, possibly non-Abelian ones [48]. In this case, the local unitary also acts on some additional degree of freedom, which we shall refer to as the flavor. Here, we show that it is possible to realize such scenarios by exploiting two or three orthogonal directions of vibration as the different flavors of the non-Abelian theory.

We first exploit two main axes of vibration $\alpha = x, y$ within the plane defined by the microtrap array, the corresponding trapping frequencies being different $\omega_x \neq \omega_y$. In the regime where the bare tunneling strength is smaller than the frequency difference, these two directions are uncoupled (see equation (30)). The main idea is to use two gradients of opposite sign for each degree of freedom, and two separate periodic drivings of the same frequency but of different amplitudes

$$\begin{aligned}\omega_{x,\mathbf{i}} &= \omega_x + \Delta\omega i_1 + \eta_{\mathrm{d}x}\omega_{\mathrm{d}}\cos(\omega_{\mathrm{d}}t + \phi_{\mathbf{i}}),\\ \omega_{y,\mathbf{i}} &= \omega_y - \Delta\omega i_1 + \eta_{\mathrm{d}y}\omega_{\mathrm{d}}\cos(\omega_{\mathrm{d}}t + \phi_{\mathbf{i}}).\end{aligned} \tag{40}$$

According to equation (35), this modulation of the trap frequencies can be obtained from a single Raman-beam scheme, such that the corresponding wavevector has a component along both the axes $\eta_{\mathrm{d}x} = -\Omega_{\mathrm{L}}\eta_x^2$, $\eta_{\mathrm{d}y} = -\Omega_{\mathrm{L}}\eta_y^2$. By repeating the analysis of section 2 and considering the same type of conditions, we reveal that the dressed tunneling strengths (13) must be modified for each of the vibrational axes

$$J^{\alpha}_{\mathrm{d};\mathbf{ij}} = \tilde{J}^{\alpha}_{\mathrm{d};\mathbf{ij}}\mathrm{e}^{-\mathrm{i}\frac{f_{\alpha}(\mathbf{i},\mathbf{j})}{2}(\phi_{\mathbf{i}}+\phi_{\mathbf{j}})}, \qquad \tilde{J}^{\alpha}_{\mathrm{d};\mathbf{ij}} = J^{\alpha}_{\mathrm{t};\mathbf{ij}}\mathscr{F}_{f_{\alpha}(\mathbf{i},\mathbf{j})}(\eta_{\mathrm{d}\alpha}, \eta_{\mathrm{d}\alpha}, \Delta\phi_{\mathbf{ij}}), \tag{41}$$

where $f_{\alpha}(\mathbf{i},\mathbf{j}) = r_{\alpha}(i_1 - j_1)$, and one must introduce the following axis-dependent parameter $r_x = r, r_y = -r$. It is then straightforward to rewrite the effective Hamiltonian according to a generalized Peierls substitution

$$K_{\mathrm{eff}} = \sum_{\mathbf{i}>\mathbf{j}} \tilde{J}^{x}_{\mathrm{d};\mathbf{ij}}\mathrm{e}^{\mathrm{i}e^{*}\int_{\mathbf{j}}^{\mathbf{i}}\mathrm{d}\mathbf{r}\cdot\mathbf{A}^{x}_{\mathrm{s}}}b^{\dagger}_{x,\mathbf{i}}b_{x,\mathbf{j}} + \tilde{J}^{y}_{\mathrm{d};\mathbf{ij}}\mathrm{e}^{\mathrm{i}e^{*}\int_{\mathbf{j}}^{\mathbf{i}}\mathrm{d}\mathbf{r}\cdot\mathbf{A}^{y}_{\mathrm{s}}}b^{\dagger}_{y,\mathbf{i}}b_{y,\mathbf{j}} + \mathrm{H.c.}, \tag{42}$$

where the synthetic gauge potential now depends on the related vibrational axis, and is equivalent to $\mathbf{A}_{\mathrm{s}}^{x}(\mathbf{r}) = -\mathbf{A}_{s}^{y}(\mathbf{r}) = -B_0 y \mathbf{e}_1$, such that $B_0 = r\phi_2/e^* d_1 d_2$. Let us introduce now a bosonic spinor field operator $\Psi_{\mathbf{i}} = (b_{x,\mathrm{i}}, b_{y,i})^t$ to describe the phonon fields corresponding to vibrations in each direction. The kinetic part can be written as

$$K_{\mathrm{eff}} = \sum_{\mathbf{i}>\mathbf{j}} \Psi_{\mathbf{i}}^{\dagger} K_{\mathrm{d};\mathbf{ij}} \mathrm{e}^{\mathrm{i}e^* \int_{\mathrm{j}}^{\mathbf{i}} \mathrm{d}\mathbf{r}\cdot\mathbf{A}_{\mathrm{s}}^{\mathrm{na}}} \Psi_{\mathbf{j}} + \mathrm{H.c.}, \tag{43}$$

where $K_{\mathrm{d};\mathbf{ij}}$ is a matrix that describes the vibrational couplings for each spinor component,

$$K_{\mathrm{d};\mathbf{ij}} = \begin{pmatrix} \tilde{J}^{x}_{\mathrm{d};\mathbf{i},\mathbf{j}} & 0 \\ 0 & \tilde{J}^{y}_{\mathrm{d};\mathbf{i},\mathbf{j}} \end{pmatrix}, \tag{44}$$

and $\mathbf{A}_{\mathrm{s}}^{\mathrm{na}} = -B_0 y \tau_z \mathbf{e}_1$ is an SU(2) non-Abelian gauge field, which we write in terms of a Pauli matrix, $\tau_z$, acting on the vibrational index (i.e. flavor index). The associated magnetic field corresponds to $\mathbf{B}_{\mathrm{s}}^{\mathrm{na}} = B_0 \tau_z \mathbf{e}_z$, so that each flavor is subjected to an opposite flux piercing the lattice. For fermions, these types of gauge fields give rise to the so-called quantum spin Hall effect [49], which is the prototype of time-reversal preserving topological insulators in two dimensions [45]. We note that equation (43), together with the arguments presented in equation (19), implies that each flavor around a plaquette accumulates a non-Abelian Aharanov–Bohm phase that is governed solely by the SU(2) gauge field $\mathbf{A}_{\mathrm{s}}^{\mathrm{na}}$. However, in addition to that, each flavor $x$, $y$ is subjected to different tunnelings, $\tilde{J}^{x}_{\mathrm{d};\mathbf{i},\mathbf{j}}$, $\tilde{J}^{y}_{\mathrm{d};\mathbf{i},\mathbf{j}}$, such that a spin–orbit coupling is superimposed on the non-Abelian gauge. The latter effect may enrich the dynamics with respect to the usual situation in SU(2) gauge theories.

We remark that the above synthetic gauge field (43) is only a particular type of non-Abelian SU(2) gauge field. In order to consider more general fields, it is possible to exploit the quadratic terms of the Coulomb interaction (28) that mix the vibrational modes along $x$, $y$. By setting the frequency of the periodic driving to account for both the frequency difference ($\omega_x \neq \omega_y$) and the particular gradient, the dressed tunneling would also involve a change of the flavor index, yielding thus more general gauge fields in the group SU(2).

### *3.5. Spin-mediated disordered Hamiltonians*

The properties of solids usually differ from those of perfectly periodic crystals. In realistic samples, there is a certain amount of disorder in the form of impurities, dislocations or vacancies, which may alter dramatically the properties of the solid. The study of disorder in solids is an active and mature field of condensed matter [50], where the system Hamiltonians are usually modeled as stochastic operators. Here, the randomness is due to a statistical description of the disordered degrees of freedom. To incorporate such a randomness into a quantum simulator, which by definition should be an extremely clean and controllable setup, one can exploit the quantum parallelism by an auxiliary degree of freedom [51].

In principle, some randomness could be introduced by randomly varying the lattice constant and the trapping frequencies within the microtrap array. In the limit of large arrays, these would lead to an off-diagonal bond disorder and diagonal site disorder, respectively. In this subsection, we elaborate on two alternative directions to widen the applicability of the phonon-based quantum simulator by introducing disorder regardless of the size of the microtrap array. In both cases, we shall make use of the electronic energy levels of the ion, $\{|\uparrow_{\mathbf{i}}\rangle, |\downarrow_{\mathbf{i}}\rangle\}$, to introduce randomness in the phonon Hamiltonian and mimic the effects of disorder. We

emphasize that this setup shall allow us to control the two usual types of disorder independently, namely diagonal and off-diagonal disorder.

*3.5.1. Off-diagonal bond disorder.* We discuss how to induce randomness on the phonon tunneling by a slight modification of equation (35), so that the periodic driving will be responsible for both the disorder and the synthetic gauge fields. In the derivation of the driving, we assumed that a proper choice of the laser intensities, detunings and polarizations would lead us from equation (32) to the desired expression (33). This condition can be modified so that the periodic driving becomes spin dependent. In fact, by setting $\Omega_{\rm L} = (\Omega_{\rm ag}^{(1)})^{*}\Omega_{\rm ag}^{(2)}/2\Delta = -(\Omega_{\rm ae}^{(1)})^{*}\Omega_{\rm ae}^{(2)}/2\Delta$, one obtains

$$H_{\rm L} = \tfrac{1}{2}\Omega_{\rm L}\sum_{\mathbf{i}}\sigma_{\mathbf{i}}^{z}\mathrm{e}^{\mathrm{i}(\Delta\mathbf{k}\cdot\mathbf{r}_{\mathbf{i}}-\omega_{\rm L}t)} + \mathrm{H.c.}, \tag{45}$$

where we have introduced $\sigma_{\mathbf{i}}^{z} = |{\uparrow_{\mathbf{i}}}\rangle\langle{\uparrow_{\rm i}}| - |{\downarrow_{i}}\rangle\langle{\downarrow_{i}}|$. This expression corresponds to a differential Stark shift between the two electronic levels. In the regime where $\omega_{\rm L} \ll \omega_{\alpha}$, this term generalizes equation (35) to the following spin-dependent driving of the trapping frequencies:

$$H_{\rm L} \approx -\Omega_{\rm L}\sum_{\alpha,\mathbf{i}}\eta_{\alpha}^{2}\cos(\Delta\mathbf{k}\cdot\mathbf{r}_{\mathbf{i}}^{0} - \omega_{\rm L}t)\sigma_{\mathbf{i}}^{z}b_{\alpha,\mathbf{i}}^{\dagger}b_{\alpha,\mathbf{i}}, \tag{46}$$

where the same constraints (36) over the system parameters must be fulfilled. Since no other spin operators are involved in the Hamiltonian, one can treat $\sigma_{\mathbf{i}}^{z}$ as $c$-numbers $\sigma_{\mathbf{i}} \in \{-1, 1\}$ and carry out the same analysis made in section 2. In fact, one should simply modify Hamiltonian (39) to $H_{\rm eff} = \sum_{\{\boldsymbol{\sigma}\}} H_{\rm eff}(\{\boldsymbol{\sigma}\})|\{\boldsymbol{\sigma}\}\rangle\langle\{\boldsymbol{\sigma}\}|$, where $H_{\rm eff}(\{\boldsymbol{\sigma}\}) = K_{\rm eff}(\{\boldsymbol{\sigma}\}) + V_{\rm eff}$, such that

$$K_{\rm eff}(\{\boldsymbol{\sigma}\}) = \sum_{\alpha}\sum_{\mathbf{i}>\mathbf{j}}\tilde{J}_{\mathrm{d};\mathbf{ij}}^{\alpha}(\sigma_{\mathbf{i}},\sigma_{\mathbf{j}})\mathrm{e}^{\mathrm{i}e^{*}\int_{\mathbf{j}}^{\mathbf{i}}\mathrm{d}\mathbf{r}\cdot\mathbf{A}_{\rm s}}b_{\alpha,\mathbf{i}}^{\dagger}b_{\alpha,\mathbf{j}} + \mathrm{H.c.}, \tag{47}$$

and the tunneling amplitudes account for the different spin configurations $\tilde{J}_{\mathrm{d};\mathbf{ij}}^{\alpha}(\sigma_{\mathbf{i}},\sigma_{\mathbf{j}}) = J_{\mathrm{t};\mathbf{ij}}^{\alpha}\mathscr{F}_{f(\mathbf{i},\mathbf{j})}(\eta_{\rm d}\sigma_{\mathbf{i}},\eta_{\rm d}\sigma_{\mathbf{j}},\Delta\phi_{\mathbf{ij}})$. In figure 7, we represent the dressed tunneling amplitudes between nearest neighbors along the direction of the gradient. It can be observed that depending on the spin state, one obtains different values. In particular, for $\eta_{\rm d} \approx 1$ and $\Delta\phi \approx 3\pi/2$, the tunneling amplitude can attain four possible values

$$\mathscr{F}_{1}^{\uparrow\downarrow} = -\mathscr{F}_{1}^{\downarrow\uparrow} = \mathbf{i}\mathscr{F}_{1}^{\downarrow\downarrow} = -\mathbf{i}\mathscr{F}_{1}^{\uparrow\uparrow} \approx 0.5. \tag{48}$$

If we now consider the following initial state: $\rho_0 = |\Psi_{\rm s}\rangle\langle\Psi_{\rm s}| \otimes \rho_{\rm ph}^{0}$, where $|\Psi_{\rm s}\rangle = \sum_{\{\boldsymbol{\sigma}\}} c_{\{\boldsymbol{\sigma}\}}|\{\boldsymbol{\sigma}\}\rangle$ and $\rho_{\rm ph}^{0}$ are arbitrary spin and phonon states, then its time evolution is

$$\rho_{\rm ph}(t) = \mathrm{tr}_{s}\{\rho(t)\} = \sum_{\{\boldsymbol{\sigma}\}}|c_{\{\boldsymbol{\sigma}\}}|^{2}\mathrm{e}^{-\mathrm{i}H_{\rm eff}(\{\boldsymbol{\sigma}\})t}\rho_{\rm ph}^{0}\mathrm{e}^{+\mathrm{i}H_{\rm eff}(\{\boldsymbol{\sigma}\})t}. \tag{49}$$

Note that due to the superposition principle of quantum mechanics, the phonon state explores simultaneously the different tunneling paths $\mathbf{i} \to J(\sigma_{\mathbf{i}}\sigma_{\mathbf{j}}) \to \mathbf{j}$ with a probability that depends on the initial spin configuration $p_{\{\boldsymbol{\sigma}\}} = |c_{\{\boldsymbol{\sigma}\}}|^{2}$. In fact, the measurement of a phonon observable $O_{\rm ph}$ corresponds directly to the statistical average over all such tunneling paths

$$\begin{aligned}\langle O_{\rm ph}(t)\rangle &= \sum_{\{\boldsymbol{\sigma}\}} p_{\{\boldsymbol{\sigma}\}}\mathrm{tr}\{O_{\rm ph}\mathrm{e}^{-\mathrm{i}H_{\rm eff}(\{\boldsymbol{\sigma}\})t}\rho_{\rm ph}^{0}\mathrm{e}^{+\mathrm{i}H_{\rm eff}(\{\boldsymbol{\sigma}\})t}\}\\ &= \sum_{\{\boldsymbol{\sigma}\}} p_{\{\boldsymbol{\sigma}\}}\langle O_{\rm ph}^{\{\boldsymbol{\sigma}\}}(t)\rangle,\end{aligned} \tag{50}$$

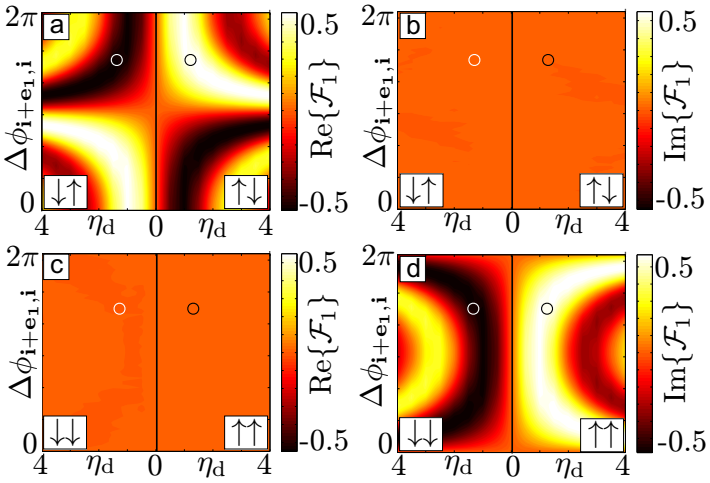


**Figure 7.** Spin-dependent modulation of the tunneling: contour plot of the real and imaginary parts of the modulation amplitude $\mathscr{F}_{r(i_1-j_1)}$ for the tunneling between nearest neighbors $\mathbf{i} \to \mathbf{j}$, such that $i_1 = j_1 + 1$, as a function of the driving parameters $\eta_d$, $\Delta\phi_{\mathbf{ij}}$ for $r = 1$. (a, b) Tunneling in the configuration of anti-parallel spins $\sigma_\mathbf{i}, \sigma_\mathbf{j} \in \{\uparrow\downarrow, \downarrow\uparrow\}$, (c, d) Tunneling in the configuration of parallel spins $\sigma_\mathbf{i}, \sigma_\mathbf{j} \in \{\uparrow\uparrow, \downarrow\downarrow\}$. Also shown in black-white circles is the region of interest for $\eta_d \approx 1$, $\Delta\phi_{ij} = 3\pi/2$.

which can be understood as the average over all possible realizations of the bond disorder. Therefore, our phonon-based simulator can explore the physics of interacting disordered bosons in a lattice pierced by an external magnetic field.

*3.5.2. Diagonal site disorder.* We now address a scheme to introduce randomness in the on-site energies [22]. The origin of such terms is independent of the periodic driving, and requires a pair of additional laser beams in the Raman configuration (31). In order to distinguish them from the previous laser beams, we will denote them with an overbar. The main difference with respect to the previous case is that the beatnote is tuned close to the transition between the internal states $\bar{\omega}_L = \bar{\omega}_1 - \bar{\omega}_2 \approx \omega_0$. In this case, the laser–ion Hamiltonian becomes

$$\bar{H}_L = \tfrac{1}{2}\bar{\Omega}_L \textstyle\sum_\mathbf{i} \sigma_\mathbf{i}^+ e^{i(\Delta\mathbf{k}\cdot\mathbf{r}_\mathbf{i} - (\omega_0 - \bar{\omega}_L)t)} + \mathrm{H.c.}, \tag{51}$$

where we have introduced $\sigma_\mathbf{i}^+ = |\uparrow_i\rangle\langle\downarrow_\mathbf{i}|$. In analogy to the derivation of the periodic driving, we express the position in terms of the local phonon operators, and expand the Hamiltonian for a small Lamb–Dicke parameter. If the laser beatnote is tuned as follows: $\bar{\omega}_L \approx \omega_0 - \omega_\alpha$, one obtains the so-called red-sideband excitation

$$\bar{H}_L \approx i\tfrac{1}{2}\bar{\Omega}_L \textstyle\sum_{\alpha,\mathbf{i}} \eta_\alpha e^{i\Delta\mathbf{k}\cdot\mathbf{r}_\mathbf{i}^0} \sigma_\mathbf{i}^+ b_{\alpha,\mathbf{i}} e^{-i\bar{\delta}_L t} + \mathrm{H.c.}, \tag{52}$$

where the bare detuning is $\bar{\delta}_L = \omega_0 - \omega_\alpha - \bar{\omega}_L \ll \omega_\alpha$, and we assume that $\bar{\Omega}_L \ll \omega_\alpha$ in order to neglect the remaining terms of the Taylor expansion. In the regime where the laser beams are weak enough $\bar{\Omega}_L \eta_\alpha \ll \bar{\delta}_L$, it is possible to find the following laser–ion Hamiltonian in perturbation theory:

$$\bar{H}_L \approx \sum_{\alpha,\mathbf{i}} \varepsilon_\alpha \sigma_\mathbf{i}^z b_{\alpha,\mathbf{i}}^\dagger b_{\alpha,\mathbf{i}}, \quad \varepsilon_\alpha = \frac{\bar{\Omega}_L^2 \eta_\alpha^2}{4\bar{\delta}_L}. \tag{53}$$

This term arises due to a second-order process where a phonon is virtually excited and re-absorbed by a single ion, and leads to a differential Stark shift of the atomic levels that depends on the number of phonons. When incorporated into the effective description of the PAT Hamiltonian (39), it modifies the kinetic energy term. If one is interested in the time span $t \approx 1/J_{\mathrm{c};\mathbf{ij}}$, the dynamics of the spins can be safely ignored, and $\sigma_{\mathbf{i}}^{z}$ can be treated once more as $c$-numbers $\sigma_{\mathbf{i}} \in \{-1, 1\}$. We note that the typical time scales for the spin flip-flop dynamics would be $J_{\mathrm{s};\mathbf{ij}} \approx$10–100 Hz, whereas the vibrational couplings lie in the range $J_{\mathrm{c};\mathbf{ij}} \approx$ 1–10 kHz. Accordingly, the kinetic energy term of equation (39) must be modified to $H_{\mathrm{eff}}(\{\boldsymbol{\sigma}\}) = K_{\mathrm{eff}}(\{\boldsymbol{\sigma}\}) + V_{\mathrm{eff}}$, where

$$K_{\mathrm{eff}}(\{\boldsymbol{\sigma}\}) = \sum_{\alpha} \sum_{\mathbf{i}>\mathbf{j}} \tilde{J}^{\alpha}_{\mathrm{d};\mathbf{ij}} \mathrm{e}^{\mathrm{i}e^{*} \int_{\mathbf{j}}^{\mathbf{i}} \mathrm{d}\mathbf{r}\cdot\mathbf{A}_{\mathrm{s}}} b^{\dagger}_{\alpha,\mathbf{i}} b_{\alpha,\mathbf{j}} + \frac{\varepsilon_{\alpha}}{2} \sigma_{\mathbf{i}} b^{\dagger}_{\alpha,\mathbf{i}} b_{\alpha,\mathbf{i}} + \mathrm{H.c.} \tag{54}$$

In this situation, it is not the tunneling strengths which depend upon the spin state (47), but rather the on-site energies. Note that the strength of these on-site energies must be much smaller than the trapping gradient $\epsilon_{\alpha} \ll \Delta\omega_{\alpha}$ in order not to affect the PAT scheme. According to equation (50), the system explores simultaneously all possible values of the on-site energies with probabilities that depend on the spin configurations of the initial state. Therefore, the measurement of phonon observables yields directly the statistical average over all possible realizations of $\varepsilon_{j}(\{\boldsymbol{\sigma}\}) \in \{-\varepsilon_{\alpha}, \varepsilon_{\alpha}\}$ with a probability distribution $p_{\{\boldsymbol{\sigma}\}} = |c_{\{\boldsymbol{\sigma}\}}|^{2}$.

Let us now comment on the extended possibilities of our quantum simulator due to the engineered disorder in equations (47) and (54). The diagonal site disorder leads to the well-known *Anderson localization* in the non-interacting limit [53]. This phenomenon is due to the interference of the different paths associated with the scattering of the particles from the random on-site fluctuations, and gives rise to exponentially localized wavefunctions and absence of diffusion. The combination of Anderson localization with strong interactions, which is also a well-studied problem [42], leads to interesting insulating, yet gapless, phases such as the *Bose glass*. In the case of strong bond disorder, a different gapless insulator known as the *Mott glass* arises, which consists of disconnected superfluid regions of random size [52]. Besides, our quantum simulator has the potential for combining both bond and site disorder, and tuning them independently, which may pave the way towards other exotic insulating phases. In addition to the aforementioned Bose and Mott glasses, the simulator can explore the *random-singlet glass* where the bosons form delocalized random pairs [54]. The possibility of exploring higher-dimensions, longer-range tunnelings and the effect of synthetic gauge fields makes our scheme a very versatile tool.

### *3.6. Decorated synthetic gauge flux lattices*

In this section, we describe an additional feature of our quantum simulator: the possibility of decorating the lattice with any desired pattern of synthetic fluxes. It is thus possible to engineer highly inhomogeneous synthetic gauge fields, even reaching inhomogeneities at the unit-cell limit. The idea is to use the spins to decorate the array with different fluxes by exploiting the differential phonon-dependent Stark shift (53).

We consider a situation where the gradient of the trapping frequencies vanishes $\Delta\omega_{\alpha} = 0$, so that the regime is different from that of the site-disorder case considered above $\varepsilon_{\alpha} \ll \Delta\omega_{\alpha}$. When the periodic driving frequency (35) and the Stark shift (53) fulfill the resonance condition $\omega_{\mathrm{L}} = 2\varepsilon_{\alpha}/r$, where $r$ is the integer representing the number of photons involved in the PAT,

the assisted tunneling will give rise to a different phase depending on the spin states of the two neighboring ions. In order to find the correct expression for the tunneling, we re-address the derivation of section 2 for this particular spin-dependent situation. Since we are interested in the phonon dynamics, the spins are effectively frozen, and we can consider $\sigma_{\mathbf{i}}^{z}$ as $c$-numbers $\sigma_{\mathbf{i}} \in \{-1, 1\}$. Hence, the dressed tunneling (13) must be modified as follows:

$$J_{\mathrm{d};\mathbf{ij}}^{\alpha} = \tilde{J}_{\mathrm{d};\mathbf{ij}}^{\alpha} \mathrm{e}^{-\mathrm{i}\frac{f(\sigma_{\mathbf{i}},\sigma_{\mathbf{j}})}{2}(\phi_{\mathbf{i}}+\phi_{\mathbf{j}})}, \quad \tilde{J}_{\mathrm{d};\mathbf{ij}}^{\alpha} = J_{\mathrm{t};\mathbf{ij}}^{\alpha} \mathscr{F}_{f(\sigma_{\mathbf{i}},\sigma_{\mathbf{j}})}(\eta_{\mathrm{d}}, \eta_{\mathrm{d}}, \Delta\phi_{\mathbf{ij}}), \tag{55}$$

where we have introduced $f(\sigma_{\mathbf{i}}, \sigma_{\mathbf{j}}) = r(\sigma_{\mathbf{i}} - \sigma_{\mathbf{j}})/2$. By considering the possible spin configurations, we find that

$$\frac{J_{\mathrm{d};\mathbf{ij}}^{\alpha}(\{\boldsymbol{\sigma}\})}{J_{\mathrm{t};\mathbf{ij}}^{\alpha}} = \begin{cases} \mathscr{F}_{r}(\eta_{\mathrm{d}}, \eta_{\mathrm{d}}, \Delta\phi_{\mathbf{ij}})\mathrm{e}^{-\mathrm{i}\frac{r}{2}(\phi_{\mathbf{i}}+\phi_{\mathbf{j}})} & \text{if } \sigma_{\mathbf{i}} = -\sigma_{\mathbf{j}} = 1, \\ \mathscr{F}_{-r}(\eta_{\mathrm{d}}, \eta_{\mathrm{d}}, \Delta\phi_{\mathbf{ij}})\mathrm{e}^{+\mathrm{i}\frac{r}{2}(\phi_{\mathbf{i}}+\phi_{\mathbf{j}})} & \text{if } \sigma_{\mathbf{j}} = -\sigma_{\mathbf{i}} = 1, \\ \mathscr{F}_{0}(\eta_{\mathrm{d}}, \eta_{\mathrm{d}}, \Delta\phi_{\mathbf{ij}}) & \text{if } \sigma_{\mathbf{j}} = \sigma_{\mathbf{i}} = \pm 1. \end{cases} \tag{56}$$

Interestingly, the phase of the tunneling between sites $\mathbf{j} \to \mathbf{i}$ depends on their internal spin state $\sigma_{\mathbf{j}} \to \sigma_{\mathbf{i}}$. If their spins are parallel $\sigma_{\mathbf{i}} = \sigma_{\mathbf{j}} = \pm 1$, the phase vanishes and thus the tunneling does not contribute to the synthetic gauge field. Conversely, when the spins are anti-parallel, the phases contribute to the gauge fluxes with a sign that depends on the particular spin ordering. We have calculated the consecutive phonon tunneling around a square plaquette $\mathbf{r}_{\mathbf{i}}^{0} \to \mathbf{r}_{\mathbf{j}}^{0} \to \mathbf{r}_{\mathbf{k}}^{0} \to \mathbf{r}_{\mathbf{l}}^{0} \to \mathbf{r}_{\mathbf{i}}^{0}$ for all the possible spin configurations

$$W_{\circlearrowleft}^{(1)} = J_{\mathrm{d};\mathbf{il}}^{\alpha}(\sigma_{\mathbf{i}}, \sigma_{\mathbf{l}}) J_{\mathrm{d};\mathbf{lk}}^{\alpha}(\sigma_{\mathbf{l}}, \sigma_{\mathbf{k}}) J_{\mathrm{d};\mathbf{kj}}^{\alpha}(\sigma_{\mathbf{k}}, \sigma_{\mathbf{j}}) J_{\mathrm{d};\mathbf{ji}}^{\alpha}(\sigma_{\mathbf{j}}, \sigma_{\mathbf{i}}). \tag{57}$$

All the possible encircled fluxes $W_{\circlearrowleft}^{(1)} = |W_{\circlearrowleft}^{(1)}|\mathrm{e}^{\mathrm{i}\phi_{\circlearrowleft}(\{\boldsymbol{\sigma}\})}$ for $r = 1$ have been represented in figure 8(a), where we observe that there are nine possible fluxes out of the $2^4 = 16$ possible spin configurations. These fluxes correspond to $\phi_{\circlearrowleft} \in \{0, \pm\phi_1, \pm\phi_2, \pm\phi_+, \pm\phi_-\}$, where $\phi_i = \Delta k_i d_i$ and $\phi_{\pm} = (\phi_1 \pm \phi_2)/2$. Accordingly, we have nine different tiles that can be used to decorate the underlying microtrap array with a particular distribution of fluxes. Let us emphasize that the particular distribution of tiles is completely determined by the spin state $|\Psi_{\mathrm{s}}\rangle = |\sigma_1, \ldots, \sigma_N\rangle$, which can be initialized at will in trapped-ion experiments. Let us also note that we could also exploit this result to introduce randomness in the gauge fields by considering a linear superposition of the spin states.

In figures 8(b) and (c), we represent two-color flux lattices that correspond to a staggered magnetic field along both the principal axes. In figures 8(d) and (e), we represent three-color flux lattices where a staggered flux alternates with a vanishing flux. In figure 8(f), we represent a checkerboard flux lattice, and finally in figure 8(g), we represent a limiting case of a six-color flux lattice, which is very interesting from a physical point of view. By setting $\phi_1 = \pi$, and $\phi_2 = \pi$, the two fluxes $\pm\phi_1 = \pm\pi = \pi \mathrm{mod} 2\pi$ are equivalent, and lead to a homogeneous $\pi$-flux model in a square lattice. Additionally, the four remaining fluxes vanish for this choice $\pm\phi_+ = \pm\phi_- = 0 \,\mathrm{mod} 2\pi$. Therefore they contribute with a local defect over the $\pi$-flux lattice, which could bind excitations with *anyonic statistics* when the longer-range tunnelings are taken into account [55].

For each of the decorated flux lattices, it is possible to find a particular inhomogeneous synthetic gauge field $\mathbf{A}_{\mathrm{s}}(\sigma_{\mathbf{i}}, \sigma_{\mathbf{j}})$ so that the effective phonon Hamiltonian is rewritten in a standard Peierls form

$$K_{\mathrm{eff}}(\{\boldsymbol{\sigma}\}) = \sum_{\alpha} \sum_{\mathbf{i}>\mathbf{j}} \tilde{J}_{\mathrm{d};\mathbf{ij}}^{\alpha}(\sigma_{\mathbf{i}}, \sigma_{\mathbf{j}}) \mathrm{e}^{\mathrm{i}e\int_{\mathbf{j}}^{\mathbf{i}} \mathrm{d}\mathbf{x}\cdot\mathbf{A}_{\mathrm{s}}(\sigma_{\mathbf{i}},\sigma_{\mathbf{j}})} b_{\alpha,\mathbf{i}}^{\dagger} b_{\alpha,\mathbf{j}} + \mathrm{H.c.} \tag{58}$$

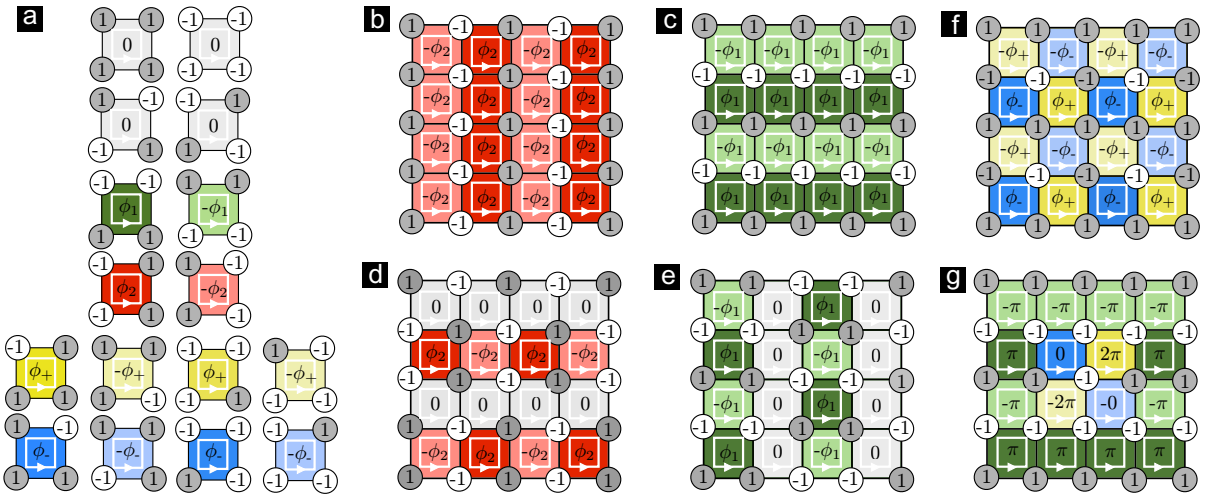


**Figure 8.** Decorated synthetic flux lattices. (a) Unit cell for a square array of microtraps with all possible configurations of spin states $\sigma_{\mathbf{i}} \in \{1, -1\}$, which are represented by circles at the vertices of the cell. According to the spin-dependent enclosed flux, we have a total of nine different plaquettes that can act as tiles to construct the decorated flux lattices. (b, c) Staggered flux lattices. (d, e) Staggered flux lattices with alternating strings of zero-flux plaquettes. (f) Tetra-flux checkerboard lattice. (g) $\pi$-flux lattice with a localized defect consisting of a zero-flux plaquette.

The particular pattern of the spins will determine the inhomogeneous gauge field, and the way the lattice is decorated with fluxes. Let us also note that the complexity of figure 8 will increase when the larger plaquettes due to long-range tunnelings are also taken into account.

## 4. Summary and outlook

We have introduced the two key ingredients for realizing PAT experiments in micro-fabricated ion traps. The first ingredient is a gradient of the trapping frequencies achieved by the local control of the trap electrodes. The second corresponds to a Raman-beam configuration, which presents different regimes that provide (i) the periodic driving of the trapping frequencies, (ii) the on-site phonon–phonon interactions, (iii) the bond/site disorder and also (iv) an exotic flux decoration of the microtrap array. We believe that such ingredients are within reach of current microtrap technology, and their correct combination will give rise to a very versatile quantum simulator for many-body bosonic models. Such a *PAT toolbox* for quantum simulations can be summarized in the following general Hamiltonian: $H_{\mathrm{eff}} = \sum_{\{\boldsymbol{\sigma}\}} (K_{\mathrm{eff}}(\{\boldsymbol{\sigma}\}) + V_{\mathrm{eff}}) |\{\boldsymbol{\sigma}\}\rangle\langle\{\boldsymbol{\sigma}\}|$, where

$$K_{\mathrm{eff}}(\{\boldsymbol{\sigma}\}) = \sum_{\alpha} \sum_{\mathbf{i}>\mathbf{j}} \tilde{J}^{\alpha}_{\mathrm{d};\mathbf{ij}}(\sigma_{\mathbf{i}}, \sigma_{\mathbf{j}}) \mathrm{e}^{\mathrm{i}e^{*} \int_{\mathbf{j}}^{\mathbf{i}} \mathrm{d}\mathbf{r}\cdot\mathbf{A}^{\alpha}_{\mathrm{s}}(\sigma_{\mathbf{i}},\sigma_{\mathbf{j}})} b^{\dagger}_{\alpha,\mathbf{i}} b_{\alpha,\mathbf{j}} + \sum_{\alpha} \sum_{\mathbf{i}} \frac{\varepsilon_{\alpha}}{2} \sigma_{\mathbf{i}} b^{\dagger}_{\alpha,\mathbf{i}} b_{\alpha,\mathbf{i}} + \mathrm{H.c.},$$

$$V_{\mathrm{eff}} = \sum_{\mathbf{i},\alpha,\gamma} \tilde{U}_{\mathbf{i},\alpha\gamma} b^{\dagger}_{\alpha,\mathbf{i}} b^{\dagger}_{\gamma,\mathbf{i}} b_{\gamma,\mathbf{i}} b_{\alpha,\mathbf{i}}, \tag{59}$$

where the particular expression for the dressed tunneling and synthetic gauge field will depend on the configuration of the frequency gradient and the periodic driving. Let us list the possibilities that have been explored in this work:

(i) *Dynamic localization:* The tunneling amplitude $\tilde{J}^{\alpha}_{\mathrm{d};\mathbf{ij}} = J^{\alpha}_{\mathrm{t};\mathbf{ij}}\mathscr{F}_0(\eta_{\mathrm{d}}, \eta_{\mathrm{d}}, \Delta\phi_{\mathbf{ij}})$ does not depend on the spin state, and the synthetic gauge field vanishes $\mathbf{A}^{\alpha}_{\mathrm{s}} = 0$. This is achieved in the regime of vanishing gradient $\Delta\omega_{\alpha} = 0$, and setting the beatnote of the Raman beams $\omega_{\mathrm{L}} \ll \omega_{\alpha}$. By tuning $\eta_{\mathrm{d}}$, one can find a value where the tunneling strength vanishes and thus the particles are dynamically localized, a phenomenon also known as coherent destruction of tunneling [25].

(ii) *Synthetic Abelian gauge fields:* The spin-independent tunneling amplitude is $\tilde{J}^{\alpha}_{\mathrm{d};\mathbf{ij}} = J^{\alpha}_{\mathrm{t};\mathbf{ij}}\mathscr{F}_{f(\mathbf{i},\mathbf{j})}(\eta_{\mathrm{d}}, \eta_{\mathrm{d}}, \Delta\phi_{\mathbf{ij}})$, where $f(\mathbf{i},\mathbf{j}) = r(i_1 - j_1)$ depends on an integer $r$. The synthetic gauge potential is $\mathbf{A}_{\mathrm{s}}(\mathbf{r}) = -B_0 y\mathbf{e}_1$, and follows from the regime with a finite gradient $\Delta\omega_{\alpha} \gg J^{\alpha}_{\mathrm{t};\mathbf{ij}}$, such that the beatnote of the Raman laser beams fulfills the resonance condition $\omega_{\mathrm{L}} = \Delta\omega_{\alpha}/r$. In this case, phonons behave as charged particles that move in a 2D plane pierced by an orthogonal magnetic field whose flux $\phi_2 = \Delta k_2 d_2$ can be modified by varying the Raman wavevector. Phenomena typical of integer quantum Hall samples [39, 40], or bosonic flux ladders [41], can also be observed in this platform. Besides, in combination with strong phonon–phonon interactions, one can find bosonic versions of the fractional quantum Hall states [43].

(iii) *Synthetic non-Abelian gauge fields:* The above scheme can be generalized to the non-Abelian gauge group SU(2), such that both in-plane vibrational modes play the role of a flavor component. We have described in detail a particular SU(2) gauge field, which requires the vibrations along each direction to be subjected to an opposite frequency gradient. Using the same assumptions as in the Abelian case, the tunneling amplitude becomes $\tilde{J}^{\alpha}_{\mathrm{d};\mathbf{ij}} = J^{\alpha}_{\mathrm{t};\mathbf{ij}}\mathscr{F}_{f_{\alpha}(\mathbf{i},\mathbf{j})}(\eta_{\mathrm{d}\alpha}, \eta_{\mathrm{d}\alpha}, \Delta\phi_{\mathbf{ij}})$, with $f_{\alpha}(\mathbf{i},\mathbf{j}) = r_{\alpha}(i_1 - j_1)$ such that $r_x = -r_y = r$. Hence, the synthetic gauge field $\mathbf{A}^{\mathrm{na}}_{\mathrm{s}} = -B_0 y\tau_z\mathbf{e}_1$ becomes an SU(2) operator acting in the flavor space. This scheme opens a route towards a bosonic counterpart of the quantum spin Hall effect [49].

(iv) *Bond and site disorder:* The dressed-tunneling amplitude $\tilde{J}^{\alpha}_{\mathrm{d};\mathbf{ij}}(\sigma_{\mathbf{i}}, \sigma_{\mathbf{j}}) = J^{\alpha}_{\mathrm{t};\mathbf{ij}}\mathscr{F}_{f(\mathbf{i},\mathbf{j})}(\eta_{\mathrm{d}}\sigma_{\mathbf{i}}, \eta_{\mathrm{d}}\sigma_{\mathbf{j}}, \Delta\phi_{\mathbf{ij}})$, and the on-site energies $\varepsilon_{\alpha}\sigma_{\mathbf{i}}$, take on different values depending on the spin configuration. If the initial state is a linear superposition of different spin configurations, the phonon dynamics is determined by a random Hamiltonian with bond and site disorder. This regime is achieved for a gradient $\Delta\omega_{\alpha} \gg J^{\alpha}_{\mathrm{t};\mathbf{ij}}$ and laser beatnote $\omega_{\mathrm{L}} = \Delta\omega_{\alpha}/r$ giving rise to a state-dependent periodic driving. Besides, an additional Raman beatnote tuned close to the atomic transition $\bar{\omega}_{\mathrm{L}} \approx \omega_0 - \omega_{\alpha}$ gives rise to a phonon-dependent Stark shift in the limit of large detuning. In the non-interacting regime, this tool allows us to explore the physics of Anderson localization [53]. By adding strong interactions, it yields gapless insulating phases such as the Bose glass [42], the Mott glass [52] and the random-singlet glass [54].

(vi) *Decorated flux lattices:* In the absence of the frequency gradient, one can tune the Raman lasers beatnote in resonance to the above phonon-dependent Stark shift $\omega_{\mathrm{L}} = 2\varepsilon_{\alpha}/r$. Once again, the dressed-tunneling amplitude becomes spin-dependent $\tilde{J}^{\alpha}_{\mathrm{d};\mathbf{ij}}(\sigma_{\mathbf{i}}, \sigma_{\mathbf{j}}) = J^{\alpha}_{\mathrm{t};\mathbf{ij}}\mathscr{F}_{f(\sigma_{\mathbf{i}},\sigma_{\mathbf{j}})}(\eta_{\mathrm{d}}, \eta_{\mathrm{d}}, \Delta\phi_{\mathbf{ij}})$ where $f(\sigma_{\mathbf{i}}, \sigma_{\mathbf{j}}) = r(\sigma_{\mathbf{i}} - \sigma_{\mathbf{j}})/2$. Moreover, the synthetic gauge field also depends on the spin configuration and we can make decorated flux lattices as

those shown in figure 8 by selecting a particular spin state. Phenomena related to charged particles under inhomogeneous magnetic fields can be explored, such as staggered fields or $\pi$-flux lattices with defects.

## Acknowledgment

This work was partially supported by the EU Specific Targeted Research Projects (STREPs) HIP, PICC, QUITEMAD S2009-ESP-1594, FIS2009-10061, CAM-UCM/910758 and Ramón y Cajal (RyC) contract no. Y200200074.

## References

[1] Anderson P W 1972 *Science* **177** 393
[2] Feynman R P 1972 *Statistical Mechanics: A Set of Lectures* (Massachusetts: Benjamin-Cummings)
[3] Feynman R P 1982 *Int. J. Theor. Phys.* **21** 467
[4] Blatt R and Wineland D 2008 *Nature* **453** 1008
[5] Porras D and Cirac J I 2004 *Phys. Rev. Lett.* **93** 263602
Deng X-L, Porras D and Cirac J I 2008 *Phys. Rev.* A **77** 03303
[6] Schneider C, Porras D and Schaetz T 2012 *Rep. Prog. Phys.* **75** 024401
[7] Cirac J I and Zoller P 1995 *Phys. Rev. Lett.* **74** 4091
Monroe C *et al* 1995 *Phys. Rev. Lett.* **75** 4714
Schmidt-Kaler F *et al* 2003 *Nature* **422** 408
[8] Brickman K-A and Soderberg Monroe C 2010 *Rep. Prog. Phys.* **73** 036401
[9] Cirac J I and Zoller P 2000 *Nature* **404** 579
Milburn G J, Schneider S and James D F V 2000 *Fortschr. Phys.* **48** 801
Mintert F and Wunderlich C 2001 *Phys. Rev. Lett.* **87** 257904
[10] Porras D and Cirac J I 2004 *Phys. Rev. Lett.* **92** 207901
[11] Friedenauer A *et al* 2008 *Nature Phys.* **4** 757
Kim K *et al* 2009 *Phys. Rev. Lett.* **103** 120502
Kim K *et al* 2010 *Nature* **465** 590
Edwards E E *et al* 2010 *Phys. Rev.* B **82** 060412
Islam R *et al* 2011 *Nature Commun.* **2** 377
[12] Barreiro J T *et al* 2011 *Nature* **470** 486
Lanyon B P *et al* 2011 *Science* **334** 57
[13] Pons M *et al* 2007 *Phys. Rev. Lett.* **98** 023003
[14] Bermudez A, Porras D and Martin-Delgado M A 2009 *Phys. Rev.* A **79** 060303
[15] Hauke P *et al* 2010 *New J. Phys.* **12** 113037
Lin G-D, Monroe C and Duan L-M 2011 *Phys. Rev. Lett.* **106** 230402
Bermudez A *et al* 2011 *Phys. Rev. Lett.* **107** 207209
[16] Ivanov P A and Schmidt-Kaler F 2011 *New J. Phys.* **13** 125008
[17] Müller M *et al* 2011 *New J. Phys.* **13** 085007
Schmied R, Wesenberg J H and Leibfried D 2011 *New J. Phys.* **13** 115011
[18] Schmied R *et al* 2008 *New J. Phys.* **10** 045017
[19] García-Mata I, Zhirov O V and Shepelyansky D L 2007 *Eur. Phys. J.* D **41** 325
Pruttivarasin T *et al* 2011 *New J. Phys.* **13** 075012
[20] Porras D, Marquardt F, von Delft J and Cirac J I 2008 *Phys. Rev.* A **78** 010101
[21] Ivanov P A *et al* 2009 *Phys. Rev.* A **80** 060301
[22] Bermudez A, Martin-Delgado M A and Porras D 2010 *New J. Phys.* **12** 123016

[23] Lamata L, Leon J, Schaetz T and Solano E 2007 *Phys. Rev. Lett.* **98** 253005
Gerritsma R *et al* 2010 *Nature* **463** 68
Gerritsma R *et al* 2011 *Phys. Rev. Lett.* **106** 060503
[24] Bermudez A, Schaetz T and Porras D 2011 *Phys. Rev. Lett.* **107** 150501
[25] Dunlap D H and Kenkre V M 1986 *Phys. Rev.* B **34** 3625
Grossman F *et al* 1991 *Phys. Rev. Lett.* **67** 516
Holthaus M 1992 *Phys. Rev. Lett.* **69** 351
[26] Grifoni M and Hänngi P 1998 *Phys. Rep.* **304** 229
[27] Drese K and Holthaus M 1997 *Chem. Phys.* **217** 201
Eckardt A *et al* 2005 *Phys. Rev. Lett.* **95** 260404
Creffield C E *et al* 2006 *Phys. Rev. Lett.* **96** 210403
Lignier H *et al* 2007 *Phys. Rev. Lett.* **99** 220403
Kierig E *et al* 2008 *Phys. Rev. Lett.* **100** 190405
Kolovsky A 2011 *Europhys. Lett.* **93** 20003
[28] Brown K R *et al* 2011 *Nature* **471** 196
Harlander M *et al* 2011 *Nature* **471** 200
[29] Schaetz T *et al* 2007 *J. Mod. Opt.* **54** 2317
Chiaverini J and Lybarger W E 2008 *Phys. Rev.* A **77** 022324
Labaziewicz J *et al* 2008 *Phys. Rev. Lett.* **100** 013001
[30] Schmied R, Wesenberg J H and Leibfried D 2009 *Phys. Rev. Lett.* **102** 233002
[31] Schmidt S *et al* 2010 *Phys. Rev.* B **82** 100507
[32] Ma R *et al* 2011 *Phys. Rev. Lett.* **107** 095301
[33] Jaksch D and Zoller P 2003 *New J. Phys.* **5** 56
see also Dalibard J, Gerbier F, Juzeliünas G and Öhberg P 2011 *Rev. Mod. Phys.* **83** 1523
[34] Abramowitz M and Stegun I A 1965 *Handbook of Mathematical Functions* (New York: Dover)
[35] Aharonov Y and Bohm D 1959 *Phys. Rev.* **115** 485
[36] Montvay I and Munster G 1994 *Quantum Fields on a Lattice* (New York: Cambridge University Press)
[37] Peierls R 1933 *Z. Phys.* **80** 763
[38] Myatt C J *et al* 2000 *Nature* **403** 269
[39] Azbel Ya M 1964 *Zh Eksp. Teor. Fiz.* **46** 929
Azbel Ya M 1964 *Sov. Phys.—JETP* **19** 634 (Engl. transl.)
Harper P G 1955 *Proc. Phys. Soc.* A **68** 874
Hofstadter D R 1976 *Phys. Rev.* B **14** 2239
[40] Thouless D J, Kohmoto M, Nightingale M P and den Nijs M 1982 *Phys. Rev. Lett.* **49** 405
Thouless D J and Niu Q 1983 *J. Phys. A: Math. Gen.* **16** 1911
Rammal R, Toulouse G, Jaekel M T and Halperin B I 1983 *Phys. Rev.* B **27** 5142
Lieb E H 1994 *Phys. Rev. Lett.* **73** 2158
[41] Vidal J, Mosseri R and Doucot B 1998 *Phys. Rev. Lett.* **81** 5888
Vidal J, Doucot B, Mosseri R and Butaud P 2000 *Phys. Rev. Lett.* **85** 3906
Creutz M 1999 *Phys. Rev. Lett.* **83** 2636
Bermudez A, Patane D, Amico L and Martin-Delgado M A 2009 *Phys. Rev. Lett.* **102** 135702
[42] Fisher M P A *et al* 1989 *Phys. Rev.* B **40** 546
[43] Sorensen A S, Demler E and Lukin M D 2005 *Phys. Rev. Lett.* **94** 086803
Hafezi M *et al* 2007 *Phys. Rev.* A **76** 023613
Möller G and Cooper N R 2009 *Phys. Rev. Lett.* **103** 105303
[44] Jaksch D *et al* 1998 *Phys. Rev. Lett.* **81** 3108
Greiner M *et al* 2002 *Nature* **415** 39
[45] Hasan M Z and Kane C L 2010 *Rev. Mod. Phys.* **82** 3045
Qi X L and Zhang S C 2011 *Rev. Mod. Phys.* **83** 1057

[46] Wineland D J *et al* 1998 *J. Res. Natl Inst. Stand. Technol.* **103** 259
Leibfried D *et al* 2003 *Rev. Mod. Phys.* **75** 281
Haeffner H *et al* 2008 *Phys. Rep.* **469** 155
[47] James D F V 1998 *Appl. Phys.* B **66** 181
[48] Zee A 2003 *Quantum Field Theory in a Nutshell* (Princeton, NJ: Princeton University Press)
[49] Kane C L and Mele E J 2005 *Phys. Rev. Lett.* **95** 146802
Bernevig B A, Hughes T L and Zhang S C 2006 *Science* **314** 1757
Goldman N *et al* 2010 *Phys. Rev. Lett.* **105** 255302
[50] Ziman J M 1979 *Models of Disorder: The Theoretical Physics of Homogeneously Disordered Systems* (Cambridge: Cambridge University Press)
[51] Gavish U and Castin Y 2005 *Phys. Rev. Lett.* **95** 020401
Paredes B, Verstraete F and Cirac J I 2005 *Phys. Rev. Lett.* **95** 140501
[52] Altman E, Kafri Y, Polkovnikov A and Refael G 2004 *Phys. Rev. Lett.* **93** 150402
Balabanyan K G, Prokofev N and Svistunov B 2005 *Phys. Rev. Lett.* **95** 055701
Sengupta P and Haas S 2007 *Phys. Rev. Lett.* **99** 050403
[53] Anderson P W 1958 *Phys. Rev.* **109** 1492
Kramer B and MacKinnon A 1993 *Rep. Prog. Phys.* **56** 1469
[54] Altman E, Kafri Y, Polkovnikov A and Refael G 2008 *Phys. Rev. Lett.* **100** 170402
[55] Weeks C, Rosenberg G, Seradjeh B and Franz M 2007 *Nature Phys.* **3** 796
Rosenberg C, Seradjeh B, Weeks C and Franz M 2009 *Phys. Rev.* B **79** 205102

PHYSICAL REVIEW A **85**, 040302(R) (2012)

# Robust trapped-ion quantum logic gates by continuous dynamical decoupling

A. Bermudez,[1] P. O. Schmidt,[2] M. B. Plenio,[1] and A. Retzker[1]

[1]*Institut für Theoretische Physik, Albert-Einstein Allee 11, Universität Ulm, 89069 Ulm, Germany*

[2]*QUEST Institute, Physikalisch-Technische Bundesanstalt and Leibniz University Hannover, 38116 Braunschweig, Germany*

(Received 20 October 2011; published 4 April 2012)

We introduce a scheme that combines phonon-mediated quantum logic gates in trapped ions with the benefits of continuous dynamical decoupling. We demonstrate theoretically that a strong driving of the qubit decouples it from external magnetic-field noise, enhancing the fidelity of two-qubit quantum gates. Moreover, the scheme does not require ground-state cooling, and is inherently robust to undesired ac Stark shifts. The underlying mechanism can be extended to a variety of other systems where a strong driving protects the quantum coherence of the qubits without compromising the two-qubit couplings.

DOI: 10.1103/PhysRevA.85.040302 PACS number(s): 03.67.Lx, 32.80.Qk, 37.10.Ty

A quantum processor is an isolated quantum device where information can be stored quantum-mechanically over long periods of time, but can be also manipulated and retrieved. This forbids its perfect isolation, making such a device sensitive to the noise introduced by either external sources, or experimental imperfections. Additionally, the interactions between distant quantum bits (qubits), as required to perform quantum logic operations, are frequently achieved by auxiliary (quasi)particles whose fluctuations introduce an additional source of noise. As emphasized recently [1], one of the big challenges of quantum-information science is the quest for methods to cope with all these natural error sources, achieving error rates that allow fault-tolerant quantum error correction.

We address this problem for trapped atomic ions [2]. Among the most relevant sources of noise in this system [3], we can list the following: (i) thermal noise introduced by auxiliary phonons, (ii) fluctuating external magnetic fields, (iii) uncompensated ac Stark shifts due to fluctuations in the laser parameters, and (iv) drifts in the phases of the applied laser beams. There are two different strategies to overcome these obstacles: (a) Minimize the thermal fluctuations by laser cooling [4], searching for gates operating faster than the time scale set by the other noise sources [5], or (b) look for schemes that are *intrinsically robust* to the noise. Among the latter, there are schemes that provide partial solutions, such as the gates robust to the thermal ion motion [6,7], or the encoding in magnetic-field-insensitive states [8] and decoherence-free subspaces [9]. Recently, there has been a growing effort to implement microwave-based quantum-information processing [10–12], exploiting the excellent control over the phase and amplitude of microwaves as compared to laser fields. Despite these efforts, it remains a key challenge to suppress all of the above sources of noise. Here, we propose to accomplish such a step, achieving fault-tolerant error bounds, by a continuous version of dynamical decoupling at reach of current technology.

While pulsed dynamical decoupling is a well-developed technique [13], already demonstrated for ions [14], its optimal combination with two-qubit gates requires a considerable additional effort [15]. Hence, simpler protocols are a subject of recent interest [11,16]. We hereby present a decoupling scheme well suited, but not limited, to trapped-ion experiments with three important properties: *generality*, *simplicity*, and *robustness*. It is sufficiently general to be applied to any type of ion qubits. It is simple since it combines two standard tools, namely, a carrier and a red-sideband excitation. In particular, it relies on the strong driving of the carrier transition, which may be realized by laser beams for optical qubits, or by microwaves for hyperfine and Zeeman qubits. With this independent driving source, we improve simultaneously the performance and the speed of the gate, as compared to the light-shift gates [17]. Besides, this driving has the potential of simplifying certain aspects of previous gate schemes [18], and is responsible for the gate robustness at different levels.

*The system.* We focus on $^{25}Mg^{+}$ to exploit the benefits of microwave technology [19], although the scheme is also valid for other species. Our qubit consists of two hyperfine states $|0\rangle,|1\rangle$ with energy difference $\omega_0$ [see Fig. 1(a) and Table I]. The ions form a string along the axis of a linear Paul trap with radial and axial frequencies $\omega_x,\omega_z$. The small radial vibrations yield a set of vibrational modes of frequencies $\omega_n$, whose excitations are the transverse phonons $a_n,a_n^\dagger$ [18]. If the qubit-qubit couplings are mediated by these quasiparticles [20], the scheme becomes less sensitive to ion heating or thermal motion, and it is easier to operate within the Lamb-Dicke regime.

As shown in Fig. 1(a), a pair of laser beams in a Raman configuration induces a transition between the qubit states. By setting their frequency beatnote $\omega_L$ close to $\omega_0-\omega_n$, such that the detuning $\delta_n=\omega_L-(\omega_0-\omega_n)$ is much smaller than the radial trap frequency [see Table I for the bare detuning $\delta_L=\omega_L-(\omega_0-\omega_x)$], one obtains the red-sideband excitation. In addition, we drive the carrier transition. For our particular qubit choice, this driving can be performed with microwave radiation of frequency $\omega_d$, such that $H_t=H_c+H_r$ is

$$H_t=\sum_i\frac{\Omega_d}{2}\sigma_i^+e^{-i(\omega_d-\omega_0)t}+\sum_{in}\mathcal{F}_{in}\sigma_i^+a_ne^{-i\delta_nt}+\text{H.c.}, \quad (1)$$

where we have introduced the microwave Rabi frequency $\Omega_d$, and the sideband coupling strengths $|\mathcal{F}_{in}|\propto\Omega_L\eta$ scale linearly with the laser Rabi frequency $\Omega_L$ and Lamb-Dicke parameter $\eta$, such that $|\mathcal{F}_{in}|\ll\delta_n$ (Table I). Here, we use the spin operators $\sigma_i^+=|1_i\rangle\langle 0_i|$, and we work in the interaction picture rotating with the phonon and qubit frequencies.

*Sideband gates and thermal noise.* We first introduce an intuitive picture. The Hamiltonian (1) for $\Omega_d=0$ combines

 

TABLE I. Specific values of the trapped-ion setup.

| $\omega_0/2\pi$ | $\omega_x/2\pi$ | $\omega_z/2\pi$ | $\eta$ | $\lvert\delta_L\rvert/2\pi$ | $\Omega_L/2\pi$ | $\Omega_d/2\pi$ | $B_0$ |
|---|---|---|---|---|---|---|---|
| 1.8 GHz | 4 MHz | 1 MHz | 0.2 | 800 kHz | 500 kHz | 5.2 MHz | 4 mT |

two noncommuting spin-dependent forces. Each one aims at displacing the normal modes along a closed trajectory in phase space determined by the eigenstates $|\pm_x\rangle,|\pm_y\rangle$ of $\sigma^x,\sigma^y$ [18]. In Fig. 1(b), we describe the action of the $\sigma^x$ force on a single ion [6,7]. Depending on the state $|\pm_x\rangle$, the ion follows a different path in phase space, and after returning to the starting point, it picks a geometric phase only determined by the enclosed area, and independent of the motional state. In contrast, for a single red sideband, $\sigma_x$ and $\sigma_y$ forces are implemented, resulting in rotations around two orthogonal axis [Fig. 1(c)]. In a Trotter decomposition, the concatenation of these orthogonal displacements spoils the closing of the trajectory, such that the qubit and phonon states remain entangled. As shown below, this makes the gate sensitive to thermal fluctuations.

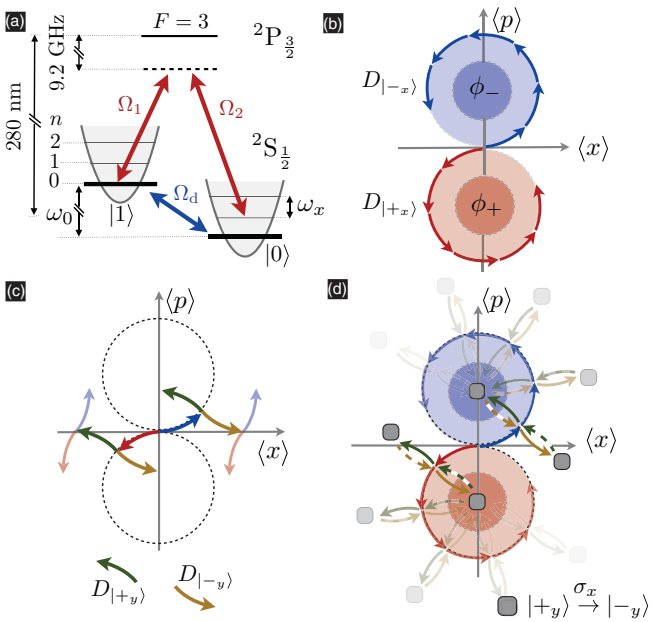


FIG. 1. (Color online) (a) Hyperfine structure of $^{25}Mg^+$. The states $|0\rangle = |F = 3, m_F = 3\rangle$ and $|1\rangle = |2,2\rangle$ form our qubit. Two laser beams $\Omega_1,\Omega_2$ drive the red sideband via an off-resonant excited state, and a microwave $\Omega_d$ directly couples to the transition. (b) Spin-dependent $\sigma^x$ force acting on a single trapped ion. The phonons associated with the states $|+_x\rangle,|-_x\rangle$ are displaced in phase space according to $D_{|\pm_x\rangle}$, and form different closed paths that lead to the geometric phases $\phi_\pm$. (c) Trotterization of the combined $\sigma^x$ and $\sigma^y$ forces. The $\sigma^x$ displacement $D_{|+_x\rangle}$ shall be followed by the two possible $\sigma^y$ displacements $D_{|\pm_y\rangle}$ since $|+_x\rangle \propto (|+_y\rangle + i|-_y\rangle$. Hence, the phase-space trajectory is not generally closed. (d) Schematic spin-echo refocusing of the $\sigma^y$ force. By applying a $\pi$-pulse $X_i^\pi = \sigma_i^x$ (box) at half the $\sigma^y$ displacements, one obtains $|\pm_y\rangle \to |\mp_y\rangle$, such that the displacements are reversed (dotted arrows), and the trajectory is refocused, yielding a well-defined geometric phase.

For large detunings $|\delta_L| \gg \Omega_L\eta$, the lasers only excite virtually the vibrational modes, and the phonons can be adiabatically eliminated. In fact, it is the process where a phonon is virtually created by an ion, and then reabsorbed by a distant one, which gives rise to the effective $XY$ couplings [21]

$$H_{\rm eff} = \sum_{ij} J_{ij}^{\rm eff}\sigma_i^+\sigma_j^-, \quad J_{ij}^{\rm eff} = -\sum_n \frac{1}{\delta_n}\mathcal{F}_{in}\mathcal{F}_{jn}^*. \tag{2}$$

At certain instants of time, the unitary evolution corresponds to a SWAP gate [22], which performs the logic operation $|1_i 0_j\rangle \leftrightarrow |0_i 1_j\rangle$ while leaving the remaining states unchanged. However, there is an additional process that spoils the performance of the gate, namely, the phonon might be reabsorbed by the same ion. This leads to a residual spin-phonon coupling

$$H_{\rm res} = \sum_i \hat{B}_i(t)\sigma_i^z, \quad \hat{B}_i(t) = \sum_{nm} B_{inm}a_m^\dagger a_n e^{-i(\omega_n-\omega_m)t}, \tag{3}$$

where $B_{inm} = -\frac{1}{2}\mathcal{F}_{in}\mathcal{F}_{im}^*(\frac{1}{\delta_n} + \frac{1}{\delta_m})$. Accordingly, the resonance frequency fluctuates in time due to the motional dynamics, leading to a *local thermal noise* in the limit of many ions that introduces dephasing. In Fig. 2(a), the critical effect of this term on the SWAP gate is displayed. We compare the numerical simulation of the full spin-phonon Hamiltonian to the effective idealized description (2). As evidenced in this figure, the gate performance is severely modified by the thermal phonon ensemble. As the mean phonon number is increased, the oscillations get a stronger damping, and the generation of Bell states at half the SWAP periods (arrows) deteriorates.

*Achieving robustness against thermal noise*. We now show how to protect the coherent spin dynamics from this thermal dephasing by switching $\Omega_d \neq 0$. Schematically, this may be

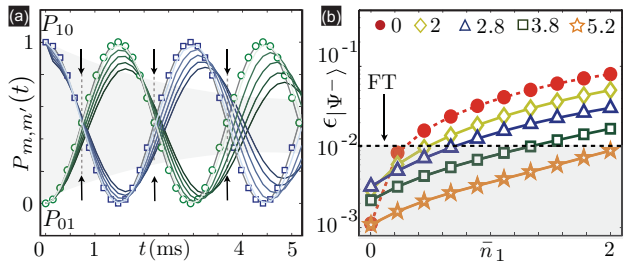


FIG. 2. (Color online) (a) Dynamics of the swap probabilities $P_{10}(t)$ (squares) and $P_{01}(t)$ (circles) for the effective gate (2), compared to the exact spin-phonon Hamiltonian for a two-ion crystal with $\bar{n} = \{0,0.1,1,2,4\}$ (solid lines). The phonon Hilbert space is truncated to $n_{\max} = 20$ excitations per mode. (b) Error $\epsilon = 1 - \mathcal{F}$ for the generation of the Bell state $|\Psi^-\rangle$ as a function of the mean phonon number and $n_{\max} = 14$. As the driving is increased, $\Omega_d/\omega_z \in \{0,2,3.8,5.2\}$, the error lies within the fault-tolerance (FT) threshold.

accomplished by refocusing one of the spin-dependent forces using a series of spin-echo pulses [23] that invert the atomic state [Fig. 1(d)]. We show that the strong driving of the carrier transition implements a continuous version of this refocusing, providing a viable mechanism for overcoming this noise. As will become clear later on, this driving also minimizes the undesired errors due to ac Stark shifts and magnetic-field noise.

A helpful account of the decoupling mechanism may be the following. In the dressed-state basis of the driving $|\pm_x\rangle_i = (|1_i\rangle \pm |0_i\rangle)/\sqrt{2}$, the residual spin-phonon coupling becomes $H_{\rm res}(t) = \sum_{inm} B_{inm}|+_x\rangle_i\langle -_x|a_m^\dagger a_n e^{i[\Omega_{\rm d}-(\omega_n-\omega_m)]t} + {\rm H.c.}$ For a strong driving strength $\Omega_{\rm d}$, this term rotates very fast even for two vibrational modes that are close in frequency, and can be thus neglected in a rotating-wave approximation. Note that the same argument applies for any stable driving phase [18].

This simple argument has to be readdressed for a combination of the carrier and red-sideband interactions (1), since the residual couplings are no longer described by Eq. (3). In order to show that a similar argument can still be applied, we have performed a polaron-type transformation [18]. We find that the dynamics is described by the effective Hamiltonian

$$\tilde{H}_{\rm eff} = \sum_{ij} \tilde{J}_{ij}^{\rm eff}\sigma_i^x\sigma_j^x + \frac{1}{2}\sum_i \Omega_{\rm d}\sigma_i^x, \quad \tilde{J}_{ij}^{\rm eff} = \tfrac{1}{4}J_{ij}^{\rm eff}, \tag{4}$$

whereas the residual spin-phonon coupling is given by

$$\tilde{H}_{\rm res} = \sum_{in} \frac{i}{2}(\mathcal{F}_{in}a_n - \mathcal{F}_{in}^* a_n^\dagger)\left(\cosh\hat{\Theta}_i\sigma_i^y - i\sinh\hat{\Theta}_i\sigma_i^z\right), \tag{5}$$

such that $\hat{\Theta}_i = \sum_m(\mathcal{F}_{im}a_m - \mathcal{F}_{im}^* a_m^\dagger)/2\delta_m$. By moving to the dressed-state basis, the residual term only involves transitions between the dressed eigenstates $|+_x\rangle \leftrightarrow |-_x\rangle$, supplemented by the transformation on the phonons encoded in the different powers of $\hat{\Theta}_i$. Fortunately, all these transitions are inhibited due to the large energy gap between the dressed states set by $\Omega_{\rm d}$. More precisely, in the strong driving regime $\Omega_{\rm d} \gg 2\delta_n$ (see Table I), the leading-order terms of the residual coupling (5) can be neglected in a rotating-wave approximation.

To check the correctness of this argument, we integrate numerically the complete Hamiltonian (1), and take into account the thermal motion of the trapped ions. After the unitary evolution $U(t_{\rm f}) = U(t_{\rm f}, \frac{1}{2}t_{\rm f}t)(\sigma_i^z\sigma_j^z)U(\frac{1}{2}t_{\rm f},0)$, we calculate the fidelity of producing the Bell state $|\Psi^-\rangle = (|10\rangle - i|01\rangle)/\sqrt{2}$, $\mathcal{F}_{|\Psi-\rangle} = \max_{t_{\rm f}}\{\langle\Psi^-|{\rm Tr}_{\rm ph}[U(t_{\rm f})\rho_0 U^\dagger(t_{\rm f})]|\Psi^-\rangle\}$. The results displayed in Fig. 2(b) demonstrate the promised decoupling from the thermal noise, where one observes that the fidelity of the gate improves considerably when $\Omega_{\rm d} \gg 2\delta_n$. For driving strengths in the 4–5 MHz range, the gate error lies within the fault-tolerance threshold $\epsilon_{\rm t} \sim 10^{-2}$–$10^{-4}$ [24] for states with mean phonon numbers $\bar{n} \leqslant 2$. However, we expect a lower fidelity when experimental imperfections are considered.

In Fig. 3, we describe the experimental steps required to create the desired Bell state. In the first step, the qubits are optically pumped to $|0\rangle$, and the initial state $|\psi_0\rangle = |10\rangle$ is prepared by a $\pi$-pulse $X_1^\pi$ obtained from a microwave resonant with the carrier transition. Three comments are now in order. First, a magnetic field $B_0 \approx 4$ mT needs to

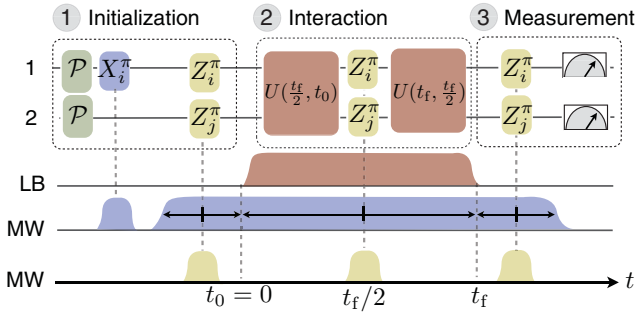


FIG. 3. (Color online) The two upper rows represent the circuit model for the two qubits, and the lower rows represent the switching of the laser beams (LB) and microwaves (MW). The initialization consists of optical pumping $\mathcal{P}$, followed by a local $\pi$-pulse $X_i^\pi = \sigma_i^x$. Global $\pi$-pulses $Z_i^\pi = \sigma_i^z$ correct possible synchronization errors. The two-qubit coupling is applied by switching on the red sideband (LB), and the carrier (MW) yields the noise decoupling.

be applied to ensure a sufficiently large Zeeman splitting between magnetic states to avoid driving unwanted transitions. Note that the motional excitation due to the microwave is negligible owing to the vanishing Lamb-Dicke factor. Second, either the ac Stark shift from an off-resonant laser beam or a magnetic-field gradient is required to effectively hide the second ion. Alternatively, one could use ion shuttling techniques [25]. Third, we account for the worst possible scenario by considering (i) different switching times of the lasers and microwaves, and (ii) imperfect timing with the microwave. By introducing global $\pi$-pulses $Z_1^\pi Z_2^\pi$ from the energy shift of an off-resonant strong microwave, we refocus the fast oscillations caused by the resonant microwave and correct the possible difference of switching times. In the second step, the two-qubit coupling is applied at $t = t_0$ by switching on the laser beams responsible for the red sideband. Again, a refocusing pulse at $t = t_{\rm f}/2$ shall correct for the imperfect synchronization. In the final step, after switching off the laser and microwaves at $t = t_{\rm f}$, the qubit state is measured by state-dependent fluorescence techniques. If the announced decoupling has worked correctly, this two-qubit gate should have generated the entangled Bell state $|\Psi^-\rangle$ regardless of the phonon state. Let us emphasize that this gate is capable of producing the remaining Bell states by choosing different initial states [18] and, together with single-qubit rotations, becomes universal for quantum computation.

*Resilience to magnetic-field noise and ac-Stark shifts.* So far, we have neglected the effects of the environment. In standard traps, the leading source of noise is due to environmental fluctuating magnetic fields, which limit the coherence times of magnetic-field-sensitive states to milliseconds [3]. This is particularly important for multi-ion entangled states [26], and will also play a role in our scheme considering that $\tilde{J}_{\rm eff}/2\pi \approx 1$ kHz. We model the global magnetic-field noise by a fluctuating resonance frequency $H_{\rm n} = \frac{1}{2}\sum_i F(t)\sigma_i^z$. Here, $F(t)$ is a stochastic Markov process [27] characterized by a diffusion constant $c$ and a correlation time $\tau$, which leads to $\langle\sigma^x(t)\rangle = e^{-t/T_2}$ with $T_2 = 2/c\tau^2$ [18]. By fixing these parameters, we can reproduce the experimentally observed $T_2 \approx 5$ ms [Fig. 4(a)], and study its consequences on the two-qubit

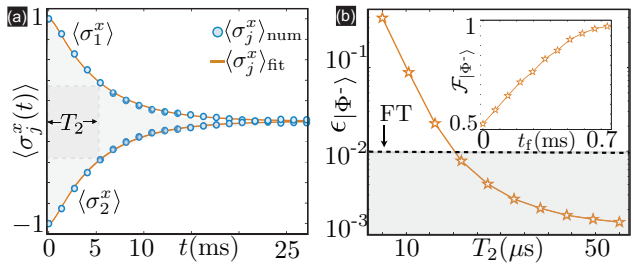


FIG. 4. (Color online) (a) Exponential decay of the coherences $\langle\sigma^x(t)\rangle$ for the initial states $|\psi_0\rangle = |\pm_x\rangle$. The circles represent the numerical statistical average of the $N = 5 \times 10^3$ evolutions, and the solid line represents the exponential fit. (b) Error in the generation of the Bell state $|\Phi^-\rangle$ for the additional magnetic-field noise, together with a strong driving $\Omega_d/2\pi = 5.2$ MHz. The error is presented as a function of the $T_2$ time. In the inset, we represent the evolution of the fidelity for the typical noise dephasing time $T_2 = 5f$ ms.

entangling gate. Notice that the evolution within the zero-magnetization subspace is not affected by this global noise, which is a decoherence-free subspace. Hence, we have studied the fidelity for the Bell state $|\Phi^-\rangle = (|11\rangle - i|00\rangle)/\sqrt{2}$.

The strong driving $\Omega_d$ protects the qubit coherences from this magnetic noise without compromising the entangling gate, and may be considered as a continuous version [11,28] of the so-called dynamical decoupling [13]. To single out the effects of the noise from those of the thermal motion, we have considered a ground-state cooled crystal, setting $\Omega_d/2\pi = 5.2$ MHz to ensure that the results can be carried out to higher temperatures [Fig. 2(b)]. We evaluate numerically the fidelity of generating the Bell state $|\Phi^-\rangle$ by averaging over different samplings of the random noise [inset of Fig. 4(b)]. Due to the decoupling, the fidelity approaches unity at the gate time $t_f = 0.7$ ms. In the main panel of Fig. 4(b), we show that the gate error for shorter coherence times still lies below the fault-tolerance threshold, which demonstrates that the decoupling mechanism supports a stronger magnetic noise. Alternatively, this tells us that the gate tolerates smaller speeds, and thus lower Rabi frequencies of the Raman beams. This shall reduce even further the thermal error studied above, and the spontaneous scattering of photons due to the Raman configuration. We have also calculated the fidelity of the quantum channel with respect to the desired quantum gate $U_{\rm eff} = e^{-i\frac{\pi}{4}\sigma_i^x\sigma_j^x}$ [18], which also lies within the fault-tolerance threshold.

As an additional advantage of our scheme, we note that it also minimizes the effects of uncompensated ac Stark shifts. In the implementations of the geometric phase gates, the shifts caused by off-resonant transitions to all possible states must be compensated by tuning the laser intensities, frequencies, and polarizations [29]. However, fluctuations of these parameters will introduce additional noise. In contrast, these energy shifts are canceled in our scheme by the strong driving, in analogy to the minimization of fluctuating Zeeman shifts. Let us finally comment on the effect of phase instabilities on the gate. In contrast to Mølmer-Sørensen (MS) gates [6], our scheme does not depend on the slow drift of the laser phases. The second-order process, whereby a phonon is virtually excited and then reabsorbed, is associated with the creation and subsequent annihilation of photons in the same pair of Raman beams, giving rise to the insensitivity to slow changes of the phase [see Eq. (2)]. In contrast, the MS scheme involves two different pairs of Raman beams, such that the crosstalk leads to the phase sensitivity. Hence, our gate (4) only relies on the phase of the microwave, which is easier to stabilize as compared to the phase of the laser beams. We note that concatenated drivings may overcome amplitude fluctuations [30].

*Conclusions*. We have introduced a scheme that merges continuous dynamical decoupling with warm quantum gates in trapped ions. The decoupling, on top of reducing the magnetic noise, is also responsible for the robustness with respect to thermal fluctuations and ac Stark shifts. Although we have focused on sideband interactions, our scheme could also protect MS gates from magnetic-field fluctuations and ac Stark shifts. Moreover, these ideas may find applications in other architectures that use a bosonic data bus to couple distant qubits, such as superconducting qubits coupled to transmission lines, or color centers in nanodiamonds coupled to nanomechanical resonators.

*Note added*. Recently we became aware of the interest in similar ideas for atoms in thermal cavities [31] and decoherence-free states in ion traps [32].

*Acknowledgment*. We are supported by HIP, PICC, AQUTE, QESSENCE, QUEST, and by the Alexander von Humboldt Foundation.

[1] T. D. Ladd *et al*., Nature (London) **464**, 45 (2010).
[2] R. Blatt *et al*., Nature (London) **453**, 1008 (2008).
[3] D. J. Wineland *et al*., J. Res. Natl. Inst. Stand. Technol. **103**, 259 (1998); D. Leibfried *et al*., Rev. Mod. Phys. **75**, 281 (2003); H. Haeffner *et al*., Phys. Rep. **469**, 155 (2008).
[4] J. I. Cirac and P. Zoller, Phys. Rev. Lett. **74**, 4091 (1995); C. Monroe, D. M. Meekhof, B. E. King, W. M. Itano, and D. J. Wineland, *ibid*. **75**, 4714 (1995); F. Schmidt-Kaler *et al*., Nature (London) **422**, 408 (2003).
[5] A. Steane *et al*., Phys. Rev. A **62**, 042305 (2000); J. J. Garcia-Ripoll, P. Zoller, and J. I. Cirac, Phys. Rev. Lett. **91**, 157901 (2003); L.-M. Duan, *ibid*. **93**, 100502 (2004).
[6] A. Sørensen and K. Molmer, Phys. Rev. Lett. **82**, 1971 (1999); J. Benhelm *et al*., Nat. Phys. **4**, 463 (2008).
[7] G. J. Milburn *et al*., Fortschr. Phys. **48**, 801 (2000); D. Leibfried *et al*., Nature (London) **422**, 412 (2003).
[8] J. J. Bollinger *et al*., IEEE Trans. Instrum. Meas. **40**, 126 (1991); C. Langer *et al*., Phys. Rev. Lett. **95**, 060502 (2005); P. C. Haljan *et al*., Phys. Rev. A **72**, 062316 (2005).
[9] D. A. Lidar, I. L. Chuang, and K. B. Whaley, Phys. Rev. Lett. **81**, 2594 (1998); D. Kielpinski *et al*., Science **291**, 1013 (2001); T. Monz *et al*., Phys. Rev. Lett. **103**, 200503 (2009).
[10] F. Mintert and C. Wunderlich, Phys. Rev. Lett. **87**, 257904 (2001); A. Khromova *et al*., e-print arXiv:1112.5302.

[11] N. Timoney *et al*., Nature (London) **476**, 185 (2011).
[12] C. Ospelkaus *et al*., Phys. Rev. Lett. **101**, 090502 (2008); Nature (London) **476**, 181 (2011).
[13] L. Viola, E. Knill, and S. Lloyd, Phys. Rev. Lett. **82**, 2417 (1999); L. Viola, S. Lloyd, and E. Knill, *ibid*. **83**, 4888 (1999).
[14] M. Biercuk *et al*., Nature (London) **458**, 996 (2009); D. J. Szwer *et al*., J. Phys. B **44**, 02550 (2011).
[15] S. Montangero, T. Calarco, and R. Fazio, Phys. Rev. Lett. **99**, 170501 (2007).
[16] P. Rabl *et al*., Phys. Rev. B **79**, 041302(R) (2009).
[17] D. Jonathan, M. B. Plenio, and P. L. Knight, Phys. Rev. A **62**, 042307 (2000); D. Jonathan and M. B. Plenio, Phys. Rev. Lett. **87**, 127901 (2001).
[18] See Supplemental Material at http://link.aps.org/supplemental/10.1103/PhysRevA.85.040302 for a detailed description of the technical aspects of this work, and for a comparison to other existing gate schemes.
[19] B. Hemmerling *et al*., Appl. Phys. B **104**, 583 (2011).
[20] D. Porras and J. I. Cirac, Phys. Rev. Lett. **92**, 207901 (2004); S.-L. Zhu, C. Monroe, and L.-M. Duan, *ibid*. **97**, 050505 (2006).
[21] E. H. Lieb *et al*., Ann. Phys. **16**, 407 (1961); A. Bermudez *et al*., New J. Phys. **12**, 123016 (2010).
[22] M. A. Nielsen and I. L. Chuang, *Quantum Computation and Quantum Information* (Cambridge University Press, Cambridge, UK, 2004).
[23] E. L. Hahn, Phys. Rev. **80**, 580 (1950).
[24] A. M. Steane, Phys. Rev. A **68**, 042322 (2003).
[25] D. Kielpinski *et al*., Nature (London) **417**, 709 (2002).
[26] T. Monz *et al*., Phys. Rev. Lett. **106**, 130506 (2011).
[27] D. T. Gillespie, Am. J. Phys. **64**, 3 (1996).
[28] P. Facchi and S. Pascazio, Phys. Rev. Lett. **89**, 080401 (2002); K. M. Fonseca-Romero, S. Kohler, and P. Hanggi, *ibid*. **95**, 140502 (2005).
[29] D. J. Wineland *et al*., Philos. Trans. R. Soc., A **361**, 1349 (2003).
[30] J.-M. Cai, F. Jelezko, M. B. Plenio, and A. Retzker, e-print arXiv:1111.0930.
[31] S.-B. Zheng, Phys. Rev. A **66**, 060303(R) (2002).
[32] A. Noguchi, S. Haze, K. Toyoda, and S. Urabe, Phys. Rev. Lett. **108**, 060503 (2012).